

Advanced Test Reactor Core Modeling Update Project

Annual Report for Fiscal Year 2013

September 2013



The INL is a U.S. Department of Energy National Laboratory
operated by Battelle Energy Alliance

DISCLAIMER

This information was prepared as an account of work sponsored by an agency of the U.S. Government. Neither the U.S. Government nor any agency thereof, nor any of their employees, makes any warranty, expressed or implied, or assumes any legal liability or responsibility for the accuracy, completeness, or usefulness, of any information, apparatus, product, or process disclosed, or represents that its use would not infringe privately owned rights. References herein to any specific commercial product, process, or service by trade name, trade mark, manufacturer, or otherwise, does not necessarily constitute or imply its endorsement, recommendation, or favoring by the U.S. Government or any agency thereof. The views and opinions of authors expressed herein do not necessarily state or reflect those of the U.S. Government or any agency thereof.

Advanced Test Reactor Core Modeling Update Project

Annual Report for Fiscal Year 2013

Edited by: David W. Nigg, Principal Investigator and
Kevin A. Steuhm, Project Manager

September 2013

**Idaho National Laboratory
Nuclear Science and Technology Directorate
for the
ATR Life Extension Program
Idaho Falls, Idaho 83415**

**Prepared for the
U.S. Department of Energy
Office of Nuclear Energy
Under DOE Idaho Operations Office
Contract DE-AC07-05ID14517**

Nuclear Science and Technology Directorate

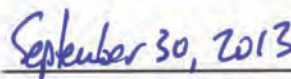
**Advanced Test Reactor Core Modeling Update Project
Annual Report for Fiscal Year 2013**

**INL/EXT-13-30085
September 2013**

Approval:



David W. Nigg, Principal Investigator



Date

EXECUTIVE SUMMARY

Legacy computational reactor physics software tools and protocols currently used for support of Advanced Test Reactor (ATR) core fuel management and safety assurance, and to some extent, experiment management, are inconsistent with the state of modern nuclear engineering practice, and are difficult, if not impossible, to verify and validate (V&V) according to modern standards. Furthermore, the legacy staff knowledge required for effective application of these tools and protocols from the 1960s and 1970s is rapidly being lost due to staff turnover and retirements. In late 2009, the Idaho National Laboratory (INL) initiated a focused effort, the ATR Core Modeling Update Project, to address this situation through the introduction of modern high-fidelity computational software and protocols. This aggressive computational and experimental campaign will have a broad strategic impact on the operation of the ATR, both in terms of improved computational efficiency and accuracy for support of ongoing DOE programs as well as in terms of national and international recognition of the ATR National Scientific User Facility (NSUF).

The ATR Core Modeling Update Project, targeted for full implementation in phase with the next anticipated ATR Core Internals Changeout (CIC) in the 2015-2016 time frame, began during the last quarter of Fiscal Year 2009, and has just completed its fourth full year. Key accomplishments so far have encompassed both computational as well as experimental work. A new suite of stochastic and deterministic transport theory based reactor physics codes and their supporting nuclear data libraries (HELIOS, KENO6/SCALE, NEWT/SCALE, ATTILA, SERPENT, MC21, and an extended implementation of MCNP5) has been installed at the INL under various licensing arrangements. Corresponding models of the ATR and ATRC are now operational with all seven codes, demonstrating the basic feasibility of the new code packages for their intended purpose. Of particular importance, an updated set of as-run core depletion HELIOS calculations for all ATR cycles since August 2009, Cycle 145A through Cycle 154A, was successfully completed during 2013, with excellent statistical consistency between calculation and measurement for key parameters such as critical shim positions and lobe powers throughout each cycle. This major effort was essential to our ability to proceed with a formal phased incorporation of the HELIOS methodology into the ATR Core Safety Analysis Package (CSAP) preparation process in parallel with the established PDQ-based methodology during the upcoming year, FY-14 and beyond.

Acquisition of the advanced SERPENT (VTT-Finland) and MC21 (DOE-NR) Monte Carlo stochastic neutronics simulation codes was also completed during the year and some basic applications of SERPENT to ATRC analysis for validation purposes were demonstrated as summarized in this Annual Report. These two new codes, unanticipated at the beginning of the Modeling Update Project, will offer significant additional capability, including the possibility of fully integrated 3D Monte Carlo core fuel management and experiment management support capabilities for the ATR at an appropriate point in the future.

On the experimental side of the project, a complete statistical analysis of the first four of six planned application-specific ATRC physics code validation measurements based on neutron activation spectrometry was completed in 2012 in accordance with applicable national and international standards and the fifth experiment was run in the ATRC late in 2013 with statistical data analysis to follow in 2014. The validation measurements will continue with one more planned experiment in 2014, which will include the introduction of additional new experimental hardware to broaden the scope of the validation protocols. Further opportunities to collaborate for code validation purposes with various other ongoing

experimental campaigns in the ATRC and ATR are also being identified as the Core Modeling Update Project proceeds, as exemplified by our successful efforts to make extensive use of additional code validation data from a “depressurized” low-power run (Cycle 152A) of the ATR that took place late in 2012, as documented in detail in this Annual Report.

A second component of the experimental validation campaign involves the possible construction of a system for non-invasive measurement of the burnup of ATR fuel elements *in-situ* in the ATR canal. Post-irradiation non-invasive ATR fuel burnup measurements can serve as a key fuel depletion model validation tool and also as an aid in improved fuel management. Initial in-canal feasibility measurements to identify appropriate engineering parameters and radiation measurement instrumentation for a system to perform this type of measurement were conducted during 2010 with significant additional progress in 2011 and early 2012. Progress in 2011-2012 included the preparation and transmittal, to the Department of Energy, of a proposal for construction of a permanent system for non-invasive *in-situ* fuel element burnup measurements in the ATR canal, as well as some feasibility studies for remote positioning of the detector used for the measurements. In 2013 additional improvements were made in the process for deconvolution of the detector signals produced by the system, as documented in this Annual report.

It is also important to recognize that the ATR Core Modeling Update Project represents not only an investment in new technology. It also represents a key investment in the new generation of INL scientific and engineering staff who will, by demographic necessity, assume leadership roles in the overall ATR enterprise over the next several years. Accordingly, several students and early-career INL Scientific and Engineering staff members have been proactively integrated into the effort, one student earned his doctoral degree in 2012, and it is anticipated that two additional students (1 MS and 1 PhD) will complete their advanced degrees early in Fiscal Year 2014 as a result of their involvement in the project.

Additionally, we note that although full implementation of the new computational models and protocols will extend over a period of time dictated by factors outside of the Modeling Update Project itself, interim applications of the new capabilities in the much nearer term have already been demonstrated. For example, these demonstrations included an analysis that was useful for understanding the cause of some ATR operational issues in February 2013 that were triggered by a larger than acceptable discrepancy between the estimated and measured critical shim position for Cycle 153A. Additionally, some initial computational support for a planned ATR irradiation experiment being conducted for a foreign customer was initiated in 2013 using the new methods. Furthermore, the new code system is being used extensively for core design calculations associated with the possible conversion of the ATR to a low-enriched uranium (LEU) type fuel at an appropriate time in the future. As the Core Modeling Update Project proceeds, we anticipate further such interim, informal applications in parallel with formal qualification of the system under applicable INL and external Quality Assurance procedures and standards.

Finally, it can be stated at this juncture that the Modeling Update Project has reached a point where all of the basic computational tools and modeling capabilities, along with corresponding validation protocols, are largely in place, and the focus during FY-2014 and beyond will be on integration of the new methods into the ATR Safety Engineering and operational environment. More specifically, the effort in 2014 will shift toward development of detailed interface protocols for computation of the large array of physics parameters required for startup and operation of each cycle. Approximately 60% of these protocols are already operational or in various stages of development and testing. The remaining 40% will be addressed as the project proceeds. In addition, extensive training in the use of the new computational systems and protocols will be provided to the ATR Engineering and Operations organizations by the Modeling Update Project team beginning in the second quarter of FY-2014, with continuing technical support afterward as needed.

CONTENTS

EXECUTIVE SUMMARY.....	v
ACRONYMS.....	viii
ACKNOWLEDGEMENTS.....	ix
1.0 INTRODUCTION	1
2.0 HELIOS-MCNP MODEL DEVELOPMENT FOR CSAP APPLICATIONS	14
3.0 VALIDATION PROTOCOL DEVELOPMENT AND DEMONSTRATION	60
4.0 VALIDATION EXPERIMENTS IN THE ATRC	94
5.0 LaBr ₃ GAMMA SPECTRAL DATA FOR ATR BURNUP VALIDATION.....	103
APPENDIX A. Element-Building Python Scripts and Input Files.....	134.

ACRONYMS

AGR	Advanced Gas Reactor
ANS	American Nuclear Society
ATR	Advanced Test Reactor
ATRC	Advanced Test Reactor Critical Facility
CIC	Core Internals Changeout
CSAP	Core Safety Assurance Package
ENDF	Evaluated Nuclear Data File
NGNP	Next Generation Nuclear Plant
NST	Nuclear Science and Technology
NSUF	National Scientific User Facility
RERTR	Reduced Enrichment for Research and Test Reactors
V&V	Verification and Validation
DHA	Detector Housing Assembly
HPGe	High Purity Germanium
HPXe	High Pressure Xenon
INL	Idaho National Laboratory
LaBr ₃	Lanthanum Bromide
OSCC	Outer Shim Control Cylinder
ESAP	Experiment Safety Analysis Package
IRPhE	OECD International Reactor Physics Experiment Evaluation (Program)
OECD	Organization for Economic Cooperation and Development
QA	Quality Assurance
LEP	(ATR) Life Extension Program
ICSBE	OECD International Criticality Safety Benchmark Experiment Evaluation (Program)
DOE	(US) Department of Energy
NR	Naval Reactors
VTT	National Research Centre (Finland)

ACKNOWLEDGEMENTS

The technical team for the ATR Core Modeling Update Project would like to gratefully acknowledge Dr. Charles Wemple, Studsvik Scandpower, for his essential assistance in the setup of the various HELIOS models, for the training of key INL staff members in the use of HELIOS, and for his overall review of the HELIOS ATR model effort as it proceeded. Additionally, we also thank Ms. Christine White (INL) for her assistance with many of the graphic illustrations in this report, Mr. Neil Boyce (INL) for the fabrication of new experimental hardware for use in the ATRC and ATR flux traps and Mr. Anthony LaPorta (INL) and the personnel of the INL Radiation Measurements Laboratory (RML) for provision of the physics measurement data for the ATR “depressurized run” support experiments that were conducted in the ATRC during 2012. Finally we wish to thank Dr. John Williams, University of Arizona for his valuable counsel with regard to the least-square adjustment based validation protocols that have been adapted for use with the ATR.

1.0 INTRODUCTION

David W. Nigg

This Annual Report documents the accomplishments of the ATR Core Modeling Update Project during Fiscal Year 2013. A brief overview of the background, rationale, organizational structure, and a basic summary of progress to-date for the project is provided below. Later sections cover additional detail on specific technical accomplishments during the fiscal year. Each section is designed to stand on its own, with its own set of references, to facilitate use of the information presented here in other reports and presentations as needed.

1.1 Description of the Advanced Test Reactor

The Advanced Test Reactor (ATR), located at the Idaho National Laboratory (INL), is one of only a few high-power research reactors of its type in the world, with a variety of missions involving accelerated testing of nuclear fuel and other materials in a very high neutron flux environment, medical and industrial isotope production, and other applications. Along with its companion critical mockup (ATRC), the ATR is one of the key nuclear engineering research and testing facilities within the US Department of Energy (DOE) National Laboratory Complex. The ATR and ATRC also serve as the centerpieces of the recently-formed ATR National Scientific User Facility (NSUF), whose purpose is to facilitate the current trend toward broadening the applications of the ATR beyond its traditional base.

The ATR (Figures 1.1 and 1.2) is a highly-heterogeneous light-water and beryllium moderated, beryllium reflected, light-water cooled system with highly-enriched (93% ^{235}U) plate-type fuel elements arranged in a serpentine pattern. Gross reactivity and power distribution control during operation is achieved through the use of eight pairs of rotating control drums with hafnium neutron absorber plates on one side as can be seen in Figure 1.1. There are several design features incorporated into the ATR and ATRC (Figures 1.3 and 1.4) to optimize experimental capabilities. These features include: a) the use of flux traps to provide high thermal neutron fluxes for irradiation or experiments in nine regions, b) incorporation of special control shim design features to retain axial flux symmetry throughout an ATR fuel cycle; and c) regional power control to provide capability for power shifting between core lobes to optimize the neutron flux distribution for a wide range of simultaneous experiments. The ATR can be operated at powers as high as 250 MW although most routine applications do not require the maximum power. Typical thermal neutron fluxes in the flux traps can be as high as 5.0×10^{14} n/cm²-s. Typical operating cycle lengths are in the range of 45–60 days. The core fuel configuration and the experiment loadings are usually rearranged between cycles and each fuel element is typically burned for two or three cycles during its useful lifetime.

The ATRC (Figures 1.3 and 1.4) is an open-pool nuclear mock-up of the ATR that typically operates at approximately 600 W and produces thermal neutron flux levels in the traps that are in the range of 1.0×10^9 n/cm²-s. As is the case for the ATR, the core consists of a 4-ft-high (122 cm), uniform-width, vertical 40-element fuel annulus shaped in a serpentine fashion between and around nine flux-trap regions located in a three-by-three square array. The cruciform fixture inside the serpentine is called the neck shim housing. The reactivity of the core is controlled by: (a) five vertically withdrawn safety rods that use cadmium as the poison material; (b) 24 vertically withdrawn hafnium neck shim rods; and (c) eight pairs of rotating outer shim control cylinders (OSCCs) that use hafnium poison plates.

ATRC criticality can normally be stably attained at a power as low as 0.25 mW and the maximum rated power is 5 kW. The ATRC facility is typically used with prototype experiments to characterize in advance, with precision and accuracy, the expected changes in core reactivity for the same experiments in the ATR. Useful physics data can also be obtained for evaluating the worth and calibration of control elements as well as thermal and fast neutron distributions.

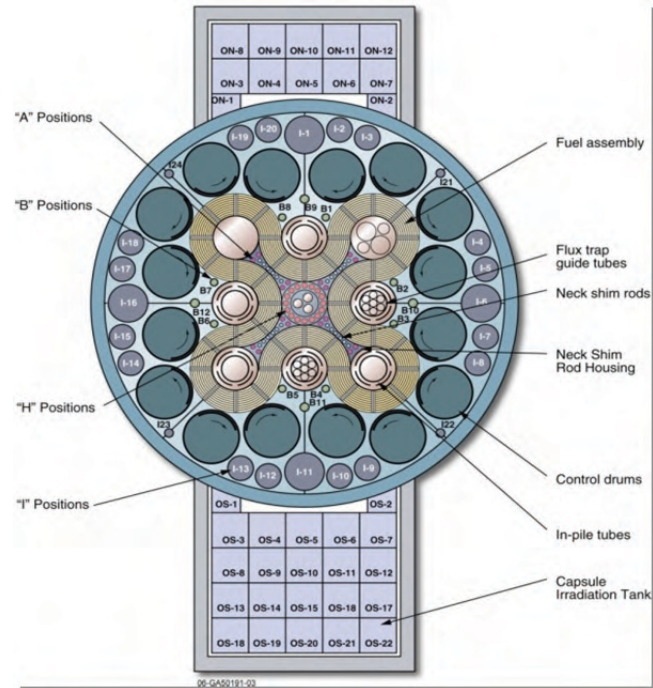


Figure 1.1. Core and reflector geometry of the Advanced Test Reactor.

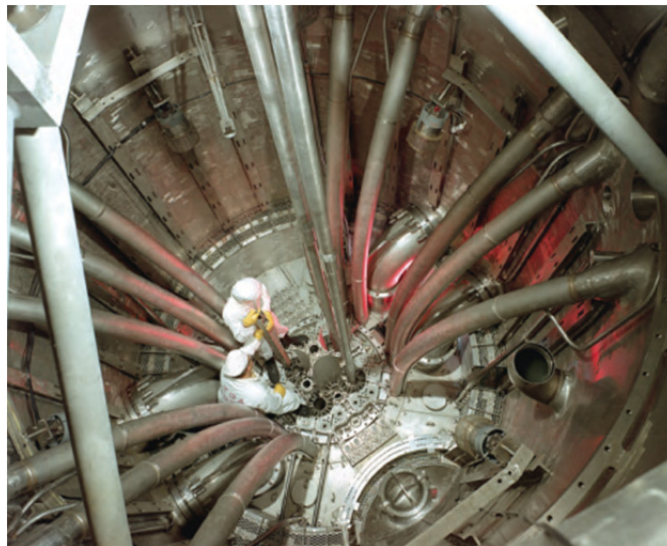


Figure 1.2. View into the ATR pressure vessel (File Photo, ca 1967).

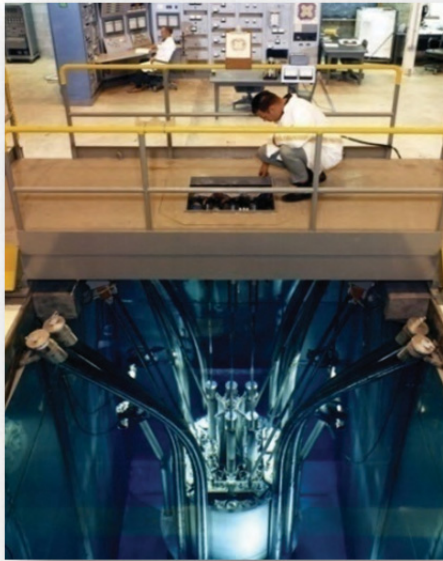


Figure 1.3. The Advanced Test Reactor Critical Facility (File Photo, ca 1967).

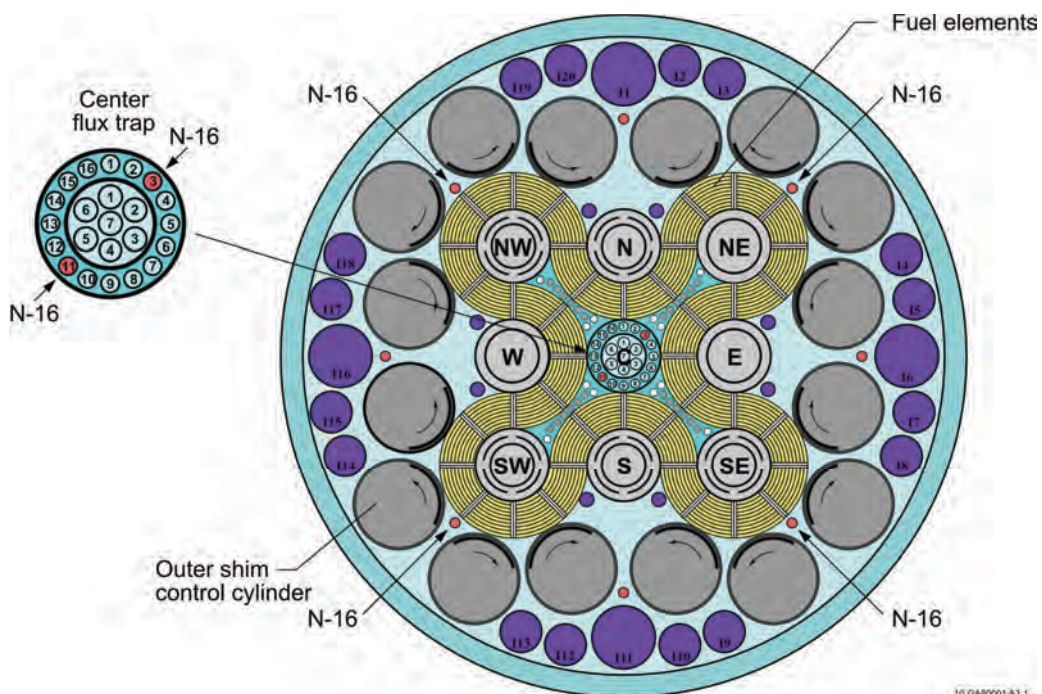


Figure 1.4. ATRC Configuration, showing the NW LIPT Flux Trap and six N-16 positions.

1.2 Rationale for the ATR Core Modeling Update Project

Computational reactor physics modeling is used extensively to support current ATR operations and HEU fuel cycle management, core and experiment safety analysis, experiment hardware design, and many other applications. Experiment hardware design and analysis for the ATR generally involves very detailed and sophisticated three-dimensional Monte Carlo analysis, typically using the internationally-recognized continuous-energy MCNP5 code (Goorley et al., 2004) or an equivalent methodology, coupled to extensive fuel isotope buildup and depletion analysis where appropriate. On the other hand, the computational reactor physics software tools and protocols currently used for ATR core fuel cycle analysis and operational support are largely based on four-group diffusion theory in Cartesian geometry as implemented in the PDQ code (Pfeifer et al., 1971) with heavy reliance on “tuned” nuclear parameter input data. The latter methods have been superseded in the general reactor physics community by high-fidelity multidimensional stochastic and deterministic transport-theory-based methods. As a result, the historical approach to ATR reactor physics operational support is no longer consistent with the state of modern nuclear engineering practice as defined, for example, in ANSI/ANS-19.3 (ANS, 2005). Furthermore, the legacy models are nearly impossible to validate against experiment according to typical modern protocols as defined in ASTM Standards E-261 (ASTM, 2010), E262 (ASTM, 2008), and E944 (ASTM, 2008) and in related documentation. Finally, some aspects of the legacy analysis process require very specialized experience, but the staff knowledge from the 1960s and 1970s, essential for the successful application of these various approximations, is rapidly being lost due to personnel turnover and retirements.

Figure 1.5 illustrates one of the challenges experienced recently with the legacy physics computational methods used for ATR operational support. A fueled experiment associated with the DOE Next Generation Nuclear Plant Advanced Gas Reactor (NGNP) development program was scheduled for irradiation in the south flux trap of the ATR as shown. However, uncertainties in the supporting computations were such that it was not possible to determine the neutronics effects of this experiment on neighboring flux traps to sufficient accuracy, and the operational margins of conservatism that were consequently required caused the experiment to be delayed until a later ATR cycle, at significant expense. In a second example of the impact of uncertainty in the current computational methods, some operational issues arose in December 2009 that were triggered by a larger than acceptable discrepancy between the calculated and measured excess core reactivity. These issues were resolved via standard procedures, but schedules were adversely impacted and the root cause was largely traced to problems with the legacy computational model of an experiment in the central flux trap.

In response to this situation, the INL is currently engaged in a major multiyear effort to modernize the computational reactor physics tools and validation protocols needed for support of ongoing ATR operations as well as for new applications. This aggressive computational and experimental campaign will have a broad strategic impact on the operation of the ATR, both in terms of improved computational efficiency and accuracy for support of ongoing DOE programs as well as national and international recognition of the ATR NSUF. The new computational methods and V&V protocols will be broadly applicable across all programs that use the ATR and ATRC. The developmental effort is in fact already leveraged with several other INL projects including the ATR Life Extension Program (LEP), the DOE Reduced Enrichment for Research and Test Reactor (RERTR) initiative, and an INL collaboration with Idaho State University (ISU), the Atomic Energy Commission of France (CEA), and the National Atomic Energy Commission of Argentina (CNEA) to evaluate various options for in-core ATR and ATRC instrumentation upgrades under the auspices of the NSUF (Rempe et al., 2010).

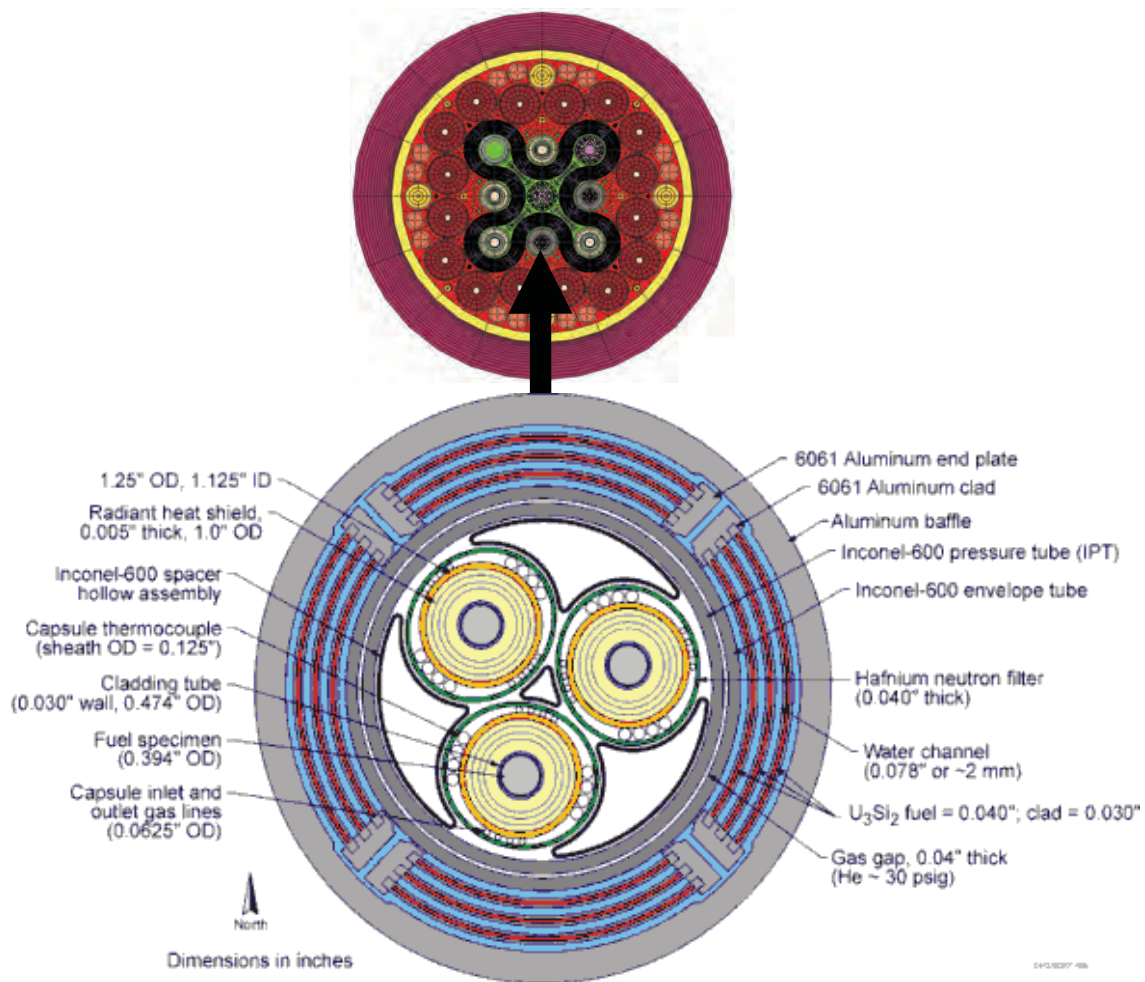


Figure 1.5. Gas Test Loop experiment designed for placement in the ATR south flux trap.

1.3 Technical Objectives of the Core Modeling Update Project

Prior to the initiation of the Core Modeling Update Project in late 2009, the INL was already making some important efforts to modernize ATR reactor physics analysis capabilities using current standard computational reactor physics tools. Those efforts have produced some important progress, especially for experiment design and analysis as noted earlier. However, this was largely on an *ad-hoc* basis, and several key tasks remained:

- Implementation of complementary, self-consistent multidimensional stochastic and deterministic neutron transport models of the ATR and ATRC cores using well-established and recognized science-based software packages consistent with current practice, with a focus on use of verified commercial products and mature, well-documented and verified US National Laboratory codes wherever possible.
- Development of standardized computational procedures and training, more easily transferred to new staff members,

- Additional ATR core physics verification and validation (V&V), with development of standard apparatus and protocols for detailed neutron flux distribution and spectrum validation measurements in the core and selected flux traps that can be adapted as needed for changing experimental conditions and repeated on a regular basis.

These activities are now well underway and some are complete or nearing completion, as summarized in this report. All of the various efforts have been conducted in recognition of the fact that the ATR and the ATRC may be converted to use low-enriched uranium (LEU) fuel at an appropriate time in the future. The same modeling and validation protocols discussed here for the current mode of operation with the current high-enriched uranium (HEU) fuel will be directly transferrable to an LEU fuel environment at such time as a final decision is made to convert to LEU and one or more prototype LEU fuel elements become available for in-core testing.

1.3.1 Computational System Description

Figure 1.6 shows the suite of new reactor physics computational tools that are being brought into operation under the ATR Core Modeling Update Project, how they generally relate to one another, and how they will support current ATR HEU operations and possible future ATR LEU operations. Some further details of the code capabilities, the selection process and various V&V strategies are available in (Aryaeinejad, 2010) and (Nigg and Steuhm, 2011, 2012). The illustration in Figure 1.6 is not a computational flow chart or procedure *per se*. Specific computational protocols using the tools shown in Figure 1.6 for routine ATR support applications will be promulgated in approved procedures and other operational documentation. These documents will prescribe the geometric modeling input files, nuclear data files, and other aspects of each specific computational protocol. For example there will be an updated procedure for computation of Core Safety Analysis Package (CSAP) physics support data for a particular ATR operational cycle using the new tools

Referring to Figure 1.6 in somewhat more detail, the most recent release of the Evaluated Nuclear Data Files (ENDF/B Version 7) is used to provide the basic cross section data and other nuclear parameters required for all of the modeling codes. The ENDF physical nuclear data files are processed into computationally-useful formats using the standard publically-available NJOY or AMPX (Radiation Safety Information Computational Center, 2010) codes as applicable to a particular module as shown at the top of Figure 2.1. Some of the modeling codes can use the output data files from NJOY or AMPX directly, while others require further processing of the data into a suitable format before use.

As noted earlier, the MCNP5 three-dimensional stochastic simulation code is already used extensively for ATR experiment design and analysis and, to some limited extent, core analysis. MCNP5 has a very broad base of users worldwide, and it is often considered to be the “Gold Standard” for cross-verification of other neutronic modeling codes per ANS 19.3 guidelines because of its very high-fidelity modeling capabilities, including the use of pointwise representations of the basic nuclear data as a function of neutron energy and the ability to represent very complicated geometric configurations essentially exactly. Furthermore, there is already a broad base of validation data for MCNP5 applications to the ATR and the ATRC at the INL.

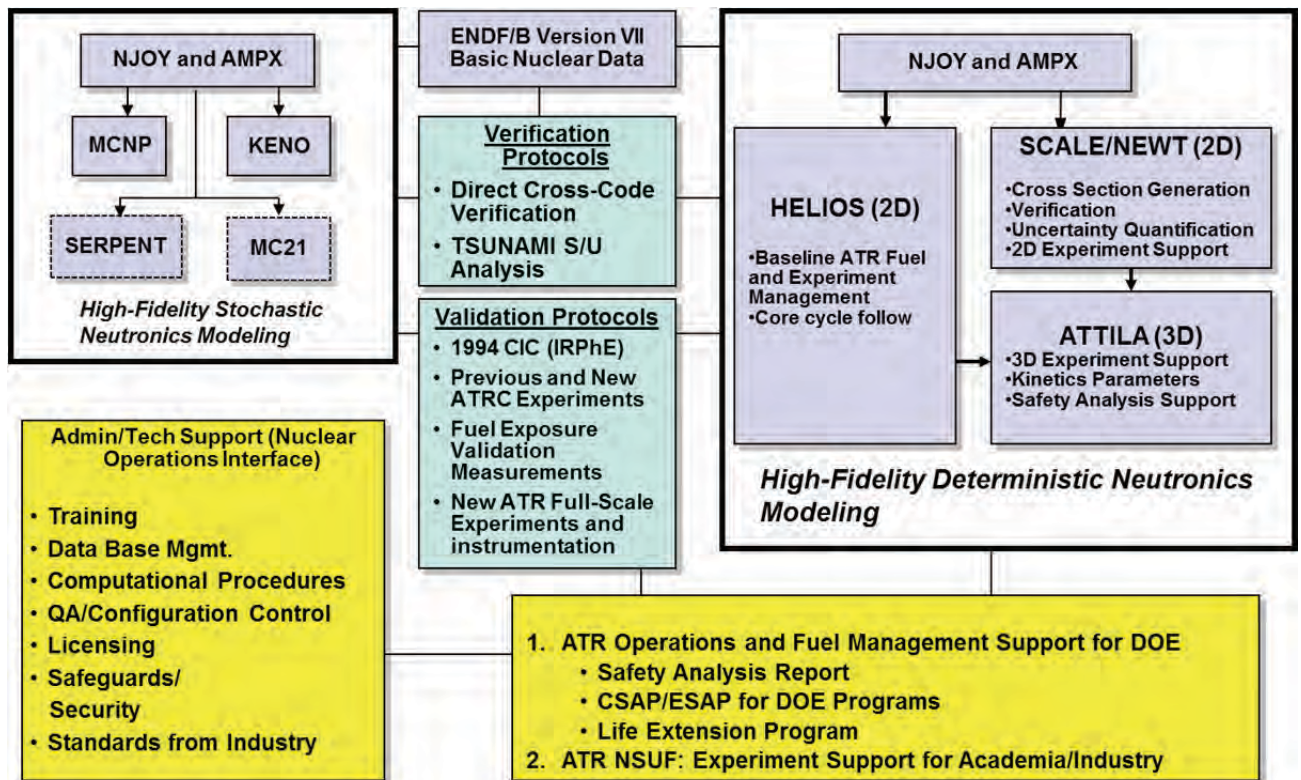


Figure 1.6. Advanced computational tool suite for the ATR and ATRC, with supporting verification, validation and administrative infrastructure.

Under the Core Modeling Update Project, we are also introducing the KENO stochastic simulation code (Hollenbach et al., 1996). The KENO code is useful both as a stand-alone analysis and verification tool as well as in conjunction with the TSUNAMI (Broadhead et al., 2004, Williams and Rearden, 2008) sensitivity-uncertainty analysis system available with the SCALE nuclear system analysis package (Bowman et al., 2009). It is this latter application of KENO that is of the most utility for ATR applications, both for HEU as well as possibly for LEU in the future. For example, details of the application of KENO/TSUNAMI to quantify the *a priori* uncertainty of the computed critical system eigenvalue (k -effective) that is due to propagation of the fundamental uncertainties of the basic input nuclear data are provided in (Aryaeinejad, 2010).

Furthermore, we are also incorporating the well-developed MC21 (Sutton et al., 2007) and the relatively new SERPENT (Leppänen, 2012) stochastic simulation and depletion codes into the new suite, as additional tools for V&V in the near term via intercode comparisons per ANS 19.3 (ANS, 2005), and possibly as advanced platforms for full 3-dimensional Monte Carlo based ATR fuel cycle analysis and fuel management in the longer term. Both of these codes feature fully-integrated capabilities for fuel depletion analysis, facilitating their long-term utility for the latter application. Furthermore, limited experience at this point suggests that MC21, originally developed for naval propulsion applications is approximately an order of magnitude faster in execution speed on massively parallel computer systems than MCNP5 for ATR applications of interest, all other factors being equal. Acquisition of SERPENT and MC21 was initiated during 2012 and completed in 2013, both are now operational at the INL, and an initial validation of the SERPENT code against a recent ATRC experiment is described in this report. Based on early experience, SERPENT was in fact selected as the initial primary physics design and analysis tool for the ATR/ATR LEU conversion effort, with MCNP5 for cross-verification, and with

MC21 possibly phased into the primary LEU design and analysis role as similar experience is gained with it.

The right-hand side of Figure 1.6 shows the new high-fidelity deterministic transport computational tools that are being integrated into the system. HELIOS (Studsvik Scandpower, 2008) is a very-mature and well-recognized commercial two-dimensional neutron transport code with general geometry and integrated fuel management and depletion capabilities. Like MCNP5, HELIOS has a very broad international base of users, and it has been validated against a wide variety of Light Water Reactor (LWR) experimental data (e.g. Wemple, et al., 2008). It features a self-contained fine-group cross section library, processed from the basic ENDF/B Version 7 files, with an integrated online resonance self-shielding capability that is well-suited for LWR applications. HELIOS is in place at the INL under a permanent sitewide license and it will serve for the foreseeable future as the primary reload core design and fuel management tool for ATR, replacing the PDQ-based few-group diffusion theory methodology.

NEWT (DeHart, 2006) together with its SCALE-based cross section processing support infrastructure (Bowman, 2009) is a well-established and verified software tool developed within the DOE National Laboratory system. It is a two-dimensional transport code based on the “step-characteristic” method. In the case of INL ATR and ATRC applications, NEWT has served primarily as a lattice code for cross-section generation and as an independent cross-verification tool for HELIOS.

ATTILA (McGhee et al., 2006) is a commercial grade software product in place at the INL under sitewide licenses. It is a three dimensional discrete-ordinates (S_n) neutron transport code that uses the Linear Discontinuous Galerkin (LDG) solution technique which is second order spatially accurate for point quantities and third order accurate for integral quantities, such as reaction rates. Geometry is represented in ATTILA using Para Solid™ (PS) files made from models in Solid Works™ (SW). Solid Works™ is a CAD/CAM code, similar to ProE or Inventor. The model is made in SW and saved to a Para Solid™ file that can be read into ATTILA to be used for meshing. The meshing tool in ATTILA is from Simmetrix, it allows surface meshing with triangles and quads and volume meshing with Tetrahedral finite elements. ATTILA requires a preprocessed, resonance-shielded cross section library as an input file, typically generated using SCALE/NEWT. Currently, ATTILA is primarily envisioned as a cross-verification tool, and as an experiment analysis tool in situations where full three-dimensional transport calculations are required, but where the stochastic nature of MCNP5 and its analogues mentioned earlier puts such codes at a disadvantage, for example when attempting to quantify the neutronic effects of small perturbations in the geometry or material composition of one or more components of the overall reactor system being modeled.

All of the code packages described above have various strengths and weaknesses, but taken together they provide the necessary high-fidelity stochastic and deterministic neutron and gamma transport capability that is required for various aspects of ATR and ATRC core physics modeling, both for current HEU operations as well as for support of possible LEU conversion.

1.3.2 Validation Protocols

As always, theory and experiment must be consistent in any scientific or engineering enterprise, and any biases and uncertainties must be quantified. This is the function of the validation process for the new code suite, both for the current HEU configuration of the ATR as well as for the possible future application to low-enrichment replacement fuel for the ATR and ATRC. In fact, careful and relevant near-term validation is particularly important for the potential ATR/ATRC LEU conversion effort because direct validation measurements in the actual target system will not be available until well into the prototype fuel development process. This situation will force initial reliance on currently-available and anticipated new physics measurement data for ATRC and ATR cores operating with HEU.

The ongoing Core Modeling Update Project includes several activities designed to incorporate historical validation data from earlier ATR and ATRC experiments as well as to develop new validation data specific to the new computational models and protocols for HEU fuel. In particular, much of the initial

model testing has been based on a very well documented critical experiment conducted as part of the 1994 ATR Core Internals Changeout (CIC) activity (Kim and Schnitzler, 2008). New core flux measurements in both ATRC and ATR are also underway, and the statistical analysis of the first four new ATRC validation experiments per ASTM Standard E944 (ASTM, 2008) was completed in FY-2012 and updated in FY-2013. Additional validation effort in FY-2012 and FY-2013 was focused on applications of data from a previously unanticipated “depressurized” low-power run (Cycle 152A) of the ATR late in 2012. Finally, an additional new validation experiment in the ATRC was conducted in 2013 and one more is planned for FY-2014 as well.

The validation protocols build on previous related INL physics code validation experience at the ATR (e.g. Rogers and Anderl, 1995) as well as at other research reactor and accelerator facilities worldwide (e.g. Nigg et al., 2000). They are primarily based on neutron activation spectrometry in the near term, in accordance with applicable national standards for high-fidelity neutron spectrum measurements, e.g. ASTM Standards E-261 (ASTM, 2010), E262 (ASTM, 2008), and E944 (ASTM, 2008). Additional validation capabilities using post-irradiation burnup measurements for selected fuel elements are anticipated in the longer term as well. The latter capabilities may be of particular importance with possible future LEU-fueled cores for the ATR, with their increased plutonium production relative to the current HEU fuel.

Some basic equipment for activation experiments in the ATRC Northwest Large In-Pile Tube (NW LIPT), and in the surrounding NW Lobe core fuel elements as well as in the diametrically opposite SE Lobe fuel elements was fabricated during FY-2010, and initial scoping measurements to determine neutron flux spectra in these regions were completed during FY-2011. Corresponding fuel element fission power distribution measurements throughout the ATRC core were also completed using standard ATRC protocols. There have been five LEP-specific ATRC validation experiments in total, and statistical analyses for the first four have been completed (Nigg et al., 2012a, 2012b) along with extensive analysis of additional fuel element power measurements made during FY-2012 in the ATRC to support Cycle 152A for “depressurized” physics testing (Nielsen et al., 2013). Further details of validation analyses completed in FY-2013 are provided in Chapter 3.

Over the course of the Core Modeling Update Project neutron spectrum measurements in the smaller flux traps and additional measurements in the core fuel elements are also planned, and some additional equipment was accordingly fabricated and assembled during FY-2012 to enable activation measurements within the southeast flux trap during 2013 and beyond. Ultimately a complete set of experimental apparatus and associated standard validation measurement protocols using neutron activation spectrometry will be available for future code and model validation measurements as needed in both the ATRC and, when feasible, in the ATR itself.

1.4 Project Structure and Technical Team

The ATR Core Modeling Update project includes 5 technical tasks. It is organized and funded as a part of the larger ATR Life Extension Program (LEP). The five tasks, which also provide the framework for the structure of this Annual Report, are as follows:

Task 1: Project Management: Includes sponsor/Collaborator interface maintenance, project documentation and planning, software licensing, travel, and university interfaces including student support.

Task 2: ATR Fuel Cycle Model Development and V&V: Includes development, verification, and validation of baseline MCNP5, KENO, HELIOS, NEWT and ATTILA models for current ATR reactor applications, along with continued testing of SERPENT and MC21 for future inclusion in the suite. The workscope includes fuel cycle management and neutronics support to core safety analysis, and limited development of capabilities for experiment analysis to the extent that experiment neutronic effects impact the operation of the reactor overall. (Detailed ATR experiment design and analysis is ordinarily handled

separately, as part of the workscope for each individual experiment series, and is not considered to be a part of the Core Modeling Update Project). Details of FY-13 activities and accomplishments in connection with this task are reported in Section 2 of this Annual Report. These activities were almost exclusively focused on demonstrating feasibility of the HELIOS system and refining the corresponding models as new primary reactor physics tools to support core fuel loading design and fuel cycle analysis tasks that are required for preparation of CSAP documentation for each ATR cycle.

Task 3: ATRC/ATR Model Development and Applications Specific to V&V: Includes development and application of baseline MCNP, KENO, HELIOS, NEWT, and ATTILA (and in the future, SERPENT and MC21) models for support of ATRC validation experiments pertinent to the Core Modeling Update Project and for the 2012 ATR depressurized run. This task also includes the development and application of new capabilities for rigorous sensitivity studies and statistical analyses pertinent to uncertainty quantification in the new computational models, with a strong emphasis on building protocols that are consistent with applicable national and international standards, especially ASTM-944 (ASTM, 2008).

Task 4: Neutronics Validation Experiments: This task includes the performance and reporting of new validation experiments in ATRC and ATR (as feasible) that are pertinent to quality assurance of the new computational models. It supports development of apparatus and protocols for a standard set of neutron activation spectrometry measurements that can be used on a more routine basis in the future for code validation as dictated by evolving ATR applications. This task also includes collaboration with various other DOE and NSUF projects where there is mutual benefit in terms of new physics validation data. Currently these collaborations include a project funded under the NSUF to investigate the feasibility of various techniques for online neutron flux measurements in the experiment positions as well as several physics experiments that were conducted in the ATRC to support depressurized operation of the ATR to support ongoing operations.

Task 5: In-Canal ATR Fuel Exposure Validation Measurements: This task has been focused on development of a non-invasive method and apparatus for measurement of the isotopic composition of used ATR fuel elements to infer the burnup. The effort included a series of scoping measurements conducted in FY-10, with ongoing data analysis through FY-11 and the first part of FY-12 (Nigg and Steuhm, 2011 and 2012). It also included the specification of a conceptual design for a permanent measurement system that can be installed in the fuel storage canal. Final design, construction and qualification of a permanent measurement system was formally proposed to the Department of Energy in 2012, completing the planned workscope of Task 5, although some subsequent additional improvements to some of the data analysis methods were made during 2013 and are summarized in this annual report.

The leadership team for the ATR Core Modeling Update Project consists of a Principal Investigator, a Project Manager, and several senior co-investigators who are responsible for various key aspects of each task listed above. It is important to recognize that the ATR Core Modeling Update Project represents not only an investment in new technology. It also represents a key investment in the new generation of INL scientific and engineering staff who will, by demographic necessity, assume leadership roles in the overall ATR enterprise over the next several years. Accordingly, several students and early-career INL Scientific and Engineering staff members are also proactively integrated into the effort, and this will accelerate in 2014 and beyond. The students supported by the project have included two from the University of Utah, two DOE Interns from Oregon State University, one student from RPI, one student from Idaho State University, and one student from the University of Texas.

1.5 Overview of Accomplishments (2010-2013)

The current Core Modeling Update Project is expected to require approximately 60 months to complete, and the various tasks are targeted for full implementation in phase with an anticipated ATR Core Internals Changeout (CIC) within the next 2-3 years. Some key accomplishments in the first 48 months of the

effort are briefly summarized below, along with a description of ongoing activities and planned next steps in several areas during FY-2014 and beyond.

- HELIOS, NEWT, ATTILA, and MCNP5 models of ATR and ATRC, with initial direct validation against experimental data are all operational.
- Acquisition of the MC21 and SERPENT 3D stochastic simulation codes from DOE-NR and VTT-Finland respectively was completed in FY-2013 and both are now operational at the INL. These codes offer significant additional V&V capability now, as well as a potential longer-term route to full 3D Monte Carlo ATR fuel management and CSAP analysis at an appropriate time in the future. Initial SERPENT models of the ATR and the ATRC have been demonstrated, and development of validated MC21 models of ATR and ATRC is underway.
- A production-level HELIOS model of the ATR with fuel depletion and replacement is operational and “as run” analyses beginning with Cycle 145A (August 2009) and proceeding through Cycle 154A as of the date of this Annual Report have been completed, with all flux trap experiments and other key core details explicitly represented in the model database. This will provide the basis for additional model upgrades as well as more formal acceptance testing and qualification of the core fuel cycle computational models and protocols in 2014, with the goal of having sufficient technical capability in place to enable a decision to rely exclusively on the new computational methods and fuel cycle models for current ATR operation using HEU fuel in Fiscal Year 2015 or any time thereafter as deemed appropriate.
- Capability for rigorous sensitivity-uncertainty analysis using KENO/TSUNAMI is available and has been demonstrated (Aryaeinejad, 2010)
- Validation protocol development and demonstration are underway, with a focus on consistency with ASTM-944, which establishes standard protocols for high-fidelity analysis of activation spectrometry data. Complete, peer-reviewed results of statistical validation analyses for the first four (of 6) ATRC irradiations specific to the Modeling Update Project were recently published (Nigg et al., 2012a, 2012b).
- The fifth of six planned project-specific validation experiments was run in the ATRC late in 2013 as described in this Annual Report, with detailed data analysis to follow in 2014. The sixth experiment is currently planned for mid-2014.
- Analysis of additional direct fuel element power validation data referenced to ATR Cycle 152A (“Depressurized Run”) and the corresponding ATRC supporting configurations was initiated in 2012 (Nigg and Steuhm, 2012) and completed in 2013 as described in Chapter 3 of this Annual Report.
- A new algorithm for fuel element power-fitting based on least-squares adjustment is now operational and is currently being applied as described in Chapter 3 for support of the depressurized operations of the ATR as well as future measurements in the ATRC. This original algorithm makes use of a novel method for estimating the fuel element-to-element power covariance matrix required for the adjustment process (Nielsen et al., 2013).
- Feasibility measurements for a permanent fuel burnup validation system were completed using actual irradiated ATR fuel in the ATR canal (Nigg and Steuhm, 2011, 2012) and a proposal for construction of the new system has been submitted to DOE-NE. Some additional improvements to the proposed system were completed in 2013.

1.6 References

ANS (American Nuclear Society), “Determination of Steady-State Neutron Reaction Rate Distributions and Reactivity of Nuclear Power Reactors”, ANSI/ANS-19.3-2005.

R. Aryaeinejad, D. Crawford, M. DeHart, G. Griffith, B. Gross, D. Lucas, J. Nielsen, D. Nigg, J. Navarro, J. Parry, J. Peterson, K. Steuhm, “Advanced Test Reactor Core Modeling Update Project – Annual Report for Fiscal Year 2010,” Idaho National Laboratory, INL/EXT-10-19940, (September 2010).

ASTM (American Society for Testing and Materials), “Standard Practice for Determining Neutron Fluence, Fluence Rate, and Spectra by Radioactivation Techniques”, ASTM-E261-10 (2010)

ASTM (American Society for Testing and Materials), “Standard Test Method for Determining Thermal Neutron Reaction Rates and Thermal Neutron Fluence Rates by Radioactivation Techniques”, ASTM-E262-08 (2008)

ASTM (American Society for Testing and Materials), “Standard Guide for Application of Neutron Spectrum Adjustment methods in Reactor Surveillance”, ASTM-E944-08 (2008)

Bowman, S. M. (Ed.), *SCALE: A Modular Code System for Performing Standardized Computer Analyses for Licensing Evaluation*, ORNL/TM-2005/39, Version 6, Vols. I–III, Oak Ridge National Laboratory, Oak Ridge, Tennessee, January 2009. Available from Radiation Safety Information Computational Center at Oak Ridge National Laboratory as CCC-750.

Broadhead, B. L., Rearden, B. T., Hopper, C. M., Wagschal, J. J. and Parks, C. V., “Sensitivity- and Uncertainty-Based Criticality Safety Validation Techniques,” *Nucl. Sci. Eng.* **146**, 340–366 (2004).

DeHart, M. D., Advancements in Generalized-Geometry Discrete Ordinates Transport for Lattice Physics Calculations, A154.pdf in Proc. of PHYSOR–2006, American Nuclear Society Topical Meeting on Reactor Physics: Advances in Nuclear Analysis and Simulation, September 10–14, 2006, Vancouver, British Columbia, Canada.

Hollenbach, D.F., Petrie, L.M., Landers, N.F., KENO-VI: A General Quadratic Version of the KENO Program, ORNL/TM-13011, Lockheed Martin Energy Research Corp., Oak Ridge National Laboratory, 1996.

Kim, S. S. and Schnitzler, B. G., Advanced Test Reactor: Serpentine Arrangement of Highly Enriched Water-Moderated Uranium-Aluminide Fuel Plates Reflected by Beryllium” HEU-SOL THERM-022, *International Handbook of Evaluated Criticality Safety Benchmark Experiments*, NEA/NSC/DOC(95)03, OECD-NEA (2008).

Leppänen, J., 2012b. "Serpent Progress Report 2011", VTT Technical Research Centre of Finland (2012), [VTT-R-05444-12](#).

McGhee, J.M., Wareing, T.A., Barnett, D.J., ATTILA Version 5: User Manual, Transpire Inc., Gig Harbour WA, USA (2006).

J.W. Nielsen, D.W. Nigg, A.W. LaPorta, A Fission Matrix Based Validation Protocol for Computed Power Distributions in the Advanced Test Reactor, International Conference on Mathematics and Computational Methods Applied to Nuclear Science & Engineering (M&C 2013), Sun Valley, Idaho, USA, May 5-9, 2013.

D.W. Nigg, C.A. Wemple, R. Risler, J.K. Hartwell, Y.D. Harker, G.E. Laramore, “Modification of the University of Washington Neutron Radiography Facility for Optimization of Neutron Capture Enhanced Fast-Neutron Therapy, *Medical Physics* **27**:359-367 (2000).

D.W. Nigg, K. Steuhm (Editors), Advanced Test Reactor Core Modeling Update Project Annual Report for Fiscal Year 2011, INL/EXT-11-23348, September 2011.

D.W. Nigg, J.W. Nielsen, B.M. Chase, R.K. Murray, K.A. Steuhm, T. Unruh, Improved Computational Neutronics Methods and Validation Protocols for the Advanced Test Reactor, Proceedings of the American Nuclear Society International Topical Meeting on Advances in Reactor Physics (PHYSOR-12), Knoxville, Tennessee, April 15-19, 2012 (2012a)

D.W. Nigg, J.W. Nielsen, G.K. Taylor, Validation Protocols to Support the Neutronics Modeling, Simulation, and V&V Upgrade for the Advanced Test Reactor, *Trans ANS*, **106**:890-893 (2012b)

D.W. Nigg and K.A. Steuhm (Editors), Advanced Test Reactor Core Modeling Update Project Annual Report for Fiscal Year 2012, INL/EXT-12-27059. September 2012 (2012)

Pfeifer, C.J., PDQ Reference Manual II, WAPD-TM-947(L), 1971.

Radiation Safety Information Computational Center, NJOY99- Code System for Producing Pointwise and Multigroup Neutron and Photon Cross Sections from ENDF/B Data and AMPX77- Modular Code System for Generating Coupled Multigroup Neutron-Gamma Libraries from ENDF/B, Oak Ridge National Laboratory (<http://www.rsicc.ornl.gov>), 2010.

Rempe, J.L., Nigg, D.W., Imel, G. R., Unruh, T., FY-10 Irradiation Experiment Plan for the ATR National Scientific User Facility – Idaho State University Project Evaluating Flux Sensors, PLN-3351, Revision 0, Idaho National Laboratory, 2010.

JW Rogers, R.A. Anderl, “ATR Neutron Spectral Characterization”, INEL-95/0494, Idaho National Laboratory, USA (1995).

Studsvik Scandpower, HELIOS Methods (Version 1.10), 2008.

Sutton, T.M., et al., The MC21 Monte Carlo Transport Code, Knolls Atomic Power Laboratory and Bettis Laboratory, LM-06K144, 2007.

Wemple, C.A. “Recent Advances in the HELIOS-2 Lattice Physics Code”, International Conference on the Physics of Reactors “Nuclear Power: A Sustainable Resource”, PHYSOR-2012, Casino-Kursaal Conference Center, Interlaken, Switzerland, September 14-19, 2008

Williams, M.L., Rearden, B.T., SCALE 6 Sensitivity/Uncertainty Methods and Covariance Data, *Nucl. Data Sheets* **109** (2008), p. 2796.

2.0 HELIOS-MCNP MODEL DEVELOPMENT FOR CSAP APPLICATIONS

Samuel E. Bays, Emily T. Swain, Douglas S. Crawford, William F. Skerjanc

This chapter summarizes the continued development and validation of the new ATR core fuel cycle analysis methodology during FY-2013. Descriptions of the two-dimensional HELIOS transverse-core models and the closely associated three-dimensional MCNP axial models are included. In addition, we provide an assessment of the current state of the new methodology and its capabilities relative to the detailed requirements for physics data that are associated with the ATR CSAP process, as a basis for defining additional development effort during FY-2014 and beyond. Finally, a supporting document (Crawford and Bays, 2013), provides a summary of a new capability that has been developed for efficiently estimating critical ATR shim rotations and corresponding lobe powers prior to expending the resources for detailed HELIOS analyses needed for final design of each ATR cycle fuel loading.

2.1 Validation of HELIOS for ATR Core Follow Analyses

This section describes validation of the Studsvik-Scandpower deterministic transport code, HELIOS, for performing reactor physics and fuel cycle calculations specific to the Advanced Test Reactor (ATR). The current physics tools employed are based on the neutron diffusion code, PDQ-7 (Pfeifer, 1971). PDQ has been used in service to the ATR since its initial startup in 1967. However, the evolution of computer speed and the continuing advancements of ATR experiments have prompted consideration of modern neutron transport codes for performing the mission of core physics safety analysis. Modern transport tools eliminate the various approximations inherent to diffusion theory, most of which are of very limited applicability to the ATR, thus enabling more accurate representation of the core physics *a priori*. More importantly, it is common practice with modern transport tools to input the core geometry and material compositions exactly in the X-Y dimension with little to no homogenization error. These features, along with easy extraction of integral data from the code output, allow easy like-to-like validation of simulation with the target reactor system.

For HELIOS to be used for ATR physics and safety analysis, it must first be validated to meet requirements, such as: calculation of core reactivity, peak power and fission density, tracking of nuclide inventories, and prediction of component lifetimes for certain situations. This work presents the validation results for core reactivity, core power distribution and the verification results for fuel nuclides. Validation without clean idealized benchmarks presents unique challenges, as the ATR is an operating reactor that has not undergone a full set of applicable power validation experiments since 1994. Also, the complex nature of simultaneous fuel and experiment configuration management presents further complications. In particular, the representation of axial detail cannot be exactly characterized with a 2D code, such as HELIOS. Much of the work presented here deals with transitioning reactivity accountancy and fuel database strategies from PDQ to HELIOS. It is shown that the HELIOS code can reliably simulate the actual ATR power history and core reactivity comparable to current expectations with PDQ. However, during the course of the transitional process, opportunities for improvement of the current bookkeeping of axial effects were discovered and are discussed for future work.

In this work we have evaluated HELIOS for (1) predicting the cold zero-power initial critical condition at startup of the ATR, (2) reproducing measured lobe powers by following the reactor over 16 operating cycles, and verifying that the code can produce a fuel nuclide inventory comparable to PDQ over those 16 cycles. This section of the 2013 Annual Report provides historical and computational background on the PDQ-based core-follow methodology, followed by details of the new computational protocols employed using HELIOS. Results of the critical shim position determinations, core-follow lobe power results, and nuclide inventory results are then presented and some conclusions and a description of future work are provided.

2.1.1 Background

The ATR is a water-moderated, beryllium-reflected, pressurized water reactor with a serpentine arrangement of plate fuel taking on a four-leaf-clover likeness (Longhurst and Brown, 2002). Each of the clover-leaves plus the center region are referred to as individual lobes. The design power rating is 250 MW. However, it is currently operated at about 110 MW, and occasionally at 155 MW to support higher power experiments. The fuel metallic plates consist of Highly Enriched (HEU 93% $^{235}\text{U}/\text{U}$) uranium-aluminide (U-Al_x) dispersed in aluminum and clad in aluminum alloy. The fuel serpentine contains 40 fuel elements, each containing 19 plates. Three different types of fuel elements are employed. The typical Mark-7 (or 7F) fuel element is loaded with boron carbide in the first four and last four fuel plates. The YA fuel element is geometrically the same as the 7F fuel element, but with the outermost plate (plate 19) without fuel. This fuel element is designed to minimize the heating rate near the beryllium reflector in order to minimize the potential for swelling and cracking of the beryllium. The “no-boron” (or NB) fuel element is the same as a 7F element but without boron carbide. A modified variation of the YA elements, which have a different side plate thickness to accommodate swelling of neighboring elements is also available. Initial criticality and lobe power shape is maintained using control drums, called Outer Shim Control Cylinders (OSCCs). The burnup reactivity decrement is made up partly with OSCCs but primarily with annular hafnium neck shims which are removed from the four aluminum neck arms in the center region. Numerous penetrations in the reflector and neck arms allow for non-instrumented “drop-in” as well as instrumented capsules, in addition to the nine flux traps. The main reactor missions are radio-isotope production (namely cobalt), and advanced materials and fuels testing for both the commercial sector and the United States Navy. A picture of a typical reactor configuration modeled by HELIOS is provided in Figure 2.1.

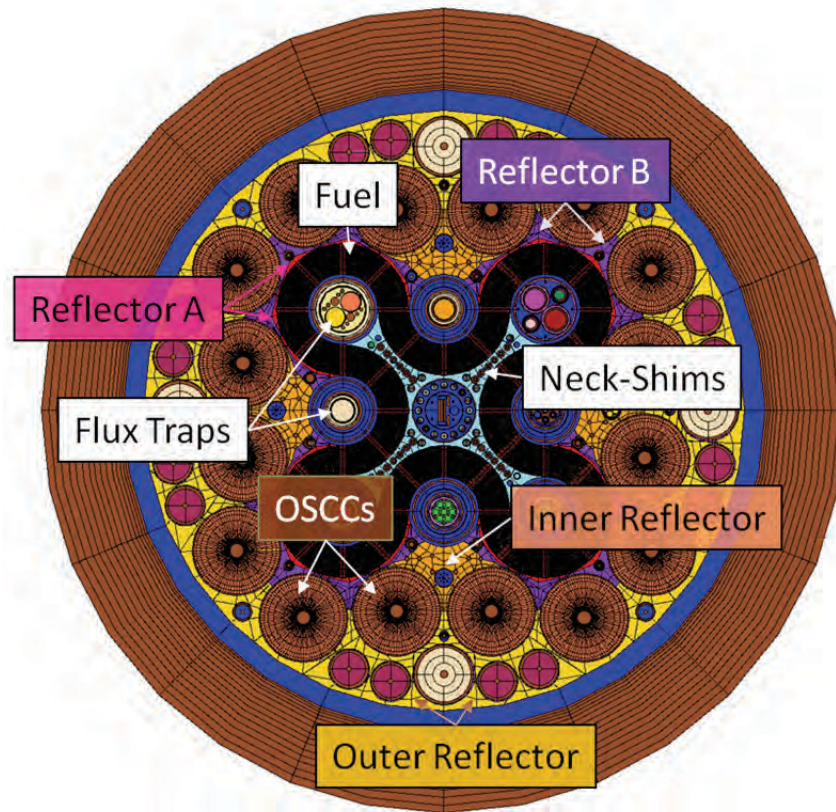


Figure 2.1 HELIOS geometry plot of Cycle 145A.

Several different types of physics analyses are performed to satisfy the ATR Updated Final Safety Analysis Report (UFSAR) requirements for each operational cycle. The analyses pertaining to the ATR core as a whole and specifically to the driver fuel are reported in the Core Safety Assurance Package (CSAP). Analyses pertaining to experiments are reported in corresponding documentation created for each experiment, namely experiment-specific Experiment Safety Assurance Packages (ESAPs). Taken together, this documentation provides the United States Department of Energy (DOE) with assurance that the UFSAR requirements are being met for each cycle. A major component of the CSAP documentation consists of physics data produced by the existing suite of codes associated with the diffusion code, PDQ. The current effort being undertaken is designed to replace the PDQ physics analysis code suite with an improved methodology capable of calculating and analyzing data that is ultimately reported in the CSAP documentation.

PDQ solves the neutron diffusion-depletion problem in 1-D, 2-D and 3-D applications. Only the 2-D implementation (in r-z and x-y) is currently in use. The PDQ model uses seven lethargy groups. Cross-section data may be in microscopic or macroscopic form. A lumped fission product model is used for all but a few fission products and actinides (Holm, 1978). Nuclear cross-section data and shielding factors, provided by the HARMONY code, is interpolated from tables as a function of the concentrations of up to three representative isotopes (Breen et. al., 1965). Current ATR calculations performed with PDQ use ENDF/B-V cross-section data libraries. Course-group diffusion constants are generated using the PHROG and INCITE codes for the fast and thermal neutron spectrum, respectively (Brown et. al., 1990). Diffusion coefficients for the nine flux traps are adjusted for the axial variation of experiments using the SCAMP code (Brown et. al., 1990).

The PDQ-based methodologies rely heavily on pre- and post-processing routines. These routines handle cross-section condensation, material homogenization and mapping into Cartesian mesh cells, de-convolution of mesh-cell fission powers to represent the actual plate powers and burnups. Furthermore, a complex system of reactivity biases, power multipliers and empirical corrections are made to correct the PDQ results for spectral shift in the fuel due to burnup, hafnium and beryllium depletion, temperature effects, flux shadowing of the neck shims, and correction for axial effects (Easson and Smith, 1981). Axial effects for lobes are handled with a generic r-z representation of the lobe (Brown et. al., 1990). Thus, the 3D-to-2D correction in PDQ is more accurately a 2D-to-1D correction applied to a higher level of dimensionality. The PDQ Cartesian mesh representation of the ATR is provided in Figure 2.2.

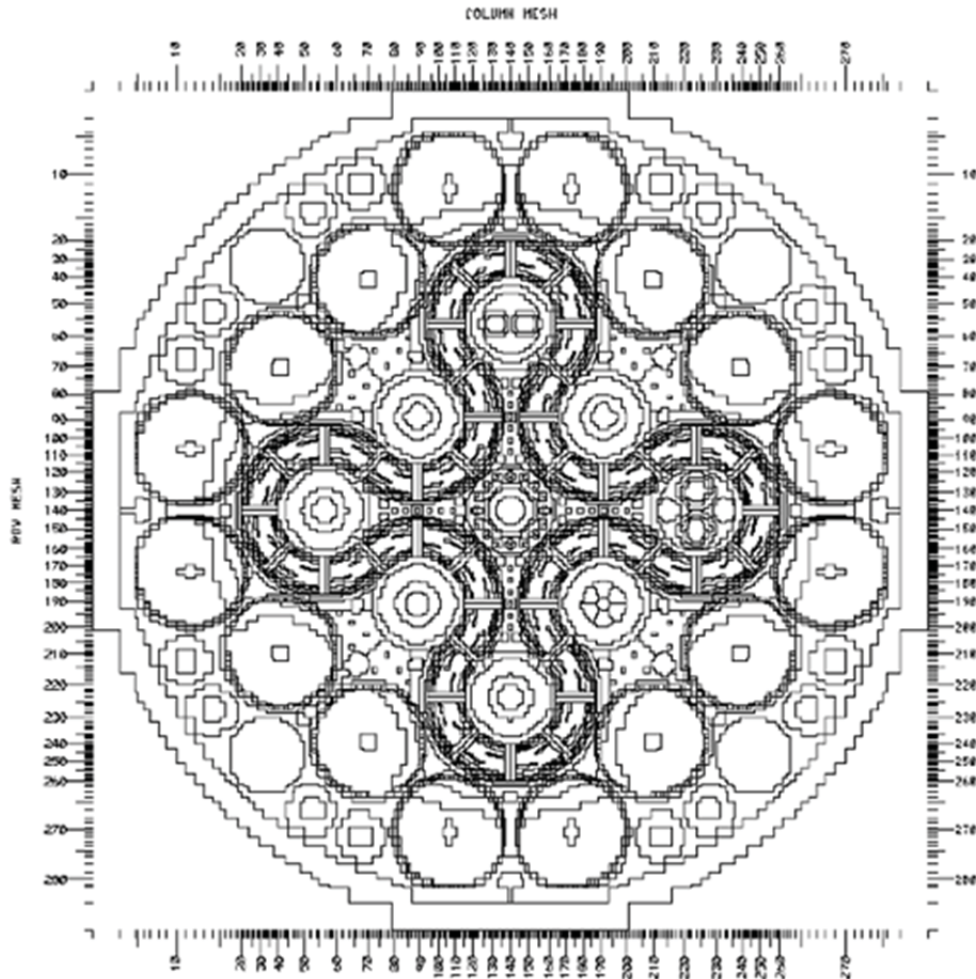


Figure 2.2 PDQ Cartesian mesh representation of ATR core.

2.1.2 As-Run Analysis

Core-follow of the ATR is performed after each cycle for the purpose of tracking fuel nuclide inventories. Also after each cycle, the neck shims' "fraction-of-original-worth" multipliers for the hafnium macroscopic cross-section are updated (Gregory, 1978). The ATR Reactor Data Acquisition System (RDAS) records surveillance data of lobe powers and OSCC and neck shim position throughout the cycle. The suite of RDAS programs that collects this information is called ATR Surveillance Data Acquisition System (ASUDAS). This data is used to create a PDQ model that is more true to the actual operating history than the one used to prepare the CSAP. Note that validation of the PDQ code suite is not a primary deliverable of these core-follow, or As-Run calculations. As-Run calculations are performed primarily for updating the PDQ nuclide inventory. In a typical As-Run, the control configuration of the model is set to ensure correct lobe-average exposures. The core follow in this work with HELIOS follows a similar strategy as a PDQ As-Run, but with some significant improvements. The most noteworthy difference is that the reactor surveillance data for each lobe, including lobe powers and positioning of the various reactivity control systems, is matched throughout the cycle of interest as closely as reasonably achievable. The other central difference between the HELIOS and PDQ As-Runs is that with HELIOS, the critical eigenvalue from the previous cycle (or cycles) are leveraged to predict the

criticality of the target cycle. With PDQ, a series of zero power physics “requalification tests” following the 1994 Core-Internals-Change-out (1994 CIC) is used to give the starting estimate for the computational critical eigenvalue.

The HELIOS fuel nuclide inventory leverages the PDQ fuel nuclide database to seed the beginning-of-cycle (BOC) fuel element loading in the absence of nuclide data with a HELIOS pedigree. As end-of-cycle (EOC) HELIOS data becomes available, it is used instead of the PDQ data. Also, the hafnium concentrations of the neck shims are tracked explicitly. Note that HELIOS does not track depletion of beryllium and its activation products. For the purpose of this work, beryllium nuclide data for the ATR reflector is borrowed from the PDQ As-Run analyses. Future work will include a depletion wrapper code for HELIOS to update the reflector region for depletion of beryllium and subsequent buildup of lithium, tritium and helium-3.

2.1.3 HELIOS Methodology

HELIOS is a general x-y coordinate deterministic transport code. Arbitrary geometry is created from user input-specified polyhedral shapes in space. Circular features can be planted within these polyhedral shapes. The code supports property overlays, such as composition, temperature and density, mapped to this arbitrary 2D geometry. Geometry-corrected resonance integrals are calculated on-the-fly for every spatial region (i.e., per single spatial mesh) of the arbitrarily heterogeneous geometry description using the subgroup resonance treatment (Studsvik Scandpower, 2009). Very large and complex geometries are supported by subdividing the geometry into smaller subsystems. Each subsystem is solved explicitly via the collision probability transport solution and then current-coupled with adjacent subsystems (Studsvik Scandpower, 2009; Stamm’ler and Abbate, 1983). The code also has a method-of-characteristics option for the transport solution (Studsvik Scandpower, 2009), though this option is not used in this work. HELIOS depletes all burnable materials as applicable in any given single spatial region (i.e., each spatial mesh is depleted separately). New property overlays can be added during the course of the depletion (e.g., change in control poison configuration, change in temperature, etc.). The code also supports tracking of gamma rays and gamma ray heating of core internals, though this feature has not been explored for the ATR at this time.

2.1.4 Nuclide Tracking

A significant challenge for transitioning from the PDQ- to a HELIOS-based methodology is the carryover of nuclide data generated by PDQ in a past cycle that is needed by HELIOS in the current and future cycles. There are three different types of carryover nuclide data: fuel, beryllium and hafnium. Fuel nuclide data of a PDQ origin is gradually phased out by the core-follow of many cycles until a new HELIOS-based fuel database is generated.

The beryllium depletion products can be transitioned in a similar matter. PDQ tracks Be-9, Li-6, H-3 and He-3 in essentially five regions in the ATR reflector. Region A is a thin region directly abutting the fuel serpentine. Region B is a slightly larger region just outside of Region A. The inner-reflector exists outside of Region B but generally inside of the OSCC’s. The outer-reflector exists outside of the OSCC’s. Finally, the OSCC’s constitute the fifth beryllium depletion region. The material overlays for the HELIOS model is refined to reasonably approximate the PDQ areas, as can be seen in Figure 2.1. Though PDQ data was used in the current analysis, future work will introduce an external depletion routine that takes into consideration the flux history in these regions (or a finer discretization thereof). The reactivity effect is only of the order of tens of cents per cycle (Smith et. al., 1990). Thus, updating the reflector composition after every cycle, as opposed to every time-step, is not expected to introduce significant modeling error on the critical eigenvalue.

PDQ does not explicitly track the hafnium nuclide concentrations of the neck shims or OSCCs. It should be expected that the OSCCs do experience a reactivity loss due to depletion. However, OSCC depletion

is fairly minor compared to that of the neck shims, thus it is not currently treated in either the PDQ or HELIOS methodologies. The neck-shim-reactivity decrement per cycle is treated via a direct multiplier against the neck shim hafnium macroscopic cross section (Gregory, 1978). This multiplier is an empirical function of lobe exposure (in Megawatt-Day) of the nearest ATR lobe. The physical meaning of the multiplier is the “fraction-of-original-worth”. Thus, it is computed by taking the rod-worth after a given lobe exposure and dividing it by the fresh rod-worth. Currently, the fraction-of-original-worth multipliers are functionalized with respect to the fresh rod in that neck shim location in the 1994 CIC requalification tests.

To generate hafnium nuclide densities for the 24 neck shims in the HELIOS model, without performing core-follow going back to the last all-fresh rod configuration (the 2004 CIC), several approximations had to be made. First, the hafnium absorption reaction rate is considered fairly invariable between the 2004 CIC, Cycle 134A, and the first cycle of this study, Cycle 145A. This is reasonable given the slow rate of hafnium depletion and the fact that the average core power and lobe power splits are very consistent from cycle to cycle. The cycle-time weighted mean and standard deviation for total core power during this time frame is 109.2 MW and 7.4 MW, respectively. It is also assumed that the hafnium depletion is not strongly affected by any spectrum differences from cycle-to-cycle. Finally, it is assumed that rod-to-rod self-shielding, or shadowing, is reasonably represented by the sub-group resonance treatment assuming all the rods are fully inserted and depleted together. This is a crude approximation for the actual rod withdrawal schedule for each cycle. With these assumptions, the hafnium cross section and flux conditions were computed with the 1994 CIC configuration at 110 MW. The flux in each lobe was scaled to the mean lobe power from 134A to 144B. This data was then input into an MS-EXCEL spreadsheet calculation containing a recursive solution to the Bateman equations for sequential decay daughters, Equation 2.1. A parallel FORTRAN routine was developed to verify the spreadsheet calculation. All hafnium depletion daughters are sequential with no feedback loops, i.e., daughter transitioning back to a parent. Thus, the recursive analytic solution of the Bateman equations is ideal for hafnium depletion (Shultis and Faw, 2002). Equation 2.1a considers only the transition of parent k to production of daughter j , assuming that the initial condition concerning isotopes downstream of k is zero. Equation 2.1b represents the constant coefficients for Equation 2.1a. Equation 2.1c uses the fact that N_j is in fact the sum of all upstream daughters.

$$n_j(t) = \frac{1}{\lambda_j} N_k(t_o) \sum_{m=1}^j C_m e^{-\lambda_m t} \quad (2.1a)$$

$$C_m = \frac{\prod_{i=1}^j \lambda_i}{\prod_{i=1, i \neq m}^j (\lambda_i - \lambda_m)} \quad (2.1b)$$

$$N_j(t) = \sum_j^k n_j(t) \quad (2.1c)$$

In these equations n_j is the contribution from parent N_k to daughter N_j , λ represents a transition coefficient equivalent to microscopic cross section multiplied by flux in each neck-shim ($\lambda = \sigma \times \phi$), C_m is the coefficient for each daughter m in the linear chain between j and k , and t is time.

Figure 2.3 shows the depletion of hafnium in the southeast-3 neck-shim. Hafnium is selected as a reactivity control material for its slow reactivity loss with burnup. This is due to the fact that Hf-176 through Hf-180 are coupled in a series relationship and that all hafnium nuclides have a reasonably significant absorption cross section. The total absorption cross sections for hafnium nuclides calculated by the 1994 CIC case-study for the southeast neck shim arm are given in Table 2.1.

Figure 2.4 shows the fraction-of-original-worth computed by HELIOS for the southeast neck-shims, using nuclide densities generated by the spreadsheet, compared with the values used by PDQ for the actual Cycles 134A-144B. As can be seen from the plot, the derived hafnium nuclide densities give

similar reactivity worth values with HELIOS as the empirical function used with PDQ. Thus, the recursive Bateman formulation was used to estimate hafnium nuclide densities for Cycle 145A BOC. From Cycle 145A on, HELIOS was used to micro-deplete hafnium in the neck-shims for each time-step in each cycle.

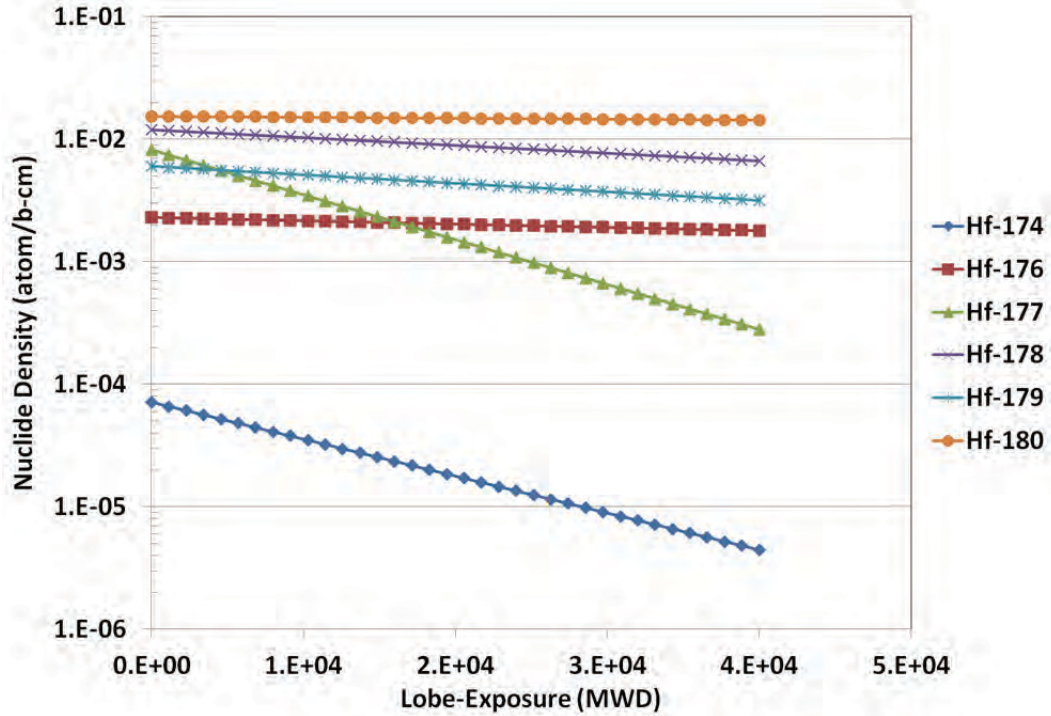


Figure 2.3 Depletion of the southeast-3 neck-shim between the 2004 CIC and beginning of Cycle 145A

Table 2.1. Hafnium absorption cross section (barns) computed for the southeast neck shims.

	SE-1	SE-2	SE-3	SE-4	SE-5	SE-6
Hf-174	38.66	33.98	31.57	30.94	31.54	34.61
Hf-176	3.00	2.85	2.77	2.75	2.77	2.87
Hf-177	44.79	40.48	38.41	37.92	38.44	41.39
Hf-178	7.94	7.11	6.70	6.60	6.69	7.25
Hf-179	7.97	7.51	7.26	7.21	7.26	7.57
Hf-180	1.04	0.93	0.87	0.85	0.87	0.95

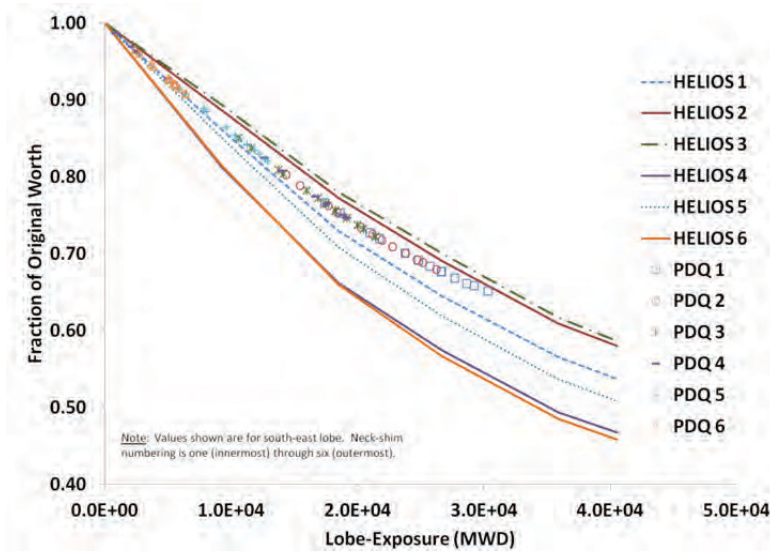


Figure 2.4 Fraction of original worth multipliers computed with HELIOS compared with PDQ empirical formulation in the southeast lobe.

2.1.5 Time Averaging of Reactor States

The second significant challenge for following the ATR core was the time discretization of hourly ASUDAS data. Following the ATR hourly or even daily ad hoc would require an excessive amount of computer resource. However, a time step greater than ten days is not sufficient to update the flux/criticality calculation. The ATR HELIOS model has an OSCC mesh discretization of 3.75° . Therefore, an OSCC rotation less than that amount is insignificant to trigger creation of a new burn-step. It was found that time increments on the order of two to ten days was sufficient to represent significant OSCC maneuvers. The same is true of neck shim movement. This discretization scheme was usually course enough to have at least one neck shim removal every burn step. Also during the course of this time interval, reactor power and lobe-power splits may have evolved slightly as the ATR operators strive to maintain constant lobe power. Thus, the ASUDAS hourly information was time averaged into burn steps, each representative of a unique control configuration and power state.

2.1.6 Evaluating the Critical Eigenvalue

Both HELIOS and PDQ (as it is used at INL) are two-dimensional codes. Therefore, they both must be corrected for axial effects. The way this is currently handled is to force an axial symmetric power distribution criterion upon the design of experiments. For the more exotic experiments, the axial fission shape is actually measured using a duplicate of the ATR core, the ATR Critical facility, ATRC. The ATRC is a near identical replica of the original ATR core, reflector, internals, etc. that reside in a pool facility adjacent to the actual ATR. ATRC was used to verify physics parameters prior to the startup of the ATR. One of the primary missions of the ATRC is to ensure that the experiment does not violate the chopped cosine power distribution in fresh fuel. The reason for this criterion is to ensure that the axial uniformity assumptions made to compute the axial reactivity and power shape corrections are valid.

The current axial reactivity bias correction is defined as the difference between a 2D r-z and a corresponding axially-homogenized (“r-polar”) PDQ critical eigenvalue calculation for each burn step along a given depletion path (Brown et. al., 1990). The r-z PDQ model approximates a typical lobe containing eight fuel elements. The r-polar PDQ model is an equivalent representation with the same average linear power. The reactivity bias curve is corrected for the 2D-to-1D geometry bias prior to depletion as shown in Equation 2.2. In current CSAP analysis, this axial reactivity bias is functionalized with lobe exposure, see Equation 2.3. Since the PDQ critical eigenvalue corresponds to the 1994 CIC,

this polynomial corrects each PDQ cycle calculation for depletion effects relative to a clean core. However, for HELIOS, we have chosen to reference the previous cycle critical eigenvalue as the reference-to-critical. Therefore, the axial depletion reactivity bias of the known critical is subtracted from the reactivity bias of the target critical, Equation 2.4.

$$\rho_{1D2D} = \frac{k_{2D}(x) - k_{1D}(x)}{k_{2D}(x)k_{1D,0}(x)} - \frac{k_{2D,0} - k_{1D,0}}{k_{2D,0}k_{1D,0}} \quad (2.2)$$

$$\rho_{1D2D} = C_0 + C_1x + C_2x^2 + C_3x^3 + C_4x^4 + C_5x^5 + C_6x^6 \quad (2.3)$$

$$\rho = \frac{k_T - k_C}{k_T k_C} + \frac{1}{8} \sum_i^{40} \rho_{T,i} - \frac{1}{8} \sum_i^{40} \rho_{C,i} \quad (2.4)$$

In the above equations ρ is the reactivity of the target system, k denotes the 2D k -effective from the HELIOS calculation, T denotes target system, i.e., the cycle being analyzed, C denotes the known critical system, e.g., corresponding to a previous cycle's zero power startup, $\rho_{T,i}$ is the ρ_{1D2D} axial reactivity biases for fuel element i having a lobe exposure x prior to irradiation in the target system, T , $\rho_{T,c}$ is same as $\rho_{T,i}$ but having a lobe exposure corresponding to the BOC of the known cycle. 2D and 1D denote the PDQ r - z and polar models, respectively, of a generalized ATR lobe. x is the lobe exposure, i.e., the summation over all previous cycles the power of the lobe for which the element resided multiplied with cycle length.

There are some obvious drawbacks to the above derivation. First, it requires strict adherence to axial symmetric depletion in the fuel for validity. Second, there is no accountancy for the fact that even with balanced OSCC maneuvers during startup; the reactor will have a power tilt between lobes. This is because each cycle will have a unique distribution of fresh and burned fuel as well as different experiment configuration loading. Thus, the above methodology does not account for differences in localized neutron importance in each lobe's overall contribution to core reactivity. It is expected that these restrictions can be overcome using a 3D-to-2D reactivity bias determination using a modern 3D transport code. This has already been demonstrated using the Monte Carlo N^{th} Particle (MCNP) code to model the 1994 CIC benchmark found in the International Reactor Physics Benchmark Experiments (IRPhE) handbook (Bays, 2012, Kim et. al., 2005). The PDQ polynomial is used to correct the HELIOS derived core reactivity for the purpose of this current work. Thus, fuel is considered to be evenly distributed axially. Also, the experiments are generally axially homogenized within the pellet, sample, test-train, etc. At times, the experiment composition at the mid-plane was used; effectively extruding the mid-plane geometry and composition the full axial length of the core.

2.1.7 Results – Core Reactivity

The ATR is brought to critical with all neck shims inserted, one of the regulating rods (SW4 and SE4) fully withdrawn, and the other regulating rod partially withdrawn. Approach to criticality is performed using the OSCCs only. The OSCCs are rotated in equal increments, i.e., balanced configuration. Once cold criticality is achieved with balanced OSCC rotation, the core is brought to full power; again using OSCCs to attain the desired lobe-power split.

The startup criterion for ATR stipulates that the initial cold critical condition must fall within +\$0.75 and -\$1.00 of the predicted OSCC position, aside: $\beta_{\text{eff}}=0.0075$. In the current methodology, the OSCC position is computed with both PDQ as well as using an empirical tabulation method based off of each experiment's reactivity worth as measured in the ATRC. These two estimates are averaged together to arrive at the startup prediction. If after two reactor power doublings it becomes apparent that the +\$0.75/- \$1.00 criterion will not be met, the approach to critical is terminated to resolve the disparity.

Table 2.2 gives the OSCC position predicted by HELIOS, PDQ and the empirical method compared with the actual critical position. With the exception of Cycle 148A and 150A, all the HELIOS cases were within seven degrees of the reported critical position. Note that the OSCC drive mechanism can

contribute an uncertainty of about two degrees, which is the amount of play between the teeth of the drive gear and the connecting gear. Also, note that the HELIOS model OSCC mesh discretization is 3.75 degrees. The standard deviation of the differences between HELIOS predicted and reported OSCC position is six degrees. Six degrees is worth roughly \$0.60 to \$0.80 in the linear region of the OSCC worth curve. The standard deviation of the PDQ and empirical method differences is 3.8° and 5.4°, respectively.

Table 2.2. Predicted and reported critical OSCC positions for initial cold startup.

Cycle	HELIOS	PDQ	Empirical	Reported
145A	52.1	48.4	37.7	45.4
145B	40.4	53.2	42.8	42.8
146A	46.9	42.9	42.2	37.9
146B	43.6	44.9	38.0	33.6
147A	45.6	51.4	47.9	45.5
148A	62.8	59.2	52.3	50.3
148B	53.7	57.8	48.5	50.2
149A	53.8	53.4	54.6	52.5
149B	42.3	43.0	44.7	38.7
150A	99.4	82.1	73.7	82.1
150B	45.5	51.9	47.3	48.8
151A	39.3	37.5	46.3	37.9
151B	32.3	36.7	34.9	38.8
152B	55.1	57.2	45.8	54.3
153B	60.9	70.9	59.7	67.8
154A	38.5	49.8	45.3	45.8

Figure 2.5 shows the reactivity value of the difference between predicted and reported OSCC position. From the figure, it is evident that HELIOS consistently predicts the critical OSCC position within the bounds of the startup criteria. The average prediction is \$0.25 higher than the reported value. The reactivity worth of the standard deviation is similar to that of the empirical method. The large discrepancy for Cycles 146A, 148A and 150A lend to this large variability. Possible reasons for the discrepancy with Cycles 146A and 148A may be uncertainties associated with insufficient fission product nuclides transcribed from PDQ into HELIOS. Recall that PDQ uses a lump fission product. Another possible source of error for these two cycles is inadequacy of the lobe-exposure polynomial to represent the burnup reactivity decrement of either the target or known critical, or both. Discrepancies may also arise from the axial homogenization scheme used to describe experiments and fuel.

Cycle 150A was a high power “PALM” cycle. This cycle has a higher loading of fresh fuel in the southwest and southeast lobes. Thus, it is possible that Cycle 149B is not a useful starting point for predicting criticality of 150A. The next PALM cycle was Cycle 153B. If using Cycle 152B as the known critical for this cycle, the predicted critical position was 80.1° or \$1.10 too high. If using Cycle 150A, the predicted critical position was 60.1° with a value of \$0.86 low.

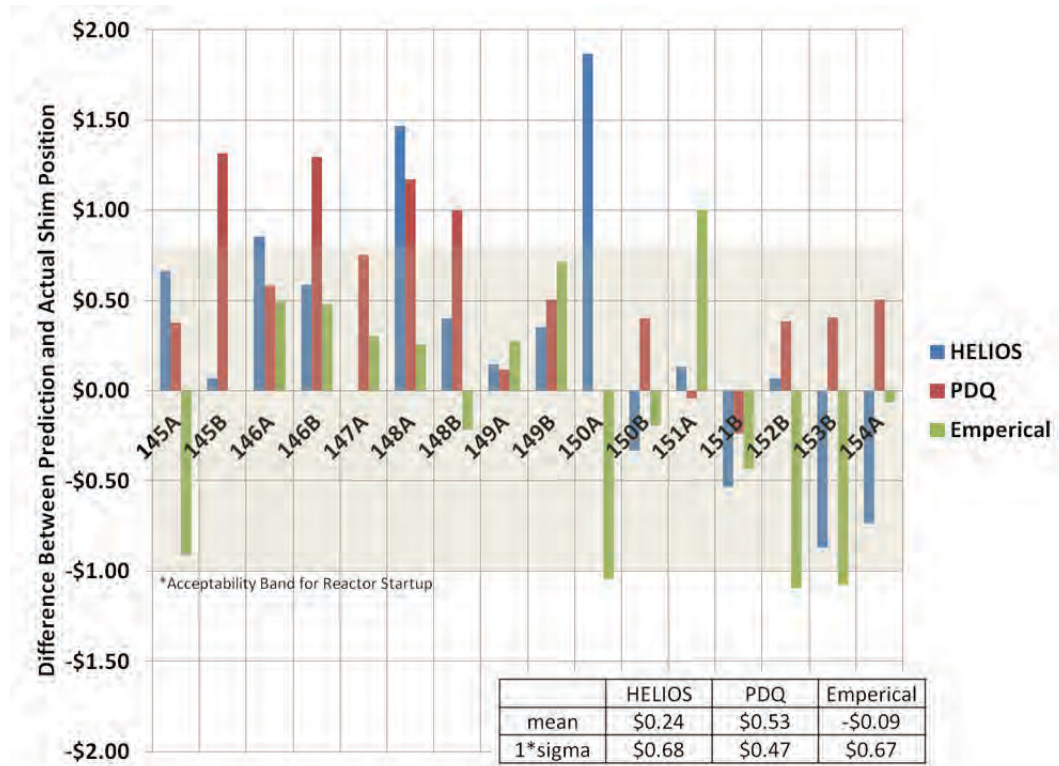


Figure 2.5 Reactivity worth of differences between predicted and reported OSCC critical position.

2.1.8 Results – Lobe Powers

The lobe-power distribution in the ATR is sensitive to fuel loading, flux trap and capsule loading, OSCC and neck-shim position. To create an accurate representation of the ATR lobe powers, the exact configuration of the reactor had to be recreated for all of the 16 cycles. Over the course of this work it was found that even the smallest capsules had to be modeled with sufficient resolution to capture localized spatial shielding, local reactivity importance or both. Lack of sufficient capsule detail could lead to lobe-power errors, $\epsilon = (\text{lobe}P_{\text{HELIOS}} - \text{lobe}P_{\text{ASUDAS}}) / \text{lobe}P_{\text{ASUDAS}}$, in excess of 15% (Nigg and Steuhm., 2012). Thus, in the course of this work the following non-fuel features required modeling attention: 22 capsule experiments, four isotope production capsule types, seven civilian flux trap experiments, 20 flux-trap experiments for the United States Navy, and five flux-trap backups (i.e., place-holder hardware). In addition, ten different types of fillers, plugs, flow-reducers and fixed burnable shims were modeled.

The lobe-power result of this modeling effort is given in Figures 2.6 through 2.10. As can be seen from the curves, the HELIOS core-follow results consistently stayed within 10% or less of the hourly ASUDAS data, Figure 2.11. One important global detail necessary for close agreement was the need to input the exact heavy metal mass loading of the core. HELIOS requires system-specific power as input, as opposed to total system power. HELIOS does have the ability to leverage its ray tracing scheme to compute the exact volume and heavy metal mass of every mesh-cell. The drawback is that a transport calculation must be performed in order to get this side benefit. Therefore, it is logistically advantageous to perform the power-independent branch calculations needed for startup critical OSCC positions before performing the at-power core follow.

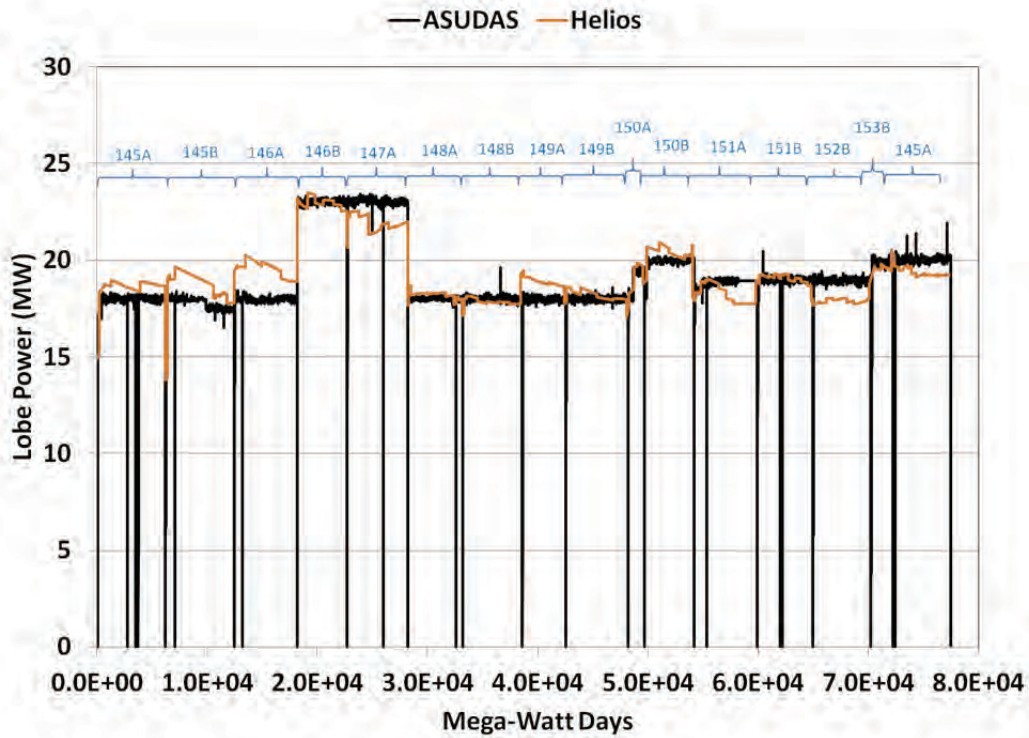


Figure 2.6 Northwest lobe power comparison between ASUDAS surveillance data and HELIOS

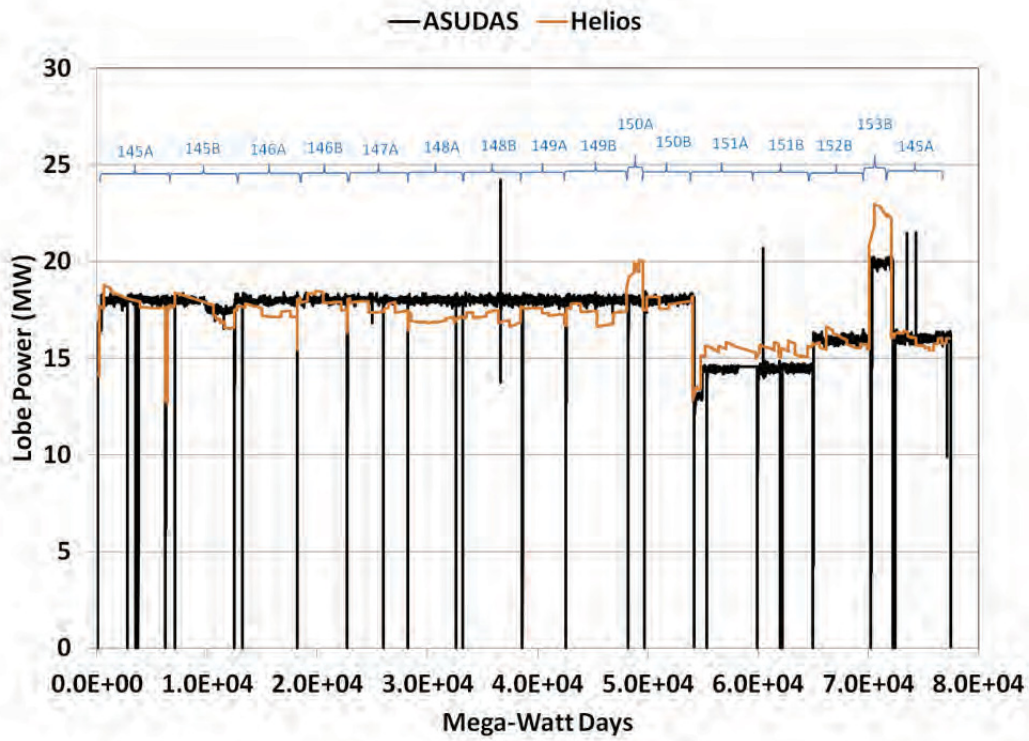


Figure 2.7 Northeast lobe power comparison between ASUDAS surveillance data and HELIOS

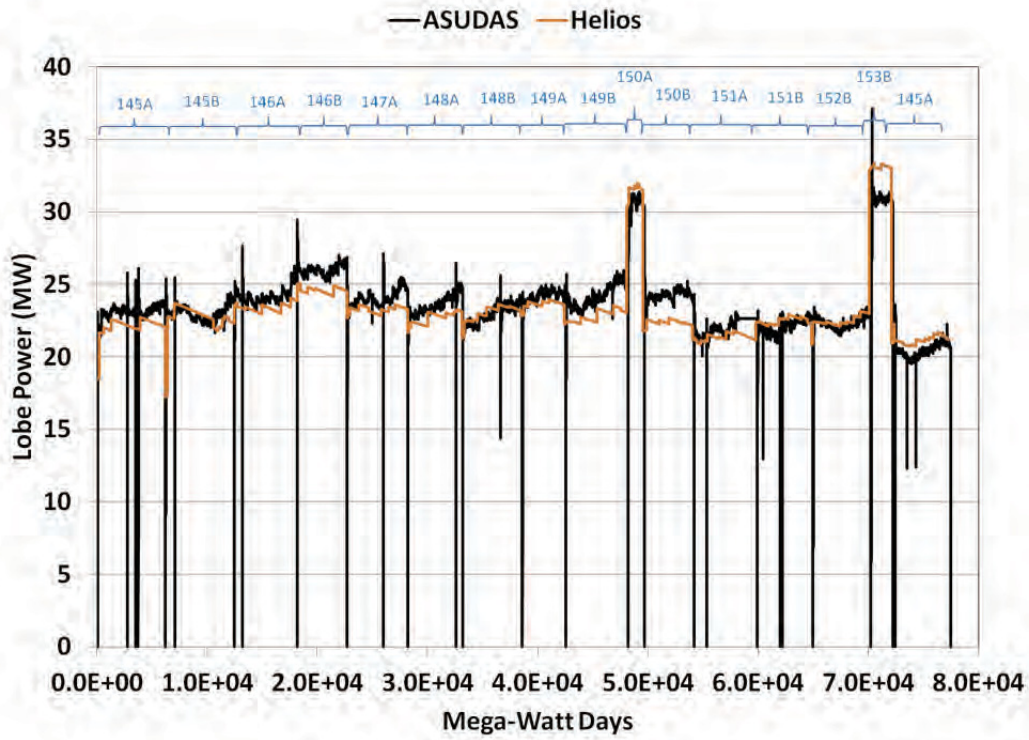


Figure 2.8 Center lobe power comparison between ASUDAS surveillance and HELIOS

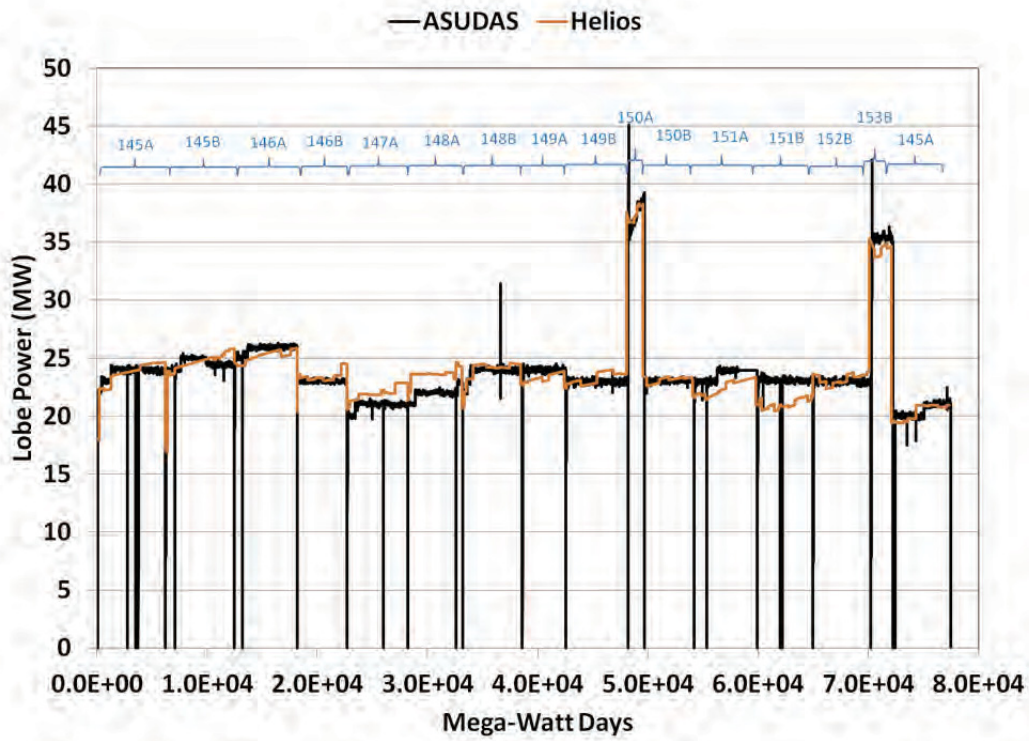


Figure 2.9 Southwest lobe power comparison between ASUDAS surveillance and HELIOS

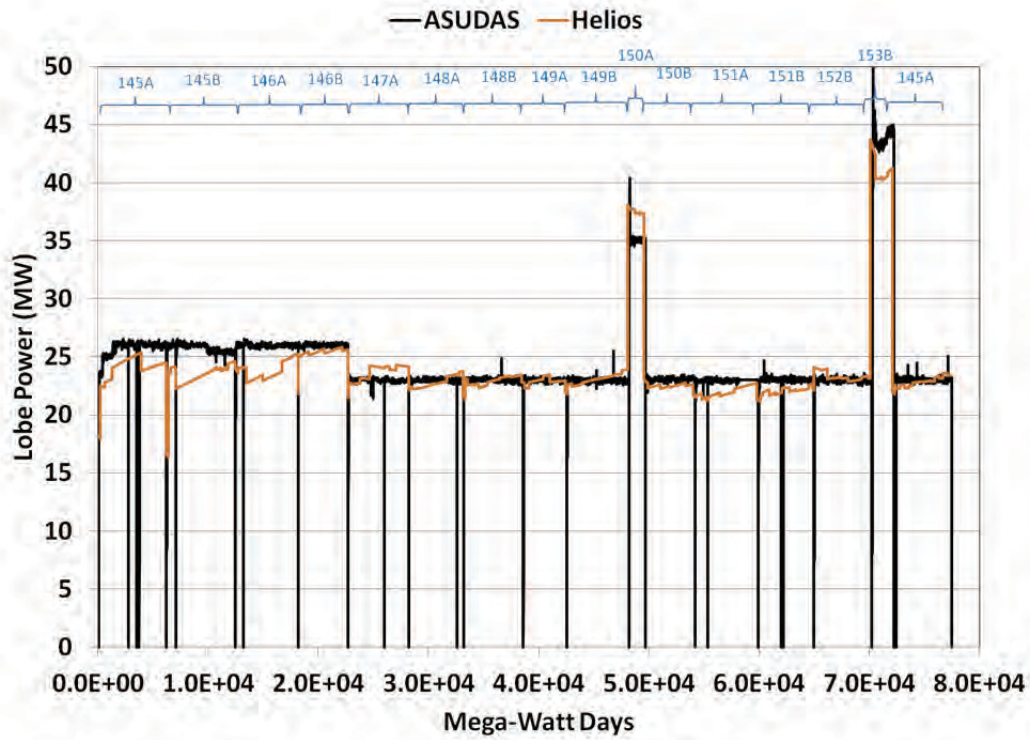


Figure 2.10 Southeast lobe power comparison between ASUDAS surveillance and HELIOS

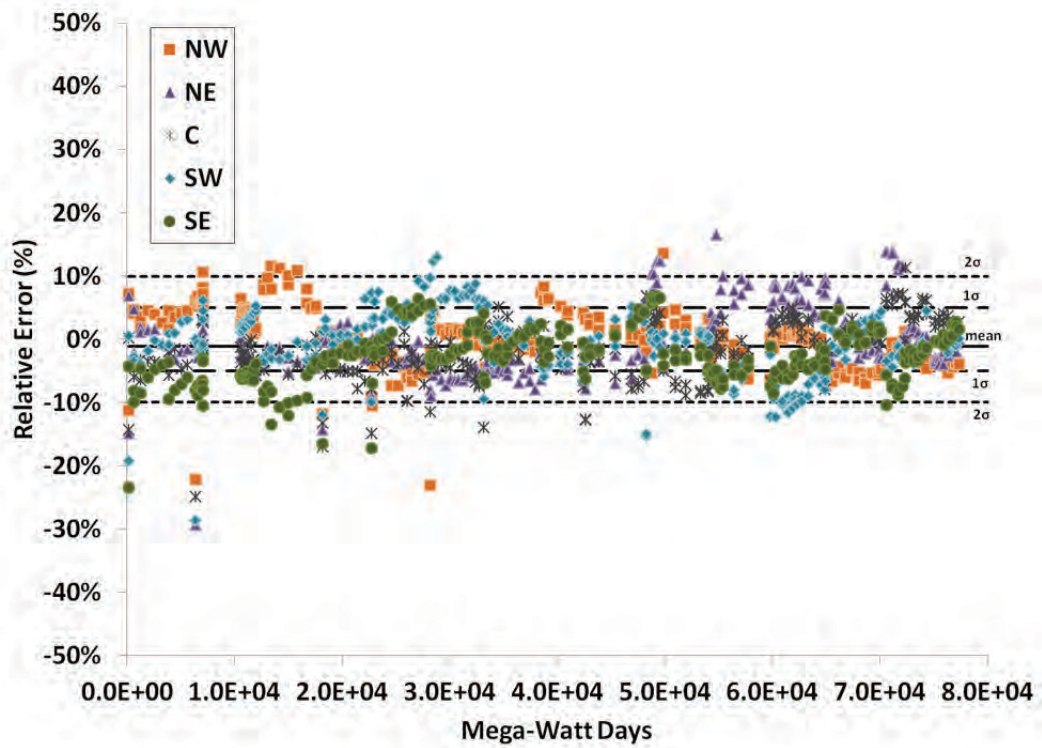


Figure 2.11 Relative error between lobe-powers reported by ASUDAS versus calculated by HELIOS

Just as with differences in the cold critical OSCC position, lack of axial information could lead to possible errors in the model. Another source of error is with the lobe-power measurement itself. Lobe power is not directly measured as is with self-powered-neutron-detectors in commercial light water reactors. Instead, it is inferred from sensing the N-16 activation generated in water flowing through ten flow-tubes that penetrate the ATR reflector. The N-16 product decays by beta emission back into O-16 with a half-life of 7.13 sec. This decay is detected by proportional counters outside of the core. The current from these counters is used as the response function in a least-squares correlation between the N-16 activation in the flow tubes and the power in each of the five lobes. The N-16 correlation matrix was last calibrated during the 1994 CIC. ASUDAS collects the lobe-powers calculated by the least-squares algorithm and saves this data to file during operation. Therefore, there is likely to be at least some measurement error associated with the N-16 least-squares correlation.

Another check for accuracy of the core-follow is the adherence to criticality throughout the entire cycle. Figure 2.12 shows the 2D transport eigenvalue for each state and burnup point from the core-follows plotted against the 2D transport eigenvalue associated with the cold startup criticality. As can be seen from the plot, the discretization methodology chosen for establishing each core state (i.e., burn step) was sufficiently fine to closely match the critical eigenvalue from startup. Note that the negative temperature feedback effect on core reactivity is not considered in this comparison. Also plotted in Figure 2.12 is the reactivity worth for each burn-step, $\rho = (k - k_c) / (k \times k_c)$. This curve shows that the discretization methodology very rarely, if ever, deviated from the actual critical condition by more than one dollar once xenon equilibrium is attained.

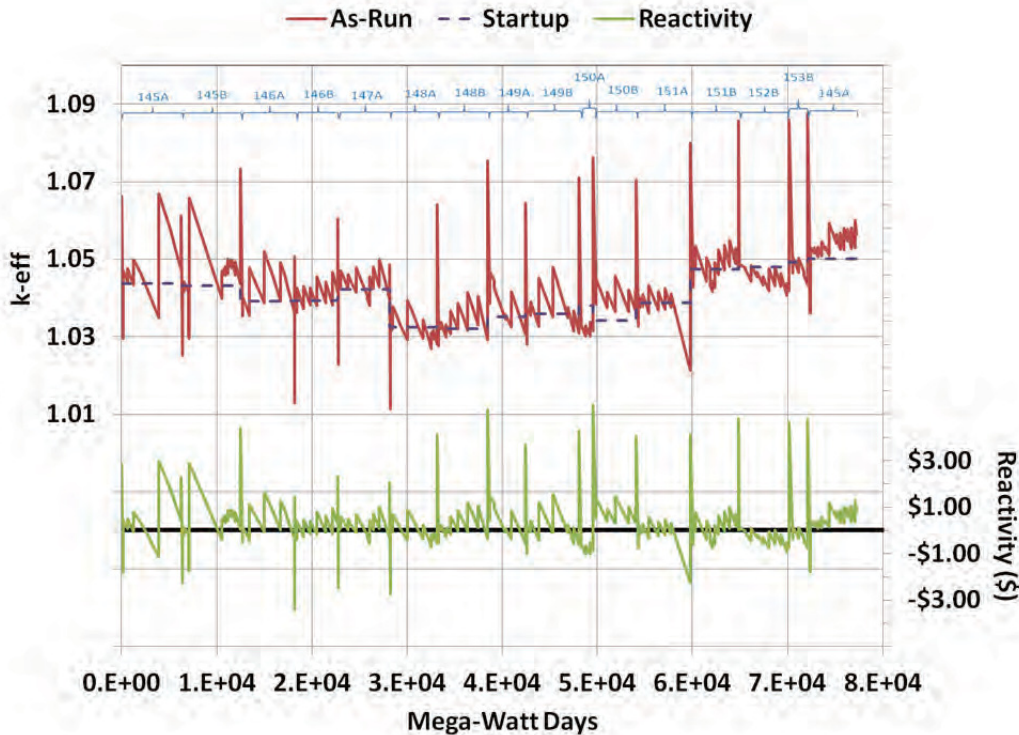


Figure 2.12. Reactivity worth at beginning and end of each burn step

The spiked nature of the BOC eigenvalues for each cycle is due in part to the fact that the core-follow cycles do not consider the first few hours between cold startup and hot-full-power. The HELIOS “C” option was used for all burn steps which is a standard predictor-corrector treatment. The predictor step uses the flux from the beginning-of-step transport solution to create end-of-step nuclide densities. The corrector step uses these end-of-step nuclide densities to re-deplete the beginning-of-step nuclides. The

final end-of-step nuclide densities reported by HELIOS are the average of the predictor and the corrector steps. Therefore, the BOC transport calculation for each cycle considers the xenon concentration to be zero when in reality it has had some time to buildup. The lack of the negative reactivity contribution from this neutron poison results in the seemingly large BOC reactivity spikes.

2.1.8 Fuel Inventory

In the absence of a direct method for burnup validation, such as chemical assay, we can only cross-validate the fuel loading of each HELIOS core-follow calculation with the PDQ As-Run data, as is accommodated by the applicable standard (ANS, 2005). Figure 2.13 compares the relative difference in the fuel element-averaged U-235 nuclide density between HELIOS and PDQ, $\epsilon = ({}^{235}\text{U}_{\text{HELIOS}} - {}^{235}\text{U}_{\text{PDQ}}) / {}^{235}\text{U}_{\text{PDQ}}$. All 40 fuel elements in each of the 16 cycles are plotted. The plot does not contain the fuel element position along the serpentine or the fuel element serial numbers themselves, as this information is irrelevant to showing the variability between HELIOS and PDQ. Note that the BOC agreement between the codes is nearly perfect for the first few cycles. This is because the first few cycles nearly exclusively borrow data from the PDQ database, thus the relative differences is round-off error associated with translating the PDQ database to the HELIOS database.

The mean relative difference over all of the $40 \times 16 \times 2 = 1280$ nuclide comparisons was 0.78%. Fifty-three percent of the relative differences were positive. One can observe from inspection of Figure 2.13 that the magnitude of positive relative errors is generally greater than the negative relative errors. This means that in general, the HELIOS solutions depleted the U-235 at a somewhat lesser rate than PDQ. In fact, the mean of positive EOC relative differences is 2.6% with a standard deviation of 2.1%, whereas the mean for negative relative differences is -1.0% with a standard deviation of 0.9%.

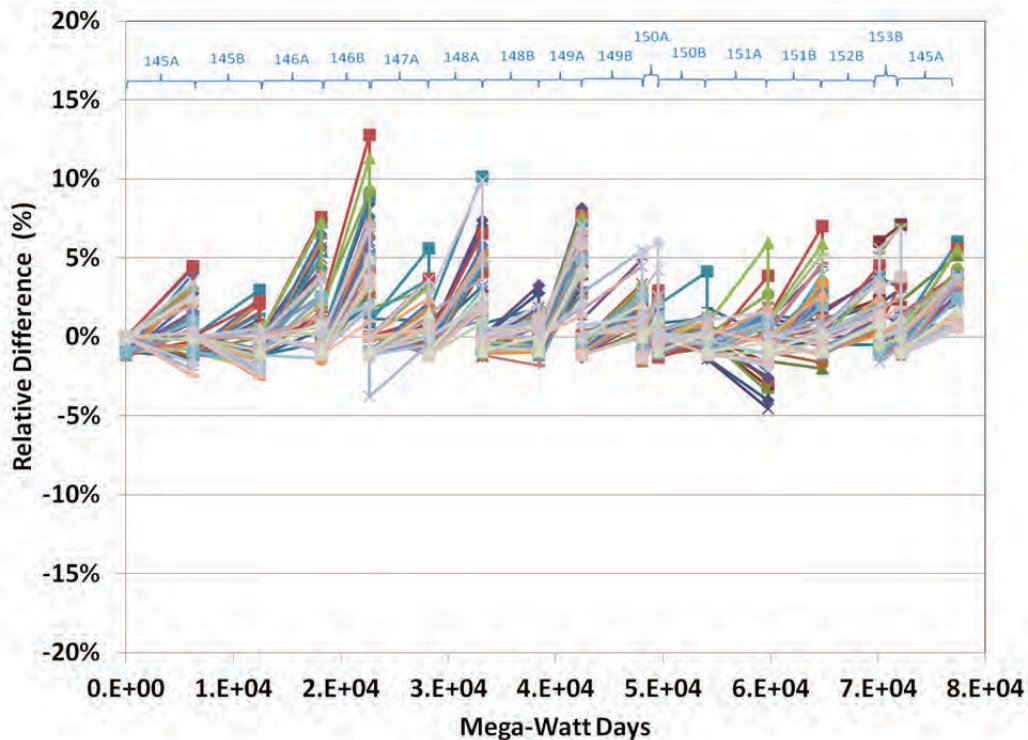


Figure 2.13. Relative difference in fuel element averaged U-235 atom density between HELIOS and PDQ

2.1.9 Conclusions

In order for HELIOS to be accepted as the next generation physics code for ATR reactor safety analysis, it must first be verified against current PDQ-based computational protocols and validated against relevant measurement data. The legacy code PDQ is used to predict core reactivity, power and fission density distributions and maintain a fuel nuclide database. This work presents the validation results from modeling 16 ATR cycle depletions that were operated between the fall of 2009 through fall of 2013. It was found that the ATR's lobe powers could be determined with $\pm 10\%$ accuracy of actual ASUDAS reactor surveillance data, which typically has its own estimated uncertainty that is ordinarily maintained in the range of 5%, via a process that involves comparison with the ATR water-power indicator, an independent power measurement system (Atkinson and McCracken, 1997). Also, the Outer Shim Control Cylinder configuration for initial criticality was computed for each cycle. HELIOS successfully predicted criticality within the tolerance set by the ATR startup procedure for 13 out of the 16 cycles modeled. This is compared to 12 times for PDQ and 12 times for the empirical reactivity tabulation method, respectively. If the HELIOS startup predictions were averaged with those of the reactivity tabulation method, as is currently done with PDQ, the ATR startup criterion would have been met for all 16 cycles. The depletion results for U-235 nuclide densities computed by HELIOS for each cycle were compared with the PDQ database. The maximum relative difference for any given fuel element was 12 percent. However, the average and standard deviation of relative differences were only on the order of a few percent.

Over the course of this work it was found that it is important to model all fuel and experiments, including the smallest of drop-in capsules, to the greatest reasonable modeling detail. This is necessary for accurately determining reaction integrals as well as the localized reactivity importance. The close agreement between PDQ and HELIOS nuclide data suggests that fuel element powers are being computed accurately. The validation of inter- and intra-element powers is currently being conducted via activation spectroscopy measurements in the ATRC and is reported in Chapter 3.

Areas of improvement have been identified for advancing the current practice. Though HELIOS avoids much of the reactivity and power correction factors needed by PDQ, it still must rely on an outside source for providing information relevant to the axial dimension. From inspection of the current 2D-to-1D axial reactivity bias correction employed by PDQ, it seems that a similar 3D-to-2D scheme can be implemented using a 3D neutron transport code such as MCNP. Completion of this 3D-to-2D correction methodology is the subject for FY-14.

2.2 Demonstration of Axial Profile Analysis

This section documents the development and initial demonstration of a set of MCNP5 (MCNP Team, 2005; X-5 Monte Carlo Team, 2003) models and supporting computational protocols (e.g., scripts) that can be used to routinely characterize axial power factors associated with ATR Core Safety Assurance Package (CSAP). These axial power factors, to be used in conjunction with the new HELIOS core safety analysis and fuel management methodology, represent adjustments to 2D calculations that account for axial fission profile effects. The demonstration-level neutronic evaluations presented here were performed using the planned reactor operating conditions and configurations for ATR Cycle 152B (Stanley, 2012). This cycle was selected as an example because extensive physics measurements performed during the previous ATR cycle, 152A (which was a so-called “depressurized run”) and the associated supporting experiments performed in the ATRC provided a great deal of new experimental code validation data pertinent to the current configuration of the ATR.

2.2.1 Background

Several different types of physics analyses are performed to satisfy the ATR Updated Final Safety Analysis Report (UFSAR) requirements for each operational cycle. The analyses pertaining to the ATR

core as a whole and specifically to the driver fuel are reported in the CSAP. Analyses pertaining to experiments are reported in corresponding documentation created for each experiment, namely the Experiment Safety Assurance Package (ESAP). Taken together, this documentation provides DOE with assurance that the UFSAR requirements are being met for each cycle.

A major component of the CSAP documentation consists of physics data produced by the existing suite of codes associated with the diffusion code PDQ (Smith and Weaver, 1994). The current ATR physics analysis that supports the CSAP documentation is performed by utilizing a suite of computer codes that were specifically created to interact with a PDQ model of the ATR and provide data in support of ATR operation (Cook and Smith, 1996). The method incorporates the use of several different PDQ input files, some pre-processing codes that are used to collate information for use in a specific cycle, and post-processing codes that produce the necessary information to satisfy safety analysis report (SAR) commitments.

The current PDQ-based methodology used to characterize axial power factors is performed via the ROSUB code (an internally-developed INL data post-processing tool) utilizing polynomial approximations that assume a chopped cosine axial shape is maintained within ATR. The newly developed protocols can be used to verify this assumption as well as provide the potential to expand the axial shape profiles that can be modeled. In the newly developed protocols, the depletion of driver fuel elements is performed utilizing an axial fission profile representative of a typical ATR core configuration. The initial fuel loading within each region of an element for Cycle 152B is determined by ORIGEN2 (Croff, 1983) according to a) the exposure experienced by the element prior to the start of Cycle 152B and b) the typical axial fission profile determined by MCNP5. Thus, the axial loading of previously-used elements as of the beginning of Cycle 152B is assumed to be preserved.

The ROSUB code performs a variety of cycle-specific post-processing calculations and provides the results to many of the other post-processing codes in the physics analysis network. The ROSUB program also calculates several normalization factors that are ultimately used by other post-processing programs. The Power Density Normalization Factor is used to convert the power density calculated by the homogeneous PDQ model into the power density within a heterogeneous element. The Power Density Normalization Factor also contains element peak-to-average power density multipliers for converting x-y power density into a value representative of the true x-y-z behavior. Another normalization factor calculated by ROSUB and used by other post-processing programs is the Cumulative Fissioned Atom Density (CFAD) normalization factor. This factor is used to convert the fission density calculated by the homogeneous PDQ model into the fission density within a heterogeneous element. The CFAD normalization factor also contains the peak-to-average fission density multiplier.

2.2.2 Assumptions

The assumptions used in this analysis are stated below.

1. The MCNP5 models of the ATR core use three radial fuel regions to represent the ATR fuel elements (FEs), as shown by Figure 2.14.
2. The MCNP5 models of ATR utilized in this report contain ATR driver fuel loadings representative of the driver fuel loadings utilized during Cycle 152B.
3. Even axial distribution of the fuel is appropriate when modeling unirradiated fuel elements.
4. The axial fission profile is unperturbed from the standard ATR profile by the 152B experiments.

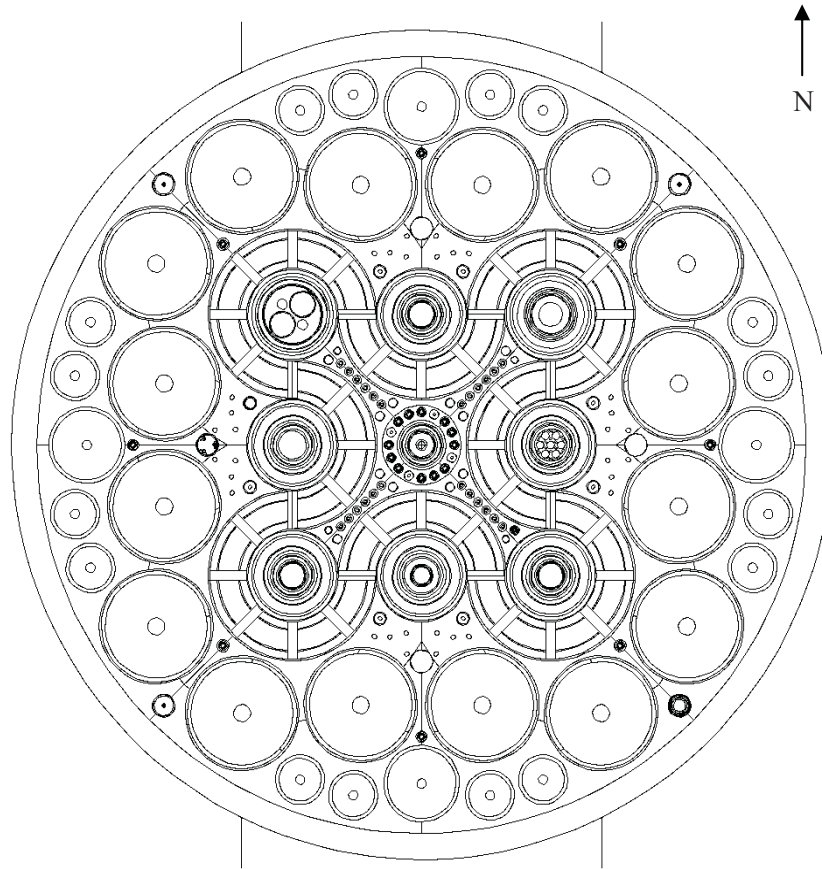


Figure 2.14 MCNP5 model of Cycle 152B configuration utilizing three-region driver fuel.

2.2.3 Computer Code Validation

MCNP5, a general purpose Monte Carlo N-Particle transport code, was used to model and evaluate the axial fission profile demonstrated during Cycle 152B. The depletion code ORIGEN2 was used to model and evaluate the depletion of the fuel for the driver fuel elements, providing an axial fission profile versus exposure time. The MCNP5 built-in cross-section data libraries and the JENDL-3.2 cross-section libraries (Nakagawa, 1995) were used to perform all MCNP5 evaluations for Cycle 152B. The ORIGEN2 library ATRXS (Schnitzler, 1991) as well as a MCNP5-generated fission profile were used to calculate the burnup within the driver elements. Both MCNP5 and ORIGEN2 are listed in the INL Enterprise Architecture Repository (Lilo and Mitchell, 2010; Mitchell and Nielsen, 2011) and are accepted as qualified scientific and engineering analysis software. MCNP5 has been validated for use at the INL by running the 42 sample problems transmitted on the Radiation Safety Information Computational Center (RSICC) installation CD and comparing the results against the standard results provided on the installation CD. Additionally, the input model for the ATR criticality benchmark (Kim and Schnitzler, 2005) was executed and results identical to the published results were obtained (Lilo and Mitchell, 2010).

2.2.4 The ROSUB Method

PDQ can be operated with a 2D r-z coordinate system. This feature was used for calculating axial multipliers due to fuel burnup (Brown and Smith, 1990). To do this, a single lobe is approximated by a right circular cylinder comprised of a generic standard in-pile tube (SIPT) encircled by eight fresh 7F-type fuel elements (See Figure 2.15, where the inner red ring represents the SIPT and the remaining rings

represent 7F fuel elements). These 7F fuel elements are represented by seven fueled concentric annuli where no side plates or non-fueled plate ends are included. The annuli describe Plate(s) 1, 2, 3-4, 5-15, 16-17, 18, and 19, respectively. Each fueled annulus is represented by a homogenized cell containing water, aluminum cladding, and UAlx fuel matrix. The generic SIPT was non-depleting and was axially homogeneous, but with a cross-section that was flux weighted in an early r-z model during cross-section condensation. This generic SIPT also contained a non-depleting test shroud.

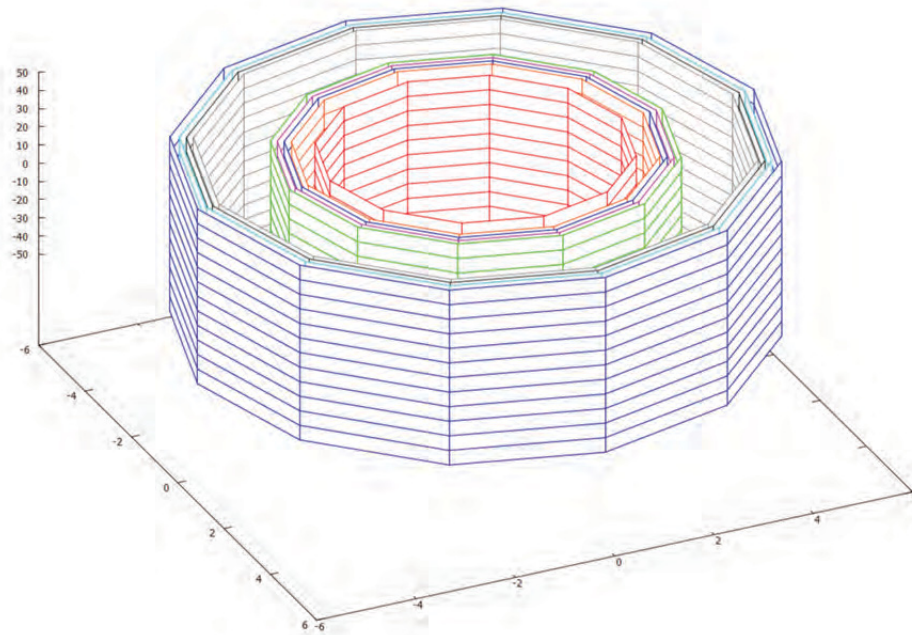


Figure 2.15 Graphical depiction of 2D r-z PDQ model. Each annulus represents a different fuel plate.

The concentric lobe model used by ROSUB is based on a factor called lobe exposure. Lobe exposure is defined by the lobe power of the lobe in which the fuel element resides multiplied by the time at power of the cycle. Thus, for any given cycle the lobe exposure value is identical for all eight fuel elements in a lobe. When utilized in the r-z model, this definition and application is appropriate. However, this definition is also utilized in the standard x-y model representing each cycle, where symmetry about the lobe cannot be assumed. Thus, this definition introduces error in the way that lobe exposure and ultimately the axial multipliers are calculated.

The PDQ-based methodology puts more emphasis on the lobe-power than on the fuel element power. This may be due to the historical perspective that the cumulative power of fuel elements in a lobe is considered more useful information as it can be directly compared with the ATR N-16 lobe power measurement system. Hence, fuel element powers are not generally used for the purpose of tracking fuel element power history. Note that using modern methods such as HELIOS and MCNP5 and rigorous modeling of the problem, fuel element powers can be trusted as exact.

The 2D r-z model was used to compute peak-to-average power density axial factors. This was done by simply taking the power density at the mid-plane and dividing by the lobe-average power density. The axial peaking factors for the power density were obtained by the following equation.

$$A(t) = \frac{P_m(t)/V_m}{\sum P_i(t)/\sum V_i} = \frac{P_r(t)}{P_a(t)} \quad (2.5)$$

In this equation A is the peak-to-average power density axial factor., P_m and V_m is the local region power and volume at the mid-plane, respectively, P_i and V_i are the local region powers and volumes of the r-z lobe system, respectively, P_r is the power density at the mid-plane, and P_a is the axial lobe average power density.

The peak-to-average power density factors were calculated for continuous operation and for shutdown intervals of 5, 10 and 25 day following durations of continuous operation. Figure 2.16 plots the axial power factors as a function of lobe exposure. The values for continuous operation are plotted on the left y-axis. The factors accounting for burnup shape effects during shutdown intervals are plotted on the right y-axis. These shutdown interval curves account for the effect of xenon decay and samarium buildup on the axial burnup shape and resulting reactivity penalty. These canal time-sensitive peak-to-average axial power multipliers are only applicable for initial criticality because the xenon and samarium nuclide concentration quickly evolves to their at-power equilibrium values, i.e., the continuous operation values. Note for this demonstration, only the continuous operation polynomial was evaluated.

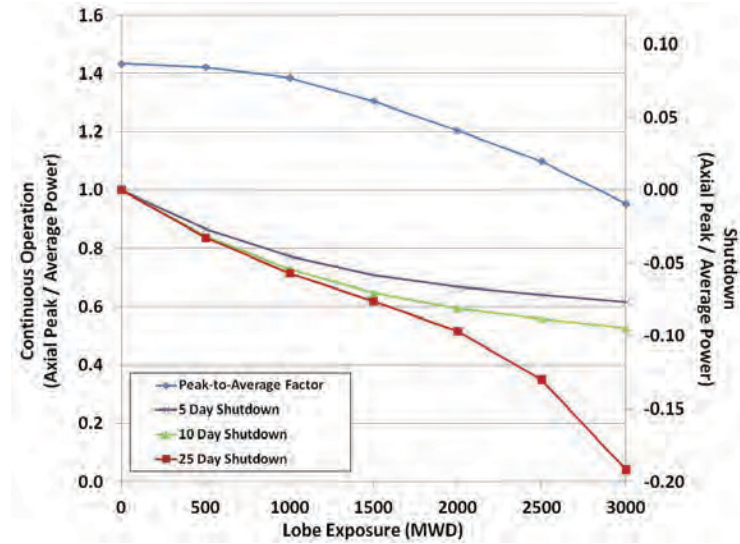


Figure 2.16 Power multiplier factors due to axial burnup shape.

2.2.5 The MCNP5 Method

The MCNP5-calculated power density multipliers were evaluated using the results from the ATR three radial-region detailed MCNP5 full core physics model of the driver fuel elements. The demonstration model utilized seven depleting axial regions to provide the evaluated axial results and included experiments from Cycle 152B, as described by Table 2.3. The MCNP5 model was then coupled to ORIGEN2 to provide depletion of the driver elements.

Fuel specifications (ATR Engineering, 2005) were used to develop fresh fuel zone loading information for each of the 21 driver element regions in the MCNP5 model. It was assumed that even axial distribution of the fuel was appropriate when modeling unirradiated fuel elements. Water densities were provided for each region that corresponded to a primary coolant temperature of 27°C. Each depleting region also contained a fission energy deposition tally to determine the fission characteristics of the region.

Table 2.3 Experiment Loading for Cycle 152B

Position	Actual Loading	Modeled Loading
NW Flux Trap	2E-NW-160	2E-NW-160
N Flux Trap	ID-N-106	ID-N-106
NE Flux Trap	AGR-3/4	AGR-3/4
W Flux Trap	1C-W-75	1C-W-75
C Flux Trap	2A-C-BU	2A-C-BU
E Flux Trap	AGC-3	AGC-3
SW Flux Trap	2D-SW-218	2D-SW-218
S Flux Trap	SPICE 9	SPICE 9
SE Flux Trap	2B-SE-192	2B-SE-192
A-1	IASFR	IASFR
A-2	IASFR	IASFR
A-3	IASFR	IASFR
A-4	IASFR	IASFR
A-5	IASFR	IASFR
A-6	IASFR	IASFR
A-7	IASFR	IASFR
A-8	IASFR	IASFR
A-9	SFROP	SFROP
A-10	AFC-3A	AFC-3A
A-11	SFROP	SFROP
A-12	SFROP	SFROP
A-13	LSFR	LSFR
A-14	EPRI-ZG-B	LSFR
A-15	EPRI-ZG-C	LSFR
A-16	EPRI-ZG-A	LSFR
B-1	YSFR	YSFR
B-2	YSFR	YSFR
B-3	YSFR	YSFR
B-4	YSFR	YSFR
B-5	YSFR	YSFR
B-6	YSFR	YSFR
B-7	HSIS Hardware	HSIS Hardware
B-8	YSFR	YSFR

Position	Actual Loading	Modeled Loading
B-9	MANTRA-1	Aluminum Filler
B-10	Aluminum Filler	Aluminum Filler
B-11	MANTRA-3	Aluminum Filler
B-12	AGR-2	AGR-2
H-1	LSA Cobalt	LSA Cobalt
H-2	Aluminum Filler	Flux Wire Monitor Holder
H-3	N-16 Monitor	N-16 Monitor
H-4	LSA Cobalt	LSA Cobalt
H-5	LSA Cobalt	LSA Cobalt
H-6	LSA Cobalt	LSA Cobalt
H-7	LSA Cobalt	LSA Cobalt
H-8	LSA Cobalt	LSA Cobalt
H-9	LSA Cobalt	LSA Cobalt
H-10	Aluminum Filler	Flux Wire Monitor Holder
H-11	N-16 Monitor	N-16 Monitor
H-12	LSA Cobalt	LSA Cobalt
H-13	LSA Cobalt	LSA Cobalt
H-14	LSA Cobalt	LSA Cobalt
H-15	LSA Cobalt	LSA Cobalt
H-16	LSA Cobalt	LSA Cobalt
I-1 through I-20	Beryllium Filler	Beryllium Filler
I-21	Aluminum Filler	Aluminum Filler
I-22	UCSB-2	UCSB-2
I-23	Aluminum Filler	Aluminum Filler
I-24	Aluminum Filler	Aluminum Filler

ORIGEN2-calculated depletions require fission energy deposition profile results to provide appropriate axial depletions. Average fission profiles were obtained from the ATR MCNP5 full core physics model by modeling a typical cycle loading (namely Cycle 144A) using high-resolution 3D depletion of driver elements (Sterbentz, 2011). This model provided the data needed to calculate power fractions by region. As a proof-of-concept approximation, a single set of average results over multiple time steps and over all elements for each region were then provided as input into each of three Element Fuel Loading files, one for each element type available. This

information was then used as a basis for depleting fresh fuel elements to the exposures necessary for a given cycle.

Element exposure for Cycle 152B was estimated based on the amount of U-235 present in each element, as calculated by PDQ (Poling, 2012). First, ORIGEN2-calculated depletions were generated for Mark VII elements over a range of exposures to correlate U-235 loadings, as listed in Table 2.4 and illustrated in Figure 2.17. A set of Python scripts, namely ‘makeburn.py’ and several underlying scripts (as detailed in Appendix A), were used to generate the correlation. Note that the ORIGEN2-calculated depletions were evaluated using what was assumed to be an average fission profile.

Table 2.4 Mark VII element exposure vs. grams of fuel as obtained by ORIGEN2

Element MWD	U-235 (g)	B-10 (g)	U-238 (g)
1.00E-05	1075.325	0.662053	80.94429
15.00001	1056.184	0.565175	80.75731
20.00001	1049.803	0.536049	80.6947
25.00001	1043.424	0.508382	80.6315
30.00001	1037.046	0.482114	80.56791
35.00001	1030.665	0.457175	80.50331
40.00001	1024.288	0.433508	80.43929
45.00001	1017.91	0.411053	80.37464
50.00001	1011.543	0.38975	80.30972
55.00001	1005.168	0.369548	80.24393
60.00001	998.7941	0.35039	80.17808
65.00001	992.4183	0.332234	80.11162
70.00001	986.0475	0.315022	80.04551
75.00001	979.6745	0.298714	79.97862
80.00001	973.3013	0.283262	79.91113
85.00001	966.9379	0.268629	79.84357
90.00001	960.5673	0.254769	79.77575
95.00001	954.2063	0.241648	79.70705
100.00001	947.8383	0.229226	79.6384
105.00001	941.4752	0.217467	79.56917
110.00001	935.1106	0.206338	79.49975
115.00001	928.7513	0.19581	79.42962
120.00001	922.3825	0.185848	79.35933
125.00001	916.0255	0.176424	79.28848
130.00001	909.6641	0.16751	79.21771
135.00001	903.3076	0.159077	79.14615
140.00001	896.9499	0.151103	79.07422
145.00001	890.5976	0.143562	79.0017
150.00001	884.2384	0.136431	78.92934
155.00001	877.8871	0.129687	78.85637
160.00001	871.5353	0.123311	78.78301
165.00001	865.1806	0.117281	78.70931
170.00001	858.8309	0.111579	78.63458
175.00001	852.4817	0.106188	78.56062
180.00001	846.1327	0.101088	78.48582
185.00001	839.7818	0.096266	78.41008
190.00001	833.4408	0.091702	78.33457
195.00001	827.091	0.087387	78.25882
200.00001	820.7505	0.083305	78.18202

Element MWD	U-235 (g)	B-10 (g)	U-238 (g)
205.00001	814.4137	0.079443	78.10511
210.00001	808.072	0.075786	78.02803
215.00001	801.7286	0.072324	77.95038
220.00001	795.3879	0.069048	77.87277
225.00001	789.0574	0.065944	77.79414
230.00001	782.7204	0.063003	77.71561
235.00001	776.3869	0.060218	77.63641
240.00001	770.0508	0.057577	77.55716
245.00001	763.7237	0.055074	77.47728
250.00001	757.3951	0.052699	77.39731
255.00001	751.0677	0.050444	77.31666
260.00001	744.7453	0.048306	77.23594
265.00001	738.4219	0.046275	77.15514
270.00001	732.0936	0.044346	77.07345
275.00001	725.7761	0.042512	76.99177
280.00001	719.4607	0.040768	76.90986
285.00001	713.1441	0.039109	76.82742
290.00001	706.8282	0.037531	76.74463
295.00001	700.5157	0.036028	76.66202
300.00001	694.204	0.034596	76.57878
305.00001	687.8966	0.033232	76.49555
310.00001	681.5932	0.03193	76.41143
315.00001	675.2917	0.030689	76.32806
320.00001	668.9829	0.029505	76.24358
325.00001	662.6877	0.028373	76.15914
330.00001	656.3911	0.027292	76.07532
335.00001	650.0983	0.026259	75.99027
340.00001	643.8076	**0.02527	75.90545
345.00001	637.5185	0.024325	75.82063
350.00001	631.2313	0.023419	75.73574
355.00001	624.9516	0.022552	75.65123
360.00001	618.6685	0.021722	75.56647
365.00001	612.3951	0.020925	75.48146
370.00001	606.1244	0.020162	75.39657
375.00001	599.856	0.019429	75.3122
380.00001	593.5881	0.018725	75.22822
385.00001	587.3298	0.01805	75.14438
390.00001	581.0729	0.017402	75.06065
395.00001	574.8215	0.016778	74.97722

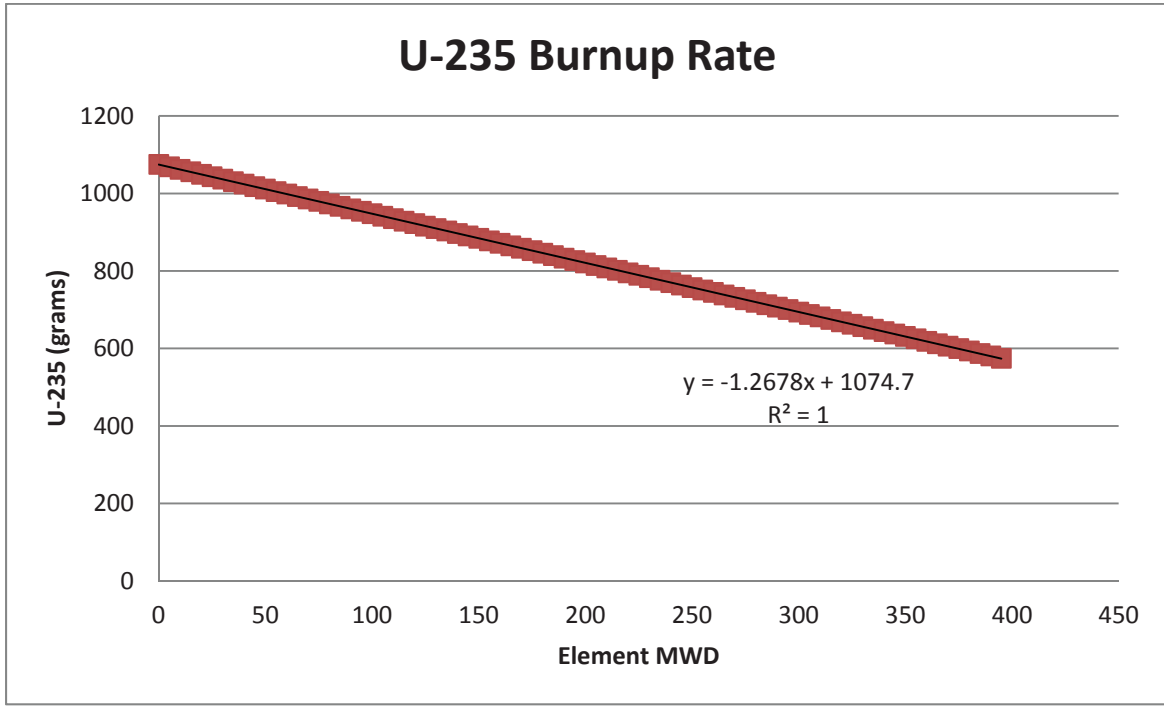


Figure 2.17 U-235 Burnup Rate obtained from Table A1 data.

Element powers requested during the parametric study were weighted to correspond to the fission energy deposition profile present in the typical MCNP5 model. Appropriate region power fractions were then used to obtain region exposures, as shown in Equation 2 below. To obtain accurate isotopic distributions over time, the requested element exposure was broken into 49 single-day time steps with corresponding region powers to obtain the intended total element exposure. Updated isotopic data were fed back into subsequent ORIGEN2 depletion time steps. The burnup rate of 1.268 grams per MWD of element exposure was calculated from this data and was used for all fuel types present in Cycle 152B.

$$\text{Region Exposure} = \left[\sum_{i=1}^{21} PF_i \right] [P_e(t)] [t] = \left[\sum_{i=1}^{21} PF_i \right] [P_e(t)] \left[\frac{t}{49 \text{ Days}} \right] [49 \text{ Days}]$$

$$\text{Region Exposure} = \left[\sum_{i=1}^{21} PF_i \right] [PC(49 \text{ Days})] [49 \text{ Days}] \quad (2.6)$$

In these equations PF_i is the region power fraction obtained from the assumed fission profile, P_e is the element power at time t , and PC is the power conversion factor used when assuming a 49-day period of exposure.

Isotopic data provided by PDQ was then utilized to determine the exposure of each element in Cycle 152B. Via additional Python scripts (“makemateds.py” and supporting scripts – Appendix A) the element exposure for each Cycle 152B element was weighted with the average MCNP5 fission profile to determine the power level utilized for each region during ORIGEN2 depletions, similar to the approach used in Equation 2.6 above. To obtain accurate isotopic distributions over time, the requested element exposures were broken into 49 single-day time steps and updated isotopic data were fed back into subsequent ORIGEN2 depletion time steps. At the conclusion of each exposure calculation, ORIGEN2-calculated data was used to provide an update to the material and cell cards of each MCNP5 region.

The beginning-of-cycle state of each element was obtained for Cycle 152B as an input into a MCNP5 model for the cycle. The states represent three-dimensional effects due to burnup of driver fuel elements at various element exposures. A final set of fission energy deposition tallies were obtained from the MCNP5 model to provide comparable data to the peak-to-average power density multipliers generated by ROSUB polynomials.

A calculation similar to Equation 2.5 was used, where the fission profile was volume-weighted to obtain a peak-to-average power density for an element. The peak value was assumed to occur at the core centerline. Note that

MCNP5 reports tally results normalized per source particle and gram of material, requiring normalization factors to convert tally results to the quantity of interest.

$$A(t) = \frac{P_m(t)/V_m}{\sum P_i(t)/\sum V_i} = \frac{P_r(t)}{P_a(t)} \quad (2.7)$$

where: P_i = [type 7 tally (MeV/g/fission neutron)] [region mass (g)] and

P_m = [core centerline type 7 tally (MeV/g/fission neutron)] [region mass (g)].

2.2.6 Axial Profile Comparisons

Comparisons between the newly developed method and the current set of multipliers, which utilize polynomial approximations calculated by ROSUB for axial power factors, were made. To provide a basis for comparison, a comparable exposure history was determined. ROSUB polynomial approximations are based upon exposures that are calculated from lobe power, not element power. Therefore, lobe exposure values for the newly developed method were derived for the purpose of utilizing the ROSUB polynomials. One simply needs to multiply the fuel element exposure in MWD by the number eight to obtain appropriate lobe exposure values. Thus, additional ROSUB multipliers were determined based upon the exposure calculated via the U-235 burnup rate method. A direct comparison could then be made between the ROSUB polynomials and the axial profile provided by MCNP5 calculations.

Table 2.5 provides the lobe exposures determined via the two methods discussed in this report, the corresponding ROSUB multipliers as determined by the polynomials currently used in the PDQ-based methodology, and the peak-to-average power density multiplier determined from the axial profile produced during MCNP5 calculations. Note that the MCNP5 multiplier is only available for the exposure determined by the U-235 burnup rate method.

Table 2.5 Peak-to-average power density multiplier comparisons.

Element Position	Serial Number	Exposure Calculation Method	BOC Lobe Exposure (MWD)	ROSUB Multiplier	MCNP5 Multiplier
1	XA819T	PDQ	1191	1.359	--
		U-235 Rate	1448	1.315	1.275
2	XA764TNB	PDQ	1418	1.320	--
		U-235 Rate	1539	1.297	1.250
3	XA879T	PDQ	1289	1.343	--
		U-235 Rate	1577	1.290	1.250
4	YA534TM	PDQ	2070	1.189	--
		U-235 Rate	1767	1.252	1.168
5	YA538TM	PDQ	2342	1.133	--
		U-235 Rate	1943	1.215	1.134
6	XA874T	PDQ	2274	1.147	--
		U-235 Rate	2284	1.145	1.169
7	XA920T	PDQ	1849	1.235	--
		U-235 Rate	1748	1.256	1.240
8	XA842T	PDQ	1313	1.339	--
		U-235 Rate	1533	1.299	1.264
9	YA520TM	PDQ	1434	1.317	--
		U-235 Rate	1224	1.354	1.266

Element Position	Serial Number	Exposure Calculation Method	BOC Lobe Exposure (MWD)	ROSUB Multiplier	MCNP5 Multiplier
10	XA891T	PDQ	1157	1.364	--
		U-235 Rate	1432	1.318	1.296
11	XA024U	PDQ	1324	1.337	--
		U-235 Rate	1211	1.356	1.340
12	XA054U	New	0	1.434	1.375
13	XA055U	New	0	1.434	1.381
14	XA056U	New	0	1.434	1.387
15	XA938T	PDQ	755	1.409	--
		U-235 Rate	839	1.402	1.384
16	YA481TM	PDQ	433	1.423	--
		U-235 Rate	435	1.423	1.386
17	XA057U	New	0	1.434	1.388
18	XA058U	New	0	1.434	1.385
19	XA059U	New	0	1.434	1.379
20	XA946T	PDQ	966	1.389	--
		U-235 Rate	1110	1.371	1.336
21	XA959T	PDQ	965	1.389	--
		U-235 Rate	1098	1.373	1.352
22	XA060U	New	0	1.434	1.376
23	XA063U	New	0	1.434	1.379
24	XA954T	New	0	1.434	1.376
25	XA010U	PDQ	1059	1.378	--
		U-235 Rate	959	1.390	1.350
26	XA942T	PDQ	966	1.389	--
		U-235 Rate	1022	1.383	1.350
27	XA904T	PDQ	847	1.401	--
		U-235 Rate	940	1.392	1.359
28	XA967T	New	0	1.434	1.392
29	XA983T	New	0	1.434	1.367
30	XA244T	PDQ	1185	1.360	--
		U-235 Rate	1199	1.358	1.336
31	XA011U	PDQ	1289	1.343	--
		U-235 Rate	1293	1.342	1.304
32	XA985T	New	0	1.434	1.347
33	XA939T	PDQ	755	1.409	--
		U-235 Rate	669	1.414	1.327

Element Position	Serial Number	Exposure Calculation Method	BOC Lobe Exposure (MWD)	ROSUB Multiplier	MCNP5 Multiplier
34	YA490TM	PDQ	463	1.423	--
		U-235 Rate	461	1.423	1.301
35	XA863T	PDQ	663	1.415	--
		U-235 Rate	877	1.399	1.300
36	XA932T	PDQ	755	1.409	--
		U-235 Rate	839	1.402	1.311
37	YA529TM	PDQ	463	1.423	--
		U-235 Rate	442	1.423	1.316
38	YA527TM	PDQ	463	1.423	--
		U-235 Rate	423	1.424	1.309
39	XA986T	New	0	1.434	1.337
40	XA950T	PDQ	1324	1.337	--
		U-235 Rate	1394	1.325	1.280

Table 2.6 provides a comparison between the various means of calculating lobe exposure and the corresponding ROSUB multiplier. The two methods for calculation of lobe exposure resulted in fairly significant differences, with the maximum difference of 32.3% from the PDQ-based lobe exposure method. The PDQ methodology calculates lobe power and applies the corresponding lobe exposure to all eight elements in a lobe. The U-235 burnup rate methodology determines element powers via isotopic data that is retained for each element, which ultimately reflects element exposure. It is assumed that lobe exposure calculated as eight times the element exposure is a more accurate representation of the definition of lobe exposure assumed during the development of the ROSUB polynomials. Thus, the calculated exposure differences represent an increase in accuracy.

Ultimately, the effect of exposure differences on the corresponding ROSUB multiplier is significantly less than the direct effect on lobe exposure. The largest difference in calculated ROSUB multiplier was seen in Position 5 with an increase of 7.3% from the ROSUB multiplier calculated from the PDQ-based exposure determination. Note that the exposure calculation method seems to be a secondary effect since a disproportionally larger effect on the ROSUB multiplier is seen by elements with extensive exposure.

Table 2.7 provides a comparison between the MCNP5 results used to develop a multiplier and the multipliers determined by the ROSUB polynomials utilizing the various calculated exposures. The second column of this table (titled 'Using PDQ Exposure') effectively provides a comparison between the current power density multiplier and the multiplier that would be generated using the MCNP5 method. The vast majority of the elements analyzed during this demonstration have a positive percent difference when compared to the MCNP5 multiplier. This would indicate that use of the MCNP5 multiplier should generally result in a decrease in multiplier value, ultimately resulting in a decrease in calculated Effective Plate Power. Negative percent differences tend to be present in elements with extensive exposure, which can be expected to not limit operation of the core. Thus, increased margin to Effective Plate Power limits is expected when the MCNP5 multiplier method is implemented. Increased margin could provide ATR with an increase in operational flexibility that could more readily meet customer needs, provide customers with the ability to run experiments at higher powers, and/or more efficiently utilize fuel. Note that quantification of the potential increases in margin will need to occur before any of these benefits can be realized.

Comparing the ROSUB polynomial and MCNP5 results that both utilized the lobe exposure determined by the U-235 burnup rate method provides an assessment of the ROSUB polynomial itself without the influence of the two exposure calculation methods. Some interesting trends emerge during this assessment, as shown in the last column of Table 2.7. For instance, most elements differ by only 1-5%. Another interesting trend is that elements with no exposure and outside the NW lobe are consistently near a 4% increase from the multiplier calculated by

MCNP5. However, this effect may be an artifact of the polynomials being used in ROSUB. It also may be due to the slight depression prevalent in the upper section of element profiles, as shown by Figures 2.18 - 2.21. This depression is expected to a result of the safety rod bite present in the top 3 inches of the core, although this has not been confirmed.

Table 2.6 Percent Difference Relative to the PDQ-based Methodology.

Element Position	Calculated Exposure Difference	ROSUB Multiplier Difference
1	21.3%	-3.2%
2	8.6%	-1.7%
3	22.4%	-4.0%
4	-14.7%	5.3%
5	-17.0%	7.3%
6	0.4%	-0.2%
7	-5.5%	1.7%
8	16.8%	-3.0%
9	-14.6%	2.8%
10	23.8%	-3.4%
11	-8.5%	1.4%
12	--	0.0%
13	--	0.0%
14	--	0.0%
15	11.1%	-0.5%
16	0.5%	0.0%
17	--	0.0%
18	--	0.0%
19	--	0.0%
20	14.9%	-1.3%

Element Position	Calculated Exposure Difference	ROSUB Multiplier Difference
21	13.8%	-1.2%
22	--	0.0%
23	--	0.0%
24	--	0.0%
25	-9.4%	0.9%
26	5.8%	-0.5%
27	11.0%	-0.7%
28	--	0.0%
29	--	0.0%
30	1.2%	-0.2%
31	0.3%	-0.1%
32	--	0.0%
33	-11.4%	0.4%
34	-0.5%	0.0%
35	32.3%	-1.1%
36	11.1%	-0.5%
37	-4.6%	0.0%
38	-8.7%	0.1%
39	--	0.0%
40	5.3%	-0.9%

Table 2.7 Percent Difference Relative to the MCNP5 Multiplier.

Element Position	Using PDQ Exposure	Using U-235 Exposure	Element Position	Using PDQ Exposure	Using U-235 Exposure
1	6.6%	3.2%	21	2.8%	1.5%
2	5.7%	3.8%	22	4.2%	4.2%
3	7.5%	3.2%	23	4.0%	4.0%
4	1.8%	7.2%	24	4.2%	4.2%
5	-0.1%	7.2%	25	2.1%	3.0%
6	-1.9%	-2.1%	26	2.9%	2.4%
7	-0.4%	1.2%	27	3.1%	2.4%
8	6.0%	2.8%	28	3.0%	3.0%
9	4.1%	6.9%	29	4.9%	4.9%
10	5.2%	1.7%	30	1.8%	1.6%
11	-0.2%	1.2%	31	3.0%	3.0%
12	4.3%	4.3%	32	6.4%	6.4%
13	3.8%	3.8%	33	6.2%	6.6%
14	3.4%	3.4%	34	9.3%	9.3%
15	1.8%	1.3%	35	8.9%	7.6%
16	2.7%	2.7%	36	7.4%	6.9%
17	3.3%	3.3%	37	8.1%	8.2%
18	3.5%	3.5%	38	8.7%	8.7%
19	4.0%	4.0%	39	7.3%	7.3%
20	4.0%	2.6%	40	4.5%	3.5%

Another trend is that elements in Positions 32-39 consistently differ by 6-10% from the MCNP5 multiplier. Figure 2.21 shows the axial fission tallies for each element in Quadrant 4. Several elements in the NW lobe tend to deviate from the chopped cosine shape via a slight unidentified suppression in the center of the core. This trend may indicate that the experiment residing in the NW lobe (i.e. NW-160), the experiment holder (namely, the Dual Standard Holder), or the Large In-Pile Tube (LIPT) itself does not present a chopped-cosine axial shape to the driver fuel elements. Further investigation is needed to evaluate the cause of these trends, and some additional discussion pertinent to NW-160 is provided in Section 3.3.

Significant outliers from these trends also exists at Positions 4, 5, and 9. These positions correspond to the use of Modified YA elements (denoted by YA.....M serial numbers), which may indicate that the current method does not appropriately model the effects of these elements. The ROSUB multiplier in these locations is about 7% above the multiplier predicted by the MCNP5 calculations. Also of note is that several Modified YA elements reside in the NW lobe and use of these elements corresponds to high percentage values in that lobe as well. Further investigation is needed to evaluate the proper modeling of the Modified YA elements.

Position 6 has a multiplier at 2.1% below the multiplier predicted by the MCNP5 calculations. Position 6 contains a Mark VII (XA type) element, but may be compensating for errors introduced by the improper application of Modified YA element modeling. However, this trend may also indicate that the experiment residing in the NE lobe (i.e. AGR-3/4) or the Large In-Pile Tube (LIPT) itself does not present a chopped-cosine axial shape to the driver fuel elements. Figure 2.18 shows what appears to be a localized depression in the axial profile that significantly affects Positions 4-6. Further investigation is needed to evaluate the cause of these differences and the potential effects on the results obtained for nearby elements in the NE lobe.

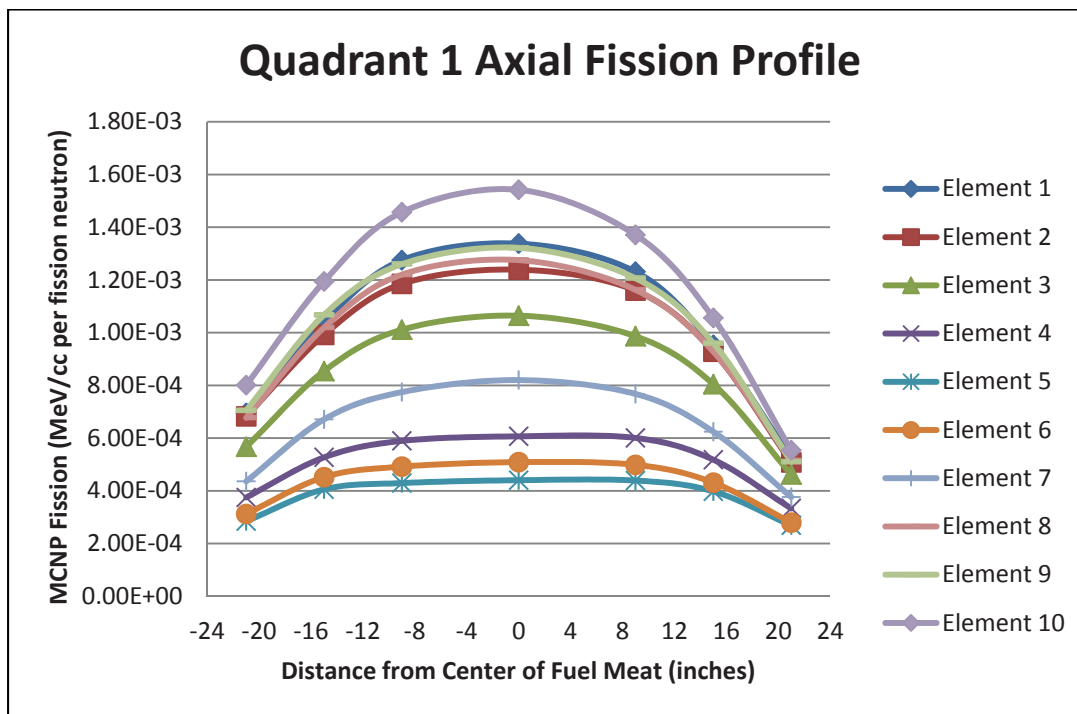


Figure 2.18 Quadrant 1 axial fission profile obtained from MCNP5 tallies (MeV/cc per fission neutron source particle). Plot represents the location of each tally as the volume centroid of the associated region.

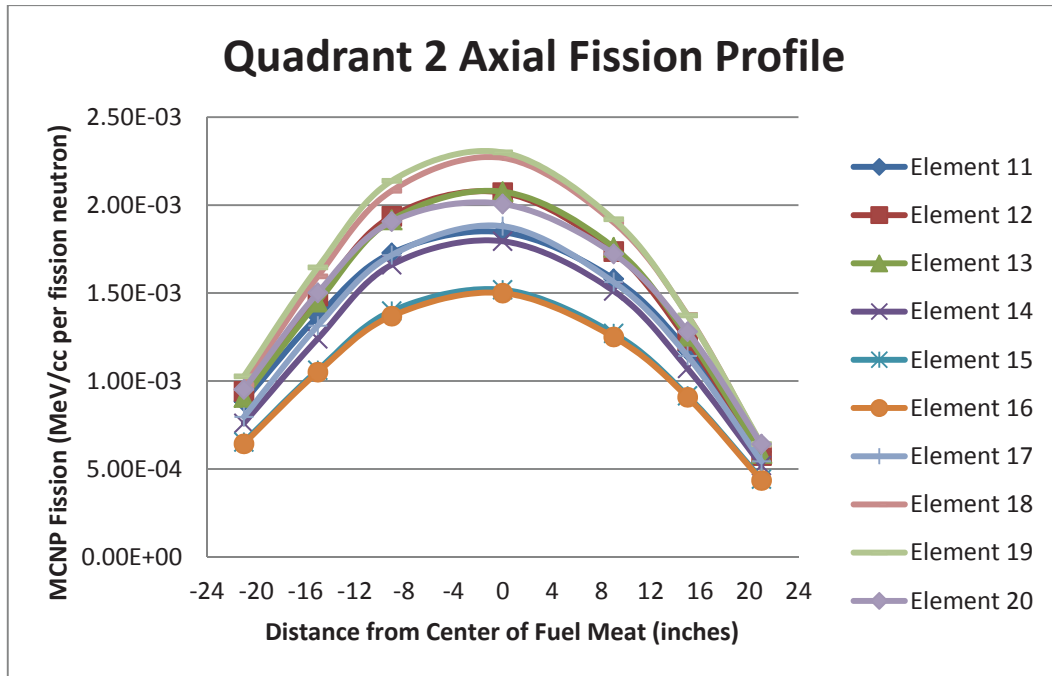


Figure 2.19 Quadrant 2 axial fission profile obtained from MCNP5 tallies (MeV/cc per fission neutron source particle). Plot represents the location of each tally as the volume centroid of the associated region.

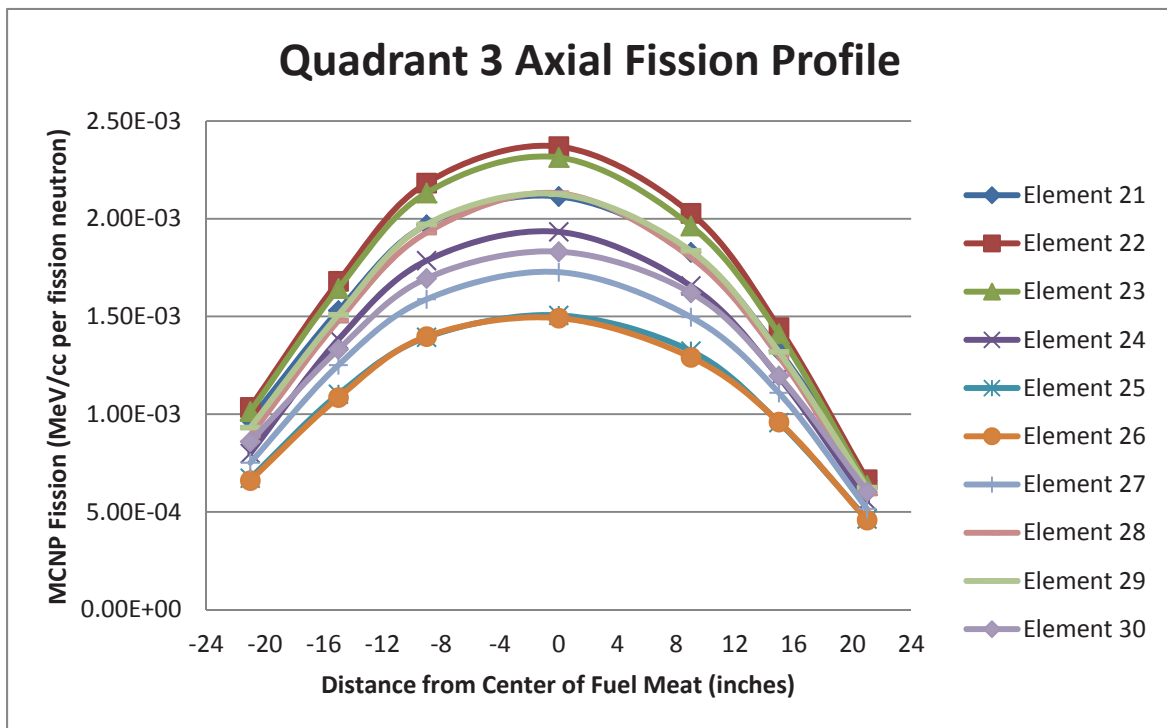


Figure 2.20 Quadrant 3 axial fission profile obtained from MCNP5 tallies (MeV/cc per fission neutron source particle). Plot represents the location of each tally as the volume centroid of the associated region.

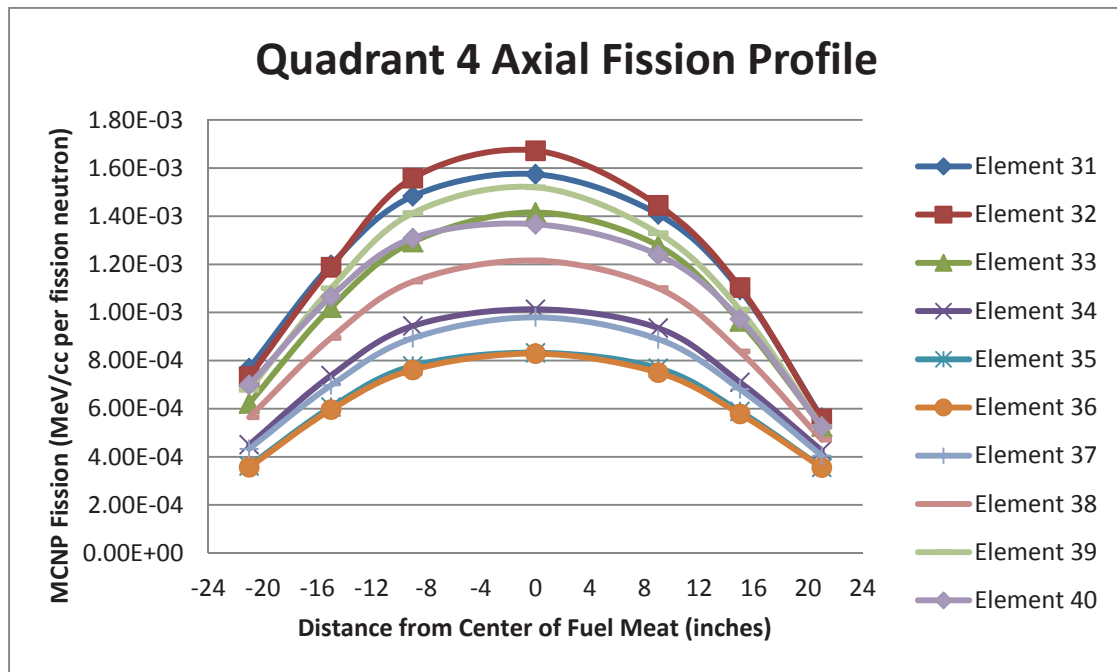


Figure 2.21 Quadrant 4 axial fission profile obtained from MCNP5 tallies (MeV/cc per fission neutron source particle). Plot represents the location of each tally as the volume centroid of the associated region.

2.2.7 Future Directions

Although initial assessments are promising, additional evaluations are needed to validate the potential replacement of the ROSUB peak-to-average power density multipliers. Additional improvements to the calculation of lobe exposure should be explored. These improvements could include a change in the assumed rate of U-235 burnup (particularly at higher exposures where the rate of change in U-235 burnup increases as various poisons are built into the fuel matrix) or could include the use of HELIOS cycle modeling to determine appropriate lobe exposures to be used in comparison with ROSUB polynomials.

Validation of element isotopic and power fraction data in the MCNP5 model should also be performed. Currently, no confirmation of the U-235 loading provided to MCNP5 is utilized. Proper loading of the elements, particularly of the YA...M elements, as well as appropriate application of power fractions over the various fuel types will be necessary to ensure that modeling errors that affect axial power density multipliers have been quantified. In future iterations of this analysis, corrections to the three zoneload.txt input files can easily be made that include removal of significant assumption errors.

Comparisons of the effects induced by core variations will need to be evaluated over a subset of core configurations such that a baseline axial profile can be determined. These variations could include homogenized representations of experiments. Preliminary homogenization of the experiment in the NW lobe at varying degrees of detail suggests that the presence of the DSH experiment holder may introduce axial perturbations that are as significant as the axial variations in the experiment itself and that the combination of these effects may explain the NW lobe deviations described above. Baseline axial profiles generated from this information can then be used to quantify when significant variations in the profile occur and what elements are potentially affected by the variation.

Axially-varied experiment effects may present long-term concerns on driver fuel as fuel shuffling over multiple cycles is performed. The internally-developed INL MOPY code, still in the verification and validation process, could be used in the future to couple MCNP5 and ORIGEN2 so that time-dependent effects of flux on the compositions utilized within the MCNP5 model could be represented explicitly. Quantifying the effect of axially-varied experiments on the power density profile and in turn quantifying the amount of experimental axial variations that can be shown to be acceptable will need to be evaluated. Quantification of acceptable experimental axial variation will allow calculations involving multiple cycles and explicit fuel shuffling to be minimized.

Proper evaluation of the power density multiplier in a variety of situations may also need to be explored. Axially-varied experiments may require the multiplier to account for variations in how experiments are modeled in the 2D HELIOS code, such as in a manner inconsistent with the current peak-to-average axial experiment profile assumption. Multipliers may need to correlate other profile assumptions (namely, peak-to-extruded experiment axial profiles) to accommodate approximations made in the 2D model.

Additional axial regions may be needed to ensure that the axial fission profile in the driver elements is appropriately captured and thus the average power density is correctly determined. Additional axial regions would also ensure that axial shapes that significantly deviate from the assumed chopped-cosine shape are accurately evaluated. Current assumptions include the use of the centerline value of the axial profile as the axial profile peak, which does not fully capture the effects in the observed profile. Quantification of the error introduced through the use of this assumption may be necessary. Also, evaluations with additional radial regions in the fuel may be necessary to ensure that the three-radial-region model adequately captures the neutronic effects experienced by the fuel.

General modeling assumptions made in the MCNP5 model should also be explored. For instance, the atom density values utilized by the fuel assume a water density associated with water at 27°C. Quantification of variations in water temperature could be accomplished relatively easily by altering the atom density values used in the Python scripts. Proper modeling of the core as it heats up during cycle startup could provide valuable neutronic effects information.

Additional polynomial approximations provided by ROSUB include fission density axial distribution and axial reactivity effects. These effects will also need to be explored to fully replace the ROSUB assumptions and potentially remove the axial profile assumption from the analysis of driver fuel. While initial results of this methodology are promising for average power density multipliers, significant additional evaluations are necessary before implementation can be fully realized.

2.3 HELIOS-Based Methodology Development Status vs. CSAP Requirements

ATR UFSAR requirements documented in the CSAP can be categorized into three general classes of information, as illustrated in Figure 2.22. These classes consist of required neutronic modeling that has traditionally been performed utilizing 2D PDQ diffusion theory core models and strict axial profile assumptions, reactivity estimates intended to conservatively account for three-dimensional effects, and requirements outside of the various neutronic calculations. The focus of the Methods Update Project has been to fully replace the required neutronic modeling with transport theory based methodologies and expand the axial profile assumptions so that an increased range of experiments can be accommodated. No new methodology is yet operational to replace the reactivity estimates designed to conservatively account for three-dimensional effects, but this class contains several potential candidates that will be evaluated as the project proceeds. Requirements outside of the various neutronic calculations are generally detached from or completely independent from neutronic calculations and thus are not expected to be replaced by Methods Update Project codes.

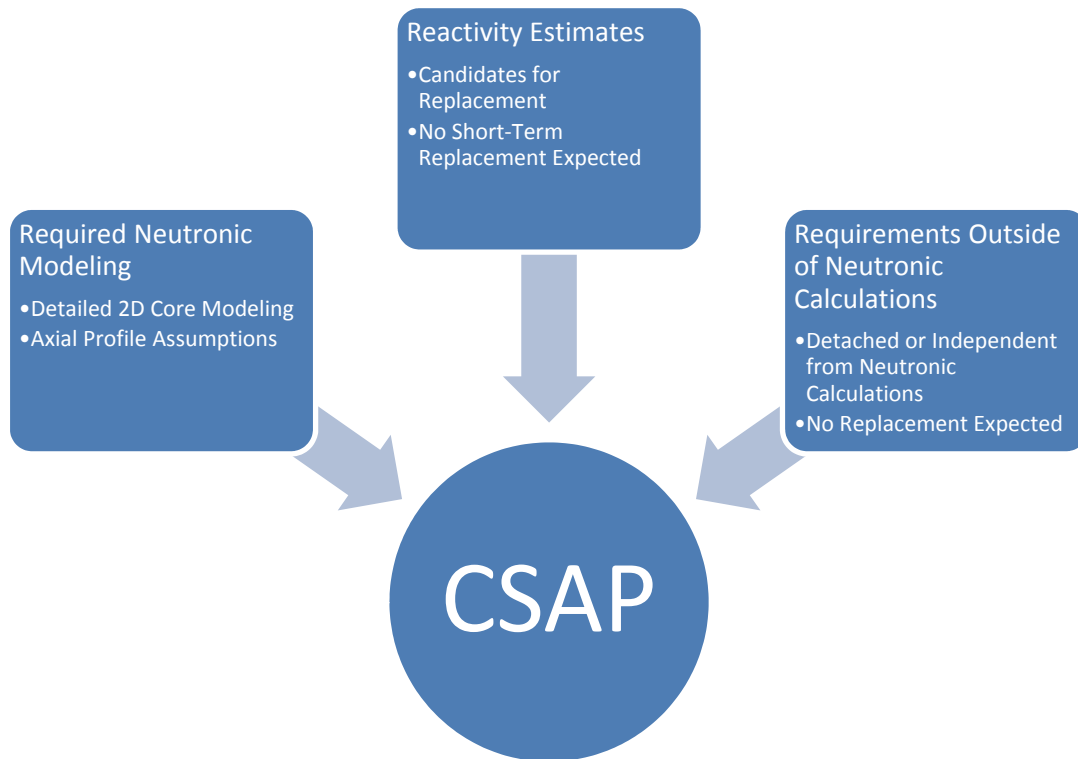


Figure 2.22 Information Classes Relevant to CSAP Production

The required neutronic modeling and associated physics data is currently produced by the existing suite of codes associated with the diffusion code PDQ as noted above. The modernization effort underway is designed to replace the current PDQ-based physics analysis methodology with an improved methodology capable of calculating and analyzing data that is ultimately reported in the CSAP documentation per current protocols. Thus, the calculational process used to determine ATR UFSAR requirements has evolved, while the UFSAR requirements themselves have not.

Figure 2.23 provides an overview of the legacy physics analysis process associated with the required neutronic modeling. This figure also includes a visual representation of the development status of the processes associated with the modernization effort. For instance, the HELIOS transport code and associated ATR model has been shown to be capable of replacing the diffusion code PDQ due to its first-principles transport theory based ability to model ATR fuel elements, internals, and experiments with essentially exact two-dimensional geometry over a range of cycles, as illustrated in Section 2.1. The HELIOS code has also been shown to support the input data needs required by the other computational processes. Although continuing improvements and corrections to the model will undoubtedly occur as experience evolves, the process used for ATR baseline physics modeling is expected to be ready for deployment in accordance with the overall Methods Update Project schedule.

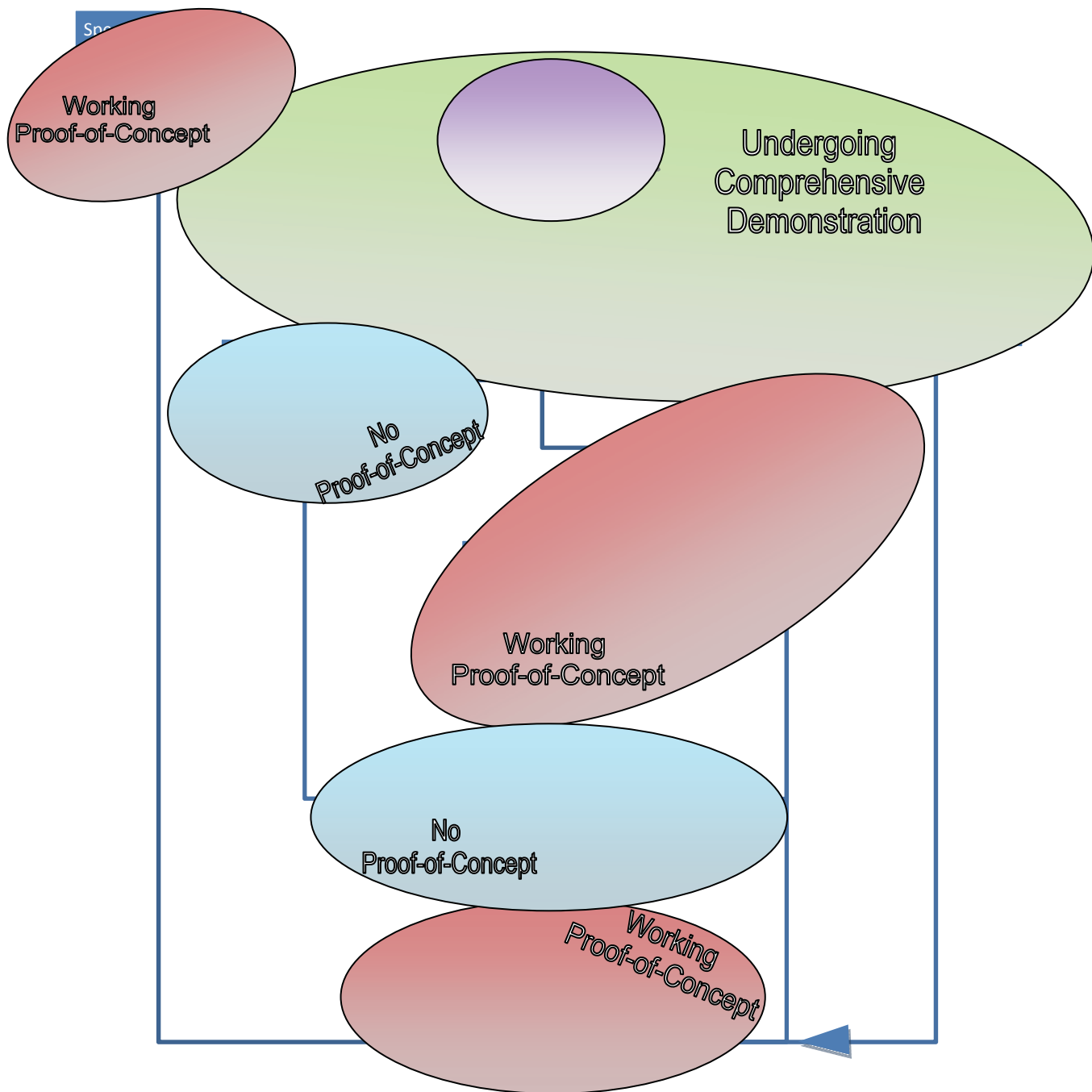


Figure 2.23 Physics Analysis Calculational Process Overview and Development Status. The major relevant PDQ-based code for each process is listed in parentheses.

Looking forward now from an operational perspective that includes a broader array of procedural specifications, Figure 2.24 provides an overview of the Methods Update Project status relative to the neutronic modeling requirements specified in the ATR UFSAR, particularly with regard to initial HELIOS deployment. A more detailed assessment pertinent to the current stage of the Methods Update Project is also available in Table 2.8 at the end of this section. This latter table, providing the data summarized in Figure 2.24, identifies several key areas where additional focus is needed in the current stages of the Methods Update Project to establish a proof of concept and to ensure that the functionality needed to meet requirements will be deployed in a timely manner. These areas comprise approximately 40% of the requirements at this juncture.

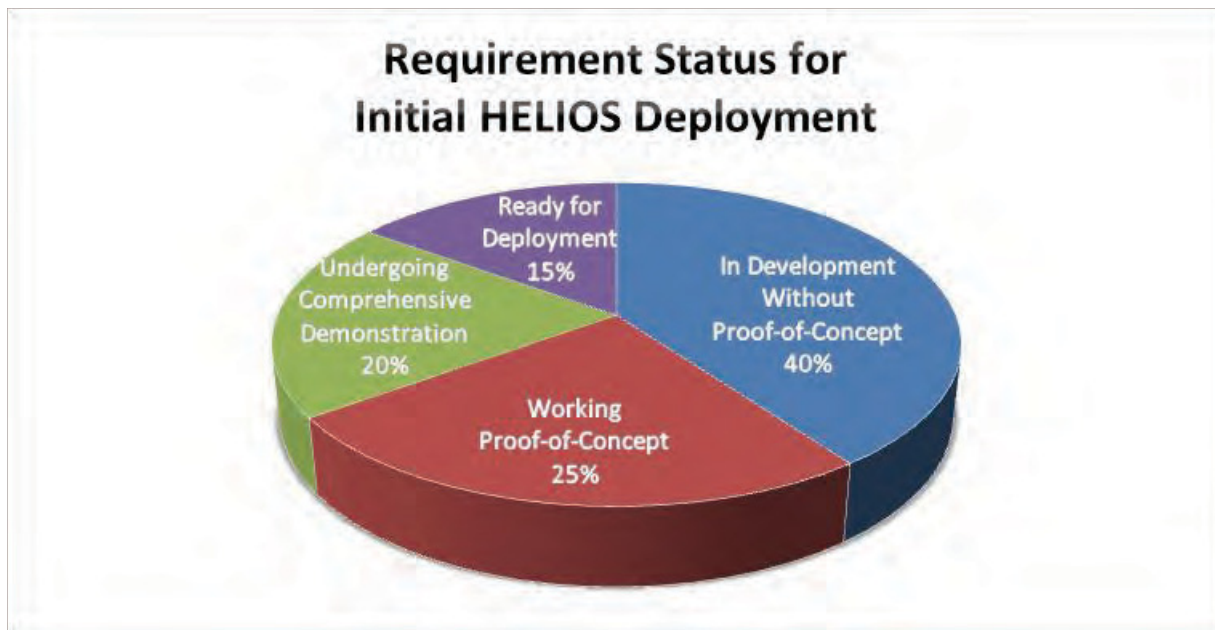


Figure 2.24. Requirement status summary for initial HELIOS deployment.

Figure 2.25 provides a slightly different view of the status of the Methods Update Project development against various categories of requirements. To successfully replace the historical methods, both the process demonstrated in Figure 2.23 and the requirements represented in Figure 2.25 must be fulfilled. Fulfillment of Figure 2.25 requirements does not guarantee a successful replacement if an appropriate process is not developed; likewise process demonstration as shown in Figure 2.23 does not guarantee a successful replacement if requirements cannot be satisfied. Successful methodology replacement implementation must include a rigorous and comprehensive demonstration of the capabilities associated with the calculational process as well as demonstration of the functionalities directly associated with the requirements (as illustrated, for instance, by the cycle modeling exercise documented in Section 2.1 that included lobe power functionality). Final verification and validation of both aspects must be completed and documented with an appropriate level of separation from the methodology developers in order to meet NQA-1 standards. Validation efforts will include both direct validation via available measurement data and code-to-code validation for components that do not have direct measurement data available. Detailed acceptance bands must also be developed in collaboration with the ATR Engineering and Operations organizations for use during acceptance testing of functionalities associated with UFSAR requirements. Reconciling all of these complementary objectives will be a key objective as the Methods Update Project evolves into the implementation readiness stage during FY-14.

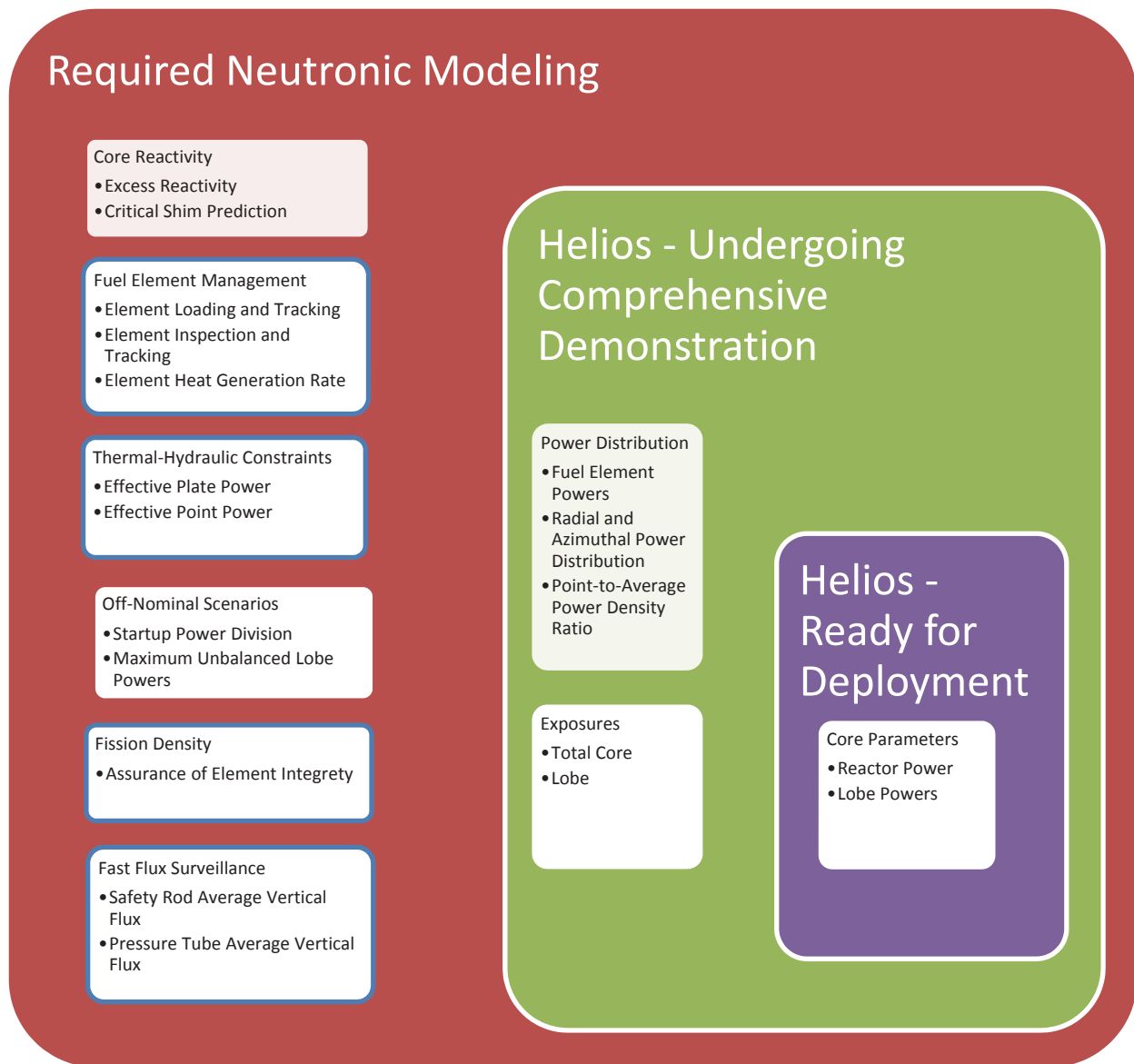


Figure 2.25 Development vs. Categories of Requirements

Since acceptance bands for some parameters produced by the computational processes have not been formally adopted, components cannot be formally deemed as ready for deployment. However, some components associated with the calculational process and/or requirement functionality are expected to be ready for deployment once additional acceptance bands are developed and appropriate feedback has been received from those who develop the CSAP documentation. Other components are currently undergoing comprehensive demonstration utilizing appropriate acceptance testing, code-to-code verification and validation (where appropriate) and/or direct validation with available experimental data. Still other components are at various earlier levels of development.

Finally, as noted earlier, Table 2.8 below contains a complete list of the 38 physics requirements applicable to ATR core safety analyses. Also included in this table is the current status of the Methods Update Project as it relates to each requirement. In summary,

- 8 requirements are associated with functionalities that are in development without a working proof-of-concept at this point, and will be key areas of emphasis during FY-2014,
- 5 requirements are associated with a working proof-of-concept,
- 4 requirements are associated with functionalities that are undergoing comprehensive demonstration,
- 3 requirements are associated with functionalities that are expected to be ready for deployment,
- 10 requirements are associated with functionalities that have no short-term plan for replacement but that may optionally be replaced in the future using the capabilities of one or more of the codes in the Methods Update Project suite,
- 7 requirements are associated with functionalities that have no immediate need nor long-term plan for replacement, and
- One requirement is unquantified due to the need for additional inquiry and interaction with ATR Engineering during FY-14 to determine how this requirement is currently met.

Table 2.8 SAR Physics Requirement Identification, Reference Information, and Current Status.

Property	Stated Limits and Surveillances	SAR Section	Current Reporting Mechanism(s)	Status	Known Deficiencies
Core parameters	Document parameters	15.0.2.4	Physics Report & CSAP	Ready for Deployment	None Identified.
Reactor power	< 142 MW (3 PCPs) < 146 MW (2 PCPs) <= 0.5 MW during depressurized operations	4.3.1.3.1, 4.3.2.2, 16.2.2.2, TSR LCO 3.3.1.1a, TSR LCO 3.3.2.1a, USQ-2010-497	Physics Report & CSAP	Ready for Deployment	None Identified.
Lobe powers	<= 60 MW SIPT <= 34 MW LIPT <= 50 MW AHTL	4.4.2.3, TSR LCO 3.6.1a Table 3.6.1-1	Physics Report & CSAP	Ready for Deployment	None Identified.
Startup Power Division	Establishes Log-N chamber positions	7.2.1.1.3.8, SD-11.2.8	Startup Power Division Letter and Requested Lobe Powers For Startup Letter.	Working Proof-of-Concept	Startup power divisions (including center power predictions) have not been explicitly demonstrated.

Property	Stated Limits and Surveillances	SAR Section	Current Reporting Mechanism(s)	Status	Known Deficiencies
Frequency of high power operations	< 20% over 34 MW lobe power < 6% over 47 MW lobe power	15.0.14, 15.6.1	CSAP	No Long-Term Plan for Replacement	None Identified.
Critical shim positions	Calculation includes reflector poison effects Detect fully inserted safety rod	4.3.2.2.7, 4.3.2.4, 4.3.2.4.7, 15.11.11.2.2, TSR AC 5.5.1e(i)	Shim Prediction Letter & CSAP	Working Proof-of-Concept	Reflector poison effects have not been fully demonstrated.
Fuel element powers	Used to calculate minimum cooling time before core is off-loaded	TSR LCO 3.5.1 Table 3.5.1-1, TSR SR 4.5.1.1	Physics Report & CSAP	Undergoing Comprehensive Demonstration	Additional validation work based on ATRC measurements may be appropriate.
Fuel element loading	Confirm procurement specifications and restrictions, Operations confirm core properly loaded	4.2.1, 4.3.2.4, TSR LCO 3.5.4, TSR SR 4.6.3.1	Physics Report & CSAP	In Development	Restriction tracking and other fuel management needs have not been fully developed.
Fuel element oxide thickness	< 1.0 mil, confirm via analysis and measurements	4.2.1.1.2, 4.2.3.1.1	CSAP	In Development	Fuel management needs have not been fully developed.
Fuel element inspection	No scratches or unclearable debris, no cladding breach, post-cycle surveillances required, restrictions tracked	4.2.1, 4.2.1.1.2, 4.2.1.8, 4.2.1.8.1, 4.2.3.1.1, 17.4.5, 17.11.2	CSAP & spent fuel database	In Development	Fuel management needs have not been fully developed.
Loop void worth	< 1.00\$ LIPT < 0.80\$ SIPT < 4.00\$ total	4.3.2.3, 10.2.6.2.2, 10.2.6.4.3, 15.4.1.1, 15.4.6.2.1, USQ-2010-497	CSAP	No Short-Term Plan for Replacement	MCNP calculations may be able to replace current methodology, but further development is needed.

Property	Stated Limits and Surveillances	SAR Section	Current Reporting Mechanism(s)	Status	Known Deficiencies
Loop minimum temperature	Determined from void worth limits	4.3.2.3, 10.2.6.2.2, 10.2.6.4.3, 15.4.1.1, 15.4.6.2.1, USQ-2010-497	CSAP	No Short-Term Plan for Replacement	MCNP calculations may be able to replace current methodology, but further development is needed.
Outer Shim Control Cylinder and Neck Shim reactivity	Subcritical with SRs withdrawn and with OSCCs and NSs fully inserted, measurements required	4.3.1.5.1, 4.3.1.5.2, 4.3.2.4	CSAP	No Short-Term Plan for Replacement	Component reactivities can likely be determined with HELIOS and/or MCNP, but further development is needed.
Minimum operable safety rods	≥ 4 safety rods Provide Safe Shutdown Earthquake (SSE) assurance	3.1.3.8.2, Table 4.3-16, USQ-2010-497	CSAP	No Short-Term Plan for Replacement	Component reactivities can likely be determined with HELIOS and/or MCNP, but further development is needed.
Shutdown worth of the N-1 least-reactive safety rods	$\geq 5.8\%$ (3 PCPs) $\geq 6.4\%$ (2 PCPs)	3.1.3.8.2, 4.3.1.5.2, 4.3.2.4, 4.3.2.4.3, TSR LCO 3.7.1.b, TSR SR 4.7.1.1	CSAP	No Short-Term Plan for Replacement	Component reactivities can likely be determined with HELIOS and/or MCNP, but further development is needed.
Regulating rod worth	$\leq 5.7\%$	Table 4.3-17	CSAP	No Short-Term Plan for Replacement	Component reactivities can likely be determined with Helios and/or MCNP, but further development is needed.

Property	Stated Limits and Surveillances	SAR Section	Current Reporting Mechanism(s)	Status	Known Deficiencies
Holddown reactivity margin	$\geq 6.7\%$	TSR SR 4.5.7.1	CSAP	No Short-Term Plan for Replacement	Holddown reactivities can likely be determined with HELIOS and/or MCNP, but further development is needed.
Xenon walk-away/ recriticality event reactivity	$\geq 2.0\%$	15.4	CSAP	No Short-Term Plan for Replacement	Recriticality reactivity can likely be determined with HELIOS and/or MCNP, but further development is needed.
Excess Reactivity	Met if critical on outer shims, $\geq 2\%$ excess at end-of-cycle	3.1.3.8.2, 4.3.2.1, 4.3.2.4, 4.3.2.5.1, 4.3.1.5.2, 7.7.1.5	Physics Report & CSAP	Working Proof-of-Concept	Additional functionality regarding quadrant excess reactivity may be needed.
Radial and azimuthal power distribution	Available for power split calculations	4.3.2.2, 4.3.2.5.2, 15.11.13.1.2	Physics Report & CSAP	Undergoing Comprehensive Demonstration	Additional verification and validation work may be appropriate.
Effective Plate Power (EPP)	Dependent upon fuel type, whether reflector is < 2 sigma from cracking, number of PCPs in use, etc.	4.4.4.5.3, TSR LCO 3.6.1a Table 3.6.1-1, USQ-2010-497	Physics Report & CSAP	Working Proof-of-Concept	Calculation should be limited to plate hot stripes. Additional EPP constraints and/or sorting methods needed. ROSUB multiplier replacements in development.

Property	Stated Limits and Surveillances	SAR Section	Current Reporting Mechanism(s)	Status	Known Deficiencies
Point-to-average power density ratio	Highest power density selected for fuel inspection ≤ 3.3 between 10 and 90% from plate edge during depressurized operations	4.2.1.8.1, TSR LCO 3.6.2a	Physics Report	Undergoing Comprehensive Demonstration	Additional acceptance testing, verification, and validation may be appropriate. Confirmation of appropriate calculation when utilizing YA elements needed.
Maximum unbalanced lobe powers	Used to calculate Quadrant ΔT setpoints	TSR LCS 3.1.1 Table 3.1.1-1	Physics Report	Working Proof-of-Concept	No explicit demonstration has been performed.
Quadrant ΔT	Based upon applicable EPP limits	TSR LCS 3.1.1 Table 3.1.1-1	CSAP	No Long-Term Plan for Replacement	None Identified.
Quadrant N-16 to thermal power ratios	≤ 1.08 or value derived from EPP results	TSR LCO 3.6.1b	CSAP	No Long-Term Plan for Replacement	None Identified.
Fuel thermal stress	$<$ unirradiated yield strength, Enforced via EPtP	4.2.1.5.1, 4.2.3.4.1, 15.0.14	CSAP	No Long-Term Plan for Replacement	None Identified.
Fuel temperature	< 700 F with 95% confidence < 500 F if $> 1.5e21$ fissions/cc, Enforced via EPtP	4.4.1.2.1, Table 4.4-5	CSAP, SINDA results	In Development	Fission density calculations have not been fully developed.

Property	Stated Limits and Surveillances	SAR Section	Current Reporting Mechanism(s)	Status	Known Deficiencies
Effective Point Power (EPtP)	Dependent upon fuel type, whether reflector is < 2 sigma from cracking, number of PCPs in use, etc. <= 1.65 MW between 10 and 90% from plate edge during depressurized operations	4.2.1, 4.4.1.2.1, Table 4.4-5, TSR LCO 3.6.2b	Physics Report & CSAP	In Development	ROSUB multiplier replacements in development. Calculations specific to EPtP needed. Additional EPtP constraints and/or sorting methods needed.
Fission Density	< 2.3e21 fissions/cc (equivalent to over 350000 MWd/MTU), Affects EPtP limits	4.2.1.2.3, 4.2.1.8.1, 4.3.1.1.2	Physics Report & CSAP	In Development	Fuel management needs and fission density calculations have not been fully developed.
Total and lobe exposures	Used to calculate reflector lifetime Used to justify compliance with fission density limits	4.2.1.2.3, 4.2.1.8.3, 4.2.3.6.1	Physics Report & CSAP	Undergoing Comprehensive Demonstration	Additional acceptance testing, verification, and validation may be appropriate.
Projected reflector lifetime	Increase inspections, use YA elements when < 2 sigma from cracking, Effects EPP limits	4.2.1.8.3, 4.2.3.6.1, 15.15, 16.2.2.12	CSAP	No Long-Term Plan for Replacement	None Identified.
Reflector temperature	< 266 F (3 PCPs) < 278 F (2 PCPs)	4.2.3.6.2	Unknown.	Unknown.	Additional research is needed to determine how this requirement is currently met.
Fast fluence of reactor vessel base metal and welds	Base Metal: < 1.2e19 n/cm2 Welds: < 3.1e18 n/cm2	4.3.2.8, 5.3.1.4	CSAP	No Long-Term Plan for Replacement	None Identified.

Property	Stated Limits and Surveillances	SAR Section	Current Reporting Mechanism(s)	Status	Known Deficiencies
Thermal fluence of reactor vessel base metal and welds	Base Metal: < 7.62e20 n/cm ² Welds: < 2.27e20 n/cm ²	4.3.2.8, 5.3.1.4	CSAP	No Long-Term Plan for Replacement	None Identified.
Safety rod average vertical fast flux	Used to calculate component fluence	4.2.1.6.2, 4.2.1.8.2	Letter to appropriate ATR engineer based upon Physics Analysis data	In Development	Surveillance needs have not been fully developed.
Hafnium component fast fluence	< 5e22 n/cm ²	4.2.1.6.2, 4.2.1.8.2, 13.1.2.2.2	CSAP	No Short-Term Plan for Replacement	Surveillance needs have not been fully developed.
Pressure tube average vertical fast flux	Used to calculate pressure tube and detector fluence	TSR AC 5.7.6	Letter to appropriate ATR engineer based upon Physics Analysis data	In Development	Surveillance needs have not been fully developed.
Element heat generation rate	<= 300 Watts decay heat	PLN-936 7.1 SAC #6	ATR Spent Fuel Element Transfer Cask Shipping List	No Short-Term Plan for Replacement	Fuel management needs have not been fully developed.

Notes:

In Development: No proof-of-concept is available to demonstrate functionality. Work is between 0% and 50% complete.

Working Proof-of-Concept: A proof-of-concept is available to demonstrate basic functionality. Full functionality that meets requirements is under development. Work is between 50% and 80% complete.

Undergoing Comprehensive Demonstration: Full functionality and accuracy is being demonstrated over multiple cycles. Demonstration is utilizing appropriate acceptance testing, verification, code-to-code validation (where appropriate) and/or direct validation with available data. Work is between 80% and 95% complete.

Ready for Deployment: Anticipate that requirement has been fulfilled and method verified and validated. Customer feedback is needed to ensure product meets expectations. Work is between 95% and 100% complete.

No Short-Term Plan for Replacement: Current methodology for completing this requirement is expected to remain in place at the time of initial HELIOS deployment.

No Long-Term Plan for Replacement: Methodology replacement has not been explored at this time.

2.4 References

ANS (American Nuclear Society), "Determination of Steady-State Neutron Reaction Rate Distributions and Reactivity of Nuclear Power Reactors", ANSI/ANS-19.3-2005.

S.A. Atkinson, R.T. McCracken, "Advanced Test Reactor Lobe Power Uncertainty", INL Document Control TRA-ATR-1211, Revision 1, March 1997.

ATR Engineering, "Specification For Advanced Test Reactor Mark VII Zone Loaded Fuel Elements, IN-F-9-ATR, Revision 17", SPC-415 Rev. 2, November 2, 2005.

S. Bays, E. Swain, D. Crawford, "Status of Validating Core-Reload and Safety Analysis of the Advanced Test Reactor using HELIOS," Idaho National Laboratory, INL/CON-12-24736, (June 2012).

R. Breen, O. Marlowe, C. Pfeifer, "HARMONY: System for Nuclear Reactor Depletion Computation," Idaho National Laboratory, WAPD-TM-478, (January 1965).

A. Brown, A. Smith, "ATR CSA Physics Model Description and Calculation Guide," Idaho National Laboratory, NRRT-N-90-011, p.p. 2-39 (April 1990).

W. C. Cook, A. C. Smith, "ATR CSAP Code Package on the Workstation Version 1," PG-T-96-002, May 1996.

A. G. Croff, "ORIGEN2: A Versatile Computer Code for Calculating the Nuclide Compositions and Characteristics of Nuclear Materials," Nuclear Technology, Vol. 62, pp. 335-352, 1983. Douglas S. Crawford, Samuel E. Bays, "Overview of Auxiliary Process and Methodology for Initial Estimation of the OSCC Position Angle for a Given/Desired Power Split for the ATR" INL Internal Report ECAR-2378, September 2013.

S.A. Easson and A. Smith, "Assessment of ROSUB for ATR/CSAP Applications," EG&G Idaho, Inc., RE-P-81-076, (1981).

B. D. Ganapol, Douglas S. Crawford, David W. Nigg, "HELIOS Semi-Analytical Benchmarks for ATR Code Verification" INL Internal Document ECAR-2379 (2013).

W. Gegory letter to J. Durney, "ATR Hafnium Burnup Program," Idaho National Laboratory, INL Internal Document GRE-33-78, (September 1978).

M. Holm, "Lumped Fission Product Cross Sections for the ATR CSAP PDQ Model," Idaho National Laboratory, RE-P-78-016, (February 1978).

S. S. Kim, B. G. Schnitzler, "Advanced Test Reactor: Serpentine Arrangement of Highly Enriched Water-Moderated Uranium-Aluminide Fuel Plates Reflected by Beryllium," INL/EXT-05-00780, September 2005; published in "International Handbook of Evaluated Criticality Safety Benchmark Experiments," NEA/NSC/DOC/(95)03/II, Volume II, HEU-MET-THERM-022, September 2005 Edition.

M. A. Lillo, J. R. Mitchell, "Software Management, MCNP Version 5, Release 1.40," INL/INT-08-15171 Rev. 0, August 2010, Enterprise Architecture Record Number 234166.

G. Longhurst and L. Brown, "Experimenters Reference Guide for the Advanced Test Reactor," Idaho National Laboratory, INEEL/INT-02-01177, (September 2002).

MCNP Team, "MCNP 5.1.40 RSICC Release Notes," LA-UR-05-8617 November 2005.

J. R. Mitchell, J. W. Nielsen, "Software Management, ORIGEN2 Version 2.2," PLN-3710 Rev. 0, October 2011, Enterprise Architecture Record Number 201298.

T. Nakagawa, et al., "Japanese Evaluated Nuclear Data Library Version 3 Revision-2: JENDL-3.2," Journal of Nuclear Science and Technology, 32, pp. 1259-1271 (December 1995).

D.W. Nigg and K.A. Steuhm (Editors), Advanced Test Reactor Core Modeling Update Project Annual Report for Fiscal Year 2012, INL/EXT-12-27059. September 2012.

C.J. Pfeifer, "PDQ-7 Reference Manual II", WAPD-TM-947(L), February, 1971.

J. E. Poling, “Results of Reactor Physics Safety Analysis for Advanced Test Reactor Cycle 152B-1”, ECAR-2080, November 5, 2012.

B. G. Schnitzler, “Origen2 Cross Section Library Assessment for ATR Applications,” BGS-6-91, Idaho National Laboratory, April 1991.

J. Shultis, R. Faw, “Fundamentals of Nuclear Science and Engineering,” Marcel Dekker, Inc., (2002)

A. Smith, W. Yoon, D. Auslander, W. Cook, “Reactivity Effect of Beryllium Reflector Poison in the ATR,” Idaho National Laboratory, NRRT-N-90-021, (1990).

A. C. Smith, R. A. Weaver, “Summary of PDQWS Development and Input Data Requirements,” INEL-94/056, December 1994.

R.A. Stamm’ler and M. Abbate, “Methods of Steady-State Reactor Physics in Nuclear Design,” Academic Press, London, (1983).

C. J. Stanley, “Advanced Test Reactor Cycle 152B Preliminary Experiment Requirements Letter, Revision 5”, Internal INL Document CJS-05-12, Rev. 5, November 27, 2012.

J. W. Sterbentz, “JMOCUP As-Run Daily Depletion Calculation for the AGR-1 Experiment in ATR B-10 Position”, ECAR-958 Rev. 1, August 18, 2011.

Studsvik Scandpower, “HELIOS Methods (Version-2.0),” Studsvik Scandpower, (March 2009).

X-5 Monte Carlo Team, “MCNP—A General Monte Carlo N-Particle Transport Code, Version 5,” Volume I, LA-UR-03-1987, Los Alamos National Laboratory, April 24, 2003 (Revised 6/30/2004) and Volume II, LA-CP-0245, Los Alamos National Laboratory, April 24, 2003 (Revised 6/30/2004) (Vol. II is available with a licensed copy of MCNP5).

3.0 VALIDATION PROTOCOL DEVELOPMENT AND DEMONSTRATION

David W. Nigg, Joseph W. Nielsen, William F. Skerjanc, Mark D. DeHart, James R. Parry

As summarized earlier, four new benchmark-quality code validation measurements based on neutron activation spectrometry were conducted at the ATRC in previous years under the auspices of the Methods Update project. Results for the first three experiments, focused on detailed neutron spectrum measurements within the Northwest Large In-Pile Tube (NW LIPT) were recently reported (Nigg et al., 2012a, Nigg and Steuhm, 2012) as were some selected results for the fourth experiment, featuring neutron flux spectra within the core fuel elements surrounding the NW LIPT and the diametrically opposite Southeast IPT (Nigg et al. 2012b, Nigg and Steuhm, 2012).

In this Chapter we first focus on computation and validation of the fuel element-to-element power distribution in the ATRC (and by extension the ATR) using data from an additional, recently completed, ATRC experiment that was conducted to support ATR Cycle 152B operations. In connection with this, we present a method developed for estimating the covariance matrix for the fission power distribution using the corresponding fission matrix computed for the experimental configuration of interest. This covariance matrix is a key input parameter that is required for the least-squares adjustment validation methodology employed for assessment of the bias and uncertainty of the various modeling codes and techniques. We also examine intra-element fission rate validation data from the same experiment.

In this Chapter we also present validation analyses of the axial power distribution at various locations in the ATRC NW and SE core lobes using data from two previous experiments that were conducted separately from the Methods Update Project to support the Naval Reactor testing program. Finally, a continuation of the development of an analytical verification benchmark for HELIOS that was initially documented in the 2012 Annual Report for the Modeling Update project (Nigg and Steuhm, 2012) is summarized in Ganapol et al. (2013).

3.1 Inter-element Power Distribution Analysis of ATRC Validation Experiment 12-5

In the new validation experiment of interest, conducted to support startup of ATR Cycle 152B, 40 ATR-type fuel elements (7F) were loaded into the ATRC in place of the standard ATRC fuel elements. Activation measurements that can be related to the total fission power of each fuel elements were then made with fission wires composed of 10% by weight ^{235}U in aluminum. The wires were 1 mm in diameter and approximately 0.635 cm (0.25") in length and were placed in 17 locations within the cooling channels of each fuel element as shown in Figure 3.1, at the core axial midplane. The total measured fission powers for the fuel elements are estimated using appropriately-weighted sums of the measured fission rates in the U/Al wires located in each element (Durney and Kauffman, 1967).

Figure 3.2 shows the computed *a priori* (MCNP5) fission powers for the 40 ATRC 7F fuel elements, along with the measured element powers based on the fission wire measurements. The top number (black) in the center of each element is the *a priori* element power (W) calculated by MCNP5. The bottom number (red) is the measurement. Total measured power was 875.5 W. Uncertainties associated with the measured element powers are approximately 5% (1σ). The powers for the five 8-element ATR core "lobes" are also key operating parameters and are formed by summing the powers of Elements 2-9 for the Northeast Lobe, Elements 12-19 for the Southeast Lobe, Elements 22-29 for the Southwest Lobe, Elements 32-39 for the Northwest Lobe and Elements 1, 10, 11, 20, 21, 30, 31, and 40 for the Center Lobe. The significance of the lobe powers will be discussed in more detail later

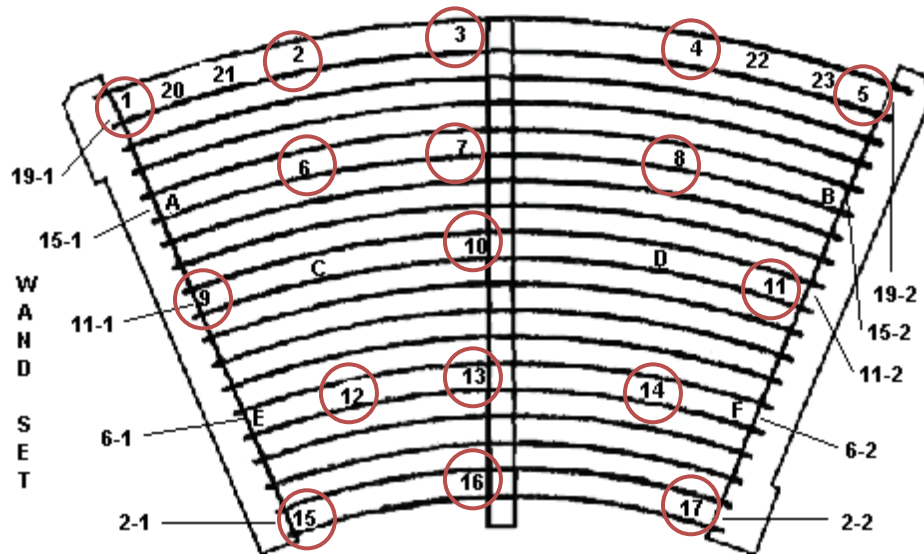


Figure 3.1. ATR Fuel element geometry, showing standard fission wire positions used for total element power measurements and for intra-element power distribution measurements.

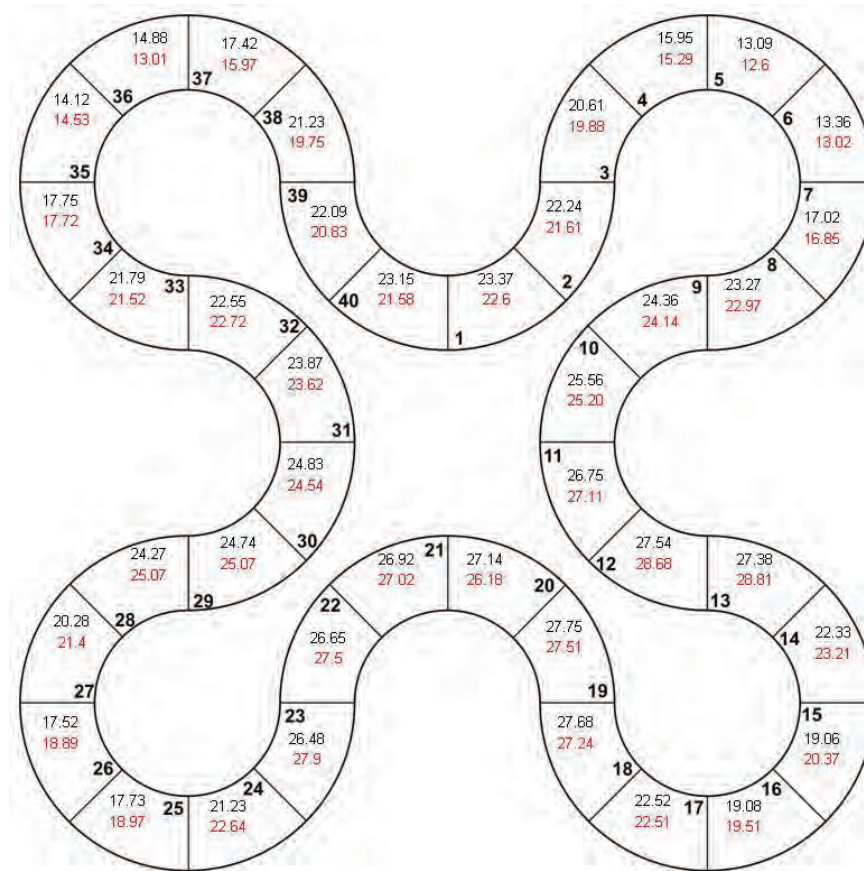


Figure 3.2. Calculated (black) and measured (red) fuel element powers (W) for ATRC Depressurized Run Support Test 12-5. The fuel element numbers are in bold type.

3.1.1 Power Distribution Adjustment Protocol

Analysis of the computed and measured power distribution for code validation purposes is accomplished by an adaptation of standard least-squares adjustment techniques that are widely used in the reactor physics community (ASTM, 2008). The least-square methodology is quite general, and can be used to adjust any vector of *a priori* computed parameters against a vector of measured data points that can be related to the parameters of interest through a matrix transform. This produces a “best estimate” of the parameters and their uncertainties, which can then be used to estimate the bias, if any, and the uncertainty of the computational model, and as a tool for improving the model as appropriate. Examples of the technique, as applied to neutron spectrum calculations and measurements in the ATR and the ATRC have been documented previously (Nigg and Steum, 2012). The adaptation to analysis of the ATRC and ATR fuel element power distribution is described below.

In the following description of the adjustment equations used in this work, matrix and vector quantities will generally be indicated by **bold** typeface. In some cases, matrices and vectors will be enclosed in square brackets for clarity. The superscripts, “-1” and “T” respectively, indicate matrix inversion and transposition respectively.

We begin the mathematical development by constructing the following overdetermined set of linear equations:

$$\begin{bmatrix} \mathbf{a}_{11} & \mathbf{a}_{12} & \mathbf{a}_{13} & \cdots & \cdots & \mathbf{a}_{1,NE} \\ \mathbf{a}_{21} & \mathbf{a}_{22} & \mathbf{a}_{23} & \cdots & \cdots & \mathbf{a}_{2,NE} \\ \vdots & \vdots & \vdots & & & \vdots \\ \mathbf{a}_{NM,1} & \mathbf{a}_{NM,2} & \mathbf{a}_{NM,3} & \cdots & \cdots & \mathbf{a}_{NM,NE} \\ \mathbf{1} & \mathbf{0} & \mathbf{0} & \cdots & \cdots & \mathbf{0} \\ \mathbf{0} & \mathbf{1} & \mathbf{0} & \cdots & \cdots & \mathbf{0} \\ \mathbf{0} & \mathbf{0} & \mathbf{1} & \cdots & \cdots & \mathbf{0} \\ \vdots & \vdots & \vdots & & & \vdots \\ \vdots & \vdots & \vdots & & & \vdots \\ \mathbf{0} & \mathbf{0} & \mathbf{0} & \cdots & \cdots & \mathbf{1} \end{bmatrix} \cdot \begin{bmatrix} \mathbf{P}_1 \\ \mathbf{P}_2 \\ \mathbf{P}_3 \\ \vdots \\ \vdots \\ \vdots \\ \mathbf{P}_{NE} \end{bmatrix} = \begin{bmatrix} \mathbf{Pm}_1 \\ \mathbf{Pm}_2 \\ \vdots \\ \mathbf{Pm}_{NM} \\ \mathbf{P}_{01} \\ \mathbf{P}_{02} \\ \mathbf{P}_{03} \\ \vdots \\ \vdots \\ \mathbf{P}_{0NE} \end{bmatrix} = [\mathbf{A}][\mathbf{P}] = [\mathbf{Z}] \quad (1)$$

and the supporting definition

$$[\mathbf{Cov}(\mathbf{Z})] = \begin{bmatrix} [\mathbf{Cov}(\mathbf{Pm})] & [\mathbf{0}] \\ [\mathbf{0}] & [\mathbf{Cov}(\mathbf{P}_0)] \end{bmatrix}, \quad (2)$$

where NE is the total number of fuel elements (i.e. 40 for ATR) and NM is the number of these elements for which element power measurements have been made. NM is typically a number between 1 and NE although multiple power measurements for the same fuel elements may optionally be included if available, possibly causing NM to be greater than NE. The vector **P** is the desired best least-squares estimate for the powers of all 40 fuel elements, the vector **Pm** (containing first NM entries in [Z]) contains the NM measured powers and the vector **P₀** (last 40 entries in [Z]) contains the 40 *a priori* estimates, **P_{0i}** for the element powers, extracted from the computational model of the validation

experiment configuration. The top NM rows of the matrix **A** each usually contain entries that are equal to zero except for the column corresponding to the element for which the measurement on the right-hand side in that row was made, where the entry would be 1.0. The bottom 40 rows of the matrix **A** correspond to the rows of a 40 x 40 identity matrix.

Equation 2 includes the NM x NM and NE x NE covariance matrices for the measured power vector and for the *a priori* power vector respectively. The covariance matrix entries for **[Cov(P_m)]** are based on the uncertainties of the experimental data values in the usual manner. The covariance matrix **[Cov(P₀)]** for the *a priori* power vector may be computed explicitly under certain circumstances, or it may be approximated based on the assumption of an element to element fission power correlation function that decreases exponentially with distance between any two elements.

Note that even if only a single measurement (i.e. NM=1) is available for inclusion in Equation 1, the augmented system will still be overdetermined (albeit by only one row) and some useful adjustment and reduction of *a priori* uncertainty may occur in the solution for the power distribution. However, if there are no measurements included in Equation 1, then one simply obtains the uninteresting solution where the adjusted power distribution is identical to the *a priori* power distribution, with the same uncertainty.

At this point it is important to recognize that in the case of ATR and ATRC a simple exponential approximation is not ideally suited for computing the fuel element power correlation matrix needed to construct **[Cov(P₀)]** in Equation 2. This is because the serpentine fuel element arrangement places several elements in close proximity even though they do not share faces (e.g. Elements 1 and 10). Thus the element power correlation matrix for these two facilities has a more complex structure than the simple diagonally-dominant arrangement that an exponential formula provides. Furthermore, the availability of an accurate, realistic power correlation matrix is a crucial prerequisite for the successful application of the least-squares methodology (Williams, 2012). In recognition of these factors, we propose a covariance matrix estimation procedure for ATR applications based on the fission matrix concept, further described below.

3.1.2. Calculation of the ATR/ATRC Fission Matrix

Each entry, f_{ij} , of the so-called “Fission Matrix”, **F** for a critical system composed of a specified number of discrete fissioning regions is defined as the number of first-generation fission neutrons born in region *i* due to a parent fission neutron born in region *j* (Carter and McCormick, 1969). The index *i* corresponds to a row of the fission matrix and the index *j* corresponds to a column. In the case of the ATR and the ATRC application of interest here the fissioning regions are defined to correspond to the fuel elements, so the fission matrix has dimensions of 40 x 40.

Assume now that the exact space, angular and energy distribution of the parent fission source neutrons within each fuel element is known from a detailed high-fidelity transport calculation and that this information is incorporated into the formation of **F**. Then construct the following eigenvalue equation:

$$\mathbf{S} = (1/k) \mathbf{F} \mathbf{S}, \quad (3)$$

where **S** is the suitably-normalized 40-element fundamental mode vector of total fission source neutrons produced in each of the 40 fuel elements and *k* is the fundamental mode multiplication factor. Under these conditions the solution to Equation 3 will be the same as is obtained by performing the corresponding high-fidelity transport calculation for the same configuration and integrating the resulting fission source over each fuel element. Of course, if one already has the solution for the detailed high-fidelity transport model then Equation 3 does not provide any new information, but the fission matrix concept can still be very useful and instructive. In particular, there has been a great deal of effort over

the years focused on acceleration of Monte Carlo calculations using fission matrix based techniques, with certain assumptions to simplify the estimation of the fission matrix elements as the calculation proceeds, without fully solving the high-fidelity problem explicitly beforehand (Carter and McCormick, 1969; Kitada and Takeda, 2001; Dufek and Gudowski, 2009; Wenner and Haghighat, 2011; Carney et al., 2012).

In the ATR application presented here we employ a fission matrix based approach to determine the fuel element to element fission power correlation matrix and thereby the associated covariance matrix $[\text{Cov}(\mathbf{P}_0)]$ that is required in Equation 2. The example uses the MCNP5 code for the required computations, but in principal the idea should be amenable to implementation using any multidimensional deterministic or stochastic transport solution method, provided that a sufficient level of spatial, angular, and energy resolution can be achieved in the detailed transport solution needed for an accurate calculation of the fission matrix.

In the case of the ATR and ATRC, the fuel element geometry (Figure 3.1) is represented essentially exactly in MCNP5. Each fuel plate has a separate region for the homogeneous uranium-aluminum fissile subregion and the adjacent aluminum cladding subregions on each side of the fueled layer. Burnable boron poison is also explicitly represented in the fuel plates where it is present. Coolant channels between the plates are explicitly represented, as are the aluminum side plate structures. The active fuel height is 1.2192 m (48") and the elements have essentially the same transverse geometric structure at all axial levels within the active height. Each fuel element contains 1075 grams of ^{235}U .

High-fidelity computation of the fission matrix with MCNP5 (or with any other Monte Carlo code that features similar capabilities) for this particular application is accomplished in two easily-automated steps as follows:

First, run a well-converged fundamental-mode eigenvalue ("K-Code" in MCNP5 parlance) calculation for the ATR or ATRC configuration of interest. Save the detailed volumetric fission neutron source information that includes all fission neutrons starting from within each fuel element. The absolute spatial, angular, and energy distribution of the fission neutrons born in each fuel element must be fully specified in the source file data for that element.

Second, using the fission neutron source file information created as described above, run a set of 40 corresponding fixed-source MCNP5 calculations for the same reactor configuration of interest, one separate well-converged calculation for each fuel element fission neutron source separately. These calculations are run with fission neutron production turned off using the "NONU" input parameter. Fissions induced by the original fission source neutrons sampled from the source file are thereby treated as capture in the sense that no additional fission neutrons are produced to be followed in subsequent histories. The "fission" rate that is tallied in this manner for each fuel element in a given MCNP fixed-source calculation thus includes only the first-generation fissions induced in that element by the original source neutrons emitted by the source fuel element that was active for that calculation. Multiplying this quantity for each fuel element in a given MCNP calculation by the average number of neutrons per fission and then dividing the result by the absolute magnitude of the original fission neutron source associated with the active fuel element then yields the column of the fission matrix corresponding to that source fuel element.

Substitution of the fission matrix from the above process into Equation 3 should reproduce (within the applicable statistical uncertainties) the eigenvalue and the fuel element-to-element fission neutron production distribution of the original MCNP K-Code calculation. Once this is verified, the fission matrix is ready for use in generating the required fuel element fission correlation matrix as described below.

3.1.3. Construction of the Fission Covariance Matrix

To begin the fission covariance matrix development, we make a key facilitating assumption that the average number of neutrons produced per fission is the same for all of the fissioning regions in the model. This is reasonable for the ATRC experiment of interest here because all 40 fuel elements were identical and unirradiated. Furthermore, MCNP calculations show that the neutron spectrum does not vary from one ATRC fuel element to the next in a manner that significantly affects the ratio of ^{238}U fissions to ^{235}U fissions. Therefore in this case each entry, f_{ij} , of the fission matrix also can be interpreted as the number of first-generation daughter fissions induced (or corresponding fission energy released) in each region i due to a parent fission occurring in region j .

Turning now to the actual computation of the fission power covariance matrix needed in Equation 2, it is important to note that the 40-element fundamental mode vector of fission powers (or fission neutron sources) for each of the 40 ATR or ATRC fuel elements may be viewed as a vector of random variables that are correlated because fission neutrons born in one fuel element can induce new fissions not only in the same element, but in any other fuel element as well, although the probability that a neutron born in one element will induce a fission in another element generally decreases with physical separation of the two fuel elements.

Referring to Equation 3, it can be seen that if the fundamental mode fission source (or power) vector is premultiplied by the fission matrix the resulting vector is, by definition, simply the original vector with all entries multiplied by k -effective. Furthermore if the fundamental mode source or power vector is arbitrarily perturbed in some manner, then premultiplication of the perturbed vector by the fission matrix will force it back toward the original fundamental mode shape, although a number of iterations may be required to converge back to the original vector in applications such as ATR, where the dominance ratio is fairly large. The above observations suggest the following stochastic estimation procedure for constructing the required fission correlation matrix:

1. Generate a vector of 40 normally-distributed random numbers whose mean is 1.0 and whose standard deviation is some nominal small fraction of the mean, e.g. 10%. The fraction specified for the standard deviation is arbitrary, but it should be small enough such that essentially no negative random numbers are ever produced and at the same time it should be large enough to avoid round-off errors in the process described below.
2. Multiply each of the 40 elements of the fundamental mode fission power vector by the corresponding element of the random number vector from Step 1. On the average, half of the fission power entries that are randomly perturbed in this manner will increase and half will decrease.
3. Premultiply the perturbed fundamental-mode fission power vector from Step 2 by the fission matrix and store the resulting perturbed “first-generation” fission power vector.
4. Repeat Steps 1-3 a statistically useful number of times, N (e.g. $N=1000$), to produce a batch of N 40-element perturbed “first-generation” fission power vectors.
5. Compute the 40x40 covariance matrix for the elements of the N 40-element perturbed “first-generation” fission power vectors using the fundamental definition of covariance. This completes an “inner iteration”, producing a statistical estimate of the fission power covariance matrix.

6. Repeat Steps 1-5 a suitable number of times, tallying a running average of the covariance matrices that are produced until satisfactory convergence is obtained. Then compute the correlation matrix associated with the converged covariance matrix.
7. Construct the covariance matrix for the *a priori* powers computed by the modeling code by combining the correlation matrix from Step 6 with a vector of assumed *a priori* uncertainties that are to be associated with the *a priori* power vector.

In mathematical terms this process can be programmed as follows:

First, define

$$[PD] = \begin{bmatrix} P_{01} & & & & \\ & P_{02} & & & \\ & & P_{03} & & \\ & & & \ddots & \\ & & & & P_{0,NE} \end{bmatrix} \quad (4)$$

where the diagonal elements of [PD] correspond to the *a priori* computed fuel element fission powers and all other entries are zero. Now define the matrix of random numbers

$$[R] = \begin{bmatrix} r_{11} & r_{12} & \cdots & \cdots & r_{1,N} \\ r_{21} & r_{22} & & & r_{2,n} \\ \vdots & \vdots & & & \vdots \\ \vdots & \vdots & & & \vdots \\ r_{NE,1} & r_{NE,2} & & & r_{NE,N} \end{bmatrix} \quad (5)$$

where N is a large number (e.g. 1000 as noted earlier) and each r_{ij} is a random number drawn from a normally distributed population whose mean is 1.0 and whose standard deviation is a small fraction of the mean (e.g. 10%). Then form the matrix product:

$$[PP] = [PD][R] = \begin{bmatrix} pp_{11} & pp_{12} & \cdots & \cdots & pp_{1,N} \\ pp_{21} & pp_{22} & & & pp_{2,n} \\ \vdots & \vdots & & & \vdots \\ \vdots & \vdots & & & \vdots \\ pp_{NE,1} & pp_{NE,2} & & & pp_{NE,N} \end{bmatrix} \quad (6)$$

where each column of [PP] is a vector of a-priori element powers perturbed by the corresponding random numbers in the same column of [R].

Now premultiply [PP] by the fission matrix [F] to obtain a matrix [FPP] of N “first-generation” fuel element power vectors corresponding to each original perturbed power vector:

$$[FPP] = [F][PP] \quad (7)$$

The elements of the randomly-perturbed power vectors comprising [PP] are uncorrelated, but the elements of each of the corresponding first-generation power vectors comprising [FPP] will be positively correlated by virtue of the fact that a fission occurring in one fuel element can cause a next-generation fission not only in that element but also in any other element, as quantified by the fission matrix

Now, recognizing that the N columns of [FPP] are random samples of an “average” first-generation fission power vector [P₁] (whose spatial shape can incidentally be shown to be statistically identical to that of the original power vector [P₀]), the covariance of the elements of [P₁] may be computed as:

$$[\text{Cov}[P_1]] = [DM][DM]^T / (N - 1) \quad (8)$$

where [DM] is the difference matrix:

$$[DM] = [FPP] - [PD][U] \quad (9)$$

and [U] is a 40-row, N-column matrix whose entries are all 1.0

Repeat the process described above a number of times, tallying a running average of [Cov(P₁)] until satisfactory convergence is obtained. Then compute the correlation matrix corresponding to the converged covariance matrix [Cov(P₁)] using the standard definition. This is the desired fuel element-to-element power correlation matrix. Finally, use this power correlation matrix to construct a matrix [Cov(P₀)] that corresponds to the actual absolute uncertainties associated with the elements of [P₀] rather than the arbitrary uniform perturbation used to obtain [Cov[P₁]].

3.1.4. Solution of the Adjustment Equations

With the fission power covariance matrix now available, Equations 1 and 2 can be combined in the usual manner to construct the covariance-weighted “Normal Equations” (e.g. Meyer, 1975) for the system, yielding:

$$\mathbf{BP} = \mathbf{A}^T [\text{Cov}(\mathbf{Z})]^{-1} \mathbf{Z} \quad (10)$$

with

$$\mathbf{B} = \mathbf{A}^T [\text{Cov}(\mathbf{Z})]^{-1} \mathbf{A}. \quad (11)$$

Equation 10 can be solved by any suitable method to yield the adjusted element power vector **P**. The difference between the adjusted power vector and the *a priori* power vector then gives an estimate of the bias of the model, if any, relative to the validation measurements.

Also, since the solution to Equation 10 is:

$$\mathbf{P} = \mathbf{B}^{-1} \mathbf{A}^T [\mathbf{Cov}(\mathbf{Z})]^{-1} \mathbf{Z} \quad (12)$$

the covariance matrix for the adjusted powers may be computed by the standard uncertainty propagation formula:

$$\mathbf{Cov}(\mathbf{P}) = \mathbf{D} \mathbf{Cov}(\mathbf{Z}) \mathbf{D}^T \quad (13)$$

where

$$\mathbf{D} = \mathbf{B}^{-1} \mathbf{A}^T [\mathbf{Cov}(\mathbf{Z})]^{-1}. \quad (14)$$

The diagonal elements of the covariance matrix for the adjusted powers can then be used to estimate the uncertainty of the modeling bias. It may also be noted in passing that the covariance matrix for the adjusted power vector is also simply the inverse of \mathbf{B} .

3.1.5 Results and Discussion

The *a priori* and measured power distributions from Figure 3.2 are plotted in Figure 3.3, along with the adjusted power distribution obtained using the measured powers of all 40 elements. The covariance matrix for the *a priori* power vector was computed as described above and normalized to an estimated *a priori* absolute uncertainty of 10% (1σ) for the diagonal entries, based on historical experience. The covariance matrix for the measured powers was assumed to have only diagonal entries of 5% (1σ) for this example. It is a simple matter to include appropriate off-diagonal elements in the latter matrix to account for correlations, for example from a common calibration of the detector used to measure the activity of the fission wires, if desired. The reduced uncertainties for the adjusted element powers in Figure 3.3, computed using Equation 7, ranged from 3.1% to 3.7%. The adjustments ranged from -9.8% in Element 37 to +6.8% in Element 25 and in fact 68% of the adjustments were within $\pm 4\%$. Thus all of the adjustments fell well within the assumed *a priori* uncertainty ($1\sigma=10\%$), indicating possible degree of conservatism in the *a priori* uncertainties assumed for the computed element powers.

The correlation matrix associated with the fission power covariance matrix used to compute the adjusted power vector in Figure 3.3 is shown as a contour plot in Figure 3.4. Key off-diagonal structural features, such as the correlations between nearby, but non-adjacent, Elements 1 and 10, or Elements 11 and 20, etc. are readily apparent. The underlying fission matrix for this example is shown in Figure 3.5. The same general structure is apparent. Note also that the fission matrix is not necessarily symmetric, while the fission correlation matrix is symmetric by definition.

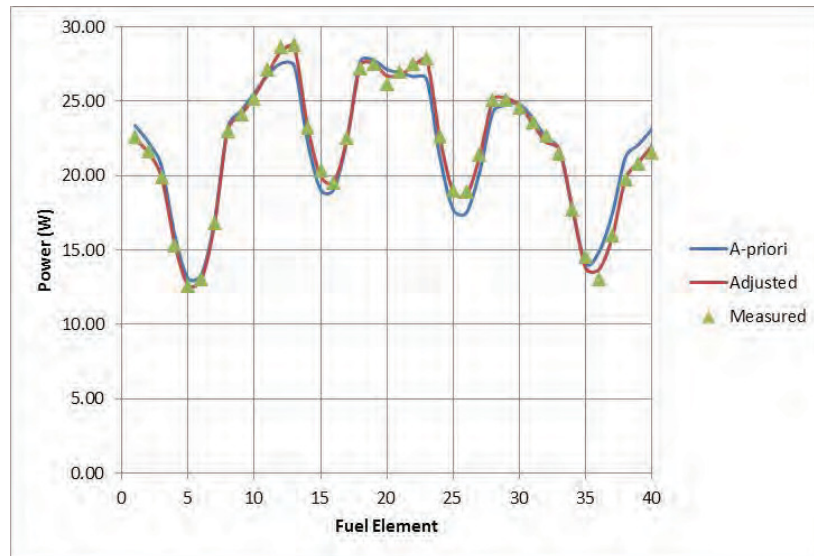


Figure 3.3. Fuel element power distributions for ATRC Cycle 152B Support Test 12-5. The adjusted power is computed using the measured powers of all 40 fuel elements.

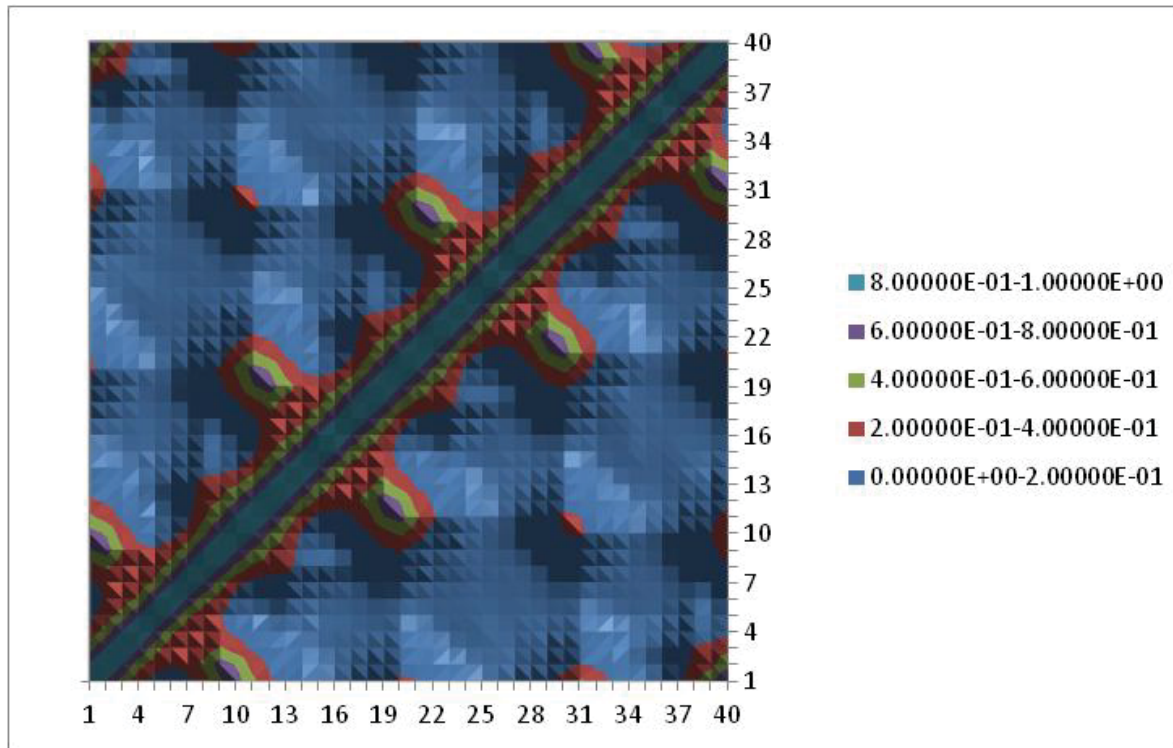


Figure 3.4. Fission power correlation matrix for the ATRC. The axis numbering corresponds to the fuel element numbers shown in Figure 3.2.

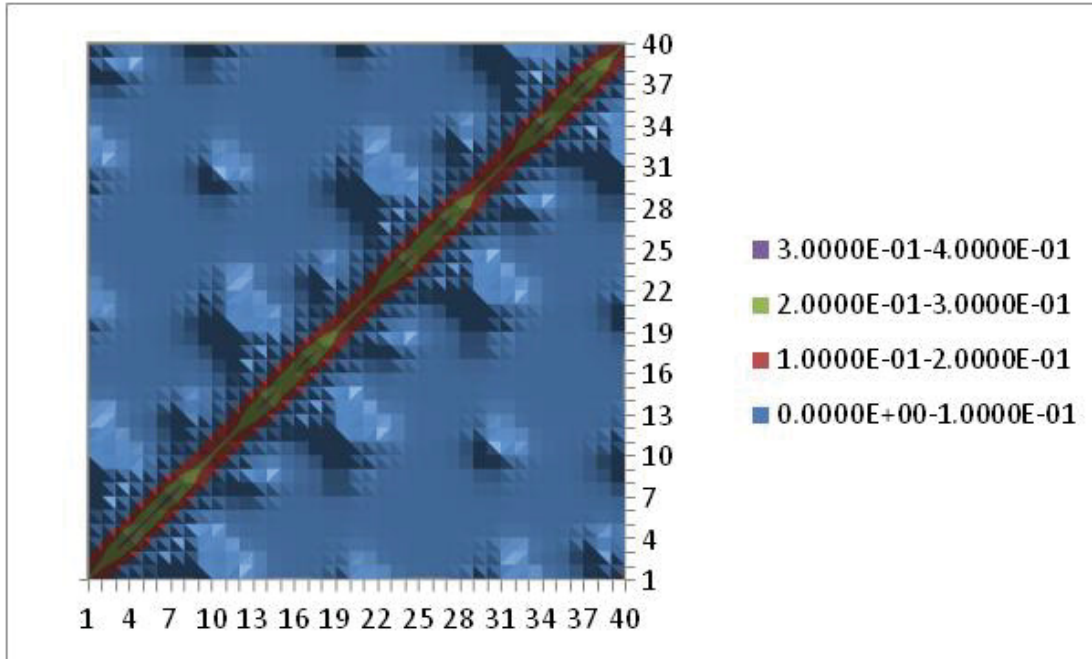


Figure 3.5. Fission matrix for the ATRC. The axis numbering corresponds to the fuel element numbers shown in Figure 3.2.

Figure 3.6 shows the result of an adjustment of the MCNP *a priori flux* where only the powers of the odd-numbered fuel elements in Test 12-5 were included in the analysis. This simulates the relatively common ATR practice where only the odd-numbered fuel element powers are actually measured, and the power for each even-numbered element is assumed to be equal to the measured power in the odd-numbered element on the opposite side of the same lobe. For example, the power in Element 2 is assumed equal to the power in Element 9, the power in Element 4 is assumed equal to the power in Element 7, and so forth around the core. The often-questionable validity of this assumption depends on the overall symmetry of the reactor configuration. In the future the assumption of symmetry can be easily replaced by the least-square adjustment procedure described here to estimate the powers in the even-numbered elements. The reduced uncertainties for the adjusted element powers in Figure 8 ranged from 3.9% to 4.3% for the odd-numbered elements and from 4.0% to 5.2% for the even-numbered elements, demonstrating how significant uncertainty reduction can occur in the adjusted powers even for elements for which no measurement is included. This is a result of the weighted interpolation effect provided by the element power covariance matrix.

Economizing on the number of measurements even further, Figure 3.7 shows an adjustment where only the measured powers for Elements 8, 18, 28, and 38 were included in the analysis. This arrangement simulates another ATR protocol that is sometimes used because these elements are representative of the highest-powered elements in each outer lobe. In this case the reduced uncertainties for the adjusted element powers ranged from 4.4% to 4.5% for Elements 8, 18, 28 and 38, from 6.6% to 7% for the immediately adjacent elements and up to 9.9% for the elements that were the most distant from the elements for which measurements were made. It is notable here that some uncertainty reduction and element power adjustment occurs even for the most remote fuel elements.

Proceeding further with this 4-element example, summing the 40 element powers corresponding to the adjusted power curve in Figure 3.7 yields a total adjusted reactor power of 867.95 watts with an

uncertainty of 3.1% (1σ). The absolute uncertainty quoted for the total adjusted power is computed by the usual formula:

$$\sigma_p = (\mathbf{T}\mathbf{Cov}(\mathbf{P})\mathbf{T}^T)^{1/2} \quad (15)$$

where \mathbf{T} is a 40-element row vector whose entries are all 1.0 and $\mathbf{Cov}(\mathbf{P})$ is from Equation 13. This adjusted power is in excellent statistical agreement with the measured total reactor power of $875.56 \pm 1\%$ that is obtained by summing the original 40 measured element powers, illustrating how the total reactor power and its uncertainty can be estimated in a statistically valid manner to good accuracy using the least-squares approach even when only four fuel element powers are actually measured.

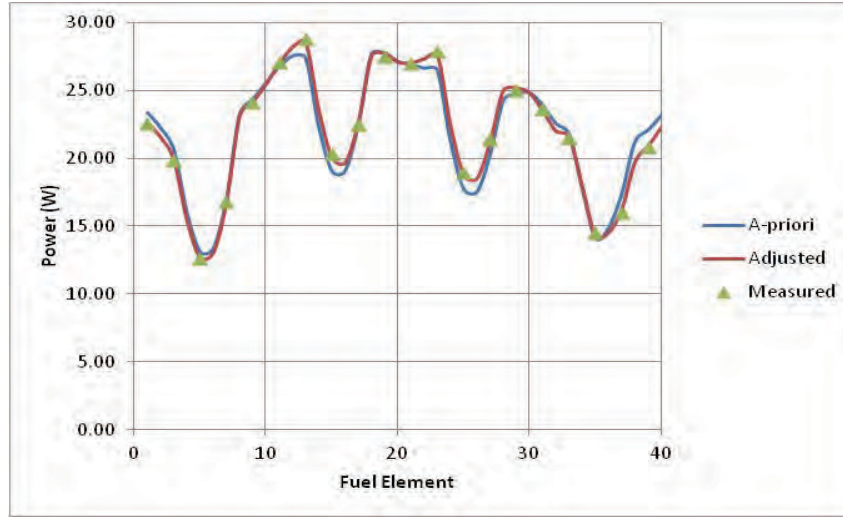


Figure 3.6. Fuel element power distributions for ATRC Depressurized Run Support Test 12-5. The adjusted power is computed using the measured powers of only the 20 odd-numbered fuel elements.

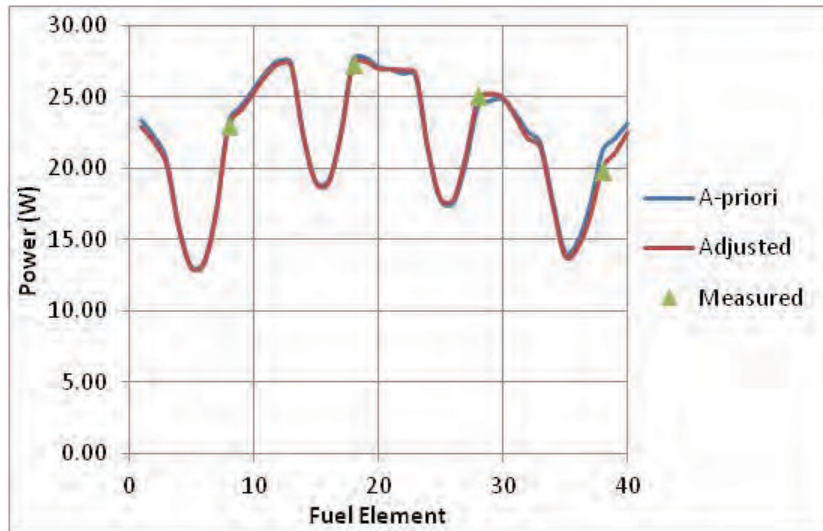


Figure 3.7. Fuel element power distributions for ATRC Depressurized Run Support Test 12-5. The adjusted power is computed using the measured powers of elements 8, 18, 28 and 38 only.

Figure 3.8 illustrates another possible use of the techniques developed in this work. The ATR has an online lobe power measurement system but it does not have an online system for measurement of individual fuel element powers. Measurements of individual element powers currently can only be done by the rather tedious fission wire technique described earlier. The least-squares methodology outlined here also offers a simple, but mathematically rigorous, approach for estimating the fission powers of all 40 fuel ATR fuel elements and their uncertainties using the online lobe power measurements as follows:

In the case of Figure 3.8 the online lobe power measurements are simulated by the fission wire measurements used for the previous examples. The first five rows of the matrix on the left-hand side of Equation 1 describe the five simulated online lobe power measurements. These rows each contain entries of 0.125 on the left-hand side for the elements included in the lobe corresponding to that row and entries of zero elsewhere. The right hand side of each of these first five rows contains the average of the measured powers from the fission wires for the lobe represented by that row. For example the first row (Lobe 1) contains entries of 0.125 for elements 2 through 9, and the average of the measured powers for elements 2 through 9 appears on the right hand side, and so forth for the other lobes. The reduced uncertainties for the adjusted powers shown in Figure 10 for the 40 elements range from 6.4% to 8.3%.

We also note that summing the 40 element powers corresponding to the adjusted power curve in Figure 3.8 yields a total adjusted reactor power of 874.65 watts with an uncertainty of 2.0% (1σ). Once again this is in excellent statistical agreement with the measured total reactor power of $875.56 \pm 1\%$ that is obtained by summing the original 40 measured element powers.

The results shown in Figure 3.8 thus illustrate a practical application where the powers for each ATR lobe that are measured online could be entered into Equation 1 each time they are updated (every few seconds), and a corresponding estimate for all of the individual element powers could be immediately produced. Of course the *a priori* power vector would need to be recalculated regularly as the core depletes, control drums rotate, and neck shims are pulled during a cycle. This could however be automated to a large extent, and it should ultimately be quite practical, for example, to update the *a priori* power vector from the model at least daily.

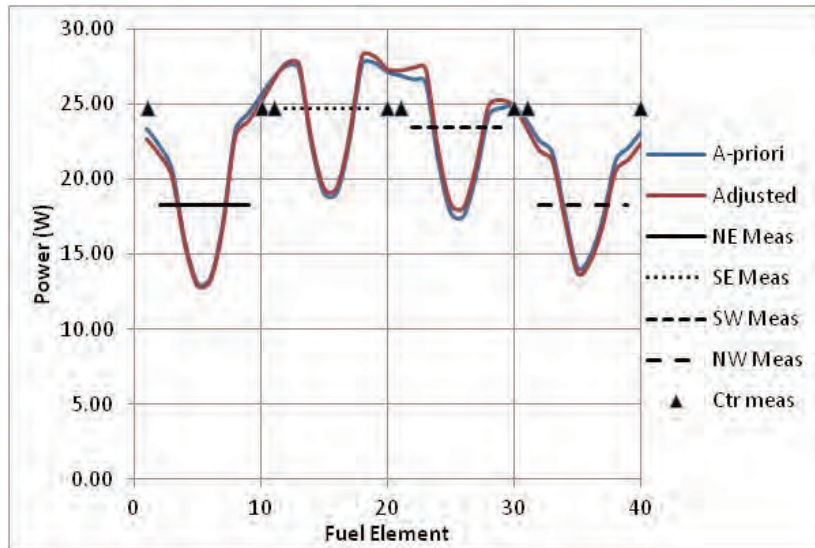


Figure 3.8. Fuel element power distributions for ATRC Depressurized Run Support Test 12-5. The adjusted power is computed using the measured powers of the five core lobes.

Finally Figure 3.9 shows a comparison of the *a priori* element powers and the adjusted element powers based on the lobe power measurements with the original detailed 40-element measured power data . Recall that the adjusted powers in this figure are based only on the measured *lobe* powers that were pre-computed by averaging the detailed element power measurements for each lobe. It is interesting to note that the adjusted power distribution curve still recaptures a significant amount of the detailed shape change relative to the *a priori* power distribution that is seen in Figure 3.3, even though the details in the measured power distribution were largely averaged out when computing the measured lobe powers used for the adjustment. The covariance matrix plays a key role in this process.

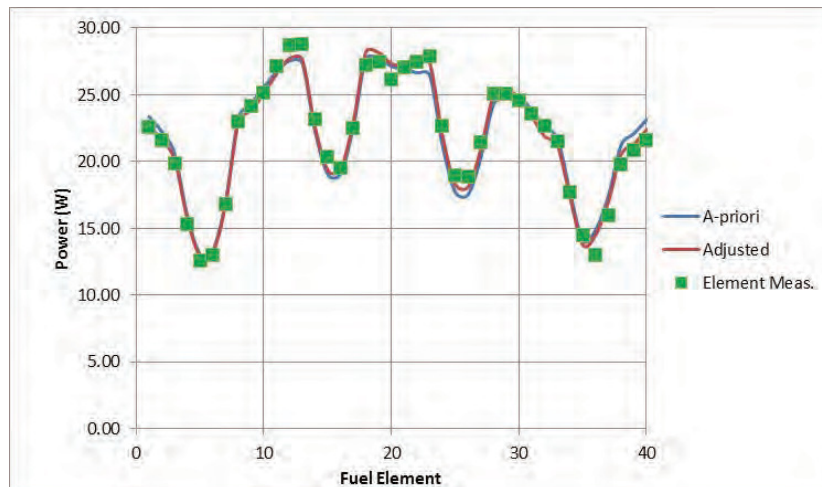


Figure 3.9. Comparison of *a priori* element powers, the adjusted element powers based on the measured lobe powers formed from the original detailed fuel element power measurements, and the actual detailed element power measurements.

In summary, a relatively simple but effective fission-matrix-based method for generating the required fuel element covariance information needed for detailed statistical validation and best-estimate adjustment analysis of fission power distributions produced by computational reactor physics models of the ATR (or for that matter, any other type of reactor) was developed and demonstrated during FY-2013. The method has been demonstrated using the MCNP5 neutronics code but it can be used with any other Monte Carlo neutronics simulation code as well as with any deterministic neutron transport code that provides a sufficient level of spatial, angular, and energy resolution within each fissioning region of interest. Analyses of this type are useful not only for quantifying the bias and uncertainty of computational models for a specific measured reactor configuration of interest, but they also can serve as guides for model improvement and for estimation of *a priori* modeling uncertainties for related reactor configurations for which no measurements are available.

3.1.6 Extension to SERPENT, HELIOS, and NEWT

SERPENT, HELIOS and NEWT were also used to model this configuration of the ATRC in addition to MCNP5. As before, the *a-priori* fuel element powers were adjusted against the measurements using the same covariance-weighted least-squares technique. Figures 3.10, 3.11, and 3.12 show the results of the adjustments for the three additional codes. Once again in all cases that 68% of the adjustments fell well within the assumed *a priori* uncertainty ($1\sigma=10\%$) and the maximum adjustments in both directions fell well within two *a priori* standard deviations. This is illustrated for one case in Figure 3.13, which shows

a histogram of the adjustment factors associated with the HELIOS results. The reduced uncertainties for the adjusted element powers were again in the range of 3.5% (1σ), consistent with the estimated 5% (1σ) uncertainties of the measured powers used for the adjustment. As expected, the adjustments associated with the 3D codes (MCNP5, SERPENT) were generally smaller than was the case for the 2D (NEWT, HELIOS) codes, reflecting somewhat greater *a priori* consistency of the 3D results with the measurements.

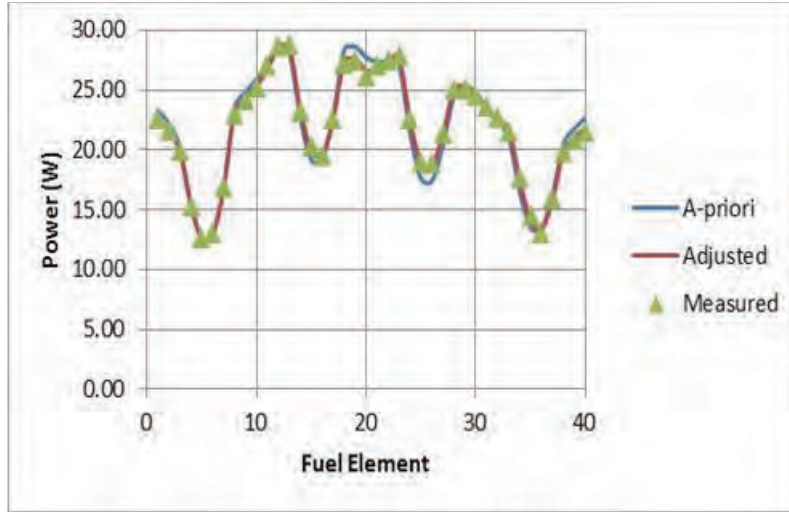


Figure 3.10. Fuel element fission rate distribution for ATRC Depressurized Run Support Test 12-5 SERPENT *a priori*). The *a priori* uncertainty was assumed to be 10% (1σ). The adjustments ranged from -3.7% in Element 20 to +7.1% in Element 26 and 68% of the adjustments were within $\pm 3.2\%$. Reduced uncertainties for the adjusted powers are in the range of 3.2% to 3.6% for all elements.

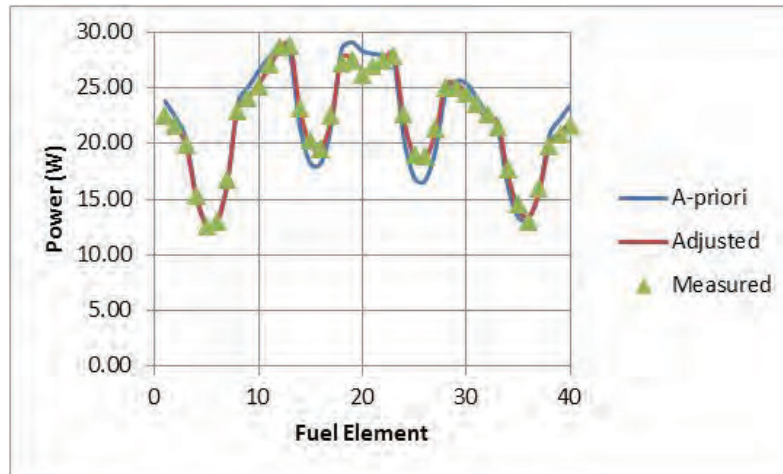


Figure 3.11. Fuel element fission rate distribution for ATRC Depressurized Run Support Test 12-5 NEWT *a priori*). The *a priori* uncertainty was assumed to be 10% (1σ). The adjustments ranged from -6.4% in Element 40 to +11.8% in Element 26 and 68% of the adjustments were within $\pm 5.1\%$. Reduced uncertainties for the adjusted powers are in the range of 3.2% to 3.6% for all elements.

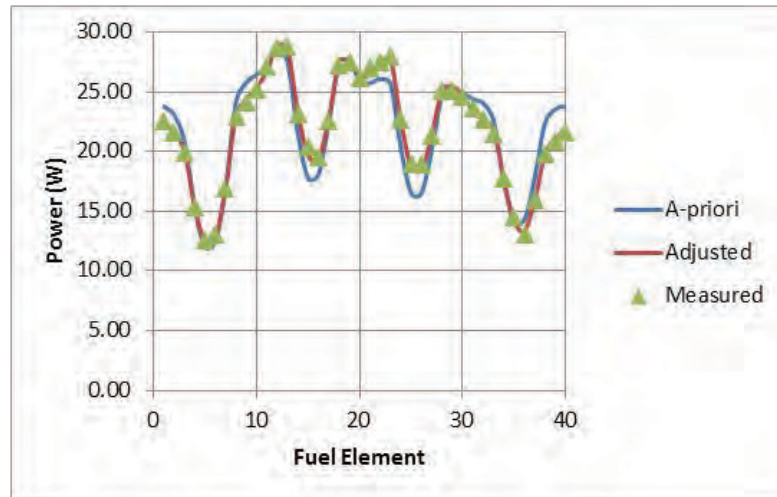


Figure 3.12. Fuel element fission rate distribution for ATRC Depressurized Run Support Test 12-5 (HELIOS *a priori*). The *a priori* uncertainty was assumed to be 10% (1σ). The adjustments ranged from -11.5% in Element 38 to +13.2% in Element 25 and 68% of the adjustments were within $\pm 6.3\%$. Reduced uncertainties for the adjusted powers are in the range of 3.1% to 3.7% for all elements

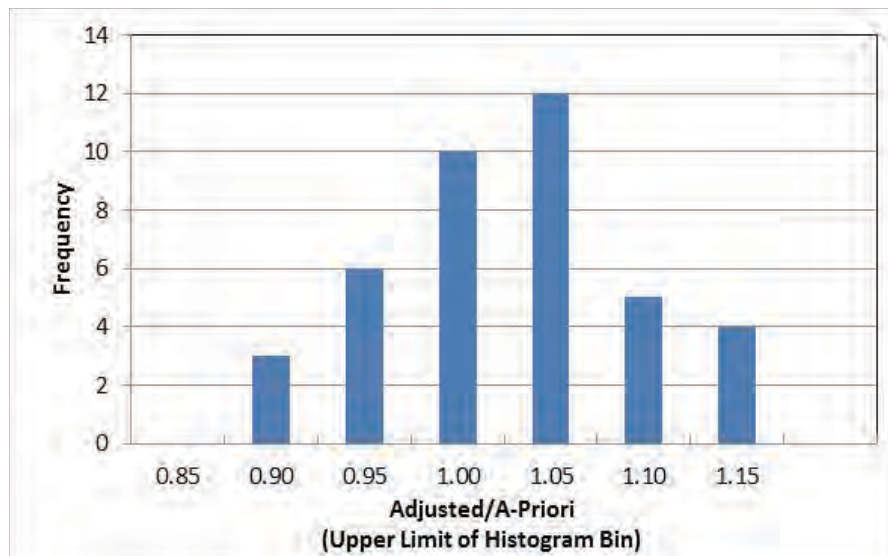


Figure 3.13 Histogram of HELIOS adjustment factors for ATRC Depressurized Run Support Test 12-5.

As one final illustration of the results described in this section, Figure 3.14 directly compares the unadjusted MCNP5 and SERPENT *a priori* element powers with the measurements. The 5% (1σ) nominal uncertainty bands for the measurements are also shown. It can be seen that for the most part the MCNP5 and SERPENT results are quite consistent with each other as well as with the measurements, even prior to the statistical adjustment process. This provides an additional measure of confidence in the cross-verification of SERPENT against MCNP5 as described earlier.

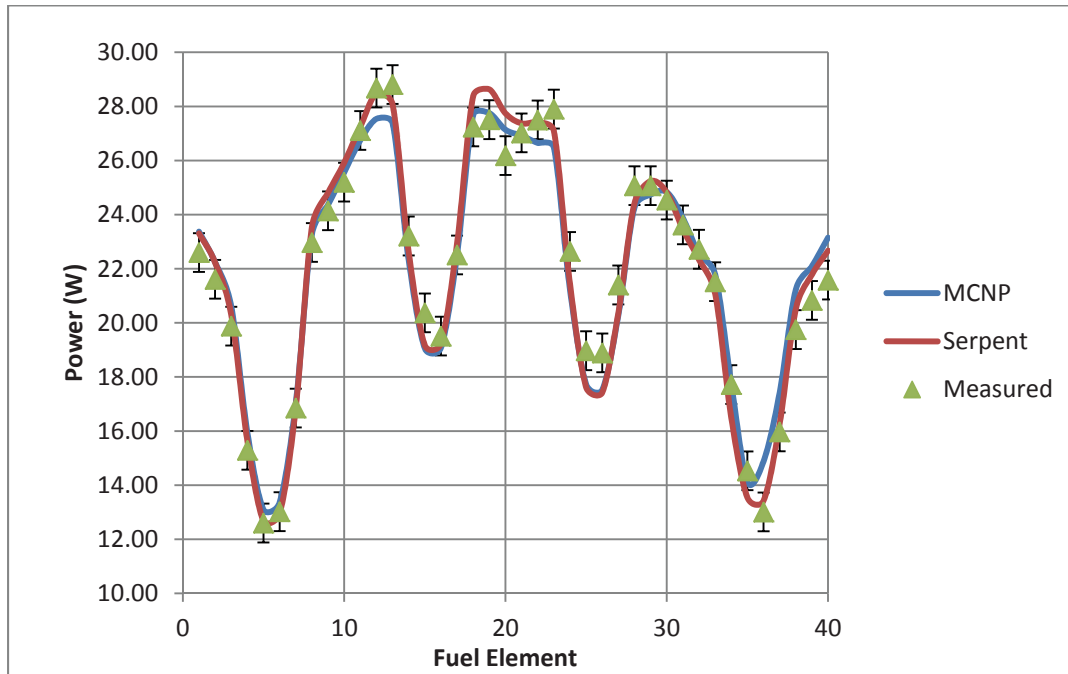


Figure 3.14. MCNP5 and SERPENT *a priori* ATRC fuel element powers, and measured element powers, for ATRC Depressurized Run Support Test 12-5. Uncertainties (5% 1σ) are shown for the measurements. Tally statistics for the computations are comparable to the line widths ($\ll 1\% 1\sigma$).

3.2 Intra-element Power Distribution Analysis of ATRC Validation Experiment 12-5

The fission wires placed in each ATRC fuel element as described previously also provided a method for quantifying the fission rate distributions within each element at the axial midplane because the fission rate in a given wire is representative of the fission rates in the immediately-adjacent fuel plates at the same axial and azimuthal locations (Durney and Kauffman, 1967).

The measured flux wire results from for Fuel Element 19 are provided as a typical example in Table 3.1. The results of the HELIOS calculations for the adjacent fuel plates are compared to the measured values for the wires in ATRC Flux Run 12-5 for Channels 2, 6, 11, 15, and 19 as functions of azimuthal position are shown in Figures 3.15 through 3.19. An axial peaking factor of 1.4 was used for the HELIOS model. A 5% uncertainty is associated with the measured values for the fission rates in the wires (Durney and Kauffman, 1967).

In general, there was good agreement between the HELIOS results and the measured results for the flux wires that were located azimuthally within the fuel meat in the two corresponding adjacent fuel plates (Channels 6, and 10). Channel 2 and 11 measured versus calculated results show disagreement at the ends where the flux wires are located azimuthally outside of the fuel meat. Flux wire 10 in channel 11

however showed good agreement with the measured results. Channel 19 showed relatively good agreement in the interior of the fuel meat but diverged on the two outside wire positions.

Table 3.1. Fuel Element 19 Fission Wires - Measured Powers (W/gU).

Channel	Wire Number	% Distance From Left Side of Plate	Measured Power (W/g)
2	15	25%	6.528E-02
	16	46%	5.310E-02
	17	75%	6.870E-02
6	12	25%	3.553E-02
	13	46%	3.369E-02
	14	75%	3.461E-02
11	9	3%	4.452E-02
	10	47%	2.961E-02
	11	97%	4.900E-02
15	6	25%	2.927E-02
	7	47%	2.940E-02
	8	75%	3.126E-02
19	1	4%	3.331E-02
	2	25%	3.313E-02
	3	46%	3.806E-02
	4	75%	4.423E-02
	5	96%	5.724E-02

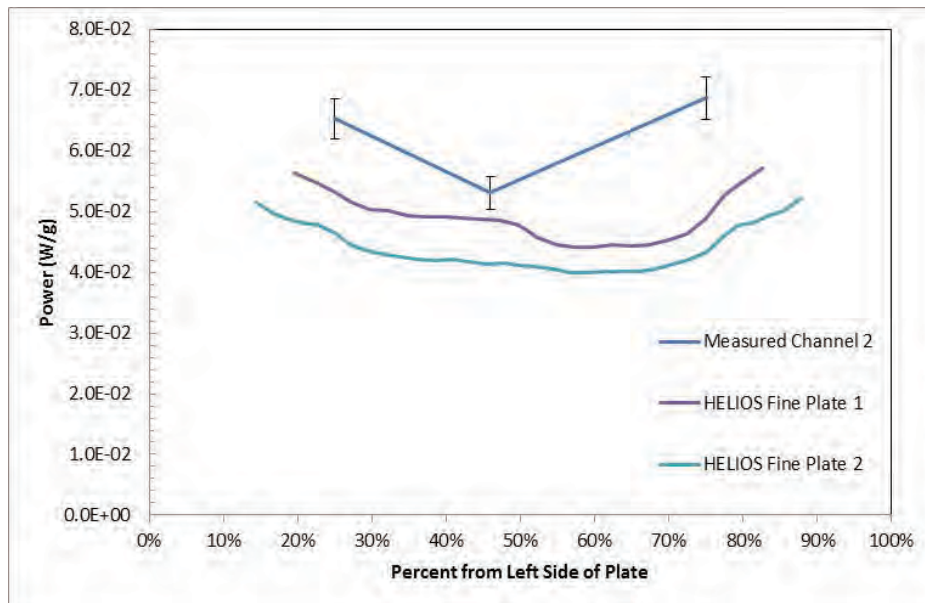


Figure 3.15. Channel 2 measured flux wire powers versus predicted specific power in the adjacent fuel plates.

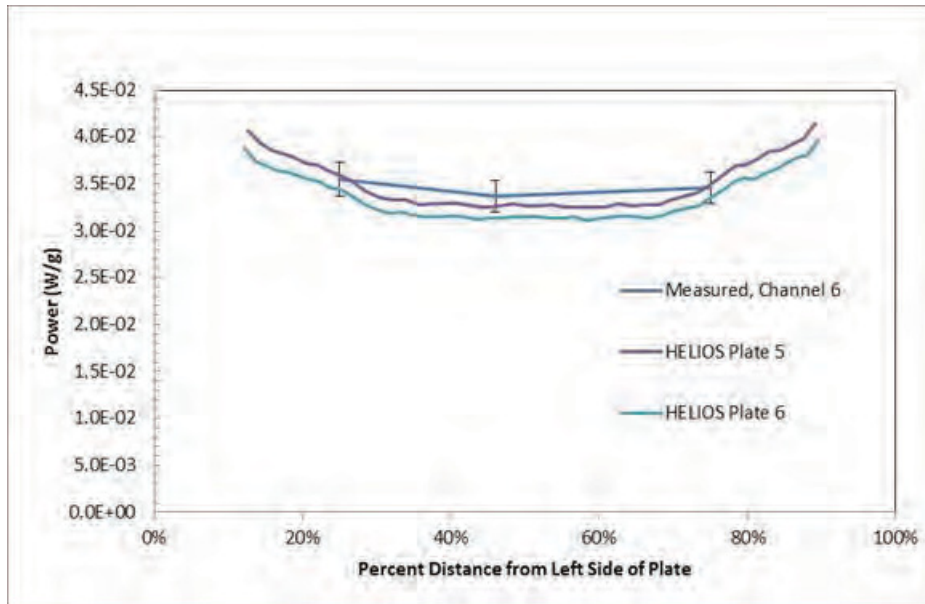


Figure 3.16 Channel 6 measured flux wire powers versus predicted specific power in the adjacent fuel plates.

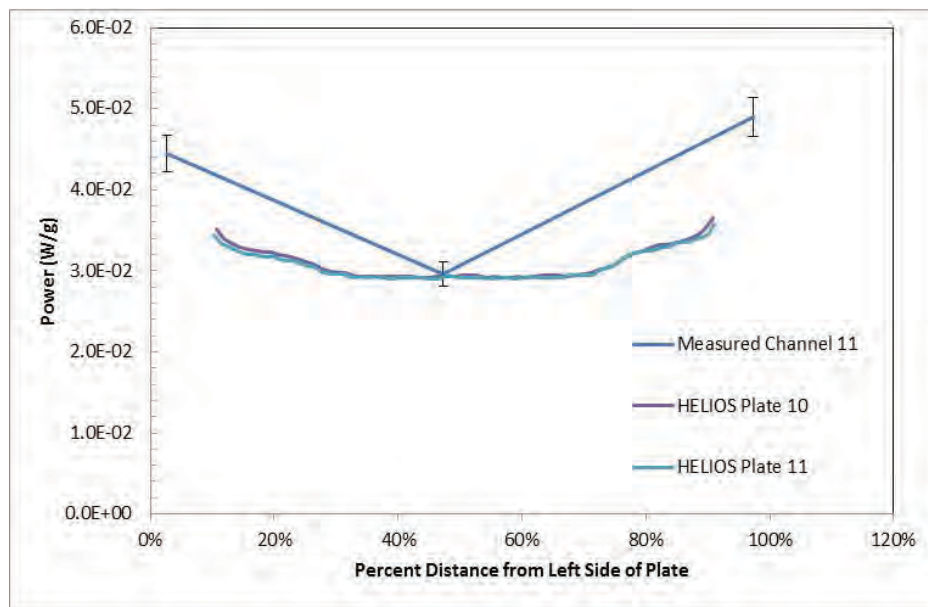


Figure 3.17. Channel 11 measured flux wire powers versus predicted specific power in the adjacent fuel plates.

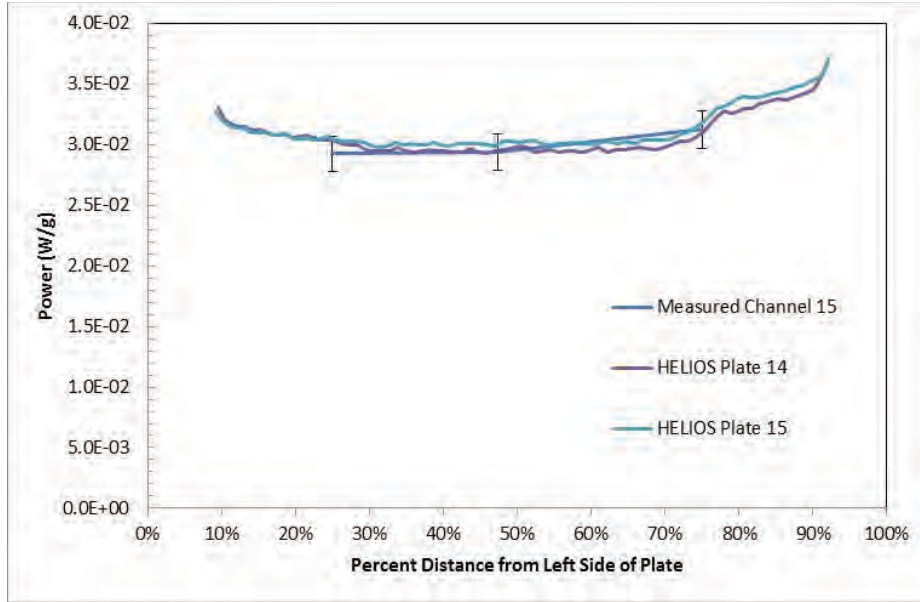


Figure 3.18. Channel 15 measured flux wire powers versus predicted specific power in the adjacent fuel plates.

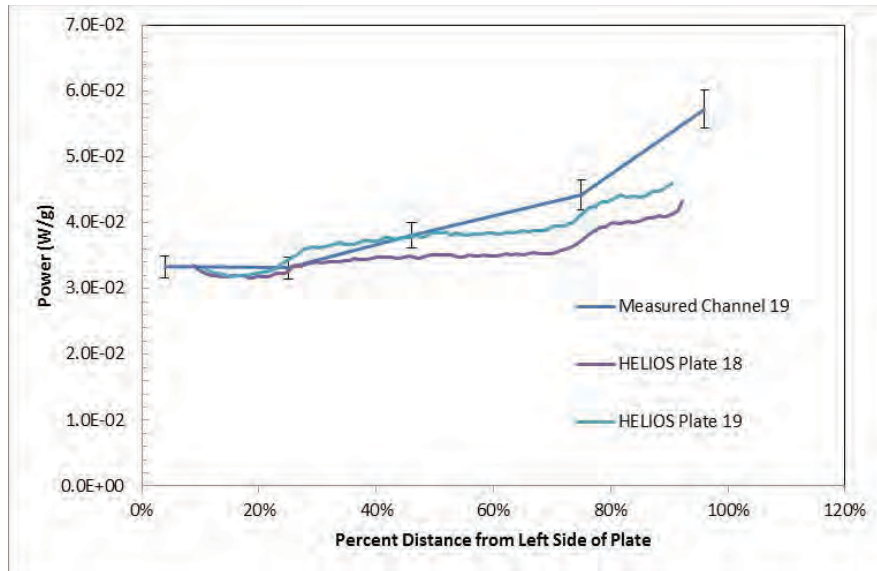


Figure 3.19. Channel 19 measured flux wire powers versus predicted specific power in the adjacent fuel plates.

Although the data shown in Figures 3.15-3.19 are qualitatively illustrative, a quantitative statistical comparison of the measured fission powers in the wires against the HELIOS-calculated values for the wires themselves provides a somewhat more rigorous validation metric. Accordingly the wires were represented explicitly in the HELIOS model and the fission powers for element 19 were computed directly, again assuming an axial peaking factor of 1.4. The results were then scaled to the average of the measured wire powers for fuel element 19 in order to allow a direct comparison of the *relative* radial and azimuthal distribution of wire powers in this element. The computed powers were then adjusted against the measured wire powers using the methodology outlined in Section 3.1. The required covariance matrix

for the adjustment was constructed using a 5% uncertainty for the measured wire powers as noted above and a 10% *a priori* uncertainty for the calculated wire powers, consistent with the element analysis outlined in Section 3.1. However, in this case no off-diagonal entries were included in the covariance matrix for the calculated powers, reflecting the fact that a fission neutron emitted in a particular wire is not very likely to cause a fission in any other wire. It is much more likely that it will cause a fission in the surrounding fuel instead. The scaled *a priori* calculated wire powers for Element 19 are shown in Table 3.2. Figures 3.20 – 3.24 compare the measured and scaled *a priori* wire powers graphically for each channel where wires were located. The adjusted wire powers are listed in Table 3.3 and the percentage adjustments relative to the *a priori* powers are shown in Table 3.4. The percentage adjustments ranged from 11% downward to about 17% upward. 68% of the adjustments were within approximately 7.5% of the average *a priori* calculated wire power for the element, well within the 10% estimated uncertainty for the *a priori* calculated powers.

Repeating the analysis described here for the other 39 fuel elements and combining results showed that 68% of the adjustments to the scaled *a priori* calculated powers of all 680 fission wires in the core fell within about 8.7% of the core-average scaled *a priori* calculated wire power, again well within the estimated *a priori* uncertainty. The distribution of percentage adjustments to the scaled *a priori* powers for all of the wires is illustrated in Figure 3.25. The distribution tends to be skewed to the right, reflecting the larger number of upward adjustments occurring for the wires located azimuthally outside the active fuel regions of the fuel plates as discussed earlier. Finally, we note that if the *absolute* fission wire powers, unscaled to the element averages, are adjusted against the measured wire powers, 68% of the adjustments fall within about 10.5% of the *a priori* calculated wire power, also lending credence to the *a priori* uncertainty estimate in an absolute sense.

Table 3.2. Fuel Element 19 Fission Wires – HELIOS Calculated Powers (W/gU) scaled to the average of the measured wire powers for the element..

Channel	Wire Number	Position Relative to Azimuthal Center (in)	Calculated Power (W/g)
2	15	-0.85	6.350E-02
	16	-0.08	5.077E-02
	17	0.85	6.493E-02
6	12	-0.59	3.708E-02
	13	-0.08	3.559E-02
	14	0.59	3.690E-02
11	9	-1.29	3.778E-02
	10	-0.08	3.186E-02
	11	1.29	3.981E-02
15	6	-0.83	3.238E-02
	7	-0.08	3.238E-02
	8	0.83	3.364E-02
19	1	-1.79	3.812E-02
	2	-0.94	3.807E-02
	3	-0.08	4.040E-02
	4	0.94	4.275E-02
	5	1.79	5.387E-02

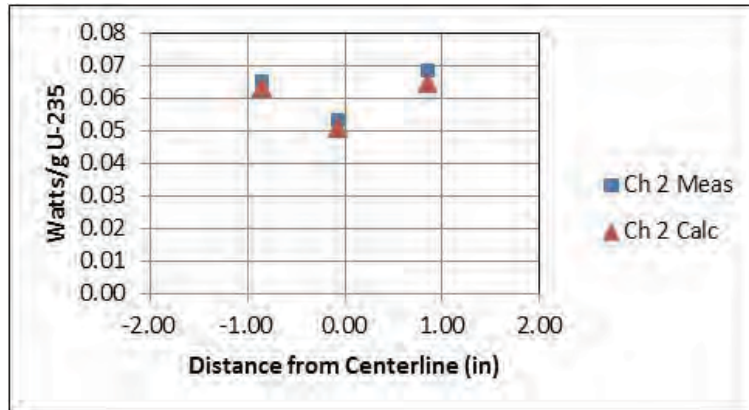


Figure 3.20. Measured fission wire powers and *a-priori* calculated wire powers (scaled to the average measured wire power) for Fuel Element 19, Channel 2.

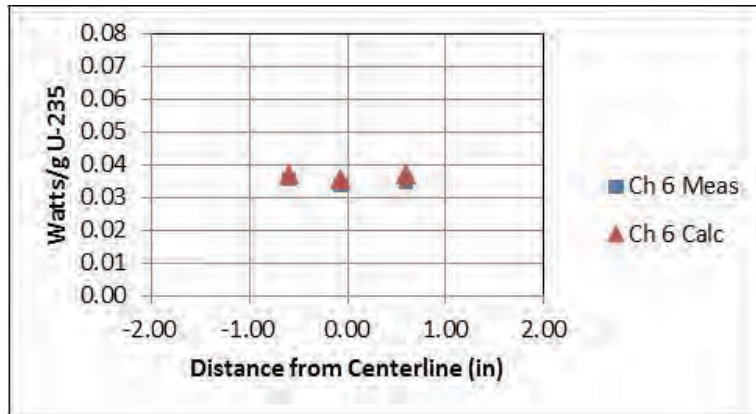


Figure 3.21. Measured fission wire powers and *a-priori* calculated wire powers (scaled to the average measured wire power) for Fuel Element 19, Channel 6.

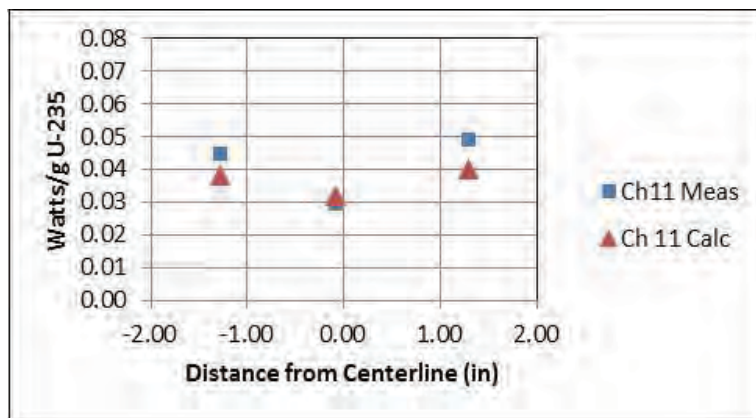


Figure 3.22. Measured fission wire powers and *a-priori* calculated wire powers (scaled to the average measured wire power) for Fuel Element 19, Channel 11.

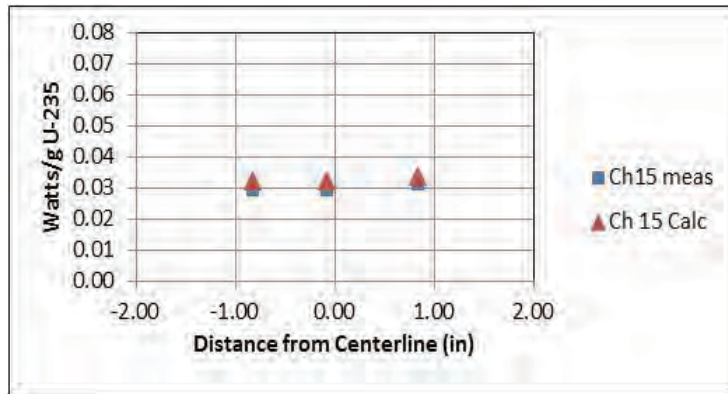


Figure 3.23. Measured fission wire powers and *a-priori* calculated wire powers (scaled to the average measured wire power) for Fuel Element 19, Channel 15.

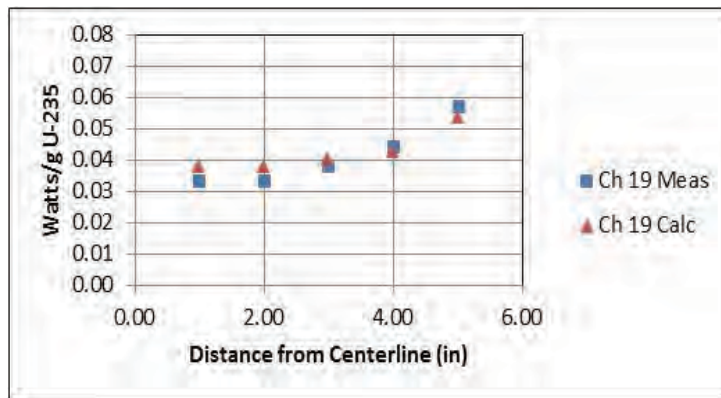


Figure 3.24. Measured fission wire powers and *a-priori* calculated wire powers (scaled to the average measured wire power) for Fuel Element 19, Channel 19.

Table 3.3. Fuel Element 19 Fission Wires – Adjusted Powers (W/gU).

Channel	Wire Number	Position Relative to Azimuthal Center (in)	Adjusted Power (W/g)
2	15	-0.85	6.491E-02
	16	-0.08	5.260E-02
	17	0.85	6.788E-02
6	12	-0.59	3.582E-02
	13	-0.08	3.404E-02
	14	0.59	3.502E-02
11	9	-1.29	4.278E-02
	10	-0.08	3.001E-02
	11	1.29	4.648E-02
15	6	-0.83	2.980E-02
	7	-0.08	2.991E-02
	8	0.83	3.168E-02
19	1	-1.79	3.408E-02
	2	-0.94	3.392E-02
	3	-0.08	3.849E-02
	4	0.94	4.392E-02
	5	1.79	5.650E-02

Table 3.4. Fuel Element 19 Fission Wires – Percent Adjustments.

Channel	Wire Number	Position Relative to Azimuthal Center (in)	Percent Adjustment
2	15	-0.85	2.22
	16	-0.08	3.60
	17	0.85	4.53
6	12	-0.59	-3.39
	13	-0.08	-4.37
	14	0.59	-5.10
11	9	-1.29	13.25
	10	-0.08	-5.81
	11	1.29	16.74
15	6	-0.83	-7.96
	7	-0.08	-7.63
	8	0.83	-5.81
19	1	-1.79	-10.60
	2	-0.94	-10.92
	3	-0.08	-4.75
	4	0.94	2.73
	5	1.79	4.88

Table 3.5. Fuel Element 19 Fission Wires – Calculated and Adjusted Powers Relative to Measured Powers

Channel	Wire Number	<i>A Priori</i> /Measured	Adjusted/Measured
2	15	0.993	0.994
	16	0.956	0.991
	17	0.945	0.988
6	12	1.044	1.008
	13	1.056	1.010
	14	1.066	1.012
11	9	0.849	0.961
	10	1.076	1.013
	11	0.813	0.949
15	6	1.106	1.018
	7	1.101	1.017
	8	1.076	1.013
19	1	1.144	1.023
	2	1.149	1.024
	3	1.062	1.011
	4	0.967	0.993
	5	0.941	0.987

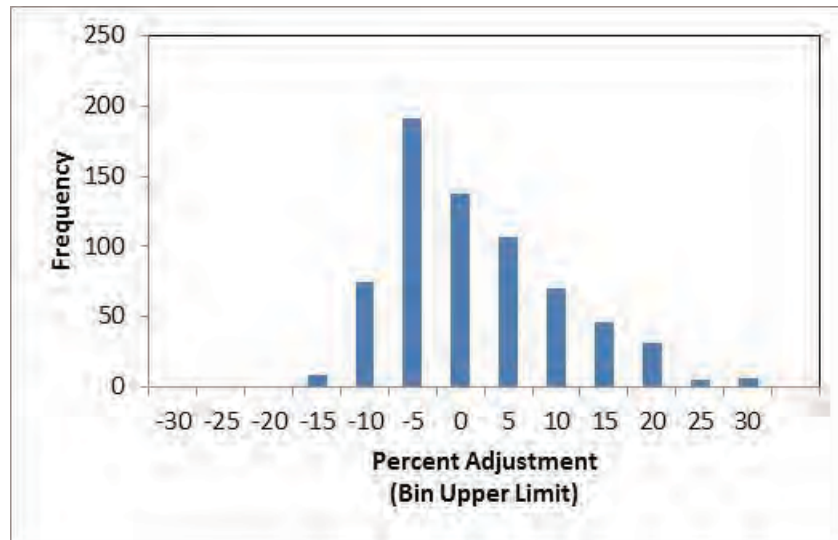


Figure 3.25. Histogram showing the distribution of percentage adjustments of the scaled *a priori* calculated fission wire powers for all 40 fuel elements combined (total of 680 fission wires).

3.3 Axial Power Distribution Analysis of ATRC NW-160 and SE-192 Experiments

Measurements have been made on many occasions in the ATRC to determine the axial fission profile shape. The axial shape has been assumed to be a chopped cosine shape and is maintained as recommended by the safety basis to ensure the assumptions of the thermal-hydraulic analysis for ATR are maintained as well as for maintaining the assumption of burn-up on fuel elements while using 2D codes. Two sets of measurements are evaluated here for the NW-160 Experiment (Clark, 2011) and SE-192 Experiment (Clark, 2012), both conducted in earlier years, separately from the Methods Update Project. This section provides a description of the methods used to measure the axial profile in an ATRC fuel element, a description of the ATRC model for each of the experiments and a comparison of the calculated results compared to the measured values.

3.3.1 NW-160 Experiment

An MCNP diagram of the NW LIPT mockup in ATRC is shown in Figure 3.26. The ATRC mockup has a configuration very similar to the actual experiment. The ATRC NW configuration consisted of a dual sample holder that allowed for installation of 2 test trains. The NW flux trap in ATR and ATRC is similar to other in-pile tubes in the ATR and ATRC except for the large size and lack of a flow tube. The insulation tube has an outer diameter (OD) and an inner radius (ID) of 4.932 in. and 4.602 in., respectively. Inside of the insulation tube is the pressure tube with an OD and ID of 4.522 and 4.0 in., respectively. An outer shroud sits on the outside of the dual experiment holder. The shroud has an OD and ID of 3.87 in. and 3.77 in., respectively. The shroud is constructed of 100% Zirconium alloy. The dual holder has an outer diameter of 3.751. The dual holder has 4 holes located in it, two for flux wire monitors (0.66 in. diameter) and two for experiment positions (1.74 in. diameter). Within the experiment positions, the experiments are placed in inner shrouds with an OD and an ID of 1.71 in. and 1.60 in.

The NW-160 experiment mockup, positioned in the NW LIPT was modeled using data provided in Tables 3.6 and 3.7. The composition of the shrouds can vary as well as the length. The intent of the shrouds is to vary the neutron spectrum in the samples as determined by the program objectives. Specimen holders are placed inside of the shroud. For modeling simplification, the mass of materials in each axial section is homogenized with the appropriate water volume fraction. This simplification will have a negligible effect on the results.

3.3.2 SE-192 Experiment

An MCNP diagram of the SE IPT mockup in ATRC is shown in Figure 3.27. The ATRC mockup once again has a configuration configuration similar to the actual experiment. The insulation tube has an outer diameter (OD) and an inner radius (ID) of 2.875 in. and 2.635 in., respectively. Inside of the insulation tube is the pressure tube with an OD and ID of 2.53 and 2.125 in., respectively. A flow tube is installed inside of the pressure tube. The flow tube has an OD and ID of 1.875 in. and 1.745 in., respectively. The experiment is placed inside of either a Zr, Hf, or mixture of Zr/Hf shroud similar to that of the inner shrouds in the NW-160 experiment. The composition of the shrouds can vary as well as the length. Specimen holders are placed inside of the shroud as in the case of the NW-160 experiment. The holder/shroud loading for the SE IPT is shown in Table 3.8. For modeling simplification, the mass of materials in each axial section is homogenized with the appropriate water volume fraction. This simplification will have a negligible effect on the results.

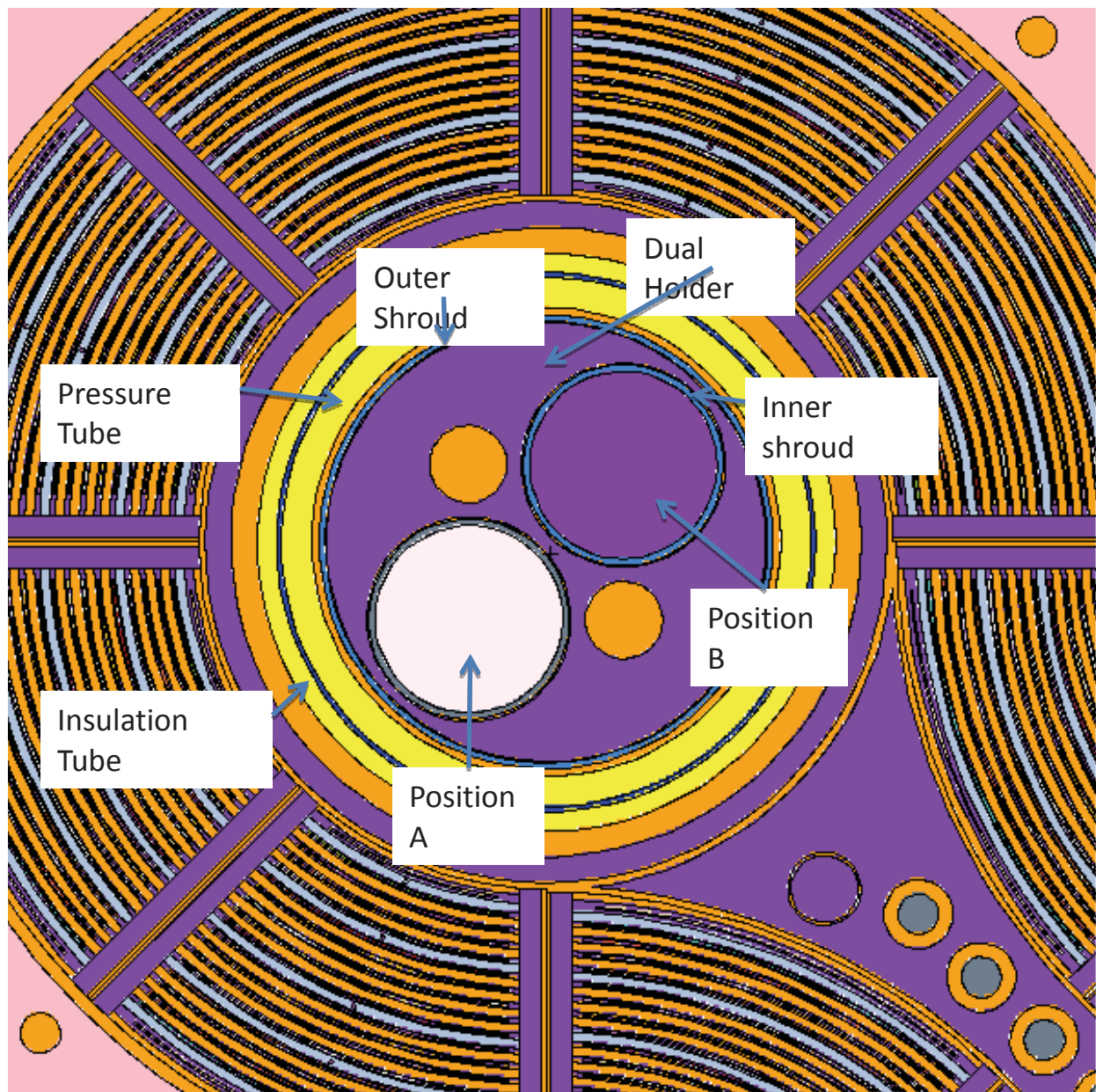


Figure 3.26. MCNP cross-section of the NW LIPT with dual holder.

Table 3.6 ATRC experiment loading for NW-160 Side A

ATRC Loading for 2E-NW-160 Side A								
Cycle 149A						Shrouds		
Component	ATRC Loading	Top Elevation	ATRC v/o H2O	ATRC Holder Loading grams	ATRC Loading (gram/in)	%HF	Length (in)	Top Elevation
9	0		100.00%			0	7	28.11
8	7" Standard Holder 4 - Red 2 - Blue 1 - Green 1 - Gold	19.52	26.38%	22.64 U235 - 3.26 Hf	3.23	100	7	19.91
7	0		100.00%			0	7	11.71
6	7" Standard Holder 7 - Gold	3.12	31.43%	0 U235 - 0 Hf	0	0	7	3.51
5	7" Standard Holder 1 - Red 7 - Gold	-5.08	27.15%	4.53 U235 - 0 Hf	0.65	70	7	-4.69
4	7" Standard Holder 3 - Red 5- Gold	-13.28	26.90%	13.59 U235 - 0 Hf	1.94	70 40 40	1.75 3.50 1.75	-12.89 -14.64 -18.14
3	0		100.00%					
2	0		100.00%					

Table 3.7. ATRC experiment loading for NW-160 Side B.

ATRC Loading for 2E-NW-160 Side B								
Cycle 149A						Shrouds		
Component	ATRC Loading	Top Elevation	ATRC v/o H2O	ATRC Holder Loading grams	ATRC Loading (gram/in)	%HF	Length	Top Elevation
9	0		100.00%			0	7	28.11
8	7" Holder 1-Red 1-Blue 5-Gold	19.52	31.18%	6.79 U235	0.97	40.00	7.00	19.91
7	0		100.00%			0	7	11.71
6	7" Holder 7-Gold	3.12	31.43%	0.0 U235 - 0.0 Hf	0.00	100.00	7.00	3.51
5	7" Holder 4-Red 1-Blue 1-Green 2-Gold	-5.08	26.52%	20.38 U235 - 3.26 Hf	2.90	100.00	7.00	-4.69
4	7" Holder 3-Red 1-Blue 1-Green 3-Gold	-13.28	26.65%	15.85 U235 - 3.26 Hf	2.26	100.00	7.00	-12.89
3	0		100.00%					
2	0		100.00%					

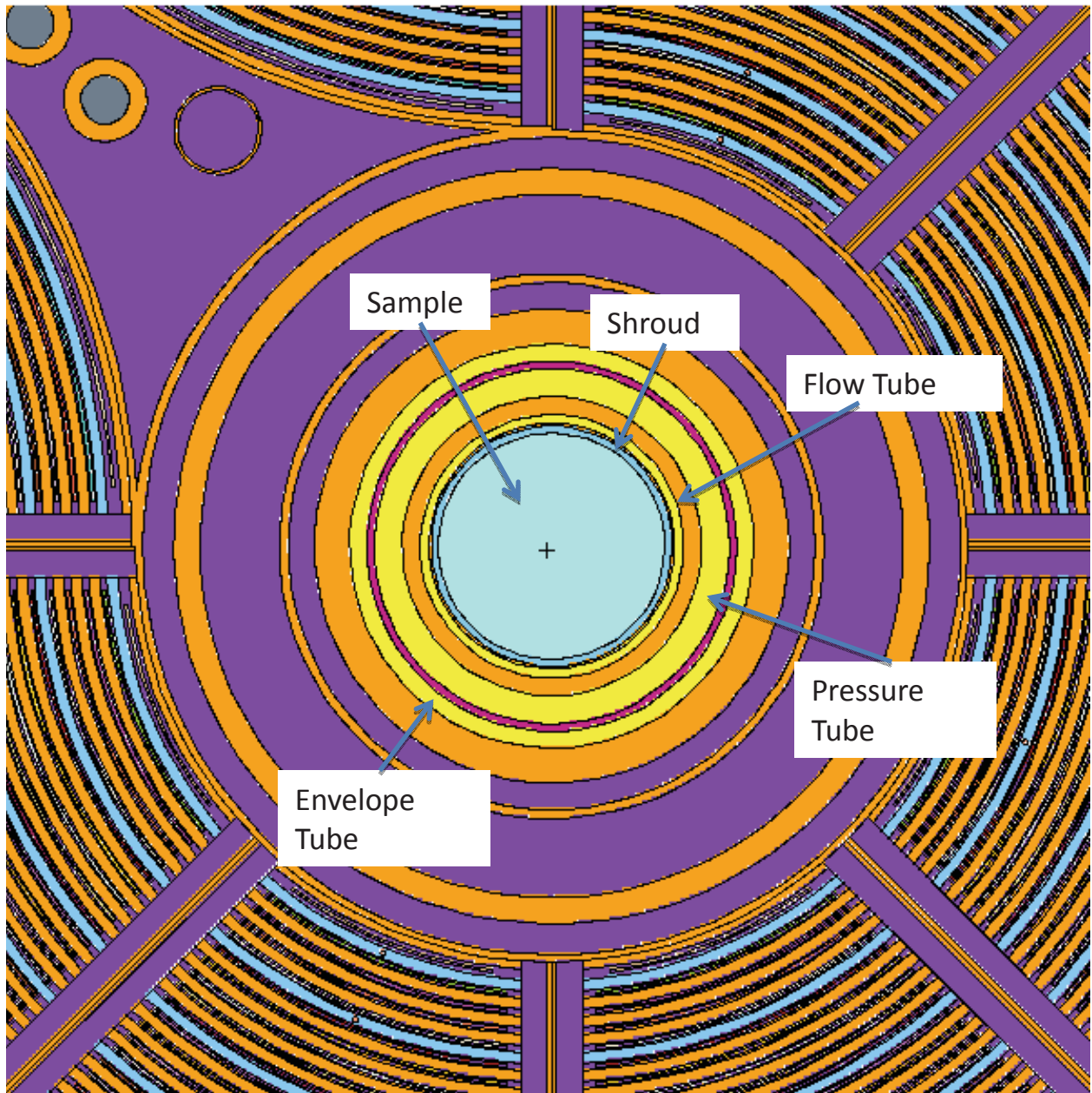


Figure 3.27. MCNP cross-section of the SE IPT.

Table 3.8 ATRC experiment loading for SE-192 mockup experiment.

ATRC Loading for 2B-SE-192									
Cycle 152B									
ATRC Component Number	ATRC Component Type	ATRC Loading*	ATRC Holder Top Elevation	ATRC w/o H ₂ O	ATRC Loading grams			ATRC Loading (grams/in)	
					U235	Hf	Other	U235	Hf
18	7 inch Standard Holder	2 - Red (4.53g U235) 6 - Gold (Dummy Al)	27.55	27.02	9.06	0		1.51	
17	7 inch Standard Holder	1 - Blue (2.26g U235) 6 - Gold (Dummy Al)	20.55	31.31	2.26	0		0.36	
16	ATRC 3.50 AL SIPT Spacer (Anodized Gold Color)	N/A	13.55	40.10					
15	1.75 AL ATRC SIPT Spacer (Anodized Gold Color)	N/A	10.05	43.50					
14	1.00 AL ATRC SIPT Spacer (Anodized Gold Color)	N/A	8.3	46.20					
13	7 inch Standard Holder	1 - Gold (Dummy Al) 2 - 0.11" Inconel (73g)	7.3	46.91	0	0	146g Inconel	0	
12	7 inch Standard Holder	1 - Gold (Dummy Al) 2 - 0.11" Inconel (73g)	0.3	46.91	0	0	146g Inconel	0	
11	1.75 AL ATRC SIPT Spacer (Anodized Gold Color)	N/A	-6.7	43.50					
10	ATRC 3.50 AL SIPT Spacer (Anodized Gold Color)	N/A	-8.45	40.10					
9	7 inch Standard Holder	1 - Red (4.53g U235) 1 - Blue (2.26g U235) 6 - Gold (Dummy Al)	-11.95	27.02	6.79	0		1.13	
8	7 inch Standard Holder	1 - Red (4.53g U235) 6 - Gold (Dummy Al)	-18.95	31.31	4.53	0		0.76	
7	Not Mocked Up		-25.95						

*The gram quantities listed are for each specimen.

ATRC Loading	Top Elevation
6.50" of Zr shrouds	27.55
7.00" of 100% Hf shrouds	21.05
25.50" of Zr shrouds	14.05
1.75" of 100% Hf shrouds	-11.45
5.25" of 70% Hf shrouds	-13.20
1.75" of 10% Hf shrouds	-18.45
8.00" of Zr shrouds	-20.20
Not Mocked Up	-25.95

3.3.3 Fission Wire Measurements

Measurements of the axial profile were performed using the same type of fission wires discussed in Section 3.1. The fission wires were placed in the azimuthal center of the fuel elements in Channels 2, 6, 11, 15, and 19. The wires were irradiated for 20 minutes at an approximate power of 600 W. The point to average fission rate ratios for each wire in each channel was calculated from the activation of those wires. The uncertainty of the measured values was taken as 5% (Durney and Kauffman, 1967), with 3% assumed to be random uncorrelated uncertainty and 2% fully-correlated uncertainty.

The wires are explicitly modeled in MCNP in each of the appropriate locations. The U-235 fission rates are determined using the F4 tally in MCNP with a U-235 fission cross-section multiplier. The MCNP results are then reported as fissions/source-particle, where source-particles in MCNP can be determined from reactor operating power. In the case of the fission wires, the operating power is not considered, as we are only interested in the axial point to average value of the wires for each channel in each fuel element, not necessarily absolute fission rate in a wire. If the absolute were taken into account, the uncertainty in the ATRC total core power/lobe power would add additional uncertainty into the models.

3.3.4 Results

The calculated point to average fission rates in the wire were determined from the MCNP model and compared to measured values for the NW-160 experiment and SE-192 experiment. In the case of the NW-160 experiment, the wires in element 33, 35, and 37 were modeled. The wires in element 13, 15, and 17 were modeled for the SE-192 experiment. The measured values for the NW-160 experiment are documented by Holtz (2012). The measured values for the SE-192 experiment are documented by Morrison (2012).

The comparison between the analytical models and the measured data is accomplished via a least-squares fit to the data as described in Section 3.1. A MATLAB program was written to manage the data. The program was compared to results in an EXCEL spreadsheet to verify that identical values are obtained. The MATLAB program allows for much larger sets of data to be processed (e.g., 15 different axial profiles in one experiment), while EXCEL is adequate for a single set of axial set of data. The covariance matrix was developed assuming an uncertainty of 5% (3% random uncorrelated uncertainty and 2% correlated uncertainty) for the measurements as noted above. The analytical uncertainty was assumed to be 5% random uncertainty in the MCNP calculation. This corresponds to the average uncertainty in the MCNP tally results. The normalization uncertainty, which adds an additional component of fully-correlated uncertainty to the computations, is assumed to be approximately 2%.

Some typical results are shown in Figure 3.28 for the NW-160 experiment and in Figure 3.29 for the SE-192 experiment. In the case of NW-160 the adjustments to the *a priori* relative wire fission rates ranged from -11% to +23%, with the larger adjustments near the upper and lower ends, which can be largely attributed to lack of detail in the computational model in these regions. The adjustments near the center of the core, ± 12 inches from the axial midplane were typically less than $\pm 10\%$, and 68% of all adjustments for all wires in all instrumented channels of the three NW lobe fuel elements of interest fell within $\pm 4.5\%$. The reduced uncertainties for the adjusted wire powers were in the range of 3%. Similar results were seen for the SE-192 experiment. The adjustments ranged approximately from -20% to +10%, with the adjustments closest to the axial core center line once again less than $\pm 10\%$, with 68% of all adjustments for all wires in the SE lobe falling within $\pm 4\%$ in this case.

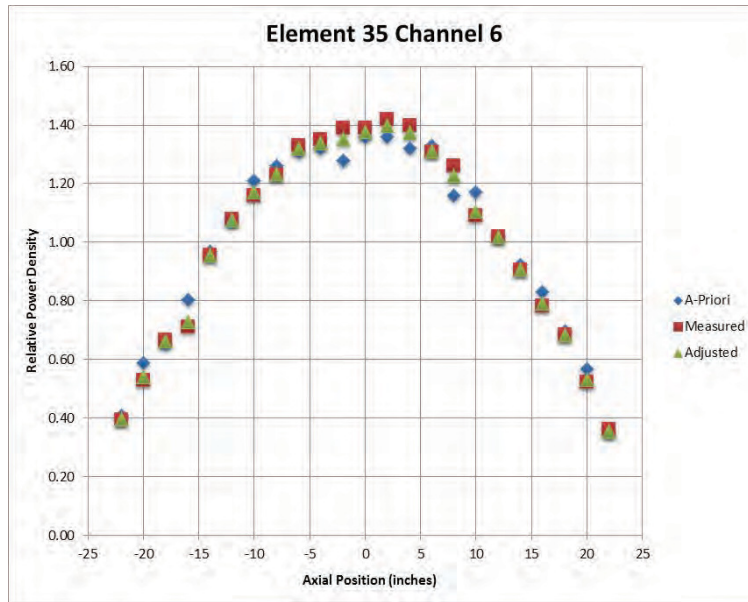


Figure 3.28. Typical relative axial fission wire power data for the NW-160 experiment in the ATRC

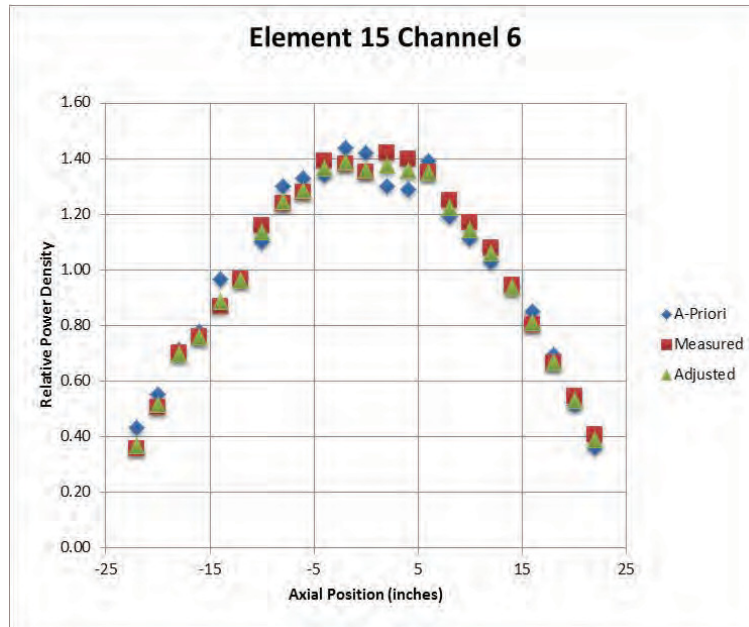


Figure 3.28. Typical relative axial fission wire power data for the SE-192 experiment in the ATRC.

3.4 References

- ASTM (American Society for Testing and Materials), "Standard Guide for Application of Neutron Spectrum Adjustment Methods in Reactor Surveillance", ASTM-E944-08 (2008).
- S. Carney, F. Brown, B. Kiedrowski, W. Martin, "Fission Matrix Capability for MCNP Monte Carlo", *Trans. Am. Nuc. Soc.*, **107**:494-497 (2012).
- L.L. Carter, N.J. McCormick, "Source Convergence in Monte Carlo Calculations", *Nuclear Science and Engineering*, **36**:438-441 (1969).
- J. A. Clark, letter to D. J. Schoonen, "ATRC Mockup Loop Loading Information for 2E-NW-160, ATR Cycle 149A", Internal INL Communication, February 9, 2011.
- J. A. Clark, letter to D. J. Schoonen, "ATR Loop Loading Information and Detailed ATRC Loading Information for SB-SE-192 (SE-Std), Cycle 152B", Internal INL Communication, May 15, 2012.
- J. Dufek, W. Gudowski, "Fission Matrix Based Monte Carlo Criticality Calculations", *Annals of Nuclear Energy*, **36**:1270-1275 (2009).
- J.L. Durney, N.C. Kaufman, *Calculating Reactor Power from Activation Techniques as Applied to Unusual Fuel Geometry (ATRC)*, IN-1047, Idaho National Laboratory, (1967).
- M. R. Holtz, "Analysis of the Effects of the NW-160 Test on the ATRC Axial Flux Profile", INL Document Control, ECAR-1866, Revision 1. April 2012.
- T. Kitada, T. Takeda, "Effective Convergence of Fission Source Distribution in Monte Carlo Simulation", *J. Nuclear Science and Technology*, **38**:324-329 (2001).
- S.L. Meyer, *Data Analysis for Scientists and Engineers*, John Wiley and Sons, USA (1975).
- M. K. Morrison, "ATRC Flux Run 12-9 TP-4-12 Data Analysis for SE-192", INL Document Control, ECAR-2101, Revision 0, November 14, 2012.
- D.W. Nigg, J.W. Nielsen, B.M. Chase, R.K. Murray, K.A. Steuhm, T. Unruh, Improved Computational Neutronics Methods and Validation Protocols for the Advanced Test Reactor, Proceedings of the American Nuclear Society International Topical Meeting on Advances in Reactor Physics (PHYSOR-12), Knoxville, Tennessee, April 15-19, 2012 (2012a)
- D.W. Nigg, J.W. Nielsen, G.K. Taylor, Validation Protocols to Support the Neutronics Modeling, Simulation, and V&V Upgrade for the Advanced Test Reactor, *Trans. ANS*, **106**:890-893 (2012b)
- D.W. Nigg and K.A. Steuhm (Editors), Advanced Test Reactor Core Modeling Update Project Annual Report for Fiscal Year 2012, INL/EXT-12-27059. September 2012 (2012)
- M. Wenner, A. Haghighat, "A Fission Matrix Based Methodology for Achieving an Unbiased Solution for Eigenvalue Monte Carlo Simulations", *Progress in Nuclear Science and Technology*, **2**:886-892 (2011).
- J.G. Williams, "The Role of the Prior Covariance Matrix in Least-Squares Neutron Spectrum Adjustment", *Trans. ANS*, **106**:881-883 (2012).

4.0 VALIDATION EXPERIMENTS IN THE ATRC

David W. Nigg, Kevin A. Steuhm, Benjamin M. Chase, Troy Unruh, Larry D. Smith

As noted earlier, a total of six LEP-specific code and model validation experiments are envisioned as part of the ATR Modeling Upgrade Project, in addition to a 2012 ATRC supporting experiment for ATR Cycle 152B that was not explicitly associated with the LEP (ATRC Validation Experiment 12-5 as discussed in Chapter 3). Four of the six LEP-specific experiments were completed prior to 2012 and detailed statistical analyses of these four were presented previously (Nigg and Steuhm, 2012).

The fifth planned LEP-specific validation experiment was conducted in the ATRC during 2013. This experiment (referred to here as “Irradiation 5”) used the same NW LIPT hardware as was used for Irradiations 1-3, described previously (Nigg and Steuhm, 2012), with minor changes in specific loading of the NW LIPT hardware. In addition, detailed neutron spectrum measurements were made in the Southeast IPT during Irradiation 5 using new hardware inserts fabricated for this purpose during 2011.

4.1 Hardware Description – ATRC Irradiation 5

Figure 4.1 shows the loading of the NW LIPT foil positioning strips for Irradiation 5. In this case the foil packages consisted only of duplicate bare and cadmium-covered gold foils to provide a simple 2-group confirmation of the neutron spectrum in the NW LIPT that was measured during Irradiations 1-3. Au/Cu flux wires were also loaded positioning strips as before, but only on one side of each foil positioning strip. Each corresponding wire position on the other side of each positioning strip (see Figure 3.3 for detail) contained a uranium-aluminum flux wire, with 10% by weight ^{235}U . These latter wires were identical to the wires used for the core fuel element fission power distribution measurements described for the depressurized run support experiment. The foil positioning strips were then loaded into the NW LIPT insert in the same manner as for Irradiations 1 and 2, with solid dummy strips in the other 8 positions.

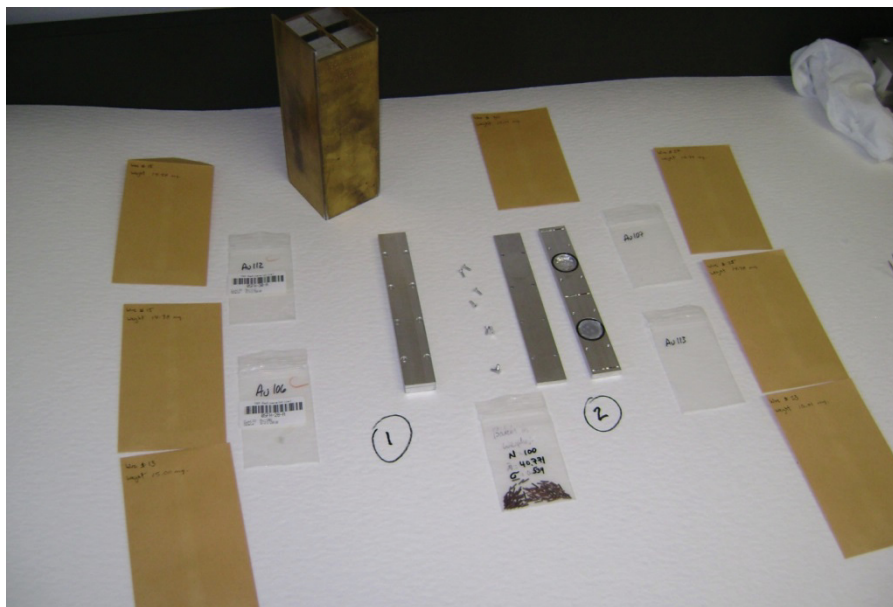


Figure 4.1. Northwest Large In-Pile Tube Fittings and Foil Positioning Strips for Irradiation 5.

Figure 4.2 shows the new SE IPT insert with a new solid aluminum fitting designed to hold a single foil positioning strip. This strip was loaded with a set of cadmium-covered indium, gold, tungsten, manganese, copper, titanium, nickel, zinc, iron and niobium foils in one foil position and a set of bare gold and manganese foils in the other foil position. In addition to obtaining detailed spectral data for the SE IPT this arrangement was also intended to test the ability of the threshold foils (In, Ti, Ni, Zn, Fe, Nb) to detect the high-energy part of the spectrum without the use of the boron sphere that was used in Irradiation 3 to suppress resonance interactions.

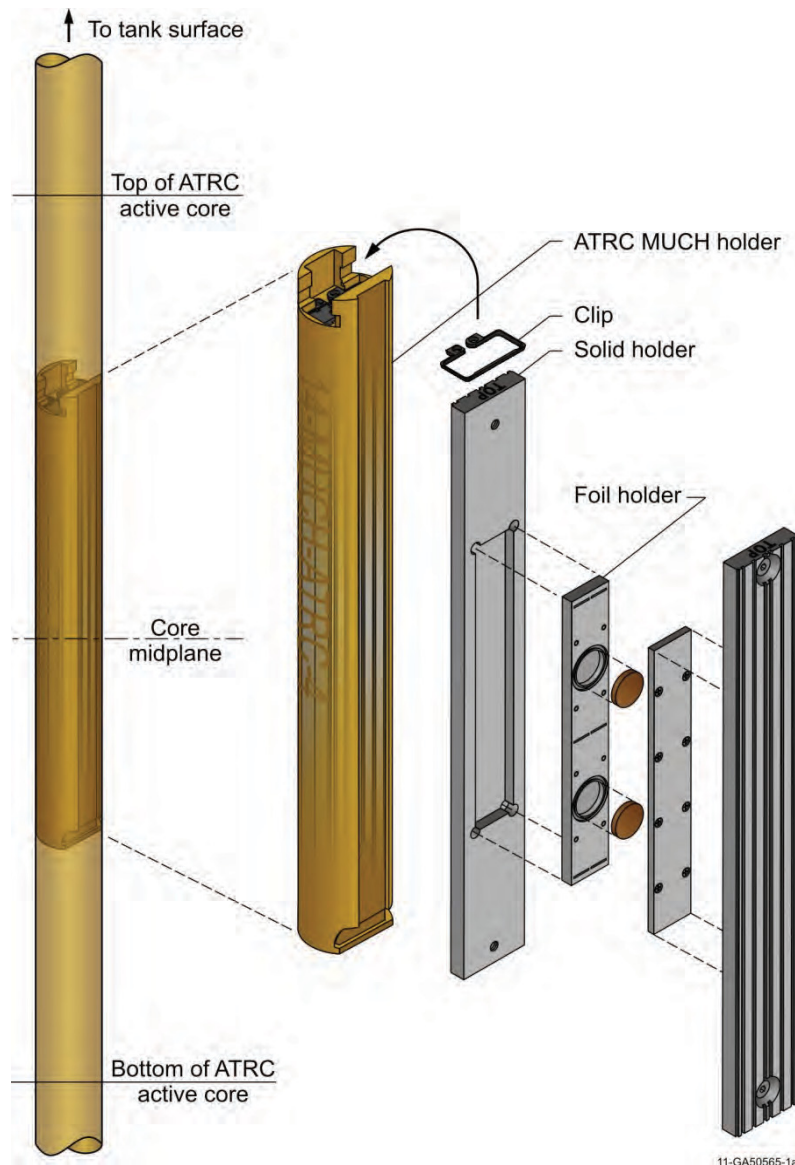


Figure 4.2. Southeast In-Pile Tube Insert Assembly (Low Water Fraction).

Figure 4.3 shows some additional detail of the foil positioning strip and the solid insert fitting for the SE IPT. Figure 4.4 shows a close up of the foil positioning strip, with the Au/Cu and the $^{235}\text{U}/\text{Al}$ wires in place at each of the three axial locations. Figure 4.5 shows the assembled insert fitting as it slides into the cylindrical SE IPT insert.



Figure 4.3. Foils, Foil Positioning Strip, and Insert Fitting for Southeast in-Pile Tube – Irradiation 5.

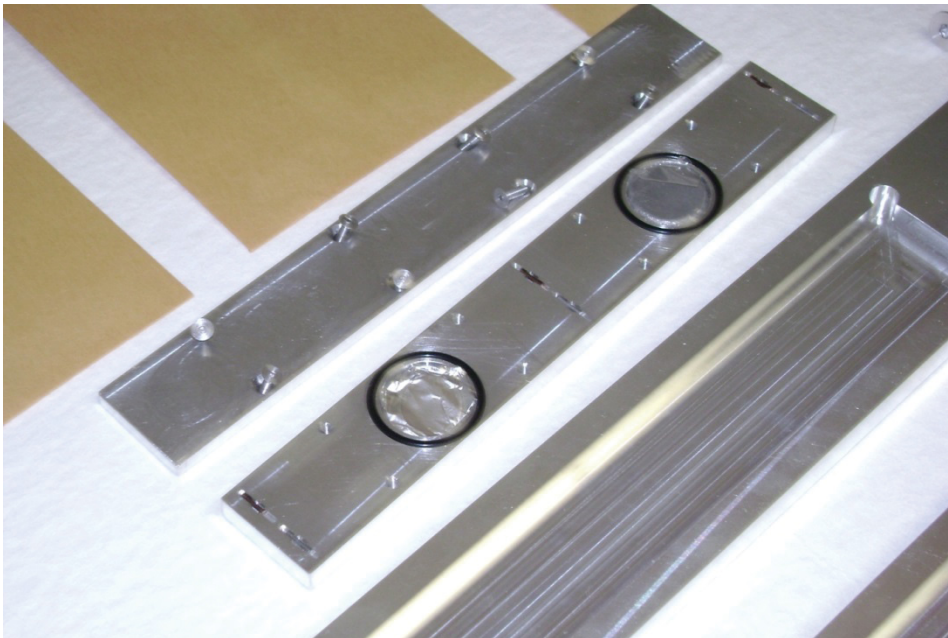


Figure 4.4. Detail of Foil and Flux Wire Positioning Strip for Southeast In-Pile Tube – Irradiation 5.

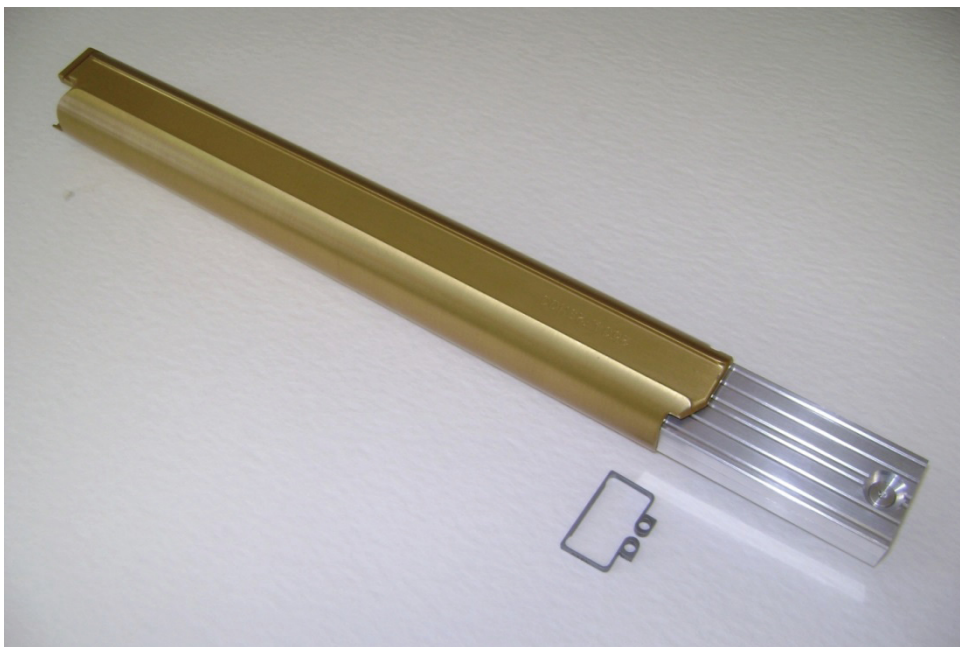


Figure 4.5. Assembled Hardware for Southeast In-Pile Tube – Irradiation 5

4.2 Preliminary Experimental Results – Irradiation 5

The Irradiation 5 experimental hardware for both the NW LIPT and the SE IPT was assembled in early Fiscal Year 2012 and Irradiation 5 was successfully conducted on August 13, 2013. The even-numbered core fuel elements were instrumented with three Au/Cu wires each, along the central rib, just as was done for Irradiation 4 (Nigg and Steuhm, 2012). As noted earlier, Irradiation 5 was intended to provide confirmatory spectral data for the NW LIPT as well as detailed spectral data for the SE IPT. In addition this experiment provided some experience with pairing of the Cu/Au wires with the $^{235}\text{U}/\text{Al}$ wires for the purpose of exploring techniques for statistically combining the ^{235}U fission rate with the Au and Cu capture rates to produce an estimate for the adjusted neutron flux spectrum at these positions that is statistically tied to the local fission rate. A complete statistical analysis of the results of Irradiation 5 will be presented in the FY-2014 ATR Methods Update Annual Report. Some initial results for the basic measured activation responses of primary interest are summarized below.

Table 4.1 shows the foil interactions that are of particular interest for ATR spectrometry purposes. Table 4.2 shows the preliminary measured results for the foil interaction rates in the southeast IPT. The measured rates for the Northwest LIPT (Nigg and Steuhm, 2012) are also shown for comparison. It should be noted that the southeast lobe of the ATRC typically operates at a power level that is about 35% higher than that of the northwest lobe hence there is a constant factor that reflects this included in the ratios provided in Table 4.2. Taking this into account it can be seen that the spectrum in the southeast lobe still appears to be somewhat harder than that in the northwest lobe. This is not unexpected, and will be analyzed in detail during the upcoming year.

Table 4.1. Activation interactions of interest for ATR model validation applications

Neutron Interaction	Nominal Mass and Composition of Standard Foil	Half-life of Product of Interest	Energy Range of Primary Response	Activation Gamma Energy of Interest (keV)
$^{115}\text{In} (n, \gamma) ^{116}\text{In}$	25 mg, 100% In	54 Minutes	1 eV Resonance	1293,1097, 416
$^{197}\text{Au} (n, \gamma) ^{198}\text{Au}$	60 mg, 100% Au	2.694 Days	Thermal & 5 eV Resonance	412
$^{186}\text{W}(n, \gamma) ^{187}\text{W}$	60 mg, 100% W	23.9 Hours	18 eV Resonance	686
$^{55}\text{Mn}(n, \gamma) ^{56}\text{Mn}$	50 mg, 80% Mn, 20% Cu	2.578 Hours	Thermal & 340 eV Resonance	847
$^{63}\text{Cu} (n, \gamma) ^{64}\text{Cu}$	140 mg, 100%Cu	12.7 Hours	Thermal & 1 keV Resonance	511 (Positron)
$^{115}\text{In} (n, n') ^{115\text{m}}\text{In}$	25 mg, 100% In	4.49 Hours	0.5 MeV Threshold	336.3
$^{47}\text{Ti} (n, p) ^{47}\text{Sc}$ $^{46}\text{Ti} (n, p) ^{46}\text{Sc}$ $^{48}\text{Ti} (n, p) ^{48}\text{Sc}$	157 mg, 100% Ti	3.349 Days 83.81 Days 43.7 Hours	1.0 MeV Threshold 3.5 MeV Threshold 5.5 MeV Threshold	159.4 1121,889 984,1312,1038
$^{58}\text{Ni} (n, p) ^{58}\text{Co}$	286 mg, 100% Ni	70.88 Days	1.2 MeV Threshold	811
$^{64}\text{Zn} (n, p) ^{64}\text{Cu}$	117 mg, 100% Zn	12.7 Hours	1.5 MeV Threshold	511 (Positron)
$^{54}\text{Fe} (n, p) ^{54}\text{Mn}$ $^{56}\text{Fe} (n, p) ^{56}\text{Mn}$	132 mg, 100% Fe	312.2 Days 2.578 Hours	1.5 MeV Threshold 5.0 MeV Threshold	834.8 847
$^{93}\text{Nb} (n, 2n) ^{92\text{m}}\text{Nb}$	270 mg, 100%Nb	10.13 Days	6.0 MeV Threshold	935

Table 4.2. Measured saturation activities for the foils irradiated in the southeast in-pile tube, Irradiation 5 and in the northwest large in-pile tube, Irradiations 1 and 3.

Interaction	SigPhi (Southeast)	$\pm 1\sigma$ (%)	Spectral Index (SE)	SigPhi (Northwest)	Spectral Index (NW)	Rate Ratio SE/NW
$^{93}\text{Nb} (n, 2n)$	3.66E-19	17.79	2.06E-06	2.64E-19	2.44E-06	1.39
$^{54}\text{Fe} (n,p)$	1.04E-16	14.65	5.86E-04	4.10E-17	3.80E-04	2.54
$^{56}\text{Fe} (n,p)$	8.58E-19	7.31	4.82E-06	5.12E-19	4.74E-06	1.68
$^{64}\text{Zn} (n,p)$	3.59E-17	2.52	2.02E-04	2.05E-17	1.90E-04	1.75
$^{58}\text{Ni} (n,p)$	9.66E-17	2.51	5.43E-04	5.72E-17	5.30E-04	1.69
$^{47}\text{Ti} (n,p)$	1.86E-17	2.52	1.04E-04	1.17E-17	1.08E-04	1.59
$^{46}\text{Ti} (n,p)$	1.06E-17	42.61	5.95E-05	5.00E-18	4.63E-05	2.12
$^{48}\text{Ti} (n,p)$	2.52E-19	7.15	1.42E-06	1.35E-19	1.25E-06	1.87
$^{115}\text{In} (n,n')$	2.38E-16	2.05	1.34E-03	1.24E-16	1.15E-03	1.92
$^{55}\text{Mn}(n, \gamma)$	1.81E-15	2.29	1.02E-02	9.81E-16	9.08E-03	1.84
$^{186}\text{W}(n, \gamma)$	5.33E-14	2.11	2.99E-01	2.83E-14	2.62E-01	1.89
$^{197}\text{Au} (n, \gamma)$	9.18E-14	2.29	5.16E-01	5.00E-14	4.63E-01	1.84
$^{115}\text{In} (n, \gamma)$	1.44E-13	2.02	8.11E-01	8.30E-14	7.69E-01	1.74
$^{55}\text{Mn}(n, \gamma)$	1.30E-14*	2.03	7.28E-02	8.50E-15*	7.87E-02	1.52
$^{197}\text{Au} (n, \gamma)$	1.78E-13*	2.36	1.00E+00	1.08E-13*	1.00E+00	1.65

* Bare foils, unshielded by cadmium.

Table 4.3 shows some preliminary measured activation rates for the Au/Cu flux wires rates and the corresponding spectral indices that were measured for both southeast IPT and the NW LIPT. The “spectral index” is simply the ratio of gold saturation activity to copper saturation activity for a given wire and it provides a simple indication of the relative “hardness” of the neutron spectrum to which the wire has been exposed. This is based on the fact that copper is relatively more sensitive to thermal neutrons compared to gold, which is roughly equally-sensitive to thermal and above-thermal neutrons. In the case of a fully-thermalized neutron field, the spectral index will asymptotically approach the ratio of the Au and Cu cross sections at 2200 m/s, assuming no spatial self-shielding. This asymptotic ratio is approximately 22.1 (i.e. 98.74 barns divided by 4.47 barns). Any physically-realistic departure from the described asymptotic spectral conditions will cause the ratio to increase, primarily due to increased resonance capture in gold. It can be seen that the spectral indices for the southeast IPT are somewhat larger than for the northwest LIPT, consistent with the results obtained with the foil packages discussed earlier.

Finally, Figure 4.6 shows the preliminary measured copper and gold saturation activities for the flux wires in the core fuel as functions of the fuel element number around the core (see Figure 3.2 for element numbering scheme). Data are presented for all three flow channels where the Au/Cu wires were located. Figure 4.7 shows the corresponding spectral indices. Consistent with earlier experiments, it can be seen that the neutron spectrum is significantly harder near the middle of the fuel elements, largely due to the under moderated nature of the ATRC core. Furthermore there is a clear geometric structure to the spectral index curve for the outer fuel plates. Once again, the core spectral index data will be fully analyzed relative to corresponding calculational model results during the first part of FY-2014.

Table 4.3. Measured saturation activities for the Au/Cu wires irradiated in the southeast and northwest in-pile tubes, Irradiation 5.

Wire ID	SE Top	SE Top	SE Middle	SE Middle	SE Bottom	SE Bottom
Nuclide	Au	Cu	Au	Cu	Au	Cu
SigPhi	2.78E-13	4.00E-15	2.96E-13	4.30E-15	2.79E-13	4.25E-15
$\pm 1\sigma$ (%)	2.73	2.67	2.51	2.62	3.04	2.60
Spectral Index (Au/Cu)	69.54		68.99		65.61	
Wire ID	NW Top 1	NW Top 1	NW Middle 1	NW Middle 1	NW Bottom 1	NW Bottom 1
Nuclide	Au	Cu	Au	Cu	Au	Cu
SigPhi	1.90E-13	3.76E-15	1.75E-13	3.07E-15	2.01E-13	4.02E-15
$\pm 1\sigma$ (%)	2.62	2.72	2.84	2.70	2.54	2.59
Spectral Index (Au/Cu)	50.61		56.86		49.91	
Wire ID	NW Top 2	NW Top 2	NW Middle 2	NW Middle 2	NW Bottom 2	NW Bottom 2
Nuclide	Au	Cu	Au	Cu	Au	Cu
SigPhi	1.92E-13	3.86E-15	1.81E-13	3.18E-15	1.89E-13	3.89E-15
$\pm 1\sigma$ (%)	2.66	2.73	2.68	2.79	2.79	2.61
Spectral Index (Au/Cu)	49.69		57.03		48.59	

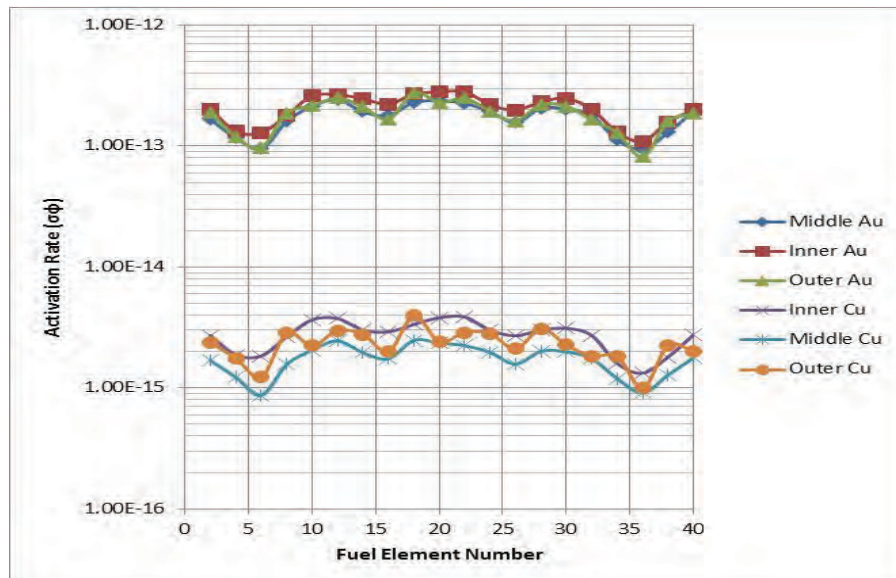


Figure 4.6. Core Au/Cu flux wire saturation activities for ATRC Validation Irradiation 5.

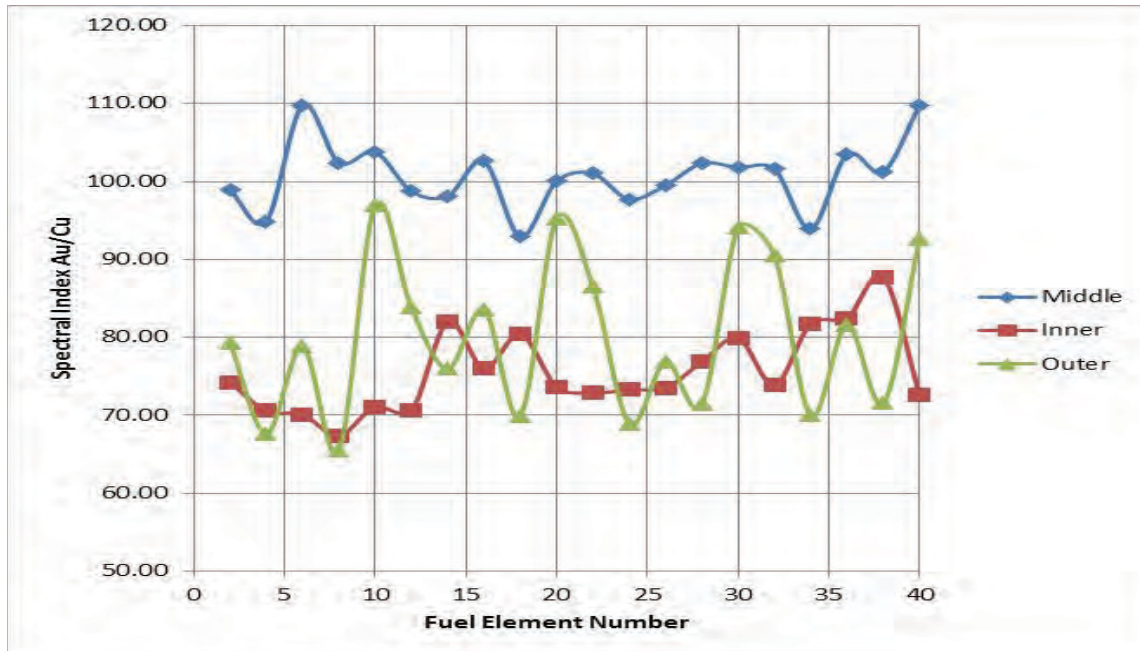


Figure 4.7. Core Au/Cu flux wire spectral indices for ATRC Validation Irradiation 5.

4.3 Future Plans – ATRC irradiation 6

Figure 4.8 shows a variation of the SE IPT hardware that has been fabricated for Irradiation 6, which is in planning for Fiscal Year 2014. In this case the insert fitting that holds the foil positioning strip will be a light aluminum framework with approximately 80% water in the same volume as the solid holder used for Irradiation 5. Allowing a large water fraction makes these flux trap positions more uniform in the axial dimension, with less axial streaming and attenuation of thermal neutrons than is the case for the solid insert fitting used in Irradiation 5. In the case of the NW LIPT insert, the same higher water fraction can be achieved by simply removing the 8 dummy strips visible in Figure 4.1. These modifications should make Irradiation 6 somewhat more suitable as a validation benchmark for the two-dimensional transport codes in the suite.

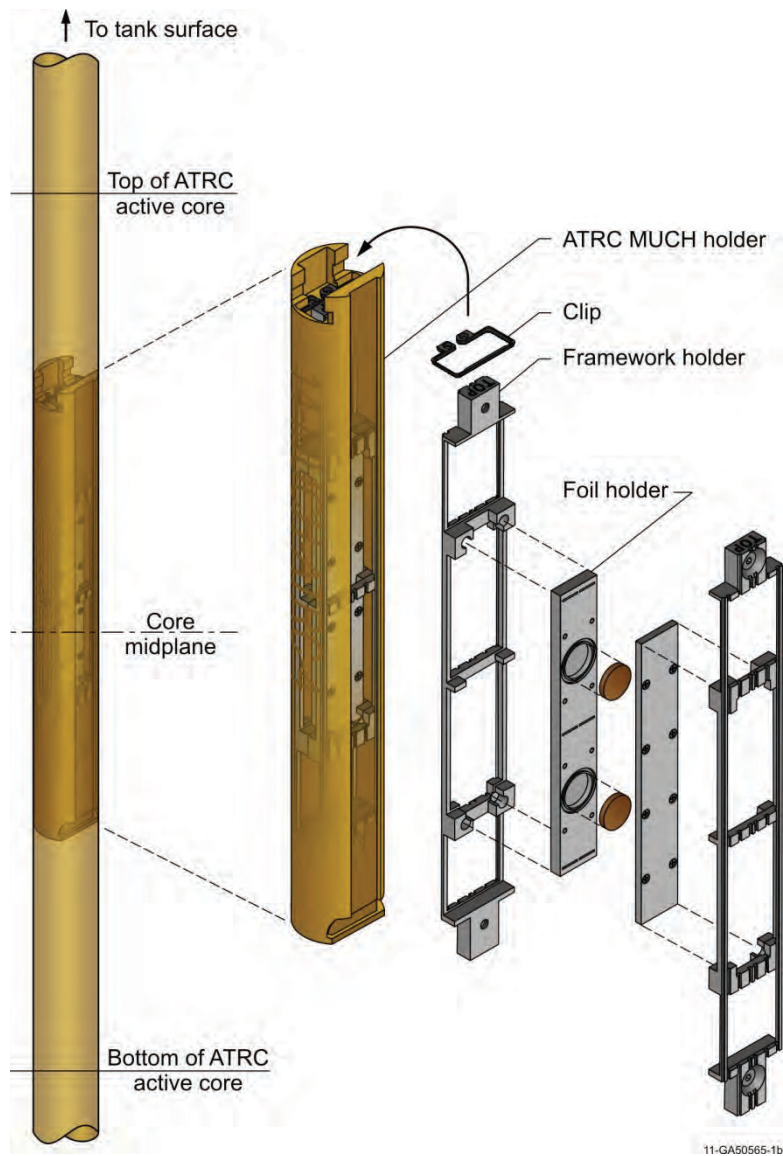


Figure 4.8. Southeast In-Pile Tube Insert Assembly (High Water Fraction).

4.4 References

D.W. Nigg and K.A. Steuhm (Editors), Advanced Test Reactor Core Modeling Update Project Annual Report for Fiscal Year 2012, INL/EXT-12-27059. September 2012 (2012)

5.0 LaBr₃ GAMMA SPECTRA DATA FOR ATR BURNUP VALIDATION

Jorge Navarro

5.1 Introduction

During the 2010 and 2011 fiscal years a feasibility study to determine if fuel isotopic data could be extracted using gamma spectrometers from the ATR canal was performed (Nigg et al., 2011 and Aryaeinejad et al., 2010). The feasibility study led to the recommendation that a fuel scanning system is a viable and necessary tool for the collection of validation fuel data as well as to aid canal fuel management operations. The final design of the ATR fuel permanent scanning apparatus requires a gamma detector capable of collecting high quality spectra needed for model validation and on-site burnup calibration predictions in a high background radiation environment. The study established a protocol to collect meaningful gamma spectral data and a method to predict fuel burnup and cooling time on-site for ATR fuel elements at the storage canal. Due to the in-situ nature of the measurements, and the variability and pace of canal operations it was necessary to design a system that can withstand the daily ATR working environment; that includes having a rugged compact gamma spectroscopy detector that is capable of providing high quality spectra without constant maintenance. The determination of which detector is better suited for the final fuel scanning permanent system cannot be made based solely on the quality of the spectra but the decision had also to take into account the fact that the detection system will be placed at the ATR canal.

The fuel scanning permanent system feasibility study used three different detectors (HPGe, HPXe and LaBr₃) for ATR canal in-situ measurements. The three detectors tested were capable of retrieving a meaningful signal at the ATR fuel canal; however the fuel burnup predictions and quality of the data varied from one detector to the other (Navarro et al., 2012). The preliminary results obtained showed as expected that the HPGe detector gives the best quality spectra from among the three detectors used in the study. However the need for HPGe detectors to be operated at cryogenic temperatures, their overall size, and fragility limit their range of applications and complicate their implementation for in-situ measurements of spent fuel elements at the ATR canal (Navarro et al., 2012). Also, HPGe detectors cannot be used in hostile environments such as in a high radiation field without adequate shielding. The HPXe detectors are excellent in-situ detectors however during the study it was determined that they could not be consider a primary option for the permanent fuel scanning system because of the quality of the spectra, high error calibration curves and the long counting time needed to obtain meaningful spectra; although they are still being considered as an alternative detector in the final design of the permanent system to measure fuels with very short cooling times (0-20 days). During the study it was also determined that because of their properties, prediction results and performance, the LaBr₃ scintillators should be explore as a possible primary alternative for the final design of the permanent system. The LaBr₃ detectors performed very well under harsh conditions and needed little maintenance making them ideal for the ATR canal operations. In addition the LaBr₃ scintillator gamma spectra obtained at the ATR canal were also used to predict ATR fuel burnup, however there was a higher error associated with the LaBr₃ burnup calibration curves when compared to calibration curves obtained using HPGe spectra (Navarro et al., 2012). Finally it was concluded that in order to improve the range and quality of the burnup predictions obtained with the LaBr₃ scintillator data, a deconvolution process had to be developed and tested. Deconvolution or enhancement methods are used in gamma spectrometry to improve the quality of spectra collected using lower resolution detectors. Deconvolution when applied properly improve the resolution of each individual photo-peaks and allow for a better identification of peaks in the spectra.

5.2 LaBr₃ 1"x1" Scintillator Energy Response Function Determination

The first step in developing a deconvolution technique for the permanent system was to determine the detector response function. Successful implementation of spectrum deconvolution process depends on accurately predicting the detector response as a function of incident gamma-ray energy. The detector response function can be obtained either experimentally or computationally, both methods are time consuming. The main drawback of the experimental technique is the need for numerous single peak energy sources and the time that it will take to obtain meaningful counts. The modeling path has three possible options for computing the response function: numerical interpolation, derivation of an empirical analytical function from available experimental response functions from and Monte Carlo simulations (Meng et al., 2000). For this study the Monte Carlo simulation route was chosen. This route is time consuming; however, it is the method that can provide better accuracy and control of the energy ranges. The simulation time can be reduced by using a computer cluster. The process to obtain the response function of the 1"x1" LaBr₃ consisted in:

- Designing an experiment.
- Performing measurements for several gamma radiation sources.
- Calculating the Gaussian Energy Broadening parameters needed in MCNPX.
- Simulating the experimental setup in MCNPX and validating the model with experimental data collected.

5.3 Experimental Measurements

The determination of the response function for the LaBr₃ detector began by setting up a simple geometry experiment, for this study the detector was placed on a stainless steel table (fig.5.1) and the source was placed 25 cm from the detectors aluminum entrance window.

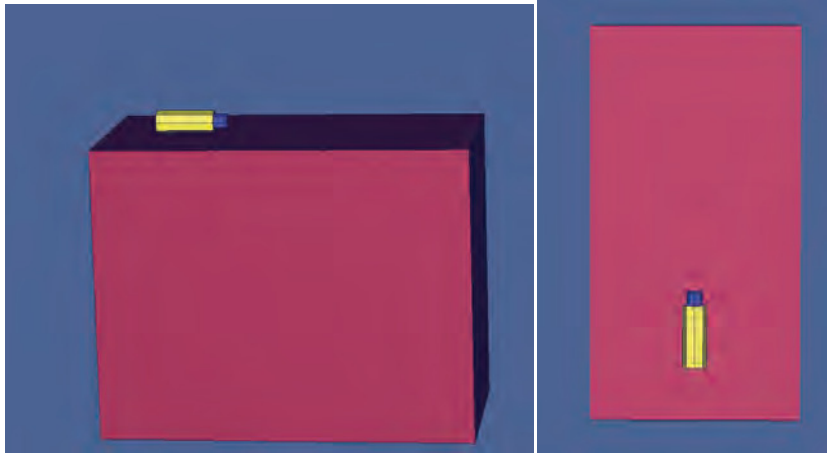


Figure 5.1 MCNPX Experimental Setup

The detector used for this study's experiments was a BrillanCe380 Saint-Gobain detector, which consists of a 1"x1" LaBr₃ scintillation crystal coupled to a photomultiplier tube. The photomultiplier and the scintillator crystal are contained in an outside aluminum sealed housing with an aluminum entrance window. Performing experimental measurements to collect data had two main purposes; to calculate the broadening parameters needed to give the MCNPX simulations Gaussian distribution energy peaks and to

validated the experiment simulation. The counting time of each experimental measurement was 68,400 seconds. Background measurements were taken in between single isotope calibration source measurements in order to obtain the net counts of each source. The radioactive sources used in this study are shown in table 5.1.

Table 5.1-Gamma Energy Sources used for GEB Parameters

Nuclide	Energy (KeV)	FWHM (keV)
Ba K_α X-ray	32.29	8.25
Eu¹⁵²	121.52	9.23
	244.8	12.88
	344.45	15.39
	778.98	24.8
	867.08	27.47
	964.01	26.96
	1408.01	39.17
Cs¹³⁷ (662 peak)	659.32	22.51

5.4 Monte Carlo Simulation

The geometrical model of the LaBr₃ detector for the experimental measurements was simulated as two concentric aluminum cylinders. The first cylinder represents the sealed photomultiplier chamber aluminum housing (44.5 cm radius-114 cm height). The second cylinder simulates the aluminum housing with an aluminum entrance window (30.4 cm radius-26.1 cm height) containing the LaBr₃ scintillator crystal (25.4 cm radius- 25.4 cm width). Accurately representing the geometry of the detector was just the first step in simulating a real system. In order to have a model that truly represents the interaction between detectors and particles measured, the pulse height simulation in MCNPX has to be given a more realistic Gaussian energy distribution. MCNPX contains a special tally option in which experimental data generated parameters can be input to the simulation in order to give the spectra the required Gaussian shape (X-5 Monte Carlo Team, 2003). The special tally within MCNPX is called the Gaussian Energy Broadening (GEB) option. The GEB tally gives the detector simulated data a Gaussian shape by using the unbroadened energy input and calculated spectral data along with user specified inputs to solve equation 1 (X-5 Monte Carlo Team, 2003).

$$f(E) = C e^{-\left(\frac{E-E_0}{A}\right)^2} \quad (5.1)$$

where E=Broadened energy, E₀=unbroadened energy of the tally, C= normalization constant and A=Gaussian width, defined by:

$$A = \frac{FWHM}{2\sqrt{\ln 2}} \quad (5.2)$$

In order to obtain the Gaussian width needed to solve equation 1, the full width at half maximum (FWHM) of real experimental data is indirectly provided by the user by specifying the three parameters (a,b and c) in equation 3 required by the GEB tally

$$FWHM = a + b\sqrt{E} + ce^2 \quad (5.3)$$

The GEB parameters for the detection system setup were obtained using the energy calibrated FWHM data acquired from experimental measurements of different gamma sources (table 5.1) and by performing a non-linear least square analysis using Matlab. Below are the GEB tally parameters calculated using the experimental measurements needed for MCNPX to give the model spectra Gaussian shape peaks:

$$a = 0.0068 \text{ MeV} \quad b = 0.0058 \text{ MeV}^{1/2} \quad c = 14.9501 \text{ MeV}^{-1}$$

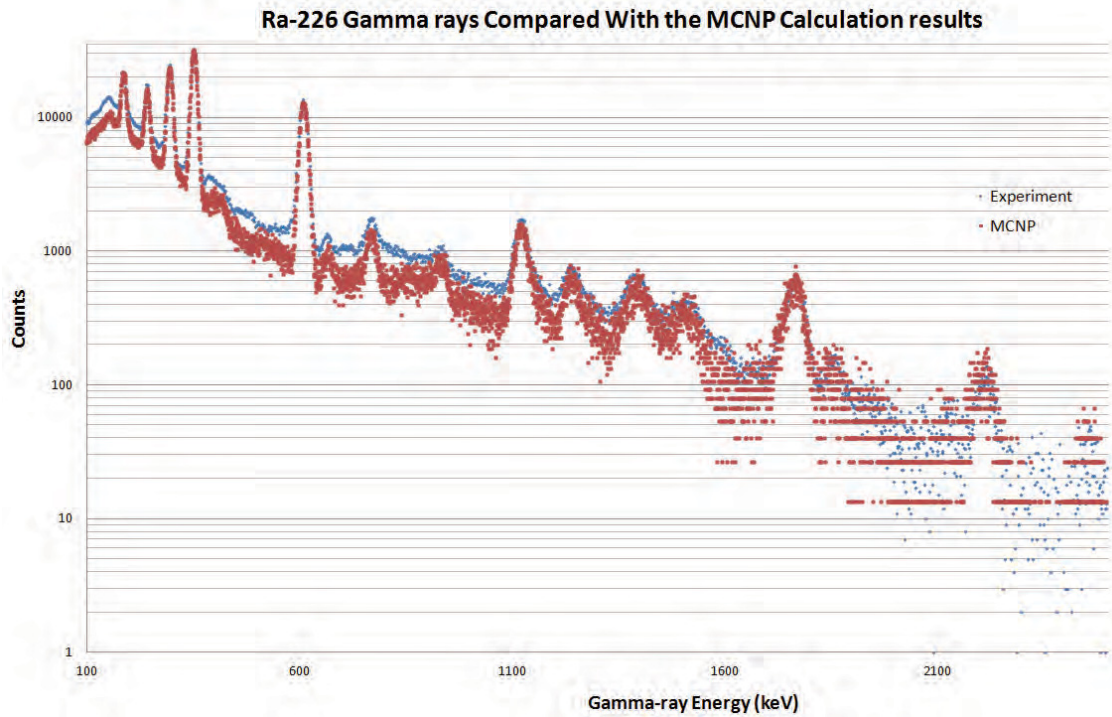


Figure 5.2 Ra-226 Experimental and Simulated MCNP Spectra

Once the simulated spectra had Gaussian pulse height distribution energy shaped peaks the next step was to corroborate that the simulation responses calculated had good agreement with the experimental gamma-ray sources measurements. The validation analysis consisted of comparing the simulated gamma-ray sources (Co^{60} , Cs^{137} and Ra^{226}) spectra against the experimental data collected to determine if there was a good agreement between the two. Figure 5.2 shows the simulation and experimental spectra of the multi-energy source Ra^{226} . Also the plot shows how adding the Gaussian energy broadening to the MCNPX pulse height broadening tally allows for a more accurate representation of the physics of the system. The plot shows that the MCNPX pulse height data peaks were broadened to match the experimental data. The plot also shows that there are some discrepancies in the areas below the peaks; however for this study because the protocol will only be applied to simulated data, the interest was only in obtaining GEB parameters that will give the simulation a realistic Gaussian peak shape not in an absolute match with the experimental data.

5.5 Response Function Calculation for Simulated Sources

After the GEB parameters were calculated using experimental measurements, the pulse height data distribution for various energy intervals for the 1"x1" LaBr₃ detector was calculated. The determination of the response function matrix based on experimental measurements was done by modeling 1301 mono-energetic point sources located at 25 cm from the detector tallying surface. The mono-energetic energy sources varied from 0 to 2.5 keV with a resolution of 0.5 keV. Each monoenergetic MCNPX simulation was done using 1×10^{10} particles. The calculations were performed using the Icestorm computer cluster at the Idaho National Laboratory; each MCNPX simulation was executed using 32 processors.

5.6 Spectra Deconvolution

Spectra deconvolution (or spectra enhancement) is a technique that has the objective of obtaining the most information out of a spectrum taken with a detector measurement system. The theory behind this technique is that especially in scintillation detectors the photon incident on the detector crystal may lose part of its energy by photoelectric absorption, Compton scattering or pair production (Monahan et al. 1967); however this information is still recorded in the spectra, it is just not observed in the appropriate energy region. The deconvolution technique improves the energy resolution of spectra by moving the counts from undesired regions to the appropriate photo-peaks (Monahan, et al., 1967).

Deconvolution is a powerful technique and when done correctly it enhances the resolution of spectra allowing for poor resolution detectors to perform tasks that otherwise would only be suitable for high resolution detectors. The unfolding process is also very time consuming and prone to errors. The deconvolution process is highly dependent on the accuracy of the response function. In addition the response function calculations are extremely geometry dependant so every time that a different configuration is introduced a new response function has to be recalculated.

The deconvolution of a gamma spectrum can be described in a general manner without reference to any particular experimental system (Monahan, et al., 1967). The problem can be posed using an equation (eq. 4.4) that describes the physical process of recording the pulse height data distribution by a detector as the convolution of the true gamma ray spectrum emitted by a source and the response function of the detector

$$M(E) = \int_0^\infty R(E, E_o)S(E) \quad (5.4)$$

where $M(E)$ is the measured spectrum, and $R(E, E_o)$ is the pulse height data distribution for various energy intervals (response function), and $S(E)$ is the incident spectrum (actual gamma ray spectrum emitted by a radioactive source).

5.7 LaBr₃ Spectra Deconvolution of Single Isotopic and Fuel Simulated Sources using the Maximum Likelihood Expectation Maximization Algorithm.

The integral representing (eq 4) the spectrum collection can be discretize and represented as a matrix in order to be solved numerically

$$M = RS \quad (5.5)$$
$$\begin{bmatrix} M_1 \\ \vdots \\ M_i \end{bmatrix} = \begin{bmatrix} R_{11} & \cdots & R_{1n} \\ \vdots & \cdots & \vdots \\ R_{i1} & \cdots & R_{in} \end{bmatrix} \begin{bmatrix} S_1 \\ \vdots \\ S_n \end{bmatrix} \quad (5.6)$$

Where M_i represents the true detector counts, R_i is the response function of the detector and S_i represents the discretized actual spectrum. Ideally equation (5.5) can be solved by a simple matrix inversion.

$$S = R^{-1}M \quad (5.7)$$

However the response function matrix for most nuclear applications is a sparse matrix. Specifically for the problem discussed in this paper it was quickly determined that the direct inverse matrix method (maximum likelihood method) was not appropriate for this study, because the response function is a lower triangular matrix (zeros in the top diagonal part of the matrix). The solution to eq. 3 can be found using least square fitting iterative algorithms such as GRV_FC33 and SAND-II (McElroy et al. 1967) as well as using the probabilistic maximum entropy method. For this study the Maximum Likelihood Fitting by Expectation Maximization (MLEM) was chosen, for the reason that it had previously shown success deconvoluting low resolution scintillator spectra (Meng et al. 2000).

The maximum likelihood fitting by expectation (MLEM) is an iterative algorithm (Shepp et al. 1982) designed to obtain the best estimate of the true measured spectrum (incident spectrum). The algorithm starts by creating an approximation of the system matrix which includes an estimate of the measured incident spectrum (x_i) for a particular set of set detector counts (y_i) (Shepp et al., 1982 and UC Berkeley class notes).

$$\begin{bmatrix} y_1 \\ \vdots \\ y_i \\ \vdots \\ y_n \end{bmatrix} = \begin{bmatrix} R_{i1} & \dots & R_{in} \\ \vdots & \ddots & \vdots \\ R_{i1} & \dots & R_{in} \end{bmatrix} \begin{bmatrix} x_1 \\ \vdots \\ x_n \end{bmatrix} \quad (5.8)$$

This can be expressed in summation form as

$$y_i = \sum_{n=1}^n R_{in}x_n \quad (5.9)$$

Assuming that the true detector counts M_i are also known, and knowing that they follow a Poisson distribution, it can be inferred that the probability of observing a value for M_i given an estimated mean value for y_i for one energy bin can be represented by:

$$p(M_i|y_i) = \frac{e^{-y_i} y_i^{M_i}}{M_i!} \quad (5.10)$$

In order to expand equation 4.10 to encompass all the true measured spectra counts (M_i) for a determine set of energy bins and the estimated of incident spectrum counts (x_i) a Poisson product distribution is calculated.

$$L(M|x) = \prod_{i=1}^i p(y_i|M_i) = \prod_{i=1}^i \frac{e^{-y_i} y_i^{M_i}}{M_i!} \quad (5.11)$$

Where $L(M|x)$ represents the likelihood probability that the true measured spectra counts (M_i) is equal to the detector counts (y_i). The MLEM algorithm goal is to maximize the likelihood function (eq. 4.10) in order to obtain the detector counts (y_i) that closely fits the measured spectra counts (M_i) by finding the “maximum-likelihood” estimate (x_i) of the actual gamma ray spectrum counts (S_i). To mathematically simplify the maximization of the likelihood function L the logarithm of the function is calculated instead.

$$\begin{aligned}\ln(L) &= \sum_{i=1}^i [-y_i + M_i \ln y_i - \ln(M_i!)] \\ &= \sum_{i=1}^i \left\{ -\sum_{n=1}^n R_{in} x_i + M_i \ln \left[\sum_{n=1}^n R_{in} x_i \right] - \ln[M_i!] \right\}\end{aligned}\quad (5.12)$$

Once the logarithm of the likelihood function is calculated the function can be maximize by taking the derivative of equation 4.12 with respect to the estimate of incident spectrum counts (x_i).

$$\frac{\partial \ln(L)}{\partial x_k} = \sum_{i=1}^i \left[\frac{\partial y_i}{\partial x_k} + \frac{M_i}{y_i} \frac{\partial y_i}{\partial x_k} \right] = 0 \quad (5.13)$$

From equation 9 is known that $y_i = \sum_{n=1}^n R_{in} x_n$, it can be derive that:

$$\frac{\partial y_i}{\partial x_k} = \frac{\partial y_i}{\partial x_k} \left[\sum_{n=1}^n R_{in} x_n \right] = R_{ik} \quad (5.14)$$

Substituting equation 4.14 into equation 13 yields

$$\sum_{i=1}^i \left[\frac{M(i)}{y_i} R_{ik} - R_{ik} \right] = 0 \quad (5.15)$$

In order to have everything in terms of (x_i) and R_{jm} substituting equation 9 into equation 15 gives

$$\sum_{i=1}^i R_{ik} = \sum_{i=1}^i \frac{M_i}{\sum_{B=1}^B R_{im} x_i} R_{ik} \quad (5.16)$$

This can be restated as:

$$\frac{1}{\sum_{d=1}^D R_{jm}} \sum_{i=1}^i \frac{M_i}{\sum_{n=1}^n R_{in} x_i} R_{ik} = 1 \quad (5.17)$$

In order to find the best estimate of the incident spectrum counts (x_i) while satisfying equation 4.11 this technique is applied. In this algorithm, it is assume that $x_k^{(n)}$ is the best estimate of the of the actual gamma ray spectrum counts (S_i).

$$x_k^{(n+1)} = x_k^{(n)} \left\{ \frac{1}{\sum_{i=1}^i R_{jk}} \sum_{i=1}^i \left[\frac{M_i}{\sum_{n=1}^n R_{in} x_i^{(n)}} R_{jk} \right] \right\} \quad (5.18)$$

The algorithm calculates a new value for $x_i^{(n+1)}$ in each iteration and it continues until a predetermine tolerance value is reached. The tolerance value is calculated using the mean squared difference between consecutive iterations

$$S = \sum_{i=1}^i \left(x_{i+1}^{(n)} - x_i^{(n)} \right)^2 \quad (5.19)$$

5.8 One Isotope Simulated Sources

The MLEM algorithm described above was implemented in MATLAB and was tested using simulated one isotope data created within MCNPX. The data was modeled based on the experimental setup discuss in the previous section; each isotopic source consisted of 1×10^{10} counts. The results for one peak source Cs^{137} , double peak source Co^{60} and multiple peaks source Ra^{226} are presented in figures 5.3, 5.4, and 5.5 respectively.

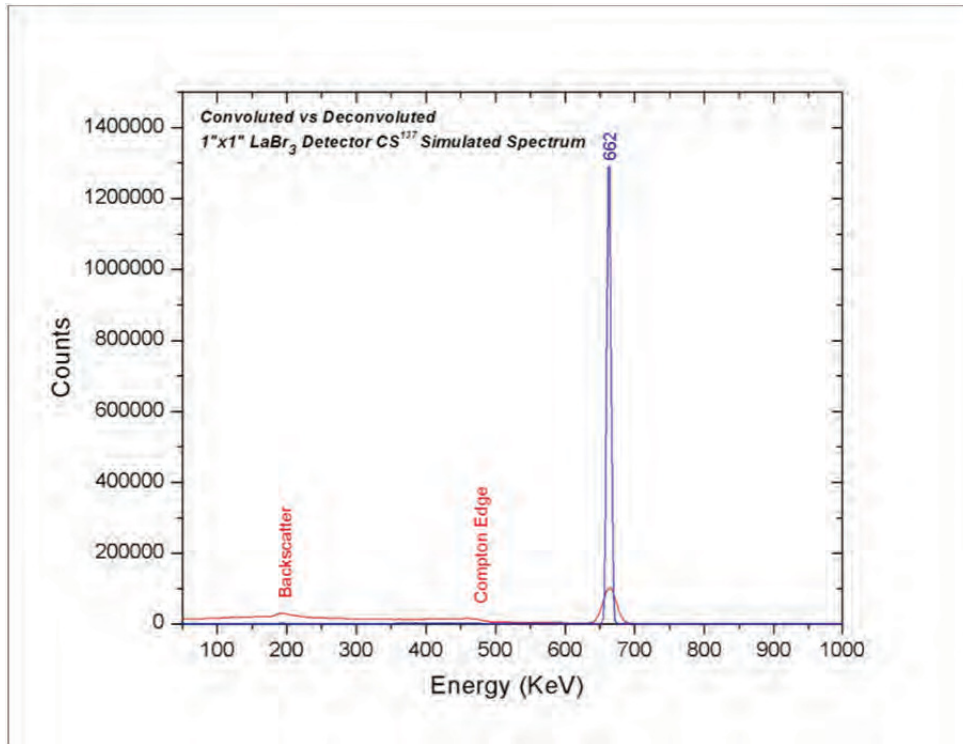


Figure 5.3 Simulated Convolved Spectrum of a Cs¹³⁷ Source

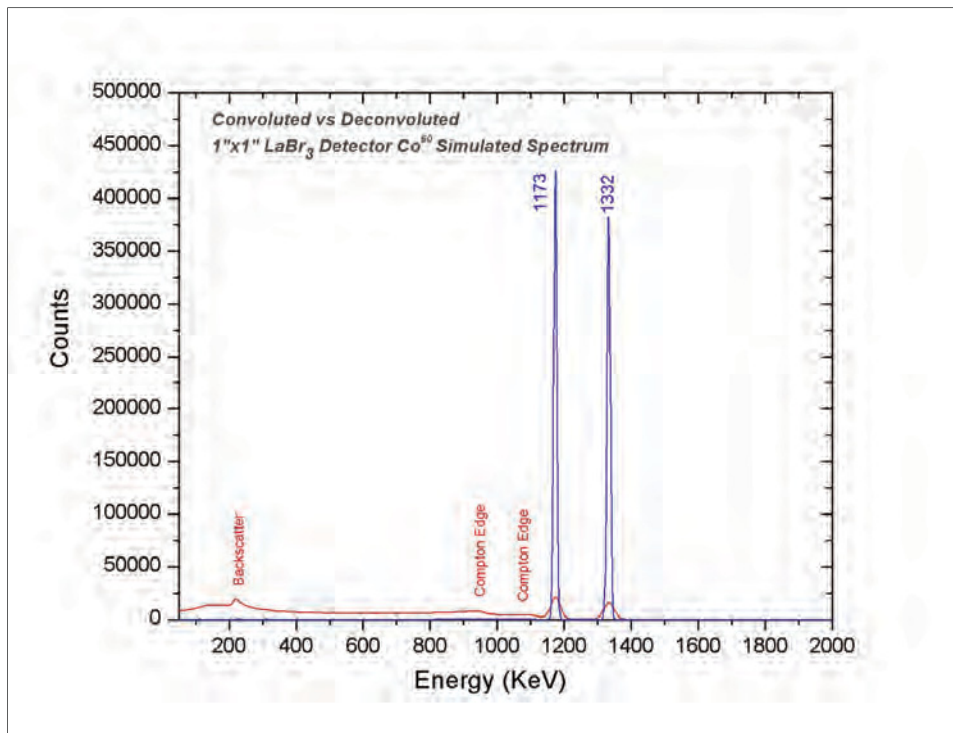


Figure 5.4 Simulated Convolved Spectrum of a Co⁶⁰ Source

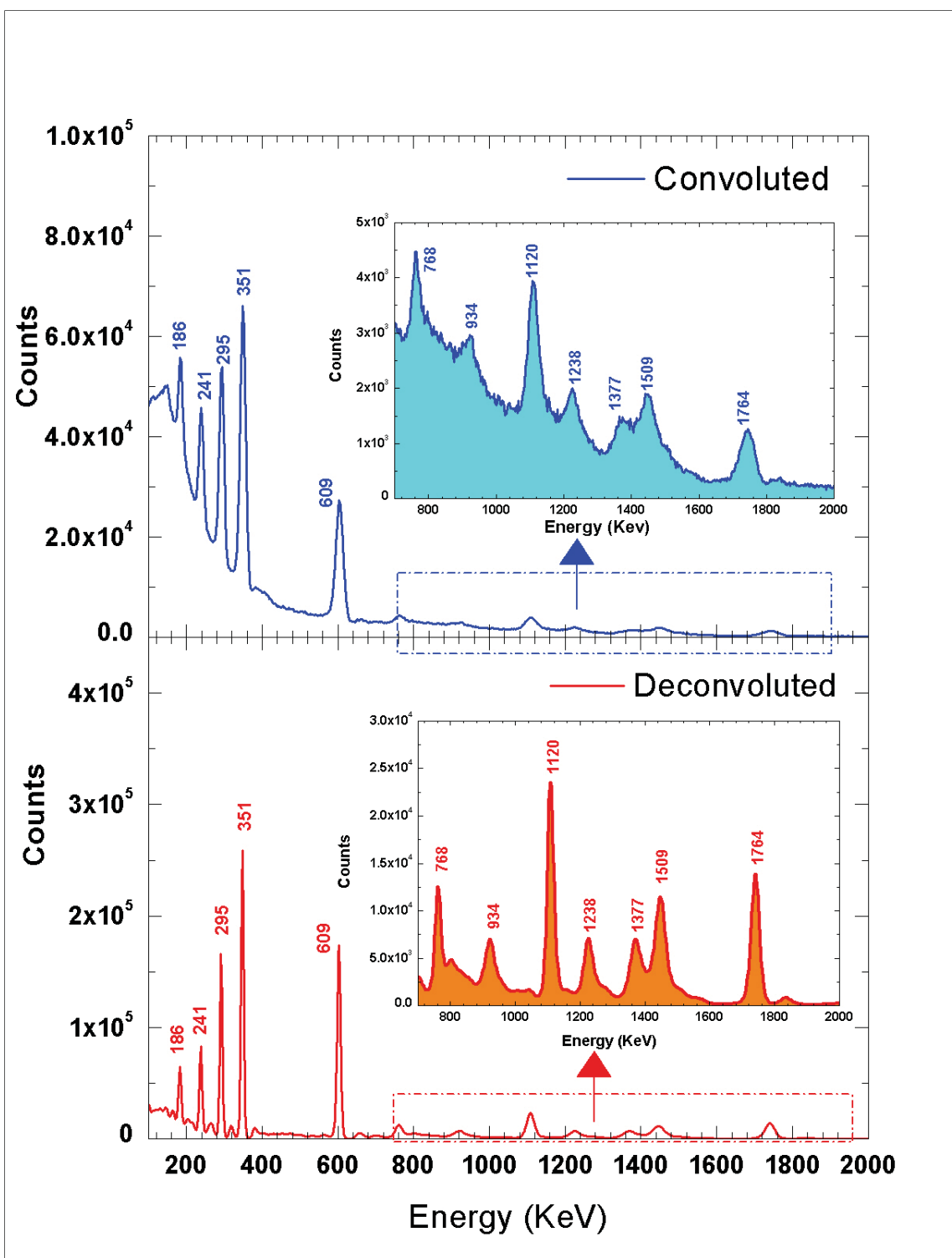


Figure 5.5 Simulated Spectrum of a Ra^{226} Source

It can be seen from the three isotopic sources (Cs^{137} , Co^{60} and Ra^{226}) MLEM spectra comparison plots that the Compton scattering region along with the backscatter peak counts were successfully move to the appropriate Gaussian shape photo-peaks. In order to further quantify the efficiency of the MLEM deconvolution, the performance parameters Peak-to-Compton and Peak-to-total ratio in conjunction with the energy resolution for the Cs^{137} and Co^{60} simulated sources were calculated. In addition the energy resolution for the Ra^{226} two major photo-peaks were also calculated. The results for all one isotopic sources parameters measured are presented in Table 5.2.

Table 5.2-Simulated One Isotope Deconvolution Performance Measurements

Source	Peak Energy (KeV)	Spectrum	Peak Resolution (%)	Peak/Compton	Peak /Total
Cs^{137}	662	Simulated Spectrum	3.35	8.43	0.49
		Simulated Deconvolution	1.05	6297.22	2.05
Co^{60}	1173	Simulated Spectrum	2.92	3.66	0.15
		Simulated Deconvolution	0.92	24402.04	0.99
	1332	Simulated Spectrum	2.81	3.78	0.13
		Simulated Deconvolution	0.87	1186.33	0.95
	351	Simulated Spectrum	4.41	-	-
		Simulated Deconvolution	0.98	-	-
Ra^{226}	609	Simulated Spectrum	3.45	-	-
		Simulated Deconvolution	1.09	-	-

The numerical results in Table 5.2 confirm that the energy resolution improves greatly for each one of the photo-peaks measured for the three one isotope sources. The table also shows a significance improvement for the deconvoluted spectra parameters Peak-to-Compton and Peak-to-total ratios for Cs^{137} and Co^{60} simulated sources.

5.9 Fuel Simulated Sources Deconvolution

Once the MLEM deconvolution algorithm was implemented and tested for the one isotope simulated sources, a fuel surrogate simulated source was created and modeled in MCNPX. The source modeled was developed because the ATR fuel data collected during the study could not be directly used to calculate the response function of the 1”x1” LaBr_3 detector for the system used and there is a need to test the performance of MLEM method for burnup applications. The detection system used in the study was a temporary set up positioned using crane and ropes. The experimental setup used during the study did not have the capability of measuring the distance between system and target (fuel) or the angle of the detection system in regards to the fuel. Consequently knowing the dimensions of the detection system

with any degree of accuracy in order to create an exact MCNPX model for the calculation of the detector response function was unfeasible. The response function calculation for deconvolution of spectra using MCNPX needs a precise representation of the experimental setup in order for the model to accurately simulate the interaction of particles with the system collimator, detector and surroundings. In addition, the access to the canal is restricted so collecting new data to test the deconvolution technique at this time is a difficult task.

The simulated fuel source was developed by first calculating the area of the individual isotope photo-peaks (A_{pp}) from ATR spectra. The second step in obtaining the normalized weighted fuel point source was to calculate the summation of the individual isotope photo-peaks areas (A_{pp}) from the ATR fuel spectra in order to estimate the total weighted fuel source area (W_{ts})

$$W_{ts} = \sum_{n=1}^n A_{pp_n} \quad (5.19)$$

Once the total weighted fuel source area was calculated the individual area photo-peaks (A_{pp}) were divided by the result of the total weighted fuel source area (W_{ts}) to obtain the fuel individual isotope concentration (W_{pp}) used to simulate the surrogate source in MCNPX

$$W_{pp_n} = \frac{A_{pp_n}}{W_{ts}} \quad (5.20)$$

The method describe above was used to create MCNPX spectral data for five fuel individual isotope weighted point sources representing different ATR fuel elements spectra. The MCNPX simulated fuel spectra model was based on the same geometrical setup that was describe in the experimental section.

Following the method described five simulated point weighted fuel sources were created based on 92% U^{235} enriched ATR fuel spectra (Fig. 4.6 bottom) taken at the canal in 2010 as part of a study dedicated to collect burnup validation data (Navarro et al.,2012) . The ATR fuel spectra data was collected as part of a feasibility study to gather data from ATR canal adjacent to the reactor. The energy intensity and isotopic composition of the simulated point source information was extracted from ATR fuel spectra with different burnup and cooling times.

The comparison of fuel data collected at the ATR canal and the weighted simulated data can be seen in Figure 5.6. The figure shows the comparison of element simulated and experimental data for element XA374T. The figure also demonstrates that the simulated weighted source was able to reproduce the isotopic peaks of interest in the ATR experimental spectra. The purpose of creating fuel simulated data during the study was not to have the same exact experiment setup that the ATR detection feasibility study (Navarro et al. 2012). The objective of simulating highly enriched ATR fuel spectra was to create data to test if the MLEM algorithm can improve the energy resolution and decrease the standard deviation of the burnup calibration curve. There are some discrepancies between the simulated and collected spectra as expected. The differences can be attributed to the fact that the fuel simulated data did not capture the full effects of the original ATR canal experimental setup, i.e. background, minor peaks or x-ray region. However the simulated data was able to capture the peaks of interest needed to perform burnup calibrations and will help determinate if deconvolution can aid in the prediction of fuel burnup using calibrations.

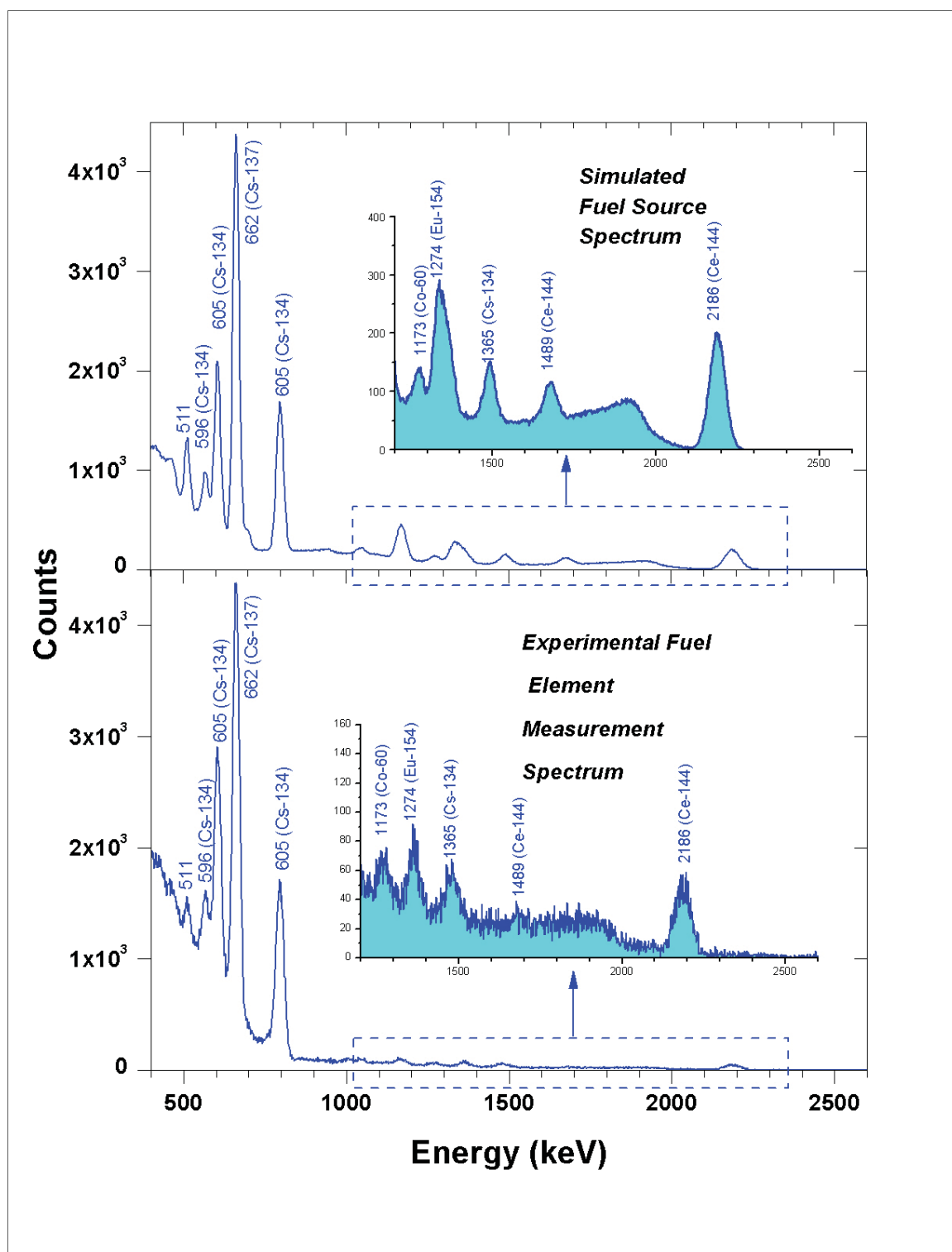


Figure 5.6 Experimental and Simulated Fuel ATR Spectra Comparison

Once the simulated ATR fuel source was proven to be a good representation of the experimental fuel source, the deconvolution algorithm was applied. Figure 5.7 shows the convoluted spectra of the surrogate ATR fuel element XA569T, while Figure 5.8 illustrates the fuel element spectra after deconvolution. Comparing the two figures it can be seen that the MLEM deconvolution algorithm was effective in moving the losses of energy in the convoluted figure to the appropriate photo-peaks in the deconvoluted plot. The deconvoluted plot also shows that the MLEM method was efficient in resolving two pair of close-lying peaks (662,696 and 1332,1274). This also proves that deconvolution by MLEM helps resolves peaks that have a low number of counts and are lost due to pile-up or lost in the continuum. The better resolution of near lying peaks and the increase of photo-peak area in small count peaks allows for a better identification of all the isotopes present in the simulated fuel source.

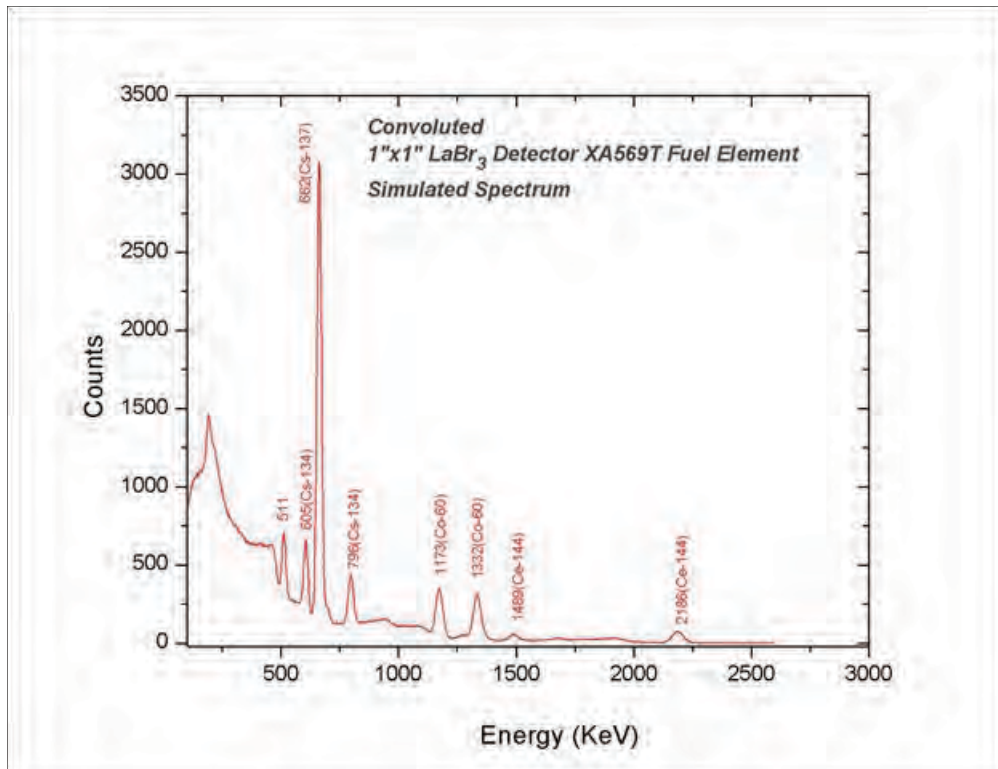


Figure 5.7 Convoluted Simulated Fuel ATR Spectra

In order to test the performance of the MLEM algorithm five different surrogate element sources representing five different ATR fuel elements were modeled within MCNPX. The five surrogate fuel source spectra were deconvoluted and the energy resolution for the peaks of interest (Cs^{134} and Cs^{137}) was calculated. Table 5.3 shows how the energy resolution for the Cs^{134} and Cs^{137} improves with deconvolution for all the surrogate ATR fuel element sources. Improving the resolution of the interested peaks means that there will be less fluctuation from pulses recorded at the same energy, yielding less area uncertainty for burnup calibrations.

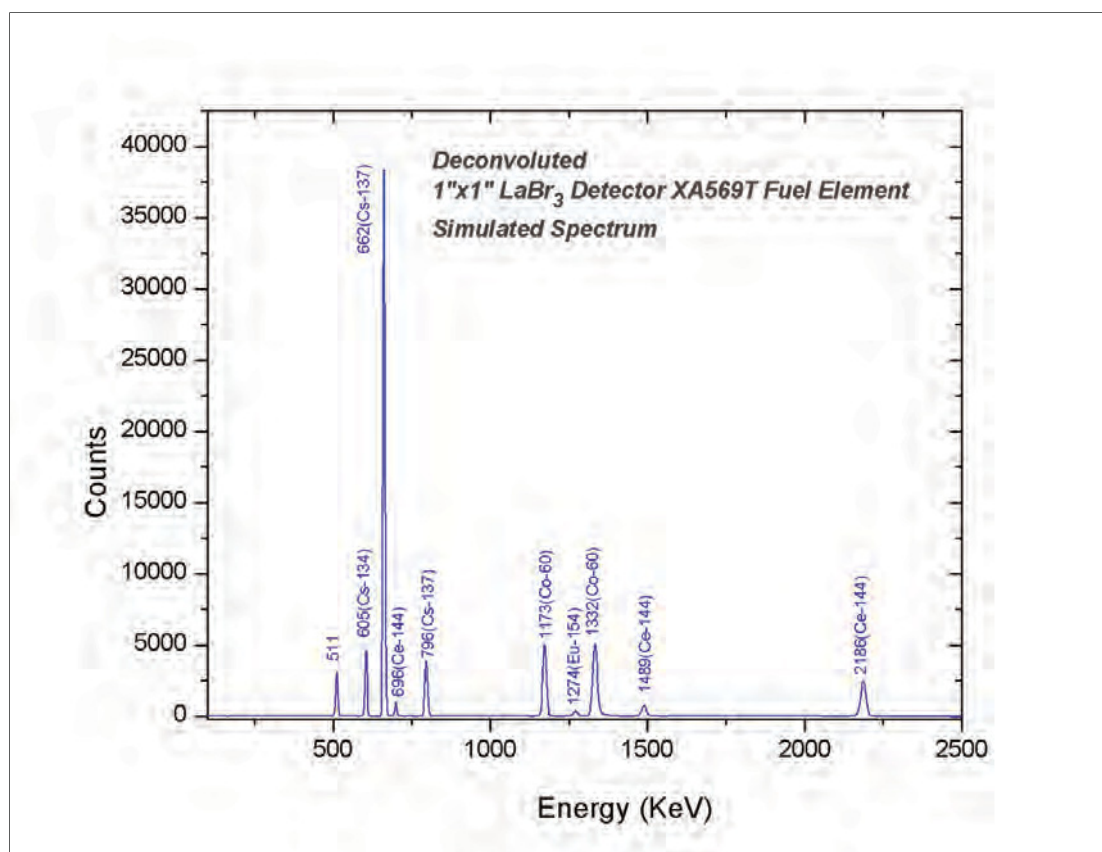


Figure 5.8 Deconvoluted Simulated Fuel ATR Spectra

5.10 Use of Deconvolution Spectra for Burnup Determination

The development of a deconvolution protocol for ATR fuel burnup prediction is aimed to improve the performance of the nondestructive burnup prediction technique for ATR fuels using scintillators. The deconvolution technique is designed to improve spectra quality. Improving the quality of the spectra will in theory allow for a more confident predictions as well as a broader range of operation of the 1"x1" LaBr₃ scintillator for burnup calibrations and ATR canal applications. Prediction of fuel burnup experimentally by fuel calibrations is a technique in which certain ratios or peak areas of absolute fission products from gamma ray spectra are used to nondestructively determine burnup. Figure 5.9 shows an example of a burnup calibration created with experimental data collected at the ATR canal using a LaBr₃ scintillator. The calibration was created using the Cs¹³⁷/Cs¹³⁴ area ratio versus several fuel elements calculated burnup.

Table 5.3.-Surrogate Fuel Elements Photo-Peaks Resolution

Source	Peak Energy (KeV)	Spectrum	Peak Resolution (%)	Peak/Compton	Peak /Total
Cs ¹³⁷	662	Simulated Spectrum	3.35	8.43	0.49
		Simulated Deconvolution	1.05	6297.22	2.05
Co ⁶⁰	1173	Simulated Spectrum	2.92	3.66	0.15
		Simulated Deconvolution	0.92	24402.04	0.99
	1332	Simulated Spectrum	2.81	3.78	0.13
		Simulated Deconvolution	0.87	1186.33	0.95
Ra ²²⁶	351	Simulated Spectrum	4.41	-	-
		Simulated Deconvolution	0.98	-	-
	609	Simulated Spectrum	3.45	-	-
		Simulated Deconvolution	1.09	-	-

Figure 5.9 illustrates how the confidence in predicting burnup by this particular nondestructive method decreases for the elements with less than 200 MWd of burnup. The three elements have a cooling time of less than 100 days. Shorter cooling time of the fuel element signifies that the spectra are dominated by short lived fission product isotopes, this makes difficult to use longer lived ratios or absolute areas commonly used for the creation of burnup calibrations (Cs¹³⁷ and Cs¹³⁴). Due to the higher standard deviation of the Cs¹³⁷/Cs¹³⁴ area ratio of elements with short cooling times (0-100 days) there is no procedure for the future ATR permanent system to calculate burnup of these elements with confidence. The goal of the deconvoluting simulated fuel data is to prove that the standard deviation of the Cs¹³⁷/Cs¹³⁴ ratio can be decrease thereby increasing the confidence in LaBr₃ burnup calibration prediction as well as increasing the cooling time range that a calibration curve can predict burn up with a certain degree of accuracy.

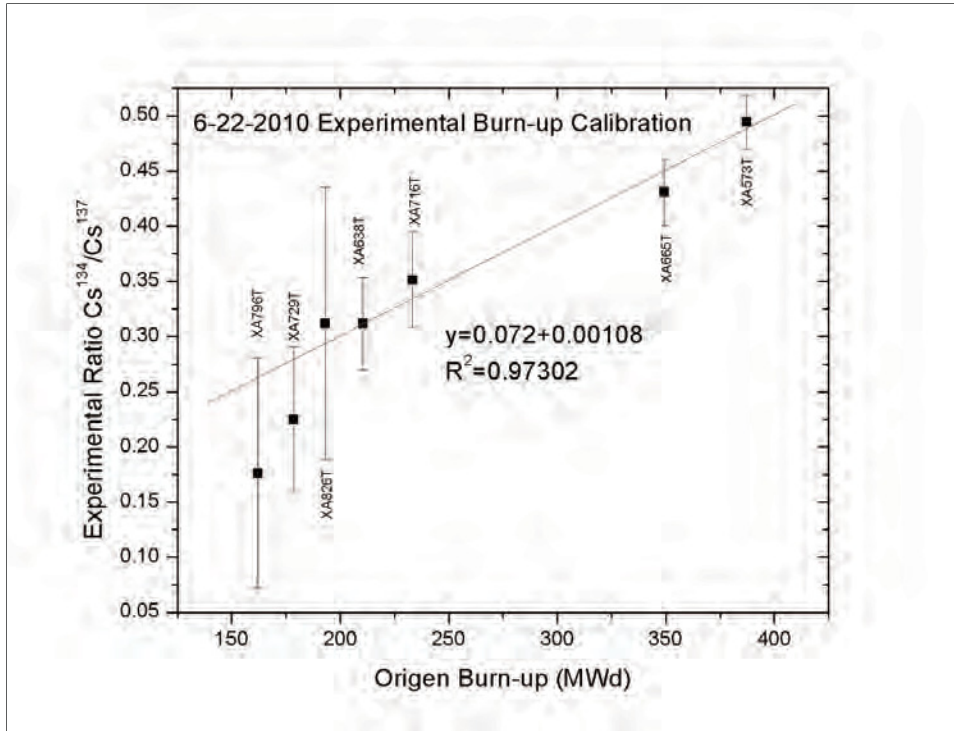


Figure 5.9 Example of an ATR Fuel Burnup Prediction Calibration

With the purpose of testing the theory that deconvolution can minimize the error of burnup calibrations two curves based on the photo-peak area Cs^{137}/Cs^{134} ratios (Table 5.3) were created. The two plots represent the original five surrogate fuel sources Cs^{137}/Cs^{134} ratios for the simulated data before and after deconvolution. Figure 5.10 represents the burnup calibration curve before deconvolution, while Figure 5.11 contains the area Cs^{137}/Cs^{134} ratios of the deconvoluted spectra.

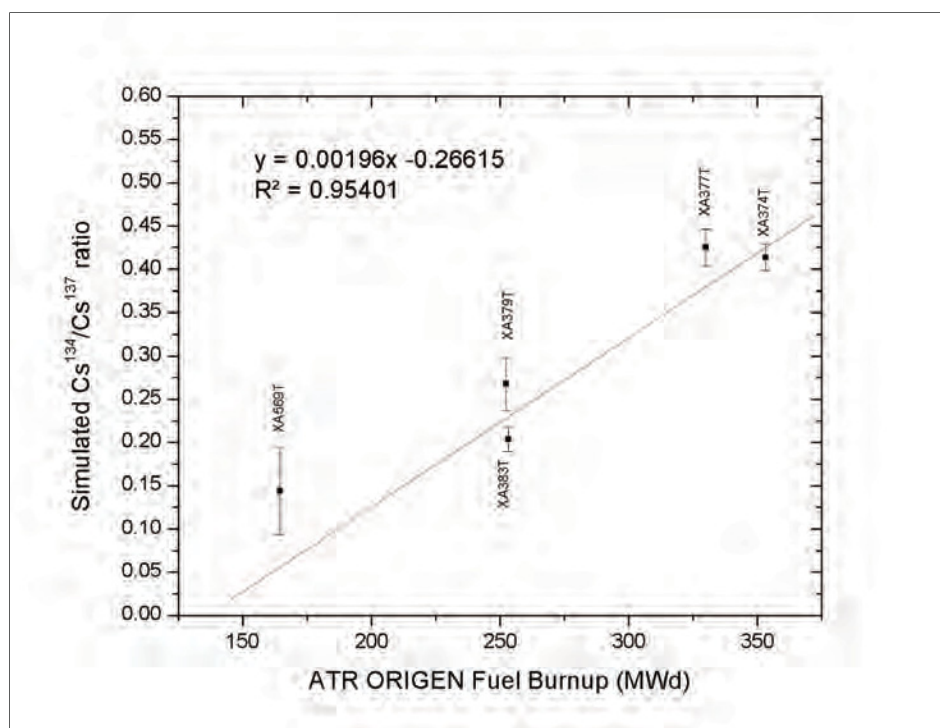


Figure 5.10- Convoluted Burnup Calibration Simulated Fuel ATR Spectra

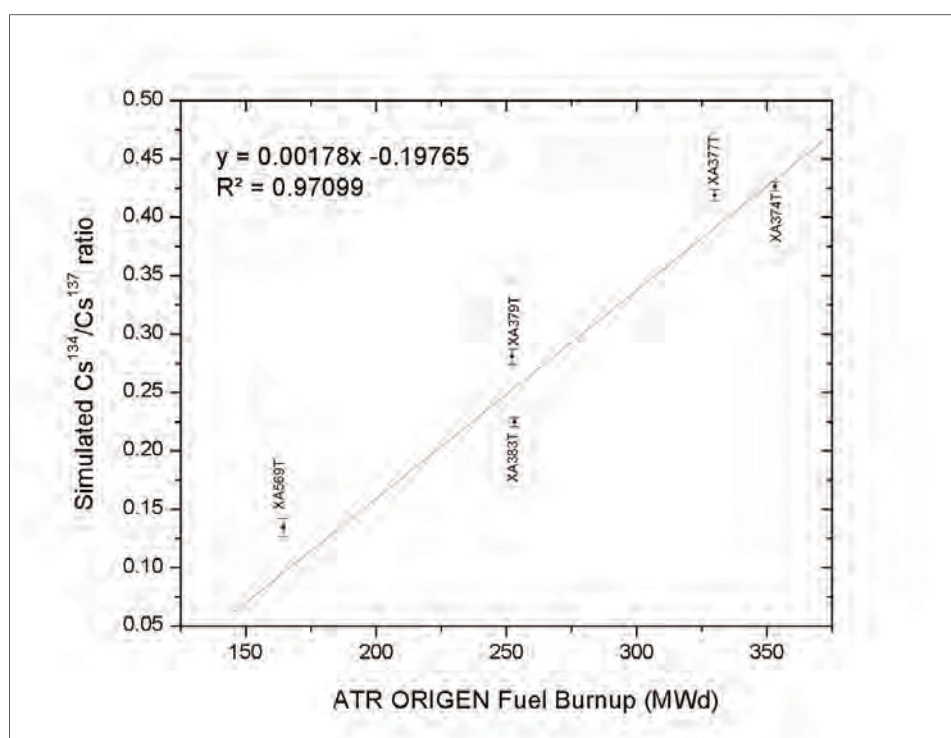


Figure 5.11 Deconvoluted Burnup Calibration Simulated Fuel ATR Spectra

It can be inferred from the plots and from linear fit parameters as well as looking at the error bars associated with the $\text{Cs}^{137}/\text{Cs}^{134}$ ratios that the calibration plot created with the deconvolution data yields a more confident ATR simulated fuel burnup prediction.

5.11 Deconvolution of Experimental Sources

Until this point it has been established that applying a deconvolution method to LaBr_3 scintillator simulated data improves not only the resolution of the photo-peaks and performance spectra parameters but also improve the confidence of the burnup calibration curves, however the method was only tested using simulated generated spectra. In order to better determine the performance of the method, the technique has to be applied to experimental data. The final objective of developing a deconvolution method for the LaBr_3 scintillator is to enhance fuel spectra resolution in order to design a rugged and low maintenance ATR fuel scanning system. However it was not feasible to test this method with the experimental fuel spectra already collected; because it was not possible to determine the system measurements with a high degree of accuracy with the system configuration used for the ATR canal measurements. Knowing the geometry of the system with precision is necessary to accurately compute the response function of the detector. In order to demonstrate that this technique will ultimately help to increase the resolution of spectra collected with a LaBr_3 detector for fuel measurements applications a surrogate fission product source was created.

The following sections of chapter 5 present the final stages of the deconvolution study that consisted in developing a highly enriched source using fission wires, collecting data using the LaBr_3 detector and applying the deconvolution technique developed previously to the experimental data collected. The surrogate fuel was created using ATR fission wires that have the same uranium enrichment as the ATR fuel elements. The surrogate source was irradiated at the AGN-201 reactor at Idaho State University. The surrogate fuel source was placed in the reactor for about 20 minutes and then the samples were taken to a laboratory where data was collected using the 1"x1" LaBr_3 detector at various decay intervals.

5.12 Experimental Measurement Setup

Figure 5.12 and 5.13 show the experimental measurement set up used to collect data. The setup consisted of a 1 inch diameter aperture bismuth collimator and the 1"x1" LaBr_3 detector surrounded by a lead shield. The bismuth collimator has a length of 10.1 cm and was placed next to the detector as it can be seen in figure 5.12. To perform the calibration experiments one isotope and multi isotopes sources along with the irradiated sample were placed at the end of the bismuth collimator. The lead shielding (Figure 5.13) purpose was to decrease the background along with minimizing the exposure to the irradiated sample.

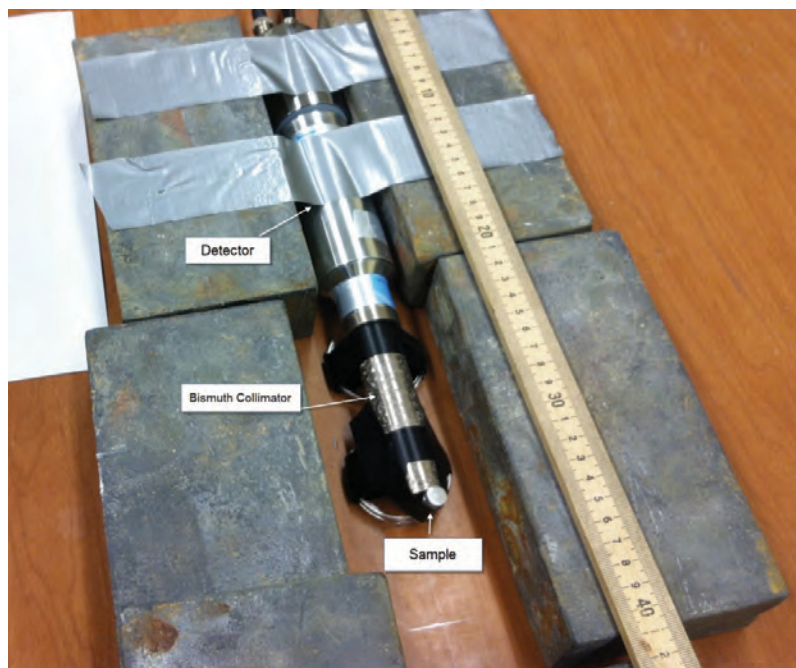


Figure 5.12 Open Shield Experimental Set-up



Figure 5.13 Closed Shield Experimental Set-up

5.13 Detector and Simulation Calibration Measurements

The first stage of the study was to create an experimental measurement setup in a laboratory adjacent to the reactor. However before performing the measurements with the multi fission product isotopic source, calibration measurements were performed. The calibration measurements consisted in collecting data

from one and multiple isotopes sources (Table 5.4) using the experimental setup discussed in the previous section. The data collected was used to validate the MXNPX model, perform the energy calibration of the detector along with obtaining the parameters needed to give the MCNPX simulations pulse height data with a realistic Gaussian photo peak shape.

Table 5.4.-Gamma Energy Sources used for Gaussian Energy Broadening parameters

Centroid (KeV)	FWHM (KeV)
86.15	9.23
105.78	9.22
123.25	9.22
246.88	14.06
344.94	17.06
592.06	24.17
661.10	24.97
778.35	28.05
872.78	35.85
1102.66	50.44
1173.40	35.01
1332.53	40.45

The GEB parameters (eq. 5.3) for this experimental setup are obtained using the full width at half maximum (FWHM) calibration data from the different sources in Table 5.4 and performing a non-linear regression:

$$a = -0.0001827 \text{ MeV} \quad b = 0.0271209 \text{ MeV}^{1/2} \quad c = 0.7812452 \text{ MeV}^{-1}$$

Once the GEB parameters for the detection system were calculated a model of the experimental set up was created in order to simulate the different calibration sources shown in Table 5.4. After the simulations were completed the model spectra generated was compared against the experimental data collected from three one isotope sources. The results of the comparisons between experimental data and simulated data obtained using MCNPX are shown in Figures 5.14-5.16.

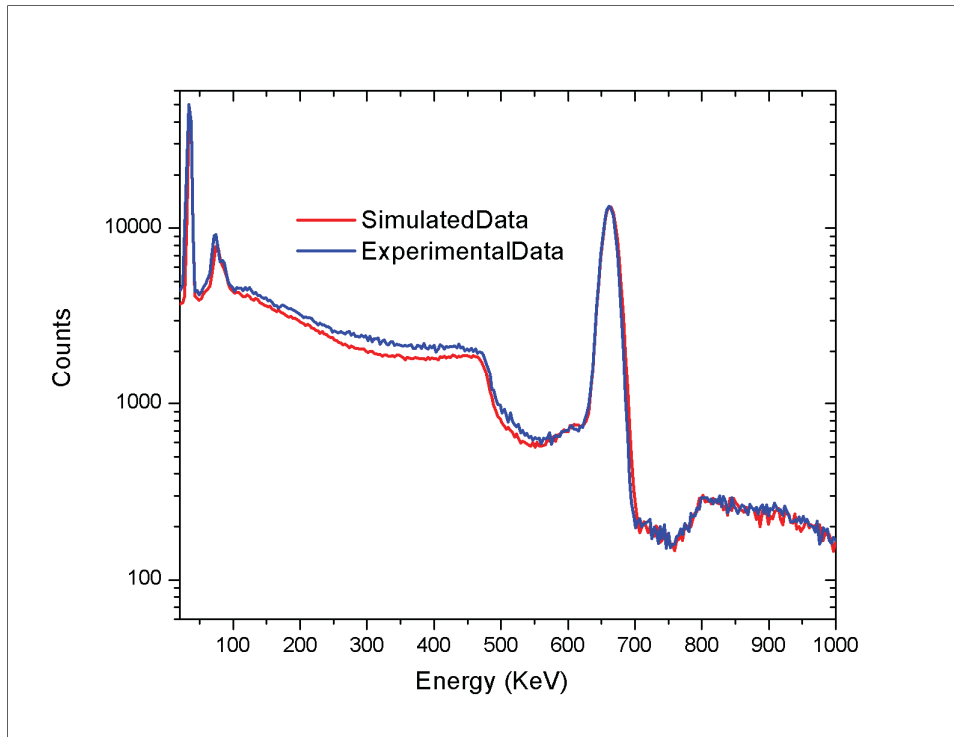


Figure 5.14 Cs^{137} Experimental and Simulated Response Function Comparison

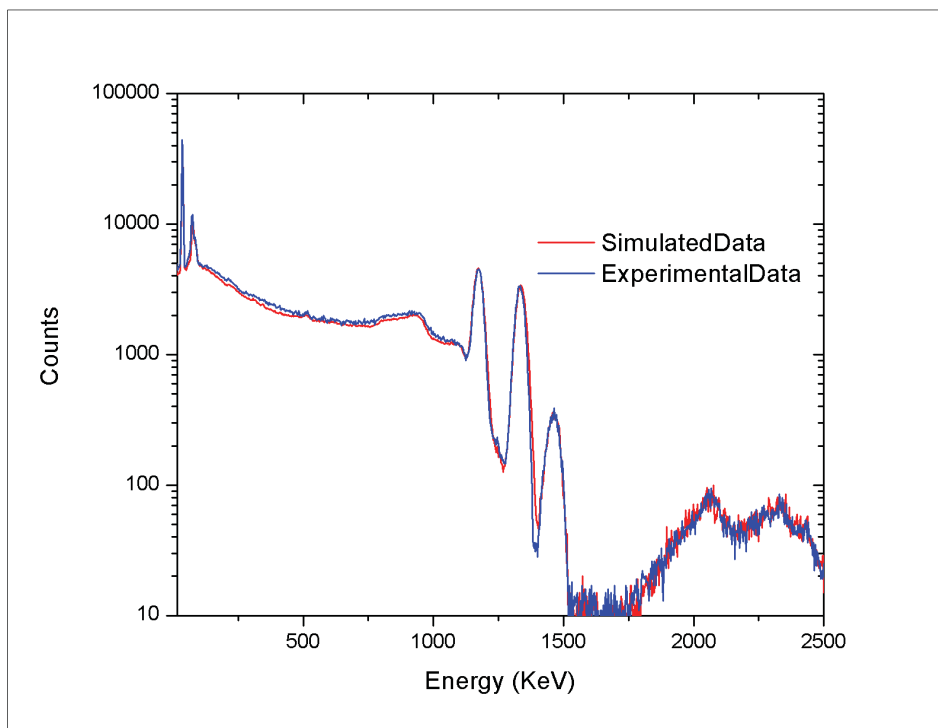


Figure 5.15 Co^{60} Experimental and Simulated Response Function Comparison

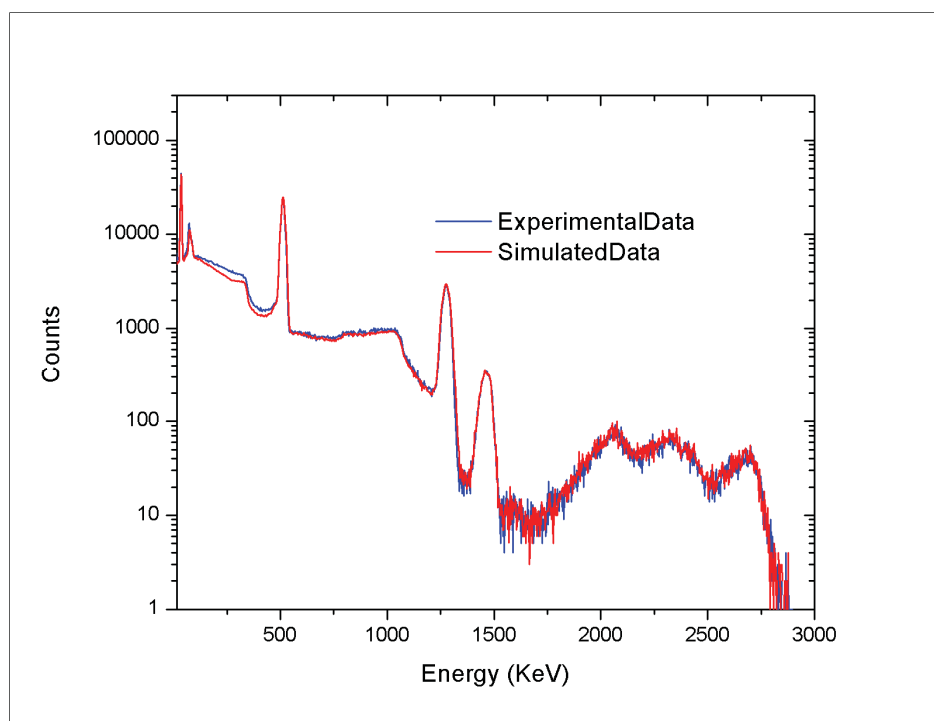


Figure 5.16 Na^{22} Experimental and Simulated Response Function Comparison

The three comparison figures presented above (Cs^{137} , Co^{60} , and Na^{22}) show that the simulated spectra created using MCNPX are in overall good agreement with the experimental data and therefore are an accurate representation of the experimental setup. The simulated spectra only diverge from the experimental data at lower energies around the Compton region. The differences are more noticeable for the Cs^{137} and Na^{22} sources. These deviations can be mainly attributed to the contributions of the X-ray emissions from the collimator and shielding materials surrounding the detector. The deviations can also be caused by modeling geometry and method discrepancies.

5.14 Response Function Calculation for Experimental Sources

Once a realistic model of the experimental set up was validated the response function of the LaBr_3 detector was calculated. The response function of the detector can be calculated experimentally, using correlations or using simulation tools (Meng et al. 2000). Simulations are the most accurate technique of calculating the response function of a detector, if a good model representation of the experimental setup is available (Meng et al. 2000). The response function of the 1"x1" LaBr_3 scintillator was calculated by modeling 1024 mono-energetic sources in MCNPX. Each simulation was performed with 1×10^{10} particles using 32 processors. This method of calculating the response function can be very accurate but is computer intensive and time consuming. The simulations were performed using the High Performance Computer cluster at the Idaho National Laboratory.

5.15 MLEM Deconvolution of One Isotope Experimental Sources

The MLEM method described in the previous section was implemented in Matlab. To test the deconvolution algorithm various one isotopic sources measured using the experimental setup describe in section 6.3 were deconvoluted as it can be seen in figure 5.17,5.18 and 5.20.

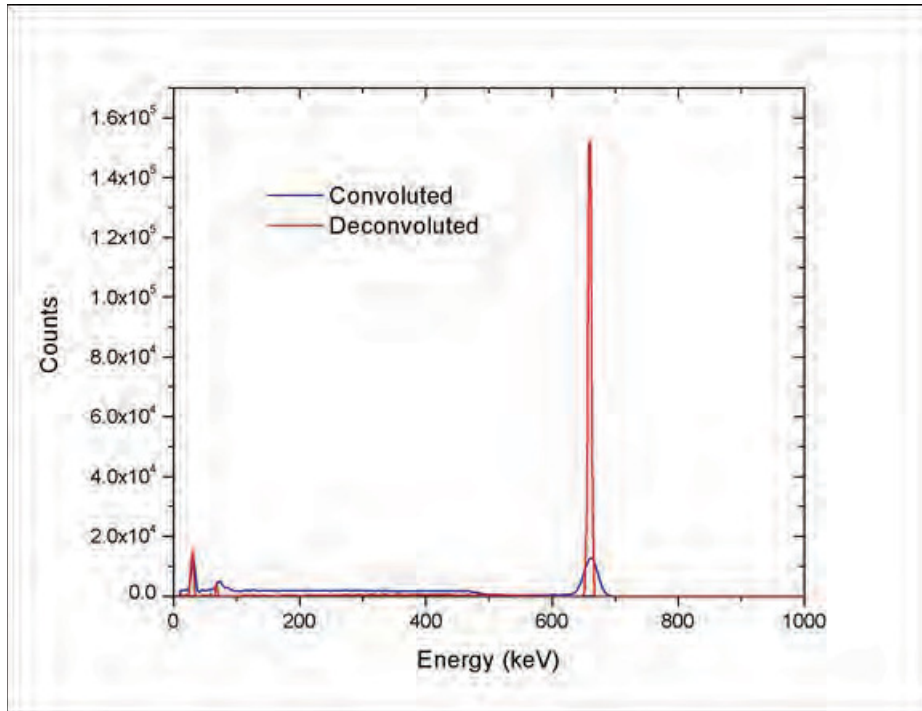


Figure 5.17 Cs^{137} Convolved and Deconvoluted Spectra Comparison

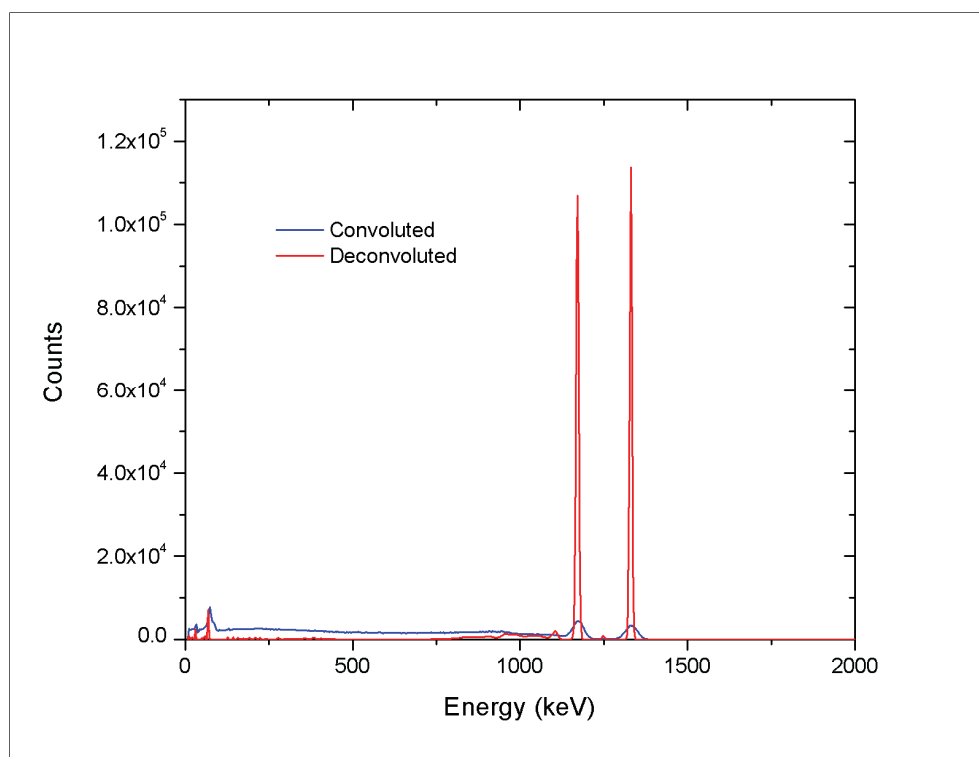


Figure 5.18 Co^{60} Convolved and Deconvoluted Spectra Comparison

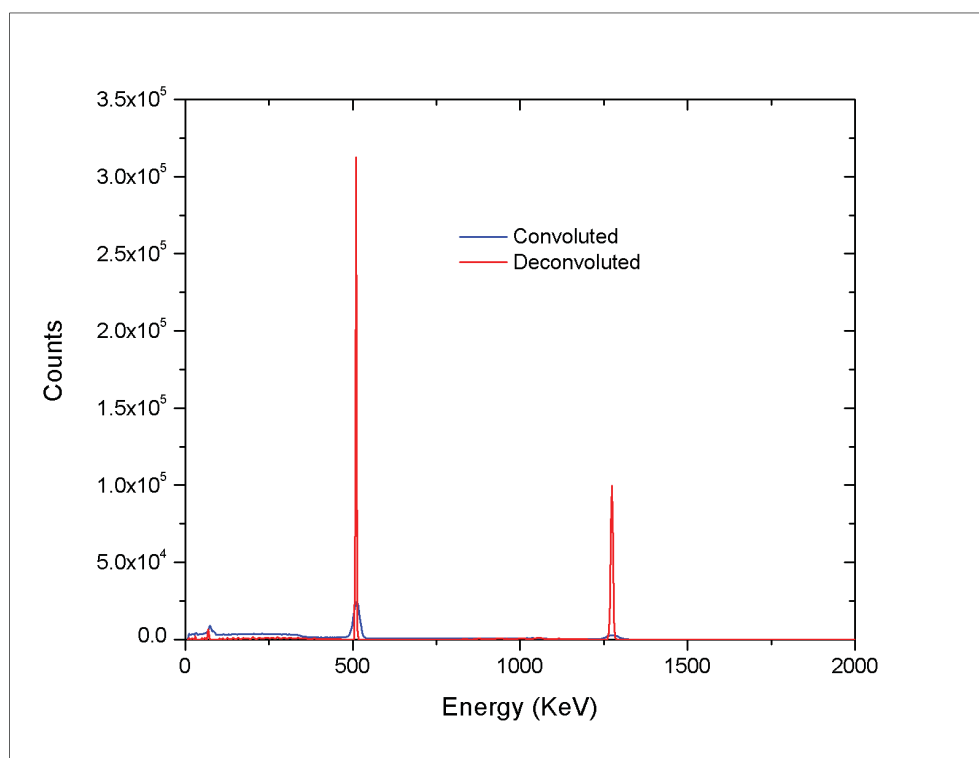


Figure 5.19 Na^{22} Convolved and Deconvoluted Spectra Comparison.

The three one isotope source comparison figures (5.17-5.19) showed the improvement in energy resolution for all the peaks in each one of the spectra. There are small discrepancies for the three figures that are located around the Compton region. The discrepancies can be attributed to the response function simulations difficulty of capturing the model x-ray region with complete accuracy as it was shown in the validation of the experimental setup figures (Fig. 5.14-5.16). In order to measure the efficiency of deconvolution method the peak to Compton and peak to total ratios were measured. In addition the resolutions of all the photo-peaks for the three one isotope sources were also calculated. The comparison of the performance parameters used to measure the efficiency of the deconvolution method can be seen in Table 5.5. The table shows improvement in both performance parameters along with the improvement of resolution for all the sources. The table shows that for all the three sources the resolution improves more than 50%. The table also shows that the peak to Compton ratio improves for the three sources, the increase of this performance parameter means that the energy losses to the Compton scattering due to inefficiencies in the detector are properly replaced in the photo-peak during deconvolution.

Table 5.5 Resolution and Performance Parameters Comparison

Source	Peak Energy (KeV)	Spectrum	Peak Resolution (%)	Peak/Compton	Peak /Total
Cs¹³⁷	662	Experimental Spectrum	3.873	7.447	1.024
		Deconvolution	0.946	399.041	2.885
Co⁶⁰	1173	Experimental Spectrum	3.051	1.903	0.207
		Deconvolution	0.798	255.489	1.267
	1332	Experimental Spectrum	3.106	3.341	0.215
		Deconvolution	0.632	120.472	1.326
Na²²	662	Experimental Spectrum	3.111	3.727	0.176
		Deconvolution	0.607	319.310	1.034

5.16 MLEM Deconvolution of a Experimental Multiple-Isotope Source

Once it was determined that the MLEM method was an effective method deconvoluting one isotope sources the method was tested with a multi-isotope source. The multi-isotope source consisted of a Eu¹⁵², Eu¹⁵⁴ and Eu¹⁵⁵ mixture. Before deconvoluting the multi-isotope europium source experimental data was smoothed to minimize the contribution that noisy data has on creating small artificial peaks. The filter used was a nine point frame quartic Savitzky-Golay filter. After the filter was applied the data was deconvoluted using the MLEM algorithm implemented in Matlab.

Figure 5.20 shows the deconvolution comparison of the europium multi-isotope source before and after deconvolution. In Figure 5.20, it can be seen that the deconvolution algorithm has an overall good performance. In addition the deconvoluted plot shows that the MLEM method was able to resolve close-lying peaks. In the plot, it can be seen that the near isotopic peaks 105 and 122 KeV were fully resolved in the deconvoluted figure. In addition the close-lying peaks 723 and 778 Kev in the deconvoluted plot were also better resolve than the in the convoluted figure. The convoluted plot layer (700-1400 KeV) also demonstrates that the MLEM algorithm was able to increase the resolution of peaks with a small number of counts and a higher continuum.

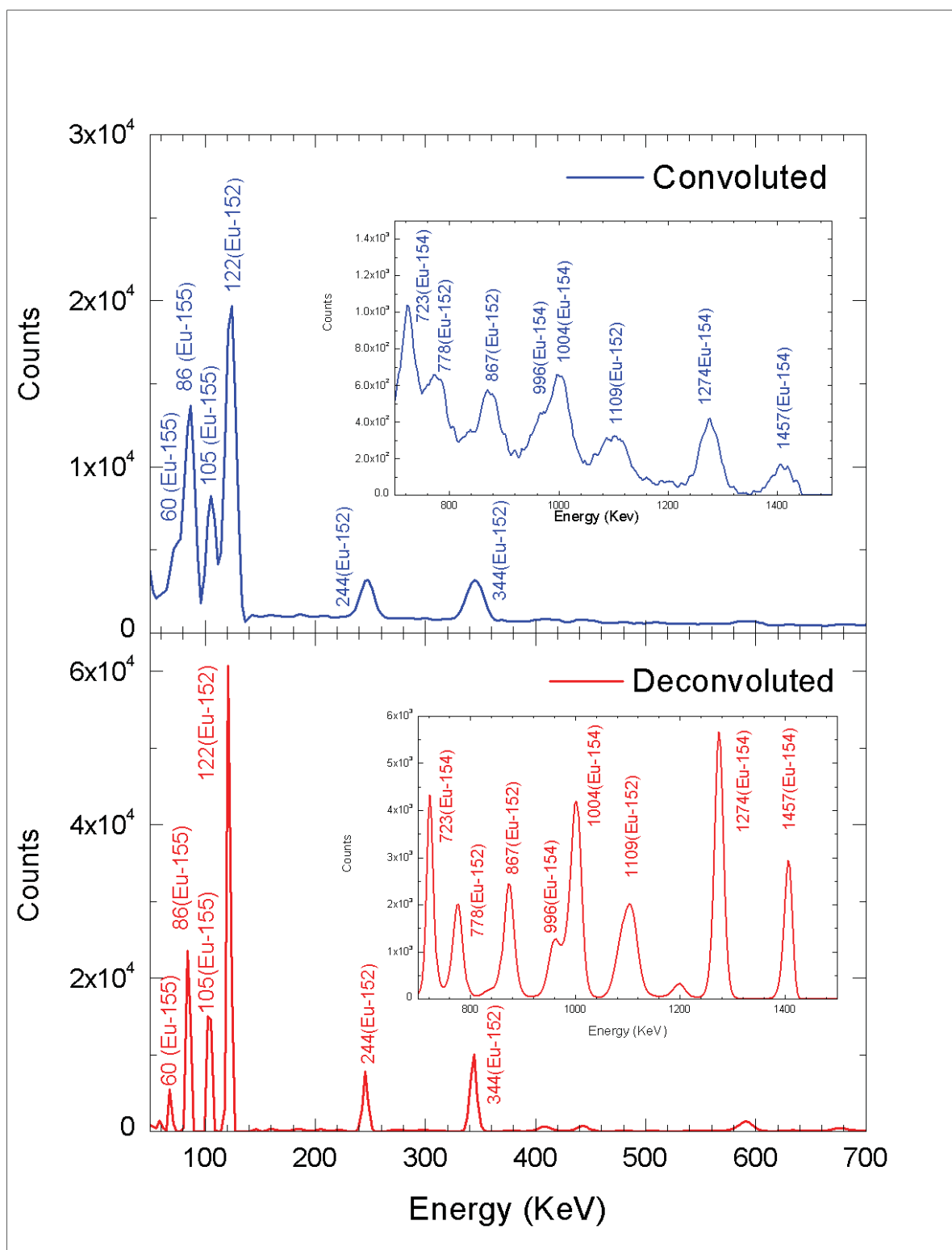


Figure 5.20 Multi-Isotope Europium Source Convolved and Deconvoluted Comparison

Table 5.6 presents the calculated resolution parameters for three major peaks at different energies. The table shows how the energy resolution for the three peaks greatly improves with deconvolution.

Table 5.6 Resolution Multi-Isotope Source Comparison

Source	Peak Energy (KeV)	Spectrum	Peak Resolution (%)
Eu^{152,154,155}	122	Experimental Spectrum	8.386
		Deconvolution	3.731
	244	Experimental Spectrum	5.681
		Deconvolution	1.740
	1274	Experimental Spectrum	3.016
		Deconvolution	1.564

5.17 Reactor Experiment and High Enriched LaBr₃ Detector Measurements

The final goal of this project was to apply a deconvolution protocol to improve highly enriched ATR fuel samples measurements for determination of burnup. However before committing personnel and monetary resources for a study at the ATR, an experiment was performed in order to determine if the deconvolution of high enriched sample spectra taken with a LaBr₃ detector is feasible. In order to test the deconvolution method highly enriched surrogate fuel samples were used. The sample consisted in ten highly enriched fission wires.

The experiment consisted on irradiating highly enriched fission wires that have the same weight composition of U²³⁵ that the actual ATR fuel elements do. The irradiation experiment was performed at the AGR reactor facility at ISU the goal of the experiment was to create a multipeak isotopic fission highly enriched source to test the 1x1 LaBr₃ scintillator deconvolution protocol. The AGN-201 is graphite moderated and self-contained user facility mainly for training reactor operators and for student projects. The reactor has a maximum power level of 5 watts. The reactor is composed of a cylindrical core enclosed in 20 cm thick graphite reflector which by itself its surrounded by a 10 cm thick lead shield, followed by a 55 cm thick water shield.

In order to create the multi-peak isotopic fission source the ten highly enriched wires were bundled and placed inside a double encapsulation system to assure containment of the fission products. The first containment was a polyethylene capsule and the second containment was an aluminum seal casing. The mass composition of the ten wires is 90% aluminum with approximately 10 % uranium. The uranium that is contained in the wires is 93 % U²³⁵ enriched. Once the wires were placed in a double containment system; the capsule was attached to an aluminum rod that slides inside the experiment port during the irradiation. The highly enriched flux wires were irradiated at a maximum power of 4.6 watts with a flux of approximately 2.3×10^8 n/cm² s for two hours. After the sample irradiation was completed the capsule was taken out of the reactor and let sit for 18 minutes before being transported to the radiation laboratory.

At the conclusion of the irradiation the polyethylene container was removed and the aluminum capsule sample was transported to the measurement laboratory. The sample inside the aluminum containment was placed in front of the bismuth collimator inside the lead shield. The sample was positioned 10.1 cm from

the LaBr₃ scintillator aluminum housing. Nine spectra of the fission products sample were taken at different decay times.

5.18 MLEM High Enriched Samples Results

After the experiment was completed and different highly enriched data was collected the deconvolution algorithm protocol was tested using high enriched multi-peak isotopic fission spectra. Figure 5.21 compares the convoluted and deconvoluted spectra for a sample taken 48 hours after discharge. The experimental data collected was smooth to minimize the contribution that noisy data can have creating small artificial peaks. The filter used was a seven point frame quadratic Savitzky-Golay filter. Following the smoothing of the experimental data the spectra was deconvoluted using the MLEM algorithm implemented in Matlab.

It can be seen from figure 5.21 that the MLEM method was able to deconvolute the multi-isotope high enriched data. Again as with the previous deconvolve samples the method showed that it can be very effective increasing the individual photo-peak resolution. Table 5.7 shows the improvement in resolution for some of the major peaks shown in Figure 5.21.

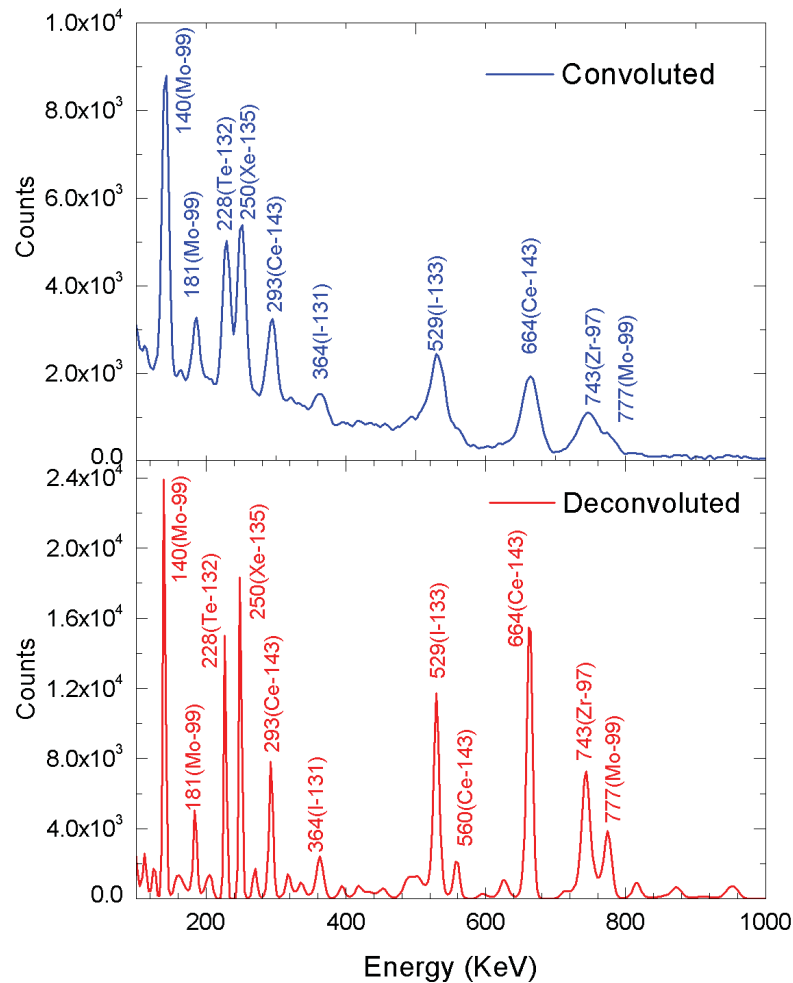


Figure 5.21 Highly Enriched Fission Products Source Convoluted and Deconvoluted Comparison

Table 5.7 Fission Product Multi-Isotope Source Resolution Comparison

Source	Peak Energy (KeV)	Spectrum	Peak Resolution (%)
Mo⁹⁹	140	Experimental Spectrum	8.114
		Deconvolution	4.017
Xe²⁵⁰	250	Experimental Spectrum	4.451
		Deconvolution	2.887
Ce⁶⁶⁴	664	Experimental Spectrum	3.909
		Deconvolution	2.295

In addition with increasing the resolution of the photo-peaks the MLEM method was successful in resolving close lying peaks. The method was able to resolve three pairs of near-lying pair peaks 228-250, 531-560, and 743-772 KeV. The close-lying pair peaks 529 and 560 KeV in the convoluted plot were not even distinguishable from each other. In the convoluted plot it appears that only the I^{133} (529 KeV) photo-peak is present, however in the deconvoluted plot the Ce^{143} (560 KeV) photo-peak can also be clearly identified. The near lying pair peaks at 743 and 772 KeV are as well hard to identify in the convoluted plot however their resolution was clearly improve in the deconvoluted figure. Figure 5.21 also shows that there are some small artificial peaks with a very small number of counts created by the deconvolution method. The small perturbations can be attributed to two main factors; the discrepancies between the simulated and true response function as well as noise in the data. The small perturbations are also a cost of the effectiveness that the MLEM method have in deconvoluting even the smallest photo-peaks.

The MLEM is a very powerful method however having noise in the convoluted spectra can cause the MLEM technique to treat the noise as if small Poisson distribution peaks were present, causing the creation of some nonexistent small perturbations during the deconvolution process. Using data filters decrease the creation of small peaks however smoothing the data too much can affect the counts of the existent photo-peaks. In order to avoid small peak creation a better resolution data set (more data points) have to be collected as well as finding or developing filtering data techniques better suited for this applications. It also has to be taken into account that having a better resolution data set will aid in avoiding the creation of artificial peaks by noise however it will also increase the number of simulations that are needed to calculate the response function of the detector system. The calculation of the response function requires of one simulation per every data channel that is taken. For this study 1024 channel data points were collected, therefore the same number of simulations were needed to calculate the response function of the system. Each simulation for every mono-energetic source during this study was performed using 1×10^{10} particles in 32 processors. In addition the increase in channels will increase the time that the iterative MLEM method takes to converge.

The second issue that can cause small perturbations is the discrepancy between the true response function and the response function obtained by simulating an experiment. Obtaining the response function using Monte Carlo simulations is regarded as the most accurate method to obtain a response function (Meng et al. 2000), however there is always inconsistencies between reality and the modeling of a system, these

discrepancies can be caused by geometry inaccuracies and assumptions as well as error in the modeling methods.

5.19 Conclusion

The study presented in this chapter consisted in developing and testing a deconvolution protocol aimed to improve the resolution of a 1 "x1" LaBr₃ scintillator. Increasing the resolution of LaBr₃ scintillator allows the possibility of designing a more rugged and less maintenance ATR fuel scanning system.

The deconvolution methodology developed consisted in calculating the response function of a 1"x1" LaBr₃ detector, validating that response function and implementing the MLEM algorithm in Matlab. The methodology was initially tested using one and multi-isotope simulated data. After it was proven that the deconvolution methodology is capable of enhancing photo-peak resolution as well as resolving close-lying peaks for one isotopic simulated data, a surrogate source based on ATR fuel elements data was created. Five fuel surrogate simulated elements were created and the results showed that deconvolution improves the confidence in burnup calibration predictions.

The final phase of the study consisted in testing the deconvolution methodology developed for the 1"x1" LaBr₃ detector with experimental isotopic sources; including spectra from a high enriched source. In order to create the high enriched fission product source an experiment that consisted in irradiating fission wires was performed. After the experiment was completed different decay fission data as well one-isotope and multi-isotope spectra were collected using the 1"x1" LaBr₃ detector. The spectra collected was then were submitted to the deconvolution methodology previously developed. The results showed that for the one-isotope deconvoluted spectra not only the resolution of the individual photo-peaks was enhanced considerably; it also proved that the peak-to-Compton and peak-to-total ratio performance parameters improved. The results also demonstrated that for the multi-isotope spectrum deconvolution improves individual photo-peak resolution as well as helping resolve close-lying peaks. Finally the deconvolution method was applied to the high enriched fission source created. The results established that the individual photo-peak resolution improves with deconvolution as well as establishing that the deconvolution aids isotope identification. In conclusion a deconvolution methodology was successfully created to increase the energy resolution of a LaBr₃ scintillator that can be applied to the design of more efficient and rugged fuel scanning detection system for the ATR canal for model validation and burnup on-site predictions.

5.20 References

Meng, L.J.; Ramsden, D. An Inter-comparison of Three Spectral-Deconvolution Algorithms for Gamma-ray Spectroscopy, *IEEE Transactions on Nuclear Science*, **2000**, Vol. 47, No. 4, 1329-1336.

Navarro, J.; Aryaeinejad, R.; Nigg, D.W. A Feasibility Study to Determine Cooling Time and Burnup of Advanced Test Reactor Fuel Using a Nondestructive Technique and Three Types of Gamma-ray Detectors. *Journal of ASTM International*, **2012**, Vol. 9, Issue 3.

Monahan, J.E. Unfolding Measured Distributions. *Scintillation Spectroscopy of Gamma Radiation*, Shafroth, S. M.; Gordon and Breach Science Publishers Inc. New York, **1967**, 371-386.

X-5 Monte Carlo Team, April 2003 *A general Monte Carlo N-Particle Transport Code, Version 5, Overview and Theory*, Vol. 1, pp. 106-107, Los Alamos, NM.

Shepp, L.A.; Vardi, Y.; Maximum Likelihood Reconstruction for Emission Tomography. *IEEE Trans. Medical Imaging*, **1982**, Vol 1(2), 113-122.

D.W. Nigg and K.A. Steuhm, Advanced Test Reactor Core Modeling Update Project: Annual Report for Fiscal Year 2011, INL/EXT-11-23348.

R. Aryaeinejad, D. Crawford, M. DeHart, G. Griffith, B. Gross, D. Lucas, J. Nielsen, D. Nigg, J. Navarro, J. Parry, J. Peterson, K. Steuhm, “Advanced Test Reactor Core Modeling Update Project – Annual Report for Fiscal Year 2010,” Idaho National Laboratory, INL/EXT-10-19940, (September 2010).

Maximum-Likelihood Expectation-Maximization (ML-EM) Iterative Reconstruction Algorithm, class notes, UC Berkeley. Retrieve from
<http://inst.nuc.berkeley.edu/NE107/Lectures/MLEM.pdf>

Appendix A. Element-Building Python Scripts and Input Files

Emily T. Swain

Script Input Files

A1. Sample Cycle-Specific File: 152BLoad.txt

Column 1	Column 2	Column 3	Column 4	Column 5	Column 6
Element Position	Element Type: 1 – XA 2 – YA 3 – NB	Current Grams of U-235 in Element	Current Grams of B-10 in Element	Initial Grams of U- 235 in Element	Element Exposure

1	1	846	0.124	1075	180.599
2	3	831	0.000	1075	192.429
3	1	825	0.104	1075	197.161
4	2	743	0.049	1023	220.820
5	2	715	0.038	1023	242.902
6	1	713	0.038	1075	285.489
7	1	798	0.078	1075	218.454
8	1	832	0.117	1075	191.640
9	2	829	0.113	1023	152.997
10	1	848	0.130	1075	179.022
11	1	883	0.156	1075	151.420
12	1	1075	0.660	1075	0.001
13	1	1075	0.660	1075	0.001
14	1	1075	0.660	1075	0.001
15	1	942	0.249	1075	104.890
16	2	954	0.309	1023	54.416
17	1	1075	0.660	1075	0.001
18	1	1075	0.660	1075	0.001
19	1	1075	0.660	1075	0.001
20	1	899	0.173	1075	138.801
21	1	901	0.176	1075	137.224
22	1	1075	0.660	1075	0.001
23	1	1075	0.660	1075	0.001
24	1	1075	0.660	1075	0.001
25	1	923	0.223	1075	119.874
26	1	913	0.198	1075	127.760
27	1	926	0.240	1075	117.508
28	1	1075	0.660	1075	0.001
29	1	1075	0.660	1075	0.001
30	1	885	0.158	1075	149.842
31	1	870	0.139	1075	161.672
32	1	1075	0.660	1075	0.001
33	1	969	0.315	1075	83.596

34	2	950	0.298	1023	57.571
35	1	936	0.257	1075	109.621
36	1	942	0.249	1075	104.890
37	2	953	0.305	1023	55.205
38	2	956	0.310	1023	52.839
39	1	1075	0.660	1075	0.001
40	1	854	0.122	1075	174.290

A2. XA Element Fuel Loading: zoneload.txt

Column n 1	Column 2	Column n 3	Column 4	Column 5	Column 6
Region Number	Fraction of Total Power in Region	Region Volume	Current Grams of U-235 in Region	Current Grams of B-10 in Region	Current Grams of U-238 in Region

1	0.010867485	87.47156	16.56	2.88E-02	1.246479307
2	0.017842942	87.47156	16.56	2.88E-02	1.246815681
3	0.022681867	87.47156	16.56	2.88E-02	1.246815681
4	0.048694121	174.9731	33.13	5.75E-02	2.493987759
5	0.020871814	87.47156	16.56	2.88E-02	1.246815681
6	0.015121304	87.47156	16.56	2.88E-02	1.246815681
7	0.006873305	87.47156	16.56	2.88E-02	1.246815681
8	0.04336593	350.767	88.32	9.97E-25	6.647503653
9	0.071923617	350.767	88.29	1.00E-24	6.645380887
10	0.09176932	350.767	88.29	1.00E-24	6.645380887
11	0.197142541	701.5339	176.57	2.00E-24	13.29058264
12	0.084662976	350.767	88.29	1.00E-24	6.645380887
13	0.061809467	350.767	88.29	1.00E-24	6.645380887
14	0.031464624	350.767	88.29	1.00E-24	6.645380887
15	0.020432599	164.4099	29.52	5.39E-02	2.222026366
16	0.034169927	164.40991	29.54	5.38E-02	2.223618805
17	0.043440071	164.40992	29.54	5.38E-02	2.223618805
18	0.092724983	328.8197	59.08	1.08E-01	4.447059481
19	0.04001279	164.4099	29.54	5.38E-02	2.223618805
20	0.029347289	164.40991	29.54	5.38E-02	2.223618805
21	0.014781029	164.40992	29.54	5.38E-02	2.223618805

A3. YA Element Fuel Loading: zoneload2.txt

Column n 1	Column 2	Column n 3	Column 4	Column 5	Column 6
Region Number	Fraction of Total Power in Region	Region Volume	Current Grams of U-235 in Region	Current Grams of B-10 in Region	Current Grams of U-238 in Region

1	0.010867485	87.47156	16.56	2.88E-02	1.246479307
---	-------------	----------	-------	----------	-------------

2	0.017842942	87.47156	16.56	2.88E-02	1.246815681
3	0.022681867	87.47156	16.56	2.88E-02	1.246815681
4	0.048694121	174.9731	33.13	5.75E-02	2.493987759
5	0.020871814	87.47156	16.56	2.88E-02	1.246815681
6	0.015121304	87.47156	16.56	2.88E-02	1.246815681
7	0.006873305	87.47156	16.56	2.88E-02	1.246815681
8	0.04336593	350.767	88.32	9.97E-25	6.647503653
9	0.071923617	350.767	88.29	1.00E-24	6.645380887
10	0.09176932	350.767	88.29	1.00E-24	6.645380887
11	0.197142541	701.5339	176.57	2.00E-24	13.29058264
12	0.084662976	350.767	88.29	1.00E-24	6.645380887
13	0.061809467	350.767	88.29	1.00E-24	6.645380887
14	0.031464624	350.767	88.29	1.00E-24	6.645380887
15	0.020432599	164.4099	22.95	3.587E-02	2.222026366
16	0.034169927	164.40991	22.95	3.587E-02	2.223618805
17	0.043440071	164.40992	22.95	3.587E-02	2.223618805
18	0.092724983	328.8197	45.89	7.175E-02	4.447059481
19	0.04001279	164.4099	22.95	3.587E-02	2.223618805
20	0.029347289	164.40991	22.95	3.587E-02	2.223618805
21	0.014781029	164.40992	22.95	3.587E-02	2.223618805

A4. NB Element Fuel Loading: zoneload3.txt

Column n 1	Column 2	Column n 3	Column 4	Column 5	Column 6
Region Number	Fraction of Total Power in Region	Region Volume	Current Grams of U-235 in Region	Current Grams of B-10 in Region	Current Grams of U-238 in Region

1	0.010867485	87.47156	16.56	1.00E-24	1.246479307
2	0.017842942	87.47156	16.56	1.00E-24	1.246815681
3	0.022681867	87.47156	16.56	1.00E-24	1.246815681
4	0.048694121	174.9731	33.13	1.00E-24	2.493987759
5	0.020871814	87.47156	16.56	1.00E-24	1.246815681
6	0.015121304	87.47156	16.56	1.00E-24	1.246815681
7	0.006873305	87.47156	16.56	1.00E-24	1.246815681
8	0.04336593	350.767	88.32	9.97E-25	6.647503653
9	0.071923617	350.767	88.29	1.00E-24	6.645380887
10	0.09176932	350.767	88.29	1.00E-24	6.645380887
11	0.197142541	701.5339	176.57	2.00E-24	13.29058264
12	0.084662976	350.767	88.29	1.00E-24	6.645380887
13	0.061809467	350.767	88.29	1.00E-24	6.645380887
14	0.031464624	350.767	88.29	1.00E-24	6.645380887
15	0.020432599	164.4099	29.52	1.00E-24	2.222026366
16	0.034169927	164.40991	29.54	1.00E-24	2.223618805
17	0.043440071	164.40992	29.54	1.00E-24	2.223618805
18	0.092724983	328.8197	59.08	1.00E-24	4.447059481
19	0.04001279	164.4099	29.54	1.00E-24	2.223618805

20	0.029347289	164.40991	29.54	1.00E-24	2.223618805
21	0.014781029	164.40992	29.54	1.00E-24	2.223618805

A5. Element Structural Material Densities: structural.txt

Column n 1	Row 1	Column 2-7				
Region Number	MCNP Isotope Cross Section	Isotope Atomic Density in Region				
29000.50c	1001.50c	8016.50c	12000.51c	13027.50c	14000.51c	24000.50c
1 2.08116E-05	3.39334E-02	1.69667E-02	2.17649E-04	2.79372E-02	1.31011E-04	2.30476E-05
2 2.08116E-05	3.39334E-02	1.69667E-02	2.17649E-04	2.79372E-02	1.31011E-04	2.30476E-05
3 2.08116E-05	3.39334E-02	1.69667E-02	2.17649E-04	2.79372E-02	1.31011E-04	2.30476E-05
4 2.08116E-05	3.39334E-02	1.69667E-02	2.17649E-04	2.79372E-02	1.31011E-04	2.30476E-05
5 2.08116E-05	3.39334E-02	1.69667E-02	2.17649E-04	2.79372E-02	1.31011E-04	2.30476E-05
6 2.08116E-05	3.39334E-02	1.69667E-02	2.17649E-04	2.79372E-02	1.31011E-04	2.30476E-05
7 2.08116E-05	3.39334E-02	1.69667E-02	2.17649E-04	2.79372E-02	1.31011E-04	2.30476E-05
8 1.5882E-05	3.9208E-02	1.9604E-02	1.6610E-04	2.1354E-02	8.6245E-05	1.5528E-05
9 1.5882E-05	3.9208E-02	1.9604E-02	1.6610E-04	2.1354E-02	8.6245E-05	1.5528E-05
10 1.5882E-05	3.9208E-02	1.9604E-02	1.6610E-04	2.1354E-02	8.6245E-05	1.5528E-05
11 1.5882E-05	3.9208E-02	1.9604E-02	1.6610E-04	2.1354E-02	8.6245E-05	1.5528E-05
12 1.5882E-05	3.9208E-02	1.9604E-02	1.6610E-04	2.1354E-02	8.6245E-05	1.5528E-05
13 1.5882E-05	3.9208E-02	1.9604E-02	1.6610E-04	2.1354E-02	8.6245E-05	1.5528E-05
14 1.5882E-05	3.9208E-02	1.9604E-02	1.6610E-04	2.1354E-02	8.6245E-05	1.5528E-05
15 2.2943E-05	3.2128E-02	1.6064E-02	2.3994E-04	2.9582E-02	1.2459E-04	2.2432E-05
16 2.2943E-05	3.2128E-02	1.6064E-02	2.3994E-04	2.9582E-02	1.2459E-04	2.2432E-05
17 2.2943E-05	3.2128E-02	1.6064E-02	2.3994E-04	2.9582E-02	1.2459E-04	2.2432E-05
18 2.2943E-05	3.2128E-02	1.6064E-02	2.3994E-04	2.9582E-02	1.2459E-04	2.2432E-05
19 2.2943E-05	3.2128E-02	1.6064E-02	2.3994E-04	2.9582E-02	1.2459E-04	2.2432E-05
20 2.2943E-05	3.2128E-02	1.6064E-02	2.3994E-04	2.9582E-02	1.2459E-04	2.2432E-05
21 2.2943E-05	3.2128E-02	1.6064E-02	2.3994E-04	2.9582E-02	1.2459E-04	2.2432E-05

A6. Isotope Correlation: isotopelist.txt

Column 1	Column 2
MCNP Isotope Cross Section Set for a Given Nuclide Identifier	ORIGEN Nuclide Identifier

5010.70c	50100	62152.70c	621520
5011.70c	50110	62153.70c	621530
36083.70c	360830	63153.70c	631530
40091.70c	400910	63154.70c	631540
40093.70c	400930	63155.70c	631550
41095.70c	410950	63156.70c	631560
42095.70c	420950	64157.70c	641570
40096.70c	400960	90232.70c	902320
42097.70c	420970	90233.70c	902330
42098.70c	420980	91231.70c	912310
43099.70c	430990	91233.70c	912330
42100.70c	421000	92232.70c	922320
44101.70c	441010	92233.70c	922330
44102.70c	441020	92234.70c	922340
44103.70c	441030	92235.70c	922350
45103.70c	451030	92236.70c	922360
45105.70c	451050	92237.70c	922370
46105.70c	461050	92238.70c	922380
46107.70c	461070	92239.70c	922390
46108.70c	461080	93237.70c	932370
47109.70c	471090	93238.70c	932380
48113.70c	481130	93239.70c	932390
49115.70c	491150	94238.70c	942380
53129.70c	531290	94239.70c	942390
54131.70c	541310	94240.70c	942400
54133.70c	541330	94241.70c	942410
55133.70c	551330	94242.70c	942420
55134.70c	551340	94243.70c	942430
54135.70c	541350	94244.70c	942440
55135.70c	551350	95241.70c	952410
57139.70c	571390	95292.32c	952420
58141.70c	581410	95243.70c	952430
59141.70c	591410	96242.70c	962420
59143.70c	591430	96243.70c	962430
60143.70c	601430	96244.70c	962440
60145.70c	601450		
60147.70c	601470		
61147.70c	611470		
62147.70c	621470		
60148.70c	601480		
61148.70c	611480		
61149.70c	611490		
62149.70c	621490		
62150.70c	621500		
62151.70c	621510		

Program Input File Templates

A7. MCNP Fuel Element Cells: *basecell.txt* (excerpt)

Placeholder Parameter	Original Value		Updated Value		Output File	
Cell Material Atomic Density	XA Fresh Fuel Value		Output from makematcards.py		newcell.txt	
60001	2001	7.968986E-02	1221	-1228	-12	51 -33 100 -110 \$Elem 1 RZ 1 AZ 1
60002	2002	7.965995E-02	1221	-1228	-12	51 -33 110 -120 \$Elem 1 RZ 1 AZ 2
60003	2003	7.963898E-02	1221	-1228	-12	51 -33 120 -130 \$Elem 1 RZ 1 AZ 3
60004	2004	7.963054E-02	1221	-1228	-12	51 -33 130 -160 \$Elem 1 RZ 1 AZ 4
60005	2005	7.964214E-02	1221	-1228	-12	51 -33 160 -170 \$Elem 1 RZ 1 AZ 5
60006	2006	7.966605E-02	1221	-1228	-12	51 -33 170 -180 \$Elem 1 RZ 1 AZ 6
60007	2007	7.970644E-02	1221	-1228	-12	51 -33 180 -200 \$Elem 1 RZ 1 AZ 7
60008	2008	8.289907E-02	1229	-1230	-12	51 -33 100 -110 \$Elem 1 RZ 2 AZ 1
60009	2009	8.286822E-02	1229	-1230	-12	51 -33 110 -120 \$Elem 1 RZ 2 AZ 2
60010	2010	8.284416E-02	1229	-1230	-12	51 -33 120 -130 \$Elem 1 RZ 2 AZ 3
60011	2011	8.283363E-02	1229	-1230	-12	51 -33 130 -160 \$Elem 1 RZ 2 AZ 4
60012	2012	8.284809E-02	1229	-1230	-12	51 -33 160 -170 \$Elem 1 RZ 2 AZ 5
60013	2013	8.287436E-02	1229	-1230	-12	51 -33 170 -180 \$Elem 1 RZ 2 AZ 6
60014	2014	8.290937E-02	1229	-1230	-12	51 -33 180 -200 \$Elem 1 RZ 2 AZ 7
60015	2015	7.852864E-02	1231	-1238	-12	51 -33 100 -110 \$Elem 1 RZ 3 AZ 1
60016	2016	7.850189E-02	1231	-1238	-12	51 -33 110 -120 \$Elem 1 RZ 3 AZ 2
60017	2017	7.848217E-02	1231	-1238	-12	51 -33 120 -130 \$Elem 1 RZ 3 AZ 3
60018	2018	7.847436E-02	1231	-1238	-12	51 -33 130 -160 \$Elem 1 RZ 3 AZ 4
60019	2019	7.848519E-02	1231	-1238	-12	51 -33 160 -170 \$Elem 1 RZ 3 AZ 5
60020	2020	7.850687E-02	1231	-1238	-12	51 -33 170 -180 \$Elem 1 RZ 3 AZ 6
60021	2021	7.853583E-02	1231	-1238	-12	51 -33 180 -200 \$Elem 1 RZ 3 AZ 7
60022	2022	7.975780E-02	1221	-1228	-72	14 50 100 -110 \$Elem 2 RZ 1 AZ 1
60023	2023	7.975780E-02	1221	-1228	-72	14 50 110 -120 \$Elem 2 RZ 1 AZ 2
60024	2024	7.975780E-02	1221	-1228	-72	14 50 120 -130 \$Elem 2 RZ 1 AZ 3
60025	2025	7.975780E-02	1221	-1228	-72	14 50 130 -160 \$Elem 2 RZ 1 AZ 4
60026	2026	7.975780E-02	1221	-1228	-72	14 50 160 -170 \$Elem 2 RZ 1 AZ 5
60027	2027	7.975780E-02	1221	-1228	-72	14 50 170 -180 \$Elem 2 RZ 1 AZ 6
60028	2028	7.975780E-02	1221	-1228	-72	14 50 180 -200 \$Elem 2 RZ 1 AZ 7
60029	2029	8.294866E-02	1229	-1230	-72	14 50 100 -110 \$Elem 2 RZ 2 AZ 1
60030	2030	8.294866E-02	1229	-1230	-72	14 50 110 -120 \$Elem 2 RZ 2 AZ 2
60031	2031	8.294866E-02	1229	-1230	-72	14 50 120 -130 \$Elem 2 RZ 2 AZ 3
60032	2032	8.294866E-02	1229	-1230	-72	14 50 130 -160 \$Elem 2 RZ 2 AZ 4
60033	2033	8.294866E-02	1229	-1230	-72	14 50 160 -170 \$Elem 2 RZ 2 AZ 5
60034	2034	8.294866E-02	1229	-1230	-72	14 50 170 -180 \$Elem 2 RZ 2 AZ 6
60035	2035	8.294866E-02	1229	-1230	-72	14 50 180 -200 \$Elem 2 RZ 2 AZ 7
60036	2036	7.870346E-02	1231	-1238	-72	14 50 100 -110 \$Elem 2 RZ 3 AZ 1
60037	2037	7.870346E-02	1231	-1238	-72	14 50 110 -120 \$Elem 2 RZ 3 AZ 2
60038	2038	7.870346E-02	1231	-1238	-72	14 50 120 -130 \$Elem 2 RZ 3 AZ 3
60039	2039	7.870346E-02	1231	-1238	-72	14 50 130 -160 \$Elem 2 RZ 3 AZ 4
60040	2040	7.870346E-02	1231	-1238	-72	14 50 160 -170 \$Elem 2 RZ 3 AZ 5

```

60041 2041 7.870346E-02 1231 -1238 -72 14 50 170 -180 $Elem 2 RZ 3 AZ 6
60042 2042 7.870346E-02 1231 -1238 -72 14 50 180 -200 $Elem 2 RZ 3 AZ 7
.
.
.

```

A88. ORIGEN Input: atr-base.inp

	Updated Value 1	Updated Value 2	Updated Value 3	Updated Value 4
Placeholder Value	power	u235	u238	b10
Description	Power (MW per Unit Fuel) Required for Region to Reach Target Exposure in 49 Days	Current Grams of U-235 in Region	Current Grams of U-238 in Region	Current Grams of B-10 in Region
Initial Input Location	Column 2 of zoneload.txt, zoneload2.txt, or zoneload3.txt	Column 4 of zoneload.txt, zoneload2.txt, or zoneload3.txt	Column 6 of zoneload.txt, zoneload2.txt, or zoneload3.txt	Column 5 of zoneload.txt, zoneload2.txt, or zoneload3.txt

```

-1
-1
-1
RDA   due code quirk, input deck cannot apparently start with a comment card -
RDA   consequently, 3 input lines as listed first provide defaults for element
RDA   fractional reprocessing recoveries, element group fractional reprocessing
RDA   recoveries, and element grouping for fractional reprocessing recovery
RDA
RDA
RDA   7890123456789012345678901234567890123456789012345678901234567890
RDA   1           2           3           4           5           6           7           8
RDA
RDA
RDA   ATR LIMITING FUEL ELEMENT CALC USING STD ORIGEN2.1 & ATR LIBRARIES
RDA
RDA
RDA   !!! NOTE: other libraries are less conservative (EDF TRA-ATRC-1755) !!!
RDA
RDA
RDA   BAS   LIMITING FUEL ELEMENT (1085 G U235) DECAY.LIB/ATRXS.LIB
RDA   BAS   LIMITING FUEL ELEMENT (1085 G U235) DECAY.LIB/PWRU.LIB
RDA   BAS   LIMITING FUEL ELEMENT (1085 G U235) DECAY.LIB/THERMAL.LIB
RDA
RDA
RDA   library printing off
RDA   LIP   0   0   0
RDA
RDA
RDA   decay and cross-section libraries

```

```

LIB 0 1 2 3 204 908 909 9 0 0 1 0
RDA LIB 0 0 2 3 0 205 206 9 0 0 1 1
RDA LIB 0 0 2 3 0 202 203 9 0 0 1 0
RDA
RDA
RDA photon libraries
PHO 101 102 103 10
RDA
RDA
RDA activation, actinide, and fission product output options
OPTL 8 8 8 8 3 8 3 8 8 8 8 8 8 8 8 8 8 8 8 8 8 8
OPTA 8 8 8 8 3 8 3 8 2 8 8 8 8 8 8 8 8 8 8 8 8 8
OPTF 8 8 8 8 3 8 3 8 2 8 8 8 8 8 8 8 8 8 8 8 8 8
RDA
RDA
RDA input composition, feed rate, and removal rate
INP 1 1 -1 -1 1 1
RDA
RDA
RDA TIT ATR FUEL ELEMENT @ 10 MW, FOR 35 DAYS, W/ DECAY
RDA
RDA
RDA BUP
DOL 10 49
IRP 1.0 power 1 2 4 1
MOV 2 1 0 1.0
CON 10
HED 1 SCRAM
DEC 2.0 1 2 4 1
DEC 3.0 2 3 4 0
DEC 6.0 3 4 4 0
DEC 10.0 4 5 4 0
DEC 20.0 5 6 4 0
DEC 40.0 6 7 4 0
DEC 80.0 7 8 4 0
DEC 100.0 8 9 4 0
DEC 120.0 9 10 4 0
OUT 10 1 0 0
RDA BUP
PCH 10 10 10
RDA
RDA
RDA due a code quirk, comments cannot apparently follow the "end" card -
RDA consequently, comments precede initial compositions as listed below
RDA
RDA input based on IN-F-9-ATR, rev 14, Mar 96, as follows:
RDA
RDA ATR fuel elements contain 1075+-10 g U235 each - core U235 loading is
RDA then (conservatively) 1085 x 40 = 43400 g - given U235 wt% of 93+-1,

```

```

RDA    total core U mass is between 1085/.94 = 1154 g and 1065/.92 = 1158 g -
RDA    using the average, core U238 loading ~ (1156 - 1085) x 40 = 2840 g -
RDA    for this (limiting) single element calculation:
RDA
RDA
END
2    922350 u235    0 0.0
2    922380 u238    0 0.0
1    50100 b10      0 0.0
0

```

Initiating Python Scripts

A9. Exposure Parametric Study Script: makeburn.py

Required Input Files	atr-base.inp	zoneload.txt, zoneload2.txt, or zoneload3.txt	
Output File	results		
Variable Fields	While loop with variable element exposure (mwd_total) values	Input file (initial_comp) of zoneload.txt, zoneload2.txt, or zoneload3.txt	Note script assumes 49-day irradiation of elements.
Called Underlying Scripts	readinitial.py	O2file.py	GetIsotopes.py

```

#!/usr/bin/python
import re
import sys
import os
import readinitial
import O2file
import GetIsotopes
initial_comp = readinitial.readfile('zoneload.txt');
#    print initial_comp
mwd_total = 0.00001
mwd_array = []
mass = []
while (mwd_total < 350.00000):
    temp_mass = {}
    mass235 = 0
    mass238 = 0
    massb10 = 0
    mwd_array.append(mwd_total);
#    print mwd_total;
    for l in range(len(initial_comp)):
        temp235 = initial_comp[l].get('u235');
        temp238 = initial_comp[l].get('u238');
        tempb10 = initial_comp[l].get('b10');
        temppower = mwd_total/49 * float(initial_comp[l].get('frac'));
#        print str(temppower),mwd_total/49;
#    print initial_comp[l];

```

```

O2file.O2file(1,str(tempower),temp235,temp238,tempb10);
tempdict = GetIsotopes.GetIsotopes();
temparray = tempdict.keys();
for m in range(len(tempdict.keys())):
    if (temparray[m] == "922350"):
        mass235 =
mass235+float(tempdict.get('922350'))*235.0439;
        if (temparray[m] == '50100'):
            massb10 =
massb10+float(tempdict.get('50100'))*10.0129
            if (temparray[m] == '922380'):
                mass238 =
mass238+float(tempdict.get('922380'))*238.0508
        temp_mass =
{'mwd':mwd_total,'mass235':mass235,'mass238':mass238,'massb10':massb10};
        mass.append(temp_mass);
        mwd_total = mwd_total+5;
        results = open ("results","w")
        for m in range(len(mass)):

results.write("%s\t%s\t%s\t%s\n"%(mass[m].get('mwd'),mass[m].get('mass235'),
        mass[m].get('massb10'),mass[m].get('mass238')));
        results.close();

```

A10. Generate MCNP Material Cards Script: makematcards.py

Required Input Files	152BLoad .txt	atr- base.inp	basecell.txt	isotopelist.txt
	zoneload. txt	zoneload2 .txt	zoneload3.txt	structural.txt
Output Files	materialfil e.txt	newcell.tx t	Note script assumes 49-day irradiation of elements.	
Called Underlying Scripts	readinitial .py	readload.p y	readstructural .py	burnelem.py

```

#!/usr/bin/python
import readisotopes
import readinitial
import O2file
import GetIsotopes
import readstructural
import burnelem
import readload

# Load Data Calls readload, which read reload file

loaddata = readload.readload();

# Calls readinitial readfile function which reads in Initial Zone Loading Data
# For Type of Fuel Element

zoneinfo = readinitial.readfile('zoneload.txt');
zoneinfo2 = readinitial.readfile('zoneload2.txt');
zoneinfo3 = readinitial.readfile('zoneload3.txt');

```

```

# Initialize elem comp and mcnpcomp arrays
elemcomp = []
mcnpcomp = []

# Read in Structural Densities for each zone
#

strucdens = readstructural.readstructural();

# Calculate Power for Each Fuel Element Assuming 49 Days of Irradiation
#

for i in range(len(loaddata)):
    elemcomp = [];
    totalpower = float(loaddata[i].get('burnup'))/49
# Run ORIGEN for each element using function burnelem
    if (loaddata[i].get('type')== '1'):
        elemcomp=burnelem.burnelem(zoneinfo,strucdens,totalpower);
    if (loaddata[i].get('type')== '2'):
        elemcomp=burnelem.burnelem(zoneinfo2,strucdens,totalpower);
    if (loaddata[i].get('type')== '3'):
        elemcomp=burnelem.burnelem(zoneinfo3,strucdens,totalpower);
    mcnpcomp.append(elemcomp);

# Returns array of compositions for each region

matbeg=2000;
matfile = open('materialfile.txt','w')
totalarray = [];

# Write material card file assuming material numbering begins at 2000

for k in range(len(mcnpcomp)):
    for l in range(len(mcnpcomp[k])):
        temptotal = 0;
        matcard = str(matbeg+1)
        matfile.write('m%s' %(matcard))
        matbeg = matbeg+1
        for n in range(len(mcnpcomp[k][l])):
            matfile.write('\t%s\t%e\n' %( mcnpcomp[k][l][n].keys()[0],
            mcnpcomp[k][l][n].get(mcnpcomp[k][l][n].keys()[0])));
            temptotal = temptotal +
            float(mcnpcomp[k][l][n].get(mcnpcomp[k][l][n].keys()[
            0]))
        totalarray.append(temptotal);

cellcards = open('basecell.txt','r');
newcells = open('newcell.txt','w');
celllines = cellcards.readlines();

# write new cell cards from base cell card fiel
for s in range(len(celllines)):
    cell = celllines[s].split()
    cell.pop(2)
    cell.insert(2,totalarray[s]);
    for t in range(len(cell)):
        newcells.write('%s ' %(cell[t]));
    newcells.write('\n');
newcells.close();
cellcards.close();

```

Underlying Python Scripts

All. Element Burnup Script: burnelem.py

Required Input File	isotopelist.txt		
Variable Fields	Isotope List Input file name (isotopearray)		
Parent Script	makematcards.py		
Called Underlying Scripts	readisotopes.py	O2file.py	GetIsotopes.py

```
#!/usr/bin/python
import os
import GetIsotopes
import sys
import re
import O2file
import readisotopes
def burnelem(zoneinfo, strucdens, totalpower):
#
    isotopearray = []
    tempmcnp = []
    elemcomp = []
    origcomp = []
    print "print temp", tempmcnp;
# Read Isotope List which contains tracked isotopes for fuel and load list into
isotopearray

    isotopearray = readisotopes.readisotopes('isotopelist.txt');

    for i in range(len(zoneinfo)):
# Calculate Zone Power from Fractional Values
        zonecomp = [];
        zonepower = totalpower*float(zoneinfo[i].get('frac'));

# Rewrite Origen 2 Base File and Run O2 Base
        O2file.o2file(i, str(zonepower), zoneinfo[i].get('u235'),
            zoneinfo[i].get('u238'), zoneinfo[i].get('b10'))

        origcomp = GetIsotopes.GetIsotopes()

        for j in range(len(isotopearray)):
            if (origcomp.get(isotopearray[j].keys()[0])):
                atmdens =
float(origcomp.get(isotopearray[j].keys()[0]))/
                    float(zoneinfo[i].get('vol'))*0.60221;
            else:
                origcomp.update({isotopearray[j].keys()[0] :
1.000E-21})

                atmdens = 1.000E-21
```

```

        zonecomp.append({isotopearray[j].values()[0]:atmdens})
    for k in range(len(strucdens[i])):
        zonecomp.append(strucdens[i][k]);
    elemcomp.append(zonecomp);
return(elemcomp)

```

A12. Build ORIGEN Input File Script: O2file.py

Required Input File	atr- base.inp	
Output File	atr-node	
Parent Scripts	makeburn. py	burnelem. py
Called Underlying Script	rundriver.s h	

```

#!/usr/bin/python
import re
import os
def o2file(region,power,u235,u238,b10):
    o2file = open ("atr-base.inp","r")
    o2new = open ("atr-node","w")
    lines = o2file.readlines();
    for s in lines:
        if re.search("power",s):
            new_line = re.sub("power",power,s)
            # print new_line;
            o2new.write(new_line);
        elif re.search("u235",s):
            new_line = re.sub("u235",u235,s);
            o2new.write(new_line);
        elif re.search("u238",s):
            new_line = re.sub("u238",u238,s);
            o2new.write(new_line);
        elif re.search("b10",s):
            new_line = re.sub("b10",b10,s);
            o2new.write(new_line);
        else:
            o2new.write(s);
    o2file.close()
    o2new.close()
    os.system('rundriver.sh atr-node')

```

A13. Run ORIGEN Script: *rundriver.sh*

Input File Specification	Provided by O2file.py		
Utilized Output File	atr-node.pch		
Assumed HPC System	Fission		
Parent Script	O2file.py		
Called Underlying Script	GetCuries.awk (not provided)	GetPhotons.awk (not provided)	GetPhotons2.awk (not provided)
	GetPhotons3.awk (not provided)	GetWatts.awk (not provided)	

```
#!/bin/sh
#set -x

# Set directory
LIBS="/apps/exp_ctl/origen/2.2/src/ORIGEN22/origen22/libs"
ORIGEN="/apps/exp_ctl/origen/2.2/src/ORIGEN22/origen22/code/origen22t-inl"

# Input and output files that ORIGEN2 uses
#     TAPE3.INP - Substitution cross sections
#     TAPE5.INP - Standard input model
#     TAPE9.INP - Decay & Activation libraries
#     TAPE10.INP - Photon library
#
#     TAPE6.OUT - Standard output file
#     TAPE7.OUT - Punch File
#     TAPE11.OUT - Alternate output for line printer (not kept, just boilerplate)
#     TAPE12.OUT - Table of Contents
#     TAPE13.OUT - TOC for alternate output (not kept)
#     TAPE15.OUT - Debugging info (not kept)
#     TAPE16.OUT - Variable cross-section info (not kept)
#     TAPE50.OUT - Temp File (not kept)
#

rm -fr TAPE[0-9][0-9]*.INP TAPE[0-9][0-9]*.OUT

# Set up input data and libraries.
cp $1 TAPE5.INP
cat $LIBS/decay.lib $LIBS/atrxs.lib > TAPE9.INP
cp $LIBS/gxuo2brm.lib TAPE10.INP

# Run origen22
$ORIGEN

cat TAPE12.OUT TAPE6.OUT > $1.out
cp TAPE7.OUT $1.pch

# Clean up files that are not needed.
```

```
#rm -fr TAPE[0-9] [0-9]*.INP TAPE[0-9] [0-9]*.OUT
GetCuries.awk $1.out > $1.Ci
GetPhotons.awk $1.out > $1.Gamma1
GetPhotons2.awk $1.out > $1.Gamma2
GetPhotons3.awk $1.out > $1.Gamma3
GetWatts.awk $1.out > $1.Watts
```

A14. Obtain ORIGEN Isotope Results Script: *GetIsotopes.py*

Input File	atr-node.pch	
Input File Source	rundriver.sh script	
Parent Scripts	makeburn.py	burnelem.py

```
#!/usr/bin/python
import os
import re
import sys
def GetIsotopes():
#     print "hello world"
    pchfile = open("atr-node.pch","r")
    lines = pchfile.readlines();
    tempdict = {}
    for i in lines:
        if re.match("\s*[1-9]",i):
            line = i.split()
            j = (len(line)-1)/2 ;
#         print j;
            for k in range(j):
#             print k, line[2*k+1]
                if (int(line[2*k+1])>0):
                    temp2 = {line[2*k+1]:line[2*k+2]}
                    tempdict.update(temp2);

#     print tempdict.keys();
#     temparray = tempdict.keys();
#     for l in range(len(temparray)):
#         print temparray[l];
    return(tempdict);
```

A15. MCNP/ORIGEN Isotope Link Script: *readisotopes.py*

Input File Specification	Provided by burnelem.py
Parent Script	makematcards.py

```
#!/usr/bin/python
#     read in initial composition of Mark 7 fuel element
#     and fraction of burnup information to set up origen run
import re
```

```

import sys
import os
def readisotopes(isotopefile):
    isotopelist = open (isotopefile,"r")
    isotopelines = isotopelist.readlines();
    initdict = {};
    initarray = []
#   initvalues = ('frac','volume','u235','b10','u238')
#   initdict = initdict.fromkeys(initvalues)
#   print initdict;
    for i in isotopelines:
        nuclide = i.split();
        initdict = {nuclide[1]:nuclide[0]}
        initarray.append(initdict);
#   print line_elem[1];
#   for j in range(len(initarray)):
#       print initarray[j];
    return(initarray);
#array = readisotopes('isotopelist.txt');
#print array

```

A16. Obtain Cycle Loading Script: readload.py

Input File	152BLoad.txt
Variable Fields	Cycle Input file (loadfile)
Parent Script	makematcards.py

```

#!/usr/bin/python
import sys
import os
import re
#   Read Reload File in Text format to get U-235 and U-235 Initial
#   Return dictionary containing element # type U-235 B10 U-235 Initial
#   Burnup in MWd
def readload():
    loadfile = open('152BLoad.txt','r');
    data = ['element','type','u235','b10','u235initial','burnup']
    coreload = loadfile.readlines();
    loadarray = []
    for i in range(len(coreload)):
        line = coreload[i].split();
        loadarray.append(dict(zip(data,line)));
    return(loadarray)

```

A17. Initial Element Fuel Loading Read Script: readinitial.py

Input File Specification	Provided by initiating script	
Parent Scripts	makeburn.py	makematcards.py

```
#!/usr/bin/python
#   read in initial composition of Mark 7 fuel element
#   and fraction of burnup information to set up origen run
import re
import sys
import os
def readfile(zonefile):
    initcomp = open (zonefile,"r")
    regions = initcomp.readlines();
    initdict = {};
    initarray = []
#   initvalues = ('frac','volume','u235','b10','u238')
#   initdict = initdict.fromkeys(initvalues)
#   print initdict;
    for i in regions:
        line_elem = i.split();
        initdict =
{'frac':line_elem[1], 'vol':line_elem[2], 'u235':line_elem[3],
        'b10':line_elem[4], 'u238':line_elem[5]}
        initarray.append(initdict);
#       print line_elem[1];
#       for j in range(len(initarray)):
#           print initarray[j];
    return(initarray);
```

A18. Element Structural Loading Script: readstructural.py

Input File	structural.txt
Variable Fields	Element Structural Input file (structural)
Parent Script	makematcards.py

```
#!/usr/bin/python
import sys
import re
import os
def readstructural():
    structural = open('structural.txt','r')
    lines = structural.readlines();
    isotopes = lines[0].split();
    structarray = []
```

```

for i in range(len(lines)):
    temparray = []
    if (i == 0):
        pass;
    else:
        dummy = lines[i].split();
        del dummy[0];
        for k in range(len(dummy)):
            temparray.append({isotopes[k]:float(dummy[k])})
        structarray.append(temparray);
return(structarray);

```

Examble Output File

A19. Cell Material Specification: materialfile.txt (excerpt)

Column 1	Column 2	Column 3
Material Specification for a Given MCNP Cell	MCNP Isotope Cross Section Set for a Given Nuclide Identifier	Atomic Fraction of Constituents
m2001	5010.70c	6.034247e-06
	5011.70c	1.579474e-09
	36083.70c	3.133336e-07
	40091.70c	2.911513e-06
	40093.70c	3.870474e-06
	41095.70c	7.095308e-07
	42095.70c	2.321431e-06
	40096.70c	3.777256e-06
	42097.70c	3.623178e-06
	42098.70c	3.511578e-06
	43099.70c	3.545313e-06
	42100.70c	3.778358e-06
	44101.70c	3.038259e-06
	44102.70c	2.558125e-06
	44103.70c	1.522262e-07
	45103.70c	1.711177e-06
	45105.70c	1.000000e-21
	46105.70c	5.612976e-07
	46107.70c	1.181404e-07
	46108.70c	5.680239e-08
	47109.70c	2.679983e-08
	48113.70c	1.186292e-09
	49115.70c	8.174130e-09
	53129.70c	4.473293e-07
	54131.70c	1.681642e-06
	54133.70c	9.853293e-14
	55133.70c	3.963624e-06
	55134.70c	4.638249e-08

54135.70c	1.000000e-21
55135.70c	5.374286e-07
57139.70c	3.867927e-06
58141.70c	1.706977e-07
59141.70c	3.363214e-06
59143.70c	3.115505e-09
60143.70c	3.451407e-06
60145.70c	2.312274e-06
60147.70c	2.263738e-10
61147.70c	1.154554e-06
62147.70c	1.118685e-07
60148.70c	1.032833e-06
61148.70c	7.385839e-12
61149.70c	2.242189e-24
62149.70c	8.583078e-08
62150.70c	5.948396e-07
62151.70c	1.092041e-07
62152.70c	2.793924e-07
62153.70c	2.828898e-27
63153.70c	1.262229e-07
63154.70c	9.600627e-09
63155.70c	1.388425e-08
63156.70c	3.256847e-11
64157.70c	2.900842e-10
90232.70c	1.543880e-13
90233.70c	1.000000e-21
91231.70c	1.921227e-13
91233.70c	6.740129e-15
92232.70c	6.374280e-15
92233.70c	2.788347e-12
92234.70c	3.266141e-09
92235.70c	4.118666e-04
92236.70c	1.317513e-05
92237.70c	3.021392e-13
92238.70c	3.531062e-05
92239.70c	1.000000e-21
93237.70c	2.036476e-07
93238.70c	1.279579e-20
93239.70c	4.972154e-18
94238.70c	3.937531e-09
94239.70c	6.033215e-07
94240.70c	3.815053e-08
94241.70c	9.221972e-09
94242.70c	2.653752e-10
94243.70c	1.000000e-21
94244.70c	1.517030e-15
95241.70c	1.611487e-10
95292.32c	8.028864e-19
95243.70c	5.690428e-12

	96242.70c	3.693333e-13
	96243.70c	1.480266e-15
	96244.70c	1.528183e-13
	1001.50c	3.393340e-02
	8016.50c	1.696670e-02
	12000.51c	2.176490e-04
	13027.50c	2.793720e-02
	14000.51c	1.310110e-04
	24000.50c	2.304760e-05
	29000.50c	2.081160e-05
m2002	5010.70c	2.507110e-06
	5011.70c	1.983326e-09